

Idiopathic pulmonary fibrosis: quantitative methods to compare structure and function to the normal lung

Yuwen Zhang

A thesis submitted in fulfilment of the requirements for the degree of Doctor of
Philosophy in Bioengineering.

This thesis is for examination purposes only and is confidential to the examination
process.

Auckland Bioengineering Institute

The University of Auckland

2019

Abstract

Idiopathic pulmonary fibrosis (IPF), the most aggressive and frequent form of idiopathic interstitial pneumonias (IIPs), is a chronic and life-threatening disease of unknown cause. It is characterised by progressive worsening of dyspnea and other lung function and is associated with a poor prognosis. IPF occurs primarily in middle-aged and elderly adults, and is more frequent in males than females. Even worse, the aetiology of IPF remains elusive, and its progression is variable and unpredictable, hence there are no biomarkers that can indicate the likely progression of the disease. A quantification scheme that allows recognition of disease consistently across radiology, pulmonary and pathology disciplines remains difficult. In this study, a combination of quantitative information extracted from high resolution computed tomography (HRCT), clinical knowledge, and computational modelling was used to help develop a better understanding of the progression of IPF.

First, an automatic lung lobe segmentation method from HRCT images was developed, which is guided by a statistical shape model that can predict the likely region of fissure locations. This new method was able to estimate the fissure location in 100% of cases including both normal healthy and IPF subjects, whereas two comparison segmentation softwares that use anatomy-based methods fail in several cases. Second, tissue abnormalities in a cohort of IPF lungs were classified, and then mapped to a statisti-

cal shape model, and quantitative approaches were used to analyse lung shape, tissue density, tissue volume, the spatial distribution of abnormalities, and regional changes in tissue over time. Fibrosis was found to present predominantly basally and peripherally in the lung. In contrast, emphysema in these subjects was mostly located in the upper lobes. The first principal statistical shape mode (explaining > 20% of the shape variation in normal lungs) is significantly different between IPF and normal and is strongly correlated with fibrosis extent in IPF. Finally, a preliminary computational model of lung function was developed which integrates quantification analysis from volumetric CT and pulmonary function test data to understand differences between IPF and normal older lungs. Ventilation (\dot{V}), perfusion (\dot{Q}) and gas exchange models were parameterized to simulate \dot{V} and \dot{Q} distributions and O_2 and CO_2 exchange. The computational model can reasonably predict abnormalities in ventilation, perfusion and gas exchange in the IPF lung, and estimate the difference of lung function between IPF patients and older normal people. Results suggest that tissue abnormalities on volumetric CT imaging do not provide enough information to explain the decline of lung function in IPF patients, and an individual impaired gas exchange appears to happen not only in tissue that is conventionally classified as "abnormal", but also in CT-visualized 'normal' tissues.

IPF is a complex and progressive disease that has multifarious physiological processes and significant individual differences. The methods and models presented in this thesis provide a basis for application to research in IPF lung function, and furthers investigations into the underlying relationship between physiological mechanisms and disease progression of IPF.

Acknowledgements

I would like to use this opportunity to express my gratitude to everyone who contributed to this research and supported me throughout my PhD.

First and foremost, I would like to express my sincere gratitude to my supervisor Professor Merryn Tawhai, Dr Alys Clark and Dr Haribalan Kumar for the tremendous patience, motivation, enthusiasm, and immense knowledge. Their continuous guidance helped me in all the time of research and writing of this thesis. This thesis would not be completed without their valuable advice and unfailing trust. It is my great honour to be their student and to have worked under their supervision.

I would like to thank Brian Bartholmai from Mayo Clinic for providing CALIPER classification data, and thank Dr David Milne and Dr Margaret Wilsher from Auckland Hospital for providing the CT image data of IPF patients. Without their constant assistance, this research would not have been possible.

I am also great thankful for the amazing people of lung and placenta groups: Mahyar, Hamed, Zay, Amir, Luca, Behdad, Toby, Kelly, Kerry, Rojan, Win, Mabelle and Izza. My special thanks goes to my lovely friends: Nancy, Wendy and Si. Thank you for giving me so much help, warm and happiness during my PhD.

A big thank to my family for supporting me spiritually throughout my life. Last but not the least, my deepest gratitude to my beloved husband, Xinjian. Thanks for

accompanying me, encouraging me, supporting me and loving me. Words would never say how grateful I am to you. Thank you!

Table of Contents

Abstract	iv
Acknowledgement	vi
Table of Contents	xii
List of Figures	xxxv
List of Tables	xxxix
List of Abbreviations	xliii
1 Introduction	1
1.1 Motivation	1
1.2 Thesis objectives	2
1.3 Thesis overview	3
2 Background	7
2.1 Introduction to idiopathic pulmonary fibrosis	7
2.1.1 Definition	7
2.1.2 Disease classification	8

2.2 Epidemiology, etiology and pathogenesis	10
2.2.1 Epidemiology	10
2.2.2 Pathogenesis and potential contributors to aetiology	10
2.3 Diagnosis	12
2.3.1 Clinical presentations	13
2.3.2 Radiographic features	14
2.3.3 Histopathology	15
2.3.4 Diagnostic criteria	17
2.4 Clinical course	19
2.4.1 Slow and rapid progressive course	20
2.4.2 Acute exacerbations of IPF	20
2.5 Complications and comorbidities	21
2.5.1 IPF and emphysema	22
2.5.2 IPF and pulmonary hypertension	23
2.6 Physiological alterations	24
2.6.1 Alterations in the mechanical properties of the lung	24
2.6.2 Alterations in pulmonary gas exchange	29
2.7 Summary	32
3 Pulmonary lobar segmentation from CT scans	35
3.1 Background	36
3.1.1 Pulmonary lobar anatomy	36
3.1.2 High resolution computed tomography	37
3.1.3 The importance of pulmonary lobar segmentation	38

3.1.4	Challenges of automatic pulmonary lobar segmentation from CT scans	39
3.2	Review of current published methods for pulmonary lobar segmentation	40
3.2.1	Lung segmentation	41
3.2.2	Fissure detection	47
3.3	Methods: automatic statistical shape model based lobar segmentation method	53
3.3.1	Lung segmentation	55
3.3.2	Statistical finite element models of lung and fissure shape	55
3.3.3	Initial prediction of lobar location in an individual	63
3.3.4	Multi-scale Hessian-based fissure detection	64
3.3.5	Interactive user control interface	72
3.4	Results for SMM segmentation	77
3.4.1	Testing CT dataset	77
3.4.2	Test and results	78
3.5	Discussion	88
3.6	Summary	92
4	Quantitative computerized analysis of idiopathic pulmonary fibrosis	93
4.1	Background	94
4.1.1	Challenges of IPF diagnosis	94
4.1.2	Advantages of quantitative analysis using HRCT	95
4.1.3	Review of current published methods of quantitative analysis of lung disease	97

4.1.4 Computer-Aided Lung Informatics for Pathology Evaluation and Ratings	101
4.2 Methods: quantitative analysis of IPF lungs	104
4.2.1 Tissue classification of IPF lungs	105
4.2.2 Tissue quantification of IPF lungs	109
4.2.3 Volume analysis of IPF lungs	111
4.2.4 SSM based shape analysis of IPF lungs	112
4.3 Results	114
4.3.1 Normalization of classified data	114
4.3.2 Tissue quantification of IPF lungs	116
4.3.3 Volume analysis of IPF lungs	134
4.3.4 SSM - shape analysis of IPF lungs	136
4.4 Discussion	143
4.5 Summary	148
5 Functional modelling of idiopathic pulmonary fibrosis	149
5.1 Respiratory structure and function in older people	150
5.1.1 Ageing-associated alterations in the chest wall and respiratory muscle function	151
5.1.2 Ageing-associated alterations in pulmonary mechanics and lung volumes	153
5.1.3 Ageing-associated alterations in gas exchange	155
5.1.4 Relationship between lung function and lung shape	156
5.2 Methods: Patient-specific modelling of IPF lung function	157
5.2.1 Clinical data	157

5.2.2	Construction of lung lobe geometry	159
5.2.3	Construction of airway/vascular geometry	161
5.2.4	Construction of computational models	167
5.2.5	Modelling lung function	177
5.3	Results	181
5.3.1	Construction of lung lobe geometry	181
5.3.2	Construction of airway/vasculature geometry	183
5.3.3	Deep inspiration modelling	188
5.3.4	Perfusion modelling	189
5.3.5	Gas exchange model	191
5.4	Discussion	196
5.5	Summary	201
6	Conclusion	203
6.1	Thesis Summary	203
6.2	Future directions	206
6.2.1	Improvement of the statistical shape model	206
6.2.2	Involvement of diffusing capacity for carbon monoxide in the lung functional model	207
Appendices		209
A	Mapped classification data for each patient	211
B	Spatial distribution of abnormalities for each patient	219
B.1	Basal-to-apical distribution over time for each patient	219
B.2	Dorso-to-ventral distribution over time for each patient	231

B.3 Lobar distribution over time for each patient	241
C Figures of V/Q ratio and arterial oxygen distribution	251
List of References	263

List of Figures

- 2.1 Classification of the interstitial lung diseases. IPF belongs to the family of interstitial lung disease (ILD), and belongs to a subgroup known as idiopathic interstitial pneumonia (IIP) (Troy and Corte, 2012). 9
- 2.2 HRCT images of UIP pattern from two patients. The first is from a woman with progressive cough and dyspnoea, showing her upper (a), lower (b) lung zones and a sagittal plane of the lungs (c). These images show lower lobe-predominant peripheral honeycomb change (**b and c, arrows**), which is typical of UIP pattern. This patient had no systemic disease or exposures that would exclude idiopathic disease: the diagnosis of IPF is certain. In contrast, the second is a woman with progressive breathlessness, who could be diagnosed with possible IPF. The upper (d), lower (e) lung zones and sagittal image of the lungs (f) demonstrate peripheral, basilar-predominant, reticular densities with traction bronchiectasis (e and f, arrows) consistent with fibrosis. Surgical lung biopsy is suggested. Reproduced from (Martinez et al., 2017). 15

2.3 Surgical lung biopsy specimens of UIP pattern. (A) Scanning power microscopy showing a patchy process with honeycomb spaces (thick arrow), some preserved lung tissue regions (thin arrow), and fibrosis extending into the lung from the subpleural regions. (B) Adjacent to the regions of more chronic fibrosis (arrow) is a fibroblast focus (asterisk), recognized by its convex shape and composition of edematous fibroblastic tissue, suggestive of recent lung injury. Reproduced from (Raghu et al., 2011).	16
2.4 Diagnostic algorithm for IPF. Patients with suspected IPF (i.e., patients with unexplained dyspnea on exertion and/or cough with evidence of ILD) should be carefully evaluated for identifiable causes of ILD. In the absence of an identifiable cause for ILD, an HRCT demonstrating UIP pattern is diagnostic of IPF. In the absence of UIP pattern on HRCT, IPF can be diagnosed by the combination of specific HRCT and histopathological patterns. The accuracy of the diagnosis of IPF increases with multidisciplinary discussion (MDD) among ILD experts. Reproduced from (Raghu et al., 2011).	18
2.5 Schematic representation of potential clinical courses of IPF. A sub-clinical period of disease progression exists during which only radiographic evidence of disease may be noted. This is followed by a symptomatic phase comprising clinical stages (both pre-diagnosis and post-diagnosis). The rate of deterioration and progression to death may be fast (line A), mixed (line B), or slow (lines C and D), with phases of relative disease stability interspersed with acute decline (asterisks). Reproduced from (Ley et al., 2011).	21

3.3 Illustration of the performance of conventional 3D thresholding lung segmentation methods on pathological lungs. Lung borders are not recognized accurately because of the higher densities of the abnormalities compared to the normal tissues. Reproduced from (Van Rikxoort and Van Ginneken, 2013).	45
3.4 (a) Segmented volumes of the vascular tree. There are no large vessels in the vicinity of lobar fissures. (b) Anatomically labeled airway tree showing lobar subtrees. The airway tree can be classified corresponding to five lobes. Reproduced from (Ukil and Reinhardt, 2009).	49
3.5 Flow diagram of the lobar segmentation process.	54
3.6 Lung segmentation result using the common thresholding method. (a) Raw CT image. (b) Segmented lungs.	55
3.7 Finite element modeling of lung lobe shape. (a) Lung surface data extracted from segmented lung masks (purple points for left lung, blue points for right lung). (b) Manual digitized fissure points in 2D sagittal image of right lung (purple points for right oblique fissure, blue points for right horizontal fissure). (c) Manual digitized fissure points shown in 3D (pink points for left oblique fissure, purple points for right oblique fissure, blue points for right horizontal fissure). (d) Lobe shape fitting with lung surface data and digitized fissure data of right lung.	60
3.8 Statistical shape model construction based on principal component analysis. (a) Procrustes aligned meshes of 50 subjects. (b) Average shape model of 50 training subjects. All the weight values are zero for this shape model.	63

3.9 Fissure prediction results compared to ground truth fissure points for one subject. The fissure surface meshes are estimated fissure locations and the red points are manual tracing fissure points by an expert. (a) Left lung. (b) Right lung.	65
3.10 The three eigenvectors of the Hessian matrix representing plane-like structure (fissure). λ_1 and λ_2 are parallel to fissure plane, λ_3 is perpendicular to fissure plane.	69
3.11 The three eigenvectors of the Hessian matrix representing tube-like structure (vessel). λ_1 is parallel to vessel tube, λ_2 and λ_3 are perpendicular to vessel tube.	71
3.12 Hessian-based multiscale fissure detection results. (a) Hessian-based plane-like structure enhancement filter. (b) Remove vessel voxels (tube-like structures). (c) Selected search regions for fissure detection based on SSM initial fissure prediction. (d) 2D and 3D eigenvector based connected component filter. (e) Fissure candidate points. (f) β -spline curve fissure surface fitting.	73
3.13 PTK User interactive interface. It consists of data input section, image visualization section, user plugin section and toolbar section.	75
3.14 Fissure detection results before and after control the search regions. (a) Fissure detection result with a search distance of default 20 voxels. (b) Fissure detection result after setting a specific search distance depending on the accuracy of initial fissure guessing.	76

3.15 Manual correction on automatic fissure detection results (a) Manually select a set of landmarks on real fissure lines shown in raw images to correct automatic fissure detection results (red landmarks are for left oblique fissure, green landmarks are for right oblique fissure, blue landmarks are for right horizontal fissure). (b) Corrected fissure detection results shown with raw images. The corrected fissure lines can match the real fissure locations.	78
3.16 Sagittal, axial, and coronal views illustrating raw image, SSM based initial fissure guessing and final automatic fissure detection results of a normal healthy subject. (a), (d), (g) are sagittal, axial and coronal raw images. (b), (e), (h) are sagittal, axial and coronal SSM based initial fissure guessing results. (c), (f), (i) are sagittal, axial and coronal automatic fissure detection results.	79
3.17 Sagittal, axial, and coronal views illustrating raw image, SSM based initial fissure guessing and automatic fissure detection results of an IPF subject. (a), (d), (g) are sagittal, axial and coronal raw images. (b), (e), (h) are sagittal, axial and coronal SSM based initial fissure guessing results. (c), (f), (i) are sagittal, axial and coronal automatic fissure detection results.	80
3.18 The spatial distribution of error between the gold-standard and semi-automatic methods for three representative subjects, highlighting localized regions of low accuracy.	83

3.19 An inaccurate initial fissure estimate for an IPF subject caused by mislabeling of lobar airway branches using marker-based interactive watershed transformation algorithm (sagittal view, left lung). (a) The mislabeling of lobar airway branches. Purple is for left upper branches and yellow is for left lower branches. The lower branches in the red box are mis-detected as upper branches. (b) The initial fissure guessing based on the erroneous airway branch labelling result. The approximate fissure has a significant erroneous shift in the red box where mislabelling of lobar airway branches occurs.	84
4.1 Computed tomography images demonstrating appearance and various visual manifestations of idiopathic pulmonary fibrosis: a) normal, b) ground glass, c) reticular changes (arrows), d) honeycombing (arrows) and e) emphysema (arrow). In training datasets, the consensus of four thoracic radiologists was used to identify multiple volumes of interest (VOIs) corresponding to normal, ground-glass density, reticular abnormalities, honeycombing and emphysema. Reproduced from (Maldonado et al., 2013).	102
4.2 Colour labelled classification result from CALIPER of one subject diagnosed with IPF. (a) Transverse plane. (b) Coronal plane. (c) Sagittal plane. (d) 3D colour labelled lung.	104
4.3 Diagram of gap filling steps within the mapped data. (a) Get axial slices of mapped data (with gaps). (b) Define lung boundary (SSM defined). (c) Get lung mask. (d) Fill the gaps within lung mask.	108

4.4 Diagram of subpleural-to-internal percentage measurement. $R_{\text{subplerual}}$ is the subpleural-to-internal percentage measurement, AB and AC are linear distance between A and B, and A and C, respectively.	110
4.5 Classified data (top row) and mapped data (bottom row) for three time points from one subject diagnosed with IPF. (a) The first time point, scan time: 0 months. (b) The second time point, scan time: 15 months. (c) The third time point, scan time: 20 months.	115
4.6 Average tissue density (g/cm^3) of each CT pattern in IPF lungs. Each data point represents the tissue density of one time point from one patient. X axis represents the month interval of scan time for each patient, and "0" represents the first scan for this patient. (a) Tissue density of left lung. (b) Tissue density of right lung.	117
4.7 Volume percentage of each tissue classification plotted against lung height (cranio-caudal axis) in IPF left and right lungs. The average percentage was calculated within 5% sections of the lung height from the base to apex. Red shows the average value at each position across all patients, and blue shows the standard deviation. (a) (b) is ground-glass distribution. (c) (d) is reticular distribution. (e) (f) is honeycomb distribution. (g) (h) is emphysema distribution.	119

4.11 Volume percentage of each tissue classification plotted in the direction of the dorso-ventral axis in IPF left and right lungs at month 0. The average percentage was calculated within 5% sections along the axis from posterior to anterior. Red shows the average value at each position across all patients, and blue shows the standard deviation. (a) (b) is ground-glass distribution. (c) (d) is reticular distribution. (e) (f) is honeycomb distribution. (g) (h) is emphysema distribution.	125
4.12 Volume percentage of each tissue classification plotted in the direction of dorso-ventral axis from one patient diagnosed with IPF in left and right lungs over time. The average percentage was calculated within 5% sections along the axis from posterior to anterior. (a) (b) is ground-glass distribution. (c) (d) is reticular distribution. (e) (f) is honeycomb distribution. (g) (h) is emphysema distribution. The time interval from time point 1 to time point 2 is 63 months, from time point 1 to time point 2 is 16 months, from time point 1 to time point 3 is 79 months. . .	127
4.13 Subpleural-to-internal percentage of connected cluster of disease in IPF left and right lung. (a) Left lung. (b) Right lung.	129
4.14 Average lobar distribution of abnormal tissue. The tissue percentage in different lobes is shown by color, and each bar represents the volume percentage of the CT pattern for one lobe across all the subjects. The black line shows the standard deviation. (a) Ground-glass lobar distribution. (b) Reticular lobar distribution. (c) Honeycomb lobar distribution. (d) Emphysema lobar distribution.	130

4.15 Lobar distribution of abnormal tissue for one patient diagnosed with IPF over time. The tissue percentage in different lobes is shown by colour, and each bar represents the volume percentage of the CT pattern for one lobe. (a) Ground-glass lobar distribution. (b) Reticular lobar distribution. (c) Honeycomb lobar distribution. (d) Emphysema lobar distribution. The time interval from time point 1 to time point 2 is 63 months, from time point 1 to time point 2 is 16 months, from time point 1 to time point 3 is 79 months.	131
4.16 CALIPER tissue classification overlapping on raw image. Green is the normal region, red is the reticular region, yellow is the ground-glass region, and blue is the mild LAA region. (a) Axial view. (b) Sagittal view.	134
4.17 Shape differences between IPF subjects and old normal subjects of the first three modes (shown with different time point). (a) Mode 1 weight. (b) Mode 2 weight. (c) Mode 3 weight.	139
4.18 PCA-derived shape variation of the first shape mode, with different values of standard deviation ($-3\sigma, -1\sigma, \mu, 1\sigma, 3\sigma$) added to the mean shape model. (a) Anterior view. (b) Basal view. (c) Posterior view. The colormap shows the extent of shape variation from the mean shape model.	140
4.19 A Linear regression of the PCA-derived first three modes with respect to overall fibrosis percentage. (a) Mode 1 weight. (b) Mode 2 weight. (c) Mode 3 weight.	142
5.1 Computational modeling framework for IPF and older normal lung function.	158

5.2 Generation of airway tree. (a) Manual digitized upper airway tree from HRCT images in 3D. Green lines are the centerlines of upper airway tree, and red points represent airway nodes. (b) Geometry of full conducting airway tree generated using volume-filling algorithm. The model is shown from the anterior view, with the left lung on right, and right lung on left.	163
5.3 Disease labeled airway nodes. For the model in (a), green is classified as normal tissue, blue is fibrosis, and red is emphysema. For the classified data in (b), the colour scheme indicates the tissue classification type . . .	178
5.4 Lung mesh for IPF subject and the predicted lung mesh for a normal control with same characteristics. (a) IPF lung mesh generated from CT imaging of a patient with IPF. (b) Control mesh predicted using the reference values for the same patient.	182
5.5 Generated normal control airway tree (top row) and IPF airway tree (bottom row) for one patient diagnosed with IPF. (a) Anterior view. (b) Left lung side. (c) Right lung side.	185
5.6 Generated geometry of the vessel trees. (a) IPF vessel tree. (b) Control vessel tree. The radius of branches are visualized as shown by the colour bars.	186
5.7 V/Q ratio distribution and end-capillary oxygen distribution of control, CT-based and PFT-based simulation result at one time point for one patient diagnosed with IPF). (a) V and Q with respect to V/Q ratio. (b) Distribution of end-capillary oxygen levels amongst alveoli.	192

5.8 Ventilation, perfusion and V/Q ratio distribution against lung height (cranio-caudal axis). (a) Ventilation distribution against lung height. (b) Perfusion distribution against lung height. (c) V/Q ratio distribution against lung height.	194
A.1 Classified data (top row) and mapped data (bottom row) of three time points of case IPF2. (a) The first time point, scan time: 0 month. (b) The second time point, scan time: 15 months. (c) The third time point, scan time: 35 months.	212
A.2 Classified data (top row) and mapped data (bottom row) of three time points of case IPF3. (a) The first time point, scan time: 0 month. (b) The second time point, scan time: 11 months. (c) The third time point, scan time: 30 months.	213
A.3 Classified data (top row) and mapped data (bottom row) of three time points of case IPF5. (a) The first time point, scan time: 0 month. (b) The second time point, scan time: 12 months. (c) The third time point, scan time: 23 months.	214
A.4 Classified data (top row) and mapped data (bottom row) of three time points of case IPF6. (a) The first time point, scan time: 0 month. (b) The second time point, scan time: 15 months. (c) The third time point, scan time: 20 months.	215
A.5 Classified data (top row) and mapped data (bottom row) of three time points of case IPF9. (a) The first time point, scan time: 0 month. (b) The second time point, scan time: 6 months. (c) The third time point, scan time: 19 months.	216

A.6 Classified data (top row) and mapped data (bottom row) of three time points of case IPF15. (a) The first time point, scan time: 0 month. (b) The second time point, scan time: 13 months. (c) The third time point, scan time: 76 months.	217
A.7 Classified data (top row) and mapped data (bottom row) of three time points of case IPF21. (a) The first time point, scan time: 0 month. (b) The second time point, scan time: 63 months. (c) The third time point, scan time: 79 months.	218
B.1 Volume percentage of each tissue classification plotted against lung height (cranio-caudal axis) of case IPF2 in left and right lungs over time. The average percentage was calculated within 5% sections of the lung height from the base to apex. (a) (b) is ground-glass distribution. (c) (d) is reticular distribution. (e) (f) is honeycomb distribution. (g) (h) is emphysema distribution.	220
B.2 Volume percentage of each tissue classification plotted against lung height (cranio-caudal axis) of case IPF3 in left and right lungs over time. The average percentage was calculated within 5% sections of the lung height from the base to apex. (a) (b) is ground-glass distribution. (c) (d) is reticular distribution. (e) (f) is honeycomb distribution. (g) (h) is emphysema distribution.	221

B.3 Volume percentage of each tissue classification plotted against lung height (cranio-caudal axis) of case IPF5 in left and right lungs over time. The average percentage was calculated within 5% sections of the lung height from the base to apex. (a) (b) is ground-glass distribution. (c) (d) is reticular distribution. (e) (f) is honeycomb distribution. (g) (h) is emphysema distribution.	222
B.4 Volume percentage of each tissue classification plotted against lung height (cranio-caudal axis) of case IPF6 in left and right lungs over time. The average percentage was calculated within 5% sections of the lung height from the base to apex. (a) (b) is ground-glass distribution. (c) (d) is reticular distribution. (e) (f) is honeycomb distribution. (g) (h) is emphysema distribution.	223
B.5 Volume percentage of each tissue classification plotted against lung height (cranio-caudal axis) of case IPF9 in left and right lungs over time. The average percentage was calculated within 5% sections of the lung height from the base to apex. (a) (b) is ground-glass distribution. (c) (d) is reticular distribution. (e) (f) is honeycomb distribution. (g) (h) is emphysema distribution.	224
B.6 Volume percentage of each tissue classification plotted against lung height (cranio-caudal axis) of case IPF10 in left and right lungs over time. The average percentage was calculated within 5% sections of the lung height from the base to apex. (a) (b) is ground-glass distribution. (c) (d) is reticular distribution. (e) (f) is honeycomb distribution. (g) (h) is emphysema distribution.	225

B.7 Volume percentage of each tissue classification plotted against lung height (cranio-caudal axis) of case IPF13 in left and right lungs over time. The average percentage was calculated within 5% sections of the lung height from the base to apex. (a) (b) is ground-glass distribution. (c) (d) is reticular distribution. (e) (f) is honeycomb distribution. (g) (h) is emphysema distribution.	226
B.8 Volume percentage of each tissue classification plotted against lung height (cranio-caudal axis) of case IPF14 in left and right lungs over time. The average percentage was calculated within 5% sections of the lung height from the base to apex. (a) (b) is ground-glass distribution. (c) (d) is reticular distribution. (e) (f) is honeycomb distribution. (g) (h) is emphysema distribution.	227
B.9 Volume percentage of each tissue classification plotted against lung height (cranio-caudal axis) of case IPF15 in left and right lungs over time. The average percentage was calculated within 5% sections of the lung height from the base to apex. (a) (b) is ground-glass distribution. (c) (d) is reticular distribution. (e) (f) is honeycomb distribution. (g) (h) is emphysema distribution.	228
B.10 Volume percentage of each tissue classification plotted against lung height (cranio-caudal axis) of case IPF21 in left and right lungs over time. The average percentage was calculated within 5% sections of the lung height from the base to apex. (a) (b) is ground-glass distribution. (c) (d) is reticular distribution. (e) (f) is honeycomb distribution. (g) (h) is emphysema distribution.	229

B.11 Volume percentage of each tissue classification plotted in the direction of dorso-ventral axis of case IPF2 in left and right lungs over time. The average percentage was calculated within 5% sections along the axis from posterior to anterior. (a) (b) is ground-glass distribution. (c) (d) is reticular distribution. (e) (f) is honeycomb distribution. (g) (h) is emphysema distribution.	231
B.12 Volume percentage of each tissue classification plotted in the direction of dorso-ventral axis of case IPF3 in left and right lungs over time. The average percentage was calculated within 5% sections along the axis from posterior to anterior. (a) (b) is ground-glass distribution. (c) (d) is reticular distribution. (e) (f) is honeycomb distribution. (g) (h) is emphysema distribution.	232
B.13 Volume percentage of each tissue classification plotted in the direction of dorso-ventral axis of case IPF5 in left and right lungs over time. The average percentage was calculated within 5% sections along the axis from posterior to anterior. (a) (b) is ground-glass distribution. (c) (d) is reticular distribution. (e) (f) is honeycomb distribution. (g) (h) is emphysema distribution.	233
B.14 Volume percentage of each tissue classification plotted in the direction of dorso-ventral axis of case IPF6 in left and right lungs over time. The average percentage was calculated within 5% sections along the axis from posterior to anterior. (a) (b) is ground-glass distribution. (c) (d) is reticular distribution. (e) (f) is honeycomb distribution. (g) (h) is emphysema distribution.	234

B.15 Volume percentage of each tissue classification plotted in the direction of dorso-ventral axis of case IPF9 in left and right lungs over time. The average percentage was calculated within 5% sections along the axis from posterior to anterior. (a) (b) is ground-glass distribution. (c) (d) is reticular distribution. (e) (f) is honeycomb distribution. (g) (h) is emphysema distribution.	235
B.16 Volume percentage of each tissue classification plotted in the direction of dorso-ventral axis of case IPF10 in left and right lungs over time. The average percentage was calculated within 5% sections along the axis from posterior to anterior. (a) (b) is ground-glass distribution. (c) (d) is reticular distribution. (e) (f) is honeycomb distribution. (g) (h) is emphysema distribution.	236
B.17 Volume percentage of each tissue classification plotted in the direction of dorso-ventral axis of case IPF13 in left and right lungs over time. The average percentage was calculated within 5% sections along the axis from posterior to anterior. (a) (b) is ground-glass distribution. (c) (d) is reticular distribution. (e) (f) is honeycomb distribution. (g) (h) is emphysema distribution.	237
B.18 Volume percentage of each tissue classification plotted in the direction of dorso-ventral axis of case IPF14 in left and right lungs over time. The average percentage was calculated within 5% sections along the axis from posterior to anterior. (a) (b) is ground-glass distribution. (c) (d) is reticular distribution. (e) (f) is honeycomb distribution. (g) (h) is emphysema distribution.	238

B.19 Volume percentage of each tissue classification plotted in the direction of dorso-ventral axis of case IPF15 in left and right lungs over time. The average percentage was calculated within 5% sections along the axis from posterior to anterior. (a) (b) is ground-glass distribution. (c) (d) is reticular distribution. (e) (f) is honeycomb distribution. (g) (h) is emphysema distribution.	239
B.20 Volume percentage of each tissue classification plotted in the direction of dorso-ventral axis of case IPF21 in left and right lungs over time. The average percentage was calculated within 5% sections along the axis from posterior to anterior. (a) (b) is ground-glass distribution. (c) (d) is reticular distribution. (e) (f) is honeycomb distribution. (g) (h) is emphysema distribution.	240
B.21 Lobar distribution of disease CT patterns of case IPF2 diagnosed with IPF over time. The tissue percentage in different lobe is shown in different color, and each bar represents the volume percentage of the CT pattern for one lobe. (a) Ground-glass lobar distribution. (b) Reticular lobar distribution. (c) Honeycomb lobar distribution. (d) Emphysema lobar distribution.	241
B.22 Lobar distribution of disease CT patterns of case IPF3 diagnosed with IPF over time. The tissue percentage in different lobe is shown in different color, and each bar represents the volume percentage of the CT pattern for one lobe. (a) Ground-glass lobar distribution. (b) Reticular lobar distribution. (c) Honeycomb lobar distribution. (d) Emphysema lobar distribution.	242

B.23 Lobar distribution of disease CT patterns of case IPF5 diagnosed with IPF over time. The tissue percentage in different lobe is shown in different color, and each bar represents the volume percentage of the CT pattern for one lobe. (a) Ground-glass lobar distribution. (b) Reticular lobar distribution. (c) Honeycomb lobar distribution. (d) Emphysema lobar distribution.	243
B.24 Lobar distribution of disease CT patterns of case IPF6 diagnosed with IPF over time. The tissue percentage in different lobe is shown in different color, and each bar represents the volume percentage of the CT pattern for one lobe. (a) Ground-glass lobar distribution. (b) Reticular lobar distribution. (c) Honeycomb lobar distribution. (d) Emphysema lobar distribution.	244
B.25 Lobar distribution of disease CT patterns of case IPF9 diagnosed with IPF over time. The tissue percentage in different lobe is shown in different color, and each bar represents the volume percentage of the CT pattern for one lobe. (a) Ground-glass lobar distribution. (b) Reticular lobar distribution. (c) Honeycomb lobar distribution. (d) Emphysema lobar distribution.	245
B.26 Lobar distribution of disease CT patterns of case IPF10 diagnosed with IPF over time. The tissue percentage in different lobe is shown in different color, and each bar represents the volume percentage of the CT pattern for one lobe. (a) Ground-glass lobar distribution. (b) Reticular lobar distribution. (c) Honeycomb lobar distribution. (d) Emphysema lobar distribution.	246

B.27 Lobar distribution of disease CT patterns of case IPF13 diagnosed with IPF over time. The tissue percentage in different lobe is shown in different color, and each bar represents the volume percentage of the CT pattern for one lobe. (a) Ground-glass lobar distribution. (b) Reticular lobar distribution. (c) Honeycomb lobar distribution. (d) Emphysema lobar distribution.	247
B.28 Lobar distribution of disease CT patterns of case IPF14 diagnosed with IPF over time. The tissue percentage in different lobe is shown in different color, and each bar represents the volume percentage of the CT pattern for one lobe. (a) Ground-glass lobar distribution. (b) Reticular lobar distribution. (c) Honeycomb lobar distribution. (d) Emphysema lobar distribution.	248
B.29 Lobar distribution of disease CT patterns of case IPF15 diagnosed with IPF over time. The tissue percentage in different lobe is shown in different color, and each bar represents the volume percentage of the CT pattern for one lobe. (a) Ground-glass lobar distribution. (b) Reticular lobar distribution. (c) Honeycomb lobar distribution. (d) Emphysema lobar distribution.	249
B.30 Lobar distribution of disease CT patterns of case IPF21 diagnosed with IPF over time. The tissue percentage in different lobe is shown in different color, and each bar represents the volume percentage of the CT pattern for one lobe. (a) Ground-glass lobar distribution. (b) Reticular lobar distribution. (c) Honeycomb lobar distribution. (d) Emphysema lobar distribution.	250

C.1 V/Q ratio distribution and end-capillary oxygen distribution of control, CT-based and PFT-based simulation result at the first time point of case IPF5. (a) V and Q with respect to V/Q ratio. (b) Distribution of end-capillary oxygen levels amongst alveoli.	252
C.2 Ventilation, perfusion and V/Q ratio distribution against lung height (cranio-caudal axis) of the first time point of case IPF5. (a) Ventilation distribution against lung height. (b) Perfusion distribution against lung height. (c) V/Q ratio distribution against lung height.	253
C.3 V/Q ratio distribution and end-capillary oxygen distribution of control, CT-based and PFT-based simulation result at the second time point of case IPF5. (a) V and Q with respect to V/Q ratio. (b) Distribution of end-capillary oxygen levels amongst alveoli.	254
C.4 Ventilation, perfusion and V/Q ratio distribution against lung height (cranio-caudal axis) of the second time point of case IPF5. (a) Ventilation distribution against lung height. (b) Perfusion distribution against lung height. (c) V/Q ratio distribution against lung height.	255
C.5 V/Q ratio distribution and end-capillary oxygen distribution of control, CT-based and PFT-based simulation result at the third time point of case IPF5. (a) V and Q with respect to V/Q ratio. (b) Distribution of end-capillary oxygen levels amongst alveoli.	256
C.6 Ventilation, perfusion and V/Q ratio distribution against lung height (cranio-caudal axis) of the third time point of case IPF5. (a) Ventilation distribution against lung height. (b) Perfusion distribution against lung height. (c) V/Q ratio distribution against lung height.	257

C.7 V/Q ratio distribution and end-capillary oxygen distribution of control, CT-based and PFT-based simulation result at the first time point of case IPF14. (a) V and Q with respect to V/Q ratio. (b) Distribution of end-capillary oxygen levels amongst alveoli.	258
C.8 Ventilation, perfusion and V/Q ratio distribution against lung height (cranio-caudal axis) of the first time point of case IPF14. (a) Ventilation distribution against lung height. (b) Perfusion distribution against lung height. (c) V/Q ratio distribution against lung height.	259
C.9 V/Q ratio distribution and end-capillary oxygen distribution of control, CT-based and PFT-based simulation result at the second time point of case IPF14. (a) V and Q with respect to V/Q ratio. (b) Distribution of end-capillary oxygen levels amongst alveoli.	260
C.10 Ventilation, perfusion and V/Q ratio distribution against lung height (cranio-caudal axis) of the second time point of case IPF14. (a) Ventilation distribution against lung height. (b) Perfusion distribution against lung height. (c) V/Q ratio distribution against lung height.	261

List of Tables

2.1	Alterations of lung function tests in idiopathic pulmonary fibrosis (IPF). Reproduced from (Plantier et al., 2018)	25
3.1	Summary of lung segmentation methods	42
3.2	Summary of fissure detection methods	48
3.3	Summarized demographics for the AGING and HLA datasets.	57
3.4	Possible structures on images in 2D and 3D, and its corresponding eigenvalues λ_k . H and L describe the absolute value of λ_k , H is high, L is low, +/- indicate the sign of the eigenvalue. The eigenvalues relationship here is: $ \lambda_1 \leq \lambda_2 \leq \lambda_3 $.	67
3.5	Summary of interactive user control parameters	74
3.6	Mean error and percentile accuracy of normal healthy and IPF subjects (mean value \pm standard deviation).	82
3.7	Mean error and percentile accuracy of left oblique fissure for each subject	85
3.8	Mean error and percentile accuracy of right horizontal fissure for each subject	86

3.9	Mean error and percentile accuracy of right oblique fissure for each subject	87
3.10	Mean square error (MSE) (mm) and percentile accuracy(%) of segmented left oblique (LO), right horizontal (RH), and right oblique (RO) fissures before and after manual correction	88
4.1	Demographic data.	106
4.2	Mean tissue density (g/cm^3) of each CT pattern for left and right lung (mean value \pm standard deviation)	116
4.3	Change in classification of tissue CT pattern (volume percentage) over time of left lung from one subject diagnosed with IPF (subject 6 with three time points) (%).	133
4.4	Change in classification of tissue CT pattern (volume percentage) over time of right lung from one subject (subject 6 with three time points) diagnosed with IPF (%).	133
4.5	Imaged volume of each lung (L) and the percentage of LAA area (%) in both lungs for each time point.	135
4.6	Lobe volume proportion comparison between IPF subjects and older normal subjects.	136
4.7	Values of the first three shape modes of IPF subjects for each time point.	138
4.8	Results for linear regression of shape mode weighting against extent of fibrosis.	141
5.1	Age-associated changes in respiratory function and their relationships to clinical presentations (Reproduced from (Sprung et al., 2006; Lalley, 2013))	152

5.2	Parameter values and their source used in computational models	176
5.3	The volume percentage of CALIPER classified disease tissues for each time point of these two patients (%).	178
5.4	Predicted reference values used as input to predict a shape model for a normal control.	182
5.5	Average lobe volume proportion of IPF lung mesh and predicted control lung mesh.	184
5.6	Parameters of control and IPF airway tree	187
5.7	Parameters of control and IPF vessel tree	187
5.8	Reference normal, simulated and PFT measured inspiration volume (L). .	188
5.9	Percentage of CT-based fibrosis from CALIPER classification and PFT-based fibrosis (CT-based plus additional fibrosis required to limit inspiration from FRC to TLC).	189
5.10	Values of total respiratory system and total lung compliance (L/cmH ₂ O) of normal control, CT-based and PFT-based modelling results.	190
5.11	Values of mPAP (mmHg), PVR (MPa·/mm ³) and PVV (ml) of normal control, CT-based and PFT-based modelling results.	190
5.12	Measured DLCO (mL/mmHg/min) for each time point, and values of PaO ₂ (mmHg), PaCO ₂ (mmHg) and P(A – a)O ₂ (mmHg) of normal control, CT-based and PFT-based modelling results.	195

List of Abbreviations

FEV₁/FVC ratio of the forced expiratory volume in the one second to the forced vital capacity of the lungs.

ADHB Auckland District Health Board.

AGING human aging cohort.

AIC Akaike information criterion.

ANNs artificial neural networks.

ATS American Thoracic Society.

BIC Bayesian information criterion.

COPD chronic obstructive pulmonary disease.

CPFE "combined pulmonary fibrosis and emphysema".

CT Computed tomography.

CVM Cramer Von Mises Distance.

DLCO diffusion capacity of the lung for carbon monoxide.

DoF degrees of freedom.

DPLD diffuse parenchymal lung diseases.

ERS European Respiratory Society.

FRC functional residual capacity.

FVC forced vital capacity.

GER gastroesophageal reflux.

GPA General Procrustes Alignment.

HDEC Health and Disability Ethics Committees.

HLA Human Lung Atlas.

HRCT high resolution computed tomography.

I-Clic Iowa Comprehensive Lung Imaging Center.

IIP idiopathic interstitial pneumonia.

ILD interstitial lung disease.

IPF idiopathic pulmonary fibrosis.

KCO carbon monoxide transfer coefficient.

LAA low attenuation areas.

MDS multi-dimensional scaling.

MLD mean lung density.

NSIP non-specific interstitial pneumonia.

PCA principal component analysis.

PFTs pulmonary function tests.

PVV pulmonary vessel volume.

QLF quantitative lung fibrosis.

QOL quality of life.

RBC red blood cell.

RMS root mean square.

RV residual volume.

SFeaL Statistical Finite element analysis of Lobe.

SSM statistical shape model.

TLC total lung capacity.

UIP usual interstitial pneumonia.

VC vital capacity.

VOIs volumes of interest.

Chapter 1

Introduction

1.1 Motivation

Idiopathic pulmonary fibrosis (IPF) is a lethal fibrosing lung disorder that typically affects adults in the sixth to seventh decade of life (Meltzer and Noble, 2008; King Jr et al., 2011). IPF is more frequent in males than females, and is associated with environmental factors such as smoking or dust exposure, but as its name suggests does not have a clear aetiology. There is no known cure, although some very new therapies have been suggested to slow the rate of physiologic decline (Raghu et al., 2011). IPF belongs to the family of interstitial lung disease (ILD), and is the most frequently diffuse occurring interstitial lung disease (Meltzer and Noble, 2008). In IPF lungs, healthy tissues are gradually replaced by an abnormal and excessive deposition of collagen (fibrosis), which may lead to a reduction in lung volumes, decreased lung compliance, mismatching of ventilation and perfusion, impaired gas exchange, and ultimately respiratory failure and death (Richeldi et al., 2017).

Diagnosis of IPF relates to a histopathological or radiological pattern typical of usual

interstitial pneumonia (UIP) (Raghu et al., 2011; Xaubet et al., 2017). UIP pattern is usually associated with honeycombing (subpleural cystic airspaces with well-defined walls), reticular opacities and ground-glass abnormalities (Raghu et al., 2011; Richeldi et al., 2017). These abnormalities in IPF typically develop preferentially in the posterior-basal lung regions, and often co-exist with emphysema, which causes a progressive and irreversible decline in lung function. Currently it is not clear how - or whether - the spatial distribution of tissue abnormalities in IPF (including classifications of tissue type) correlate with pulmonary function tests (PFTs). In addition, the progression of IPF is variable between individuals, and no established quantitative tools exist to assess its development and how the tissue abnormality changes over time contribute to lung function. Therefore, developing a computational model of lung function in IPF that can be parameterised to different time points, presents a potential novel way of investigating strategies for patient-specific diagnosis and treatment planning for IPF patients.

1.2 Thesis objectives

The broad aim of this thesis is to contribute toward developing a new quantitative tool that integrates data from volumetric imaging, PFTs, and computational models for lung function, as a step towards predicting the development of IPF over time, and to understand differences, including lung shape and lung function, between IPF and normal older lungs.

The specific objectives of this thesis are:

Objective 1: Develop an automatic lung lobe segmentation method for HRCT images that can consistently estimate lobar boundaries even if the boundary is not clear along its

entire length. The method needs to be tested on both healthy subjects and IPF subjects. Ideally the algorithm will be automatic, or semi-automatic.

Objective 2: Classify and quantify tissue abnormalities from HRCT scans of IPF lungs. Analyse the density, volume, spatial distribution, and their change over time.

Objective 3: Quantify the difference of lung shape between IPF and older normal lungs, and explore the correlation of lung shape change in IPF with the extent of fibrosis.

Objective 4: Integrate the image-based tissue quantification, pulmonary function tests and computational modelling to simulate lung function in IPF, and compare with simulated lung function in older normal people, and use these tools to estimate the impact of radiological features of IPF on lung function.

1.3 Thesis overview

Chapter 2 In order to quantitatively explore the link between structure and lung function of patients with IPF, some background knowledge of this disease is summarized in this chapter. The first part provides a basic introduction to IPF, including its epidemiology, aetiology, pathogenesis, diagnosis, clinical course and comorbidities. The second part describes some physiological alterations in IPF lungs. The changes in the mechanical properties of the lungs in IPF and the changes in pulmonary gas exchange are discussed in detail.

Chapter 3 Automatic identification of pulmonary lobes from imaging is important for image-based analysis of lung function and disease progression. In order to overcome

current difficulties in identifying pulmonary fissures, especially in disease, a statistical finite element shape model of the lobes is applied to guide lobar segmentation in this chapter. By deforming a principal component analysis-based statistical shape model (SSM) onto an individual's lung shape, the likely region of fissure locations is predicted to initialize the search region for fissures. Then, an eigenvalue of Hessian matrix analysis and a connected component eigenvector-based analysis are used to determine a set of fissure-like candidate points. A smooth multi-level B-spline curve is fitted to the most fissure-like points (those with high fissure probability) and the fitted fissure plane is extrapolated to the lung boundaries. The method is tested on 20 inspiratory and expiratory CT scans, and compared with existing algorithms in healthy young subjects and older subjects with IPF. This chapter has been published as a conference paper:

- Yuwen Zhang., Mahyar Osanlouy., Alys Clark., Haribalan Kumar., Margaret Wilsher., David Milne., Eric Hoffman., and Merryn Tawhai. (2019, February). Pulmonary lobar segmentation from computed tomography scans based on a statistical finite element analysis of lobe shape. In: SPIE Medical Imaging, International conference. San Diego, USA.

Chapter 4 This chapter details a quantitative analysis of IPF disease features in HRCT scans, including both tissue abnormality quantification and lung lobe shape analysis, to provide consistent tissue-level (distribution of abnormalities) and organ-level (shape) bio-markers that can be used as additional information to track the progression of the disease over time. Lung tissues are classified as normal, reticular, ground glass, or emphysema using CALIPER (Computer-Aided Lung Informatics for Pathology Evaluation and Ratings) software. The classified data is then mapped to a SSM, which allows a reliable comparison between different patients or within one patient at different time

points. Quantitative approaches are used to analyse tissue density, tissue volume, the spatial distribution of abnormalities, and regional changes in tissue over time. A principal component analysis (PCA) based SSM is used to understand lung shape differences between IPF and the lungs of normal subjects aged > 50 years through quantifying principal modes of shape variation of both IPF and normal subjects. The results of the chapter have been presented at two conferences:

- Yuwen Zhang., Alys Clark., Haribalan Kumar., Brian Bartholmai, and Merryn Tawhai. (2017, November). Quantitative analysis of idiopathic pulmonary fibrosis abnormality from CT imaging. In: 13th Engineering Mathematics and Applications Conference, International conference. Auckland, New Zealand.
- Yuwen Zhang., Alys Clark., Haribalan Kumar., David Milne., Margaret Wilsher., Brian Bartholmai, and Merryn Tawhai. (2018, March). High resolution CT-based characterization analysis of idiopathic pulmonary fibrosis. In: the Thoracic Society of Australia & New Zealand (TSANZ) conference, International conference. Adelaide, Australia.

Chapter 5 In this chapter, data from volumetric imaging, quantitative tissue-level and shape-level features, and PFTs are integrated to guide a patient-specific computational model of lung function in IPF. In order to compare lung function between IPF patients and normal older controls, for each patient, a subject-specific lung mesh that represents the lung shape of a normal individual with the same age, BMI and pulmonary function data is predicted using an SSM. Anatomically-based models of the airway and blood vessel trees are generated from the HRCT images, and are matched to both the IPF lung mesh and the corresponding normal control lung mesh. \dot{V} , \dot{Q} and gas exchange models

are then used to simulate \dot{V} and \dot{Q} distributions and gas transport in normal and IPF lungs. Part of this chapter has been presented as a conference poster:

- Yuwen Zhang., Alys Clark., Haribalan Kumar., Margaret Wilsher., David Milne., Brian Bartholmai, and Merryn Tawhai. (2018, March). Idiopathic pulmonary fibrosis: a study using volumetric imaging and functional data in a computational lung model, International conference. San Diego, USA.

Chapter 6 Key findings of this thesis are summarized in this chapter, with discussion of the main methods, models and outcomes. Potential future directions that need to be addressed to develop the modelling framework are also discussed.

Chapter 2

Background

To quantitatively explore the link between lung structure and function of patients with idiopathic pulmonary fibrosis (IPF), some background knowledge of the disease is required. This chapter provides an introduction to IPF epidemiology, aetiology, pathogenesis, diagnosis, clinical course, comorbidities, and physiological alterations.

2.1 Introduction to idiopathic pulmonary fibrosis

2.1.1 Definition

Idiopathic pulmonary fibrosis is a chronic, progressive, irreversible, and lethal lung disease of unknown cause. It usually manifests over several years during which progressive scarring occurs in the supporting structural framework (interstitium) of the lung tissue (Meltzer and Noble, 2008; Raghu et al., 2011). It is the scarring of the tissue that is termed fibrosis. This fibrotic condition is generally thought to result from abnormal wound healing after repeated pulmonary tissue damage (King Jr et al., 2011). Several causes of alveolar injury have been implicated in IPF, including cigarette smoke, envi-

ronmental exposure to toxins (e.g. asbestos, avian toxins), gastro-oesophageal reflux, viral infection, and internal mechanisms such as autoimmunity, genomic instability or telomerase length (Raghu et al., 2011; Ahluwalia et al., 2014).

In IPF patients' lungs, some healthy tissues are replaced by altered extracellular matrix and a destroyed alveolar architecture, which leads to decreased lung compliance, disrupted gas exchange, and ultimately respiratory failure and death (Richeldi et al., 2017). The fibrosing areas are generally observed to arise first at the basal and peripheral region of the lungs, and then gradually progress to involve all lung tissues (Martinez et al., 2017). The prominent symptoms of IPF are exercise-induced breathlessness and chronic dry cough (Meltzer and Noble, 2008), which will eventually have a devastating effect on a patient's quality of life (QOL) (Kim et al., 2015b). IPF usually affects middle-aged and elderly adults (median age at diagnosis 66 years, range 55-75 years). The disease is isolated to the lungs, and is associated with the radiological and/or histological pattern of UIP (King Jr et al., 2011; Raghu et al., 2011; Xaubet et al., 2017). A typical UIP pattern is usually characterised by 'honeycombing', traction bronchiectasis, and peripheral alveolar septal thickening (Martinez et al., 2017), which will be introduced briefly in Section 2.3.2.

2.1.2 Disease classification

IPF belongs to the family of interstitial lung disease (ILD) or, more accurately, the diffuse parenchymal lung diseases (DPLD). All ILDs result in damage to the lung interstitium, with varying patterns of inflammation and fibrosis. Within the broad category of ILDs, IPF belongs to a subgroup known as idiopathic interstitial pneumonia (IIP) (Meltzer and Noble, 2008). By definition, the aetiology of IIPs is unknown. The

distinction between IPF and other kinds of IIP is particularly important (Corte et al., 2015; Troy and Corte, 2012), as the prognosis for other IIPs is generally much more favourable than that for IPF (Meltzer and Noble, 2008). Over the past decade, IIPs have been classified into seven distinct diseases, differentiated by specific clinical features and pathological patterns, which includes: idiopathic pulmonary fibrosis, non-specific interstitial pneumonia, cryptogenic organising pneumonia, acute interstitial pneumonia, respiratory bronchiolitis-interstitial lung disease, desquamative interstitial pneumonia, and lymphocytic interstitial pneumonia (Katzenstein and Myers, 1998; Troy and Corte, 2012) (Figure 2.1).

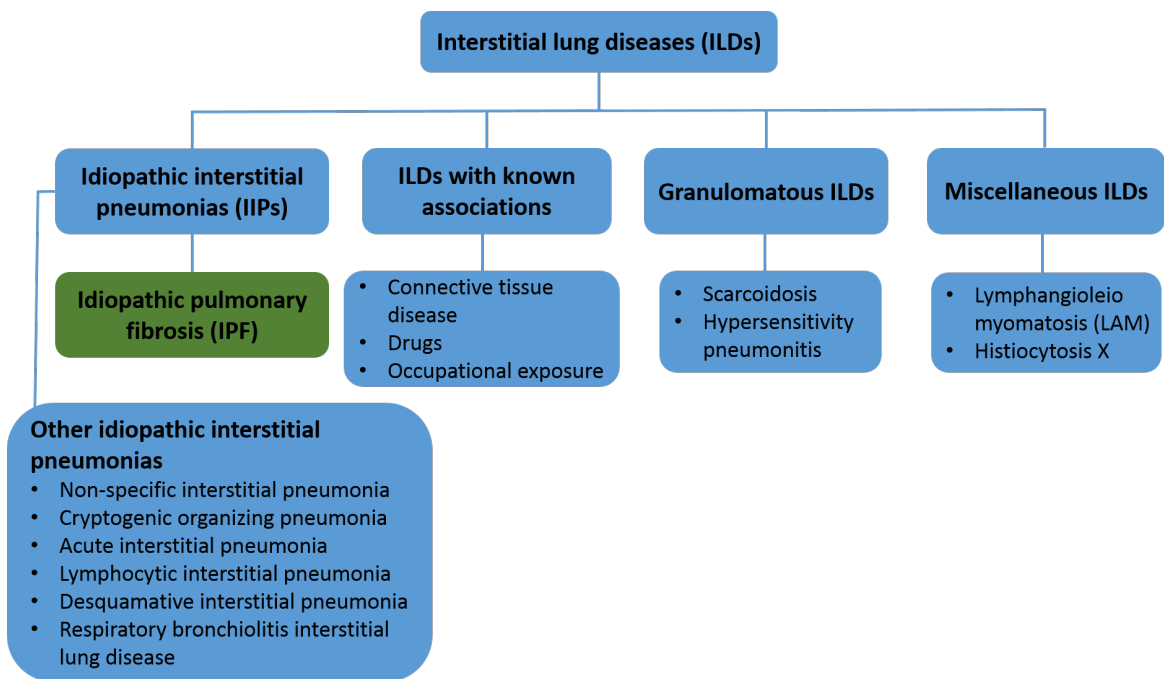


Figure 2.1: Classification of the interstitial lung diseases. IPF belongs to the family of interstitial lung disease (ILD), and belongs to a subgroup known as idiopathic interstitial pneumonia (IIP) (Troy and Corte, 2012).

2.2 Epidemiology, etiology and pathogenesis

2.2.1 Epidemiology

Although IPF is considered a rare disease, this disease is the most common form of IIP (Travis et al., 2013). The incidence of IPF is similar to that of stomach, brain, and testicular cancers and has recently been demonstrated to be rising over time (Richeldi et al., 2017). A cohort study including patients diagnosed with ILDs at Aarhus University Hospital showed that IPF was the most common diagnosis (28%) followed by connective tissue disease-related ILD (14%), hypersensitivity pneumonitis (7%) and non-specific interstitial pneumonia (NSIP) (7%) (Hyldgaard et al., 2014). Although there is little data available estimating worldwide incidence, a recent study showed that in Europe and North America, the prevalence of IPF is estimated to range between 2.8 and 18 cases per 100,000 people per year, and this value might be lower in Asia and South America, where it is estimated to range from 0.5 to 4.2 cases per 100,000 individuals per year (Richeldi et al., 2017). IPF is more likely to affect men than women, and is rare in people younger than 50 years (Raghu et al., 2011, 2006). The incidence is estimated to be 13 cases/100,000 in women and 20 cases/100,000 in men (Xaubet et al., 2017). In addition, the incidence of IPF increases with age (Meltzer and Noble, 2008). The reason that incidence has increased in recent years is most likely because of improved diagnostic methods and increased life expectancy (Xaubet et al., 2017).

2.2.2 Pathogenesis and potential contributors to aetiology

Historically, IPF was considered a chronic inflammatory disorder, which gradually progressed to established fibrosis (Richeldi et al., 2017). Now IPF is generally regarded as

a consequence of multiple interacting factors, in which repetitive local micro-injuries to an ageing alveolar epithelium plays an important role (Richeldi et al., 2017). These micro-injuries initiate aberrant epithelial-fibroblast communication, the induction of matrix-producing myofibroblasts, and considerable extracellular matrix accumulation and remodelling of lung interstitium (Richeldi et al., 2017). Although the aetiology of IPF is unknown, currently, environmental exposures and genetic factors have been supported by some researchers as providing important inducement (Taskar and Coultas, 2006; Meltzer and Noble, 2008; Xaubet et al., 2017; Richeldi et al., 2017). In addition, gastroesophageal reflux (GER), exposure to silica, brass, steel and wood dust, livestock and agriculture work, and the construction of wooden houses are also potential risk factors for the pathogenesis of IPF (Taskar and Coultas, 2006; Xaubet et al., 2017).

Environmental exposures

The relationship between environmental exposures and IPF has been consistently demonstrated by case studies. Asbestosis, for example, is a case in which environmental material is associated with pulmonary fibrosis (Meltzer and Noble, 2008). There are studies indicating that the pathogenesis and progression of IPF are influenced by particulate inhalation, which is supported by the fact that the development of IPF consistently relates to cigarette smoking history in most patients (Baumgartner et al., 1997; Richeldi et al., 2017). Additionally, other environmental factors including metal and wood dusts, agriculture and farming, viruses, and stone and silica have also been proposed (Raghu et al., 2011; Taskar and Coultas, 2006).

Genetic factors

Increasing evidence indicates that genetic predisposition plays an essential part in the development of IPF (Xaubet et al., 2017; Richeldi et al., 2017). This evidence is based on the existence of familial forms of the disease, and it has been shown that around 2.2% to 3% of IPF cases are familial (Xaubet et al., 2017). The most likely mode of genetic transmission of pulmonary fibrosis in familial cases is autosomal-dominant with variable penetrance (Steele et al., 2005; Allam and Limper, 2006; Lee et al., 2005; Musk et al., 1986). Rare genetic variants have been identified in cases where ILDs affect two or more members of the same biological family, including genes associated with alterations in host defence (MUC5B, ATP11A, TOLLIP), telomere maintenance (TERT, TERC, PARN, RTEL, OBFC1), surfactant dysfunction (SFTPC, SFTPA2) and epithelial barrier function (DSP, DPP9) (Alder et al., 2008; Raghu et al., 2011; Seibold et al., 2011; Xaubet et al., 2017). Among them, MUC5B, a promoter site of an airway mucin gene, is the most strongly associated with development of both familial and sporadic IPF (Richeldi et al., 2017). MUC5B encodes a mucin-5B precursor protein that contributes to airway mucous production and might have an important role in lung host defence. It has also been noted that members of the same biological family may be affected by different types of ILDs, such as non-specific interstitial pneumonia and cryptogenic organizing pneumonia (Xaubet et al., 2017).

2.3 Diagnosis

The diagnosis of IPF often requires a multidisciplinary discussion, involving pulmonologists, chest radiologists, and chest pathologists experienced in the field of ILDs (Flaherty et al., 2004; King Jr et al., 2011; Raghu et al., 2011). This multidisciplinary

approach has been accepted in consensus guidelines all over the world and has helped to standardize IPF diagnosis (Raghu et al., 2011; Richeldi et al., 2017). Usually, IPF is diagnosed by identification of a pattern of UIP on the basis of radiological or histological criteria in patients without evidence of an alternative cause. The biggest challenge of diagnosis for clinicians is how to exclude other idiopathic interstitial pneumonias, fibrotic nonspecific interstitial pneumonia, and interstitial lung disease associated with occupational or environmental exposure, connective tissue disease, and drugs (King Jr et al., 2011; Richeldi et al., 2017). This differential diagnosis is really important, since typical UIP is not exclusive to IPF, but may associate with some other conditions, such as chronic hypersensitivity pneumonitis and asbestosis. Many patients have a history of environmental exposures or medical treatments which clinicians need to take into consideration for diagnosis (Richeldi et al., 2017).

2.3.1 Clinical presentations

Patients with IPF usually suffer from unexplained progressive dyspnea on exertion and chronic dry cough, bibasilar inspiratory crackles, and finger clubbing. Bibasilar inspiratory crackles are heard on chest auscultation and finger clubbing is found in about 30% of patients (Raghu et al., 2011; King Jr et al., 2011; Richeldi et al., 2017). Chest pain, fatigue, malaise, and weight loss are also typical symptoms for IPF patients (Douglas et al., 2000; King Jr et al., 001b). These clinical presentations might initially be attributed to ageing or some comorbidities such as cardiovascular disease, or obesity (Richeldi et al., 2017). Therefore, in order to avoid diagnostic delays, it is necessary for primary care physicians to have clinical suspicion of IPF. Some patients may present with acute respiratory exacerbations usually accompanied by fever and

influenza-like symptoms within a few days or weeks from the first clinical symptom. In these cases, clinicians require careful diagnostic distinction from other forms of acute ILDs (Richeldi et al., 2017). Pulmonary function tests (PFTs) from IPF patients usually show a restricted pattern with low percent predicted total lung capacity (TLC) and **diffusion capacity of the lung for carbon monoxide** (DLCO). But for some patients with early disease, PFT results might be normal or mildly abnormal (Douglas et al., 2000; Raghu et al., 2006).

2.3.2 Radiographic features

HRCT of the chest has become an essential tool for the diagnosis of IPF, which is usually associated with identification of a UIP pattern. The presence of UIP pattern on HRCT is characterised by appearance of honeycombing cysts, reticular opacities and ground-glass abnormalities (Figure 2.2) (King Jr et al., 2011; Raghu et al., 2011; Richeldi et al., 2017). Honeycombing is common, and essential for a definite diagnosis (Raghu et al., 2011). On HRCT, honeycombing is presented as clustered cystic airspaces with a typical diameter of 3-10 mm but occasionally as large as 2.5 cm, and in a predominantly subpleural and posterior basal distribution (Hansell et al., 2008; Richeldi et al., 2017). Reticular opacities are often associated with traction bronchiectasis (Nishimura et al., 1992; Johkoh et al., 1999). Ground-glass is a common characteristic of UIP pattern, although it is sometimes less extensive than reticular. The distribution of abnormalities are often basal, peripheral and patchy (Raghu et al., 2011). If patients show micronodules, air-trapping, non-honeycomb cysts, extensive ground glass opacities, consolidation, or a peribronchovascular-predominant distribution, alternative diagnosis should be taken into account (Hwang et al., 2009; Souza et al., 2006). If patients show reticular ab-

normalities located in subpleural and basal regions, but no honeycombing appearance, possible UIP patterns should be taken into consideration, then a surgical lung biopsy is suggested to make a definite diagnosis (Raghu et al., 2011; Richeldi et al., 2017).

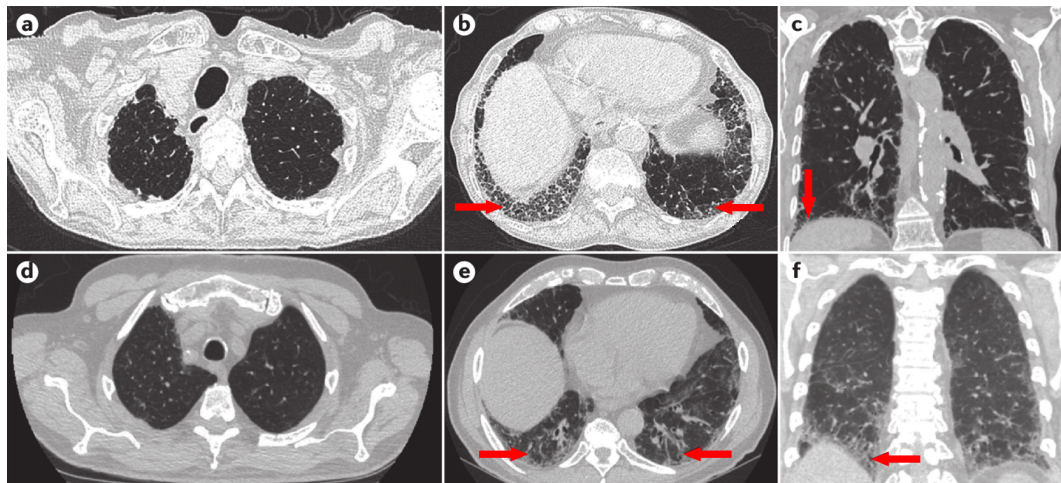


Figure 2.2: HRCT images of UIP pattern from two patients. The first is from a woman with progressive cough and dyspnoea, showing her upper (a), lower (b) lung zones and a sagittal plane of the lungs (c). These images show lower lobe-predominant peripheral honeycomb change (**b and c, arrows**), which is typical of UIP pattern. This patient had no systemic disease or exposures that would exclude idiopathic disease: the diagnosis of IPF is certain. In contrast, the second is a woman with progressive breathlessness, who could be diagnosed with possible IPF. The upper (d), lower (e) lung zones and sagittal image of the lungs (f) demonstrate peripheral, basilar-predominant, reticular densities with traction bronchiectasis (**e and f, arrows**) consistent with fibrosis. Surgical lung biopsy is suggested. Reproduced from (Martinez et al., 2017).

2.3.3 Histopathology

When HRCT features are not enough for a certain diagnosis of IPF, surgical lung biopsy is suggested (Richeldi et al., 2017). The main histopathologic hallmarks of UIP pattern is characterized by a heterogeneous appearance, best seen at low magnification, with areas of subpleural fibrosis and honeycomb (i.e. cystic fibrotic airspaces lined by bronchiolar epithelium and often filled by mucin and variable numbers of inflammatory cells),

alternating with areas of less affected or normal parenchyma (Society et al., 2000; Travis et al., 2002) (Figure 2.3). Small areas of active fibrosis (fibroblast foci) are present in the background of collagen deposition, and they reflect the temporal heterogeneity and indicate current ongoing disease (King Jr et al., 2011). Another feature of UIP pattern is that the inflammation is often absent or mild and consists of a patchy interstitial infiltrate of lymphocytes and plasma cells (Raghu et al., 2011; King Jr et al., 2011). Although surgical lung biopsy is essential for a correct diagnosis, careful consideration is required for every patient to estimate whether the risks of surgical lung biopsy outweigh the potential benefits of the histopathologic information. For older patients with comorbidities or clinically significant physiological impairment, it is suggested to avoid surgical lung biopsy (Richeldi et al., 2017).

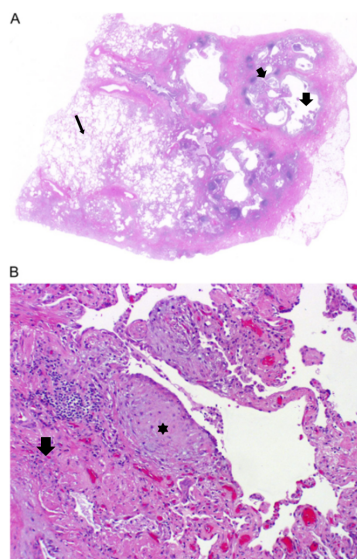


Figure 2.3: Surgical lung biopsy specimens of UIP pattern. (A) Scanning power microscopy showing a patchy process with honeycomb spaces (thick arrow), some preserved lung tissue regions (thin arrow), and fibrosis extending into the lung from the subpleural regions. (B) Adjacent to the regions of more chronic fibrosis (arrow) is a fibroblast focus (asterisk), recognized by its convex shape and composition of edematous fibroblastic tissue, suggestive of recent lung injury. Reproduced from (Raghu et al., 2011).

2.3.4 Diagnostic criteria

”Gold standard” diagnostic criteria for IPF have been developed by the American Thoracic Society (ATS) and the European Respiratory Society (ERS) in a statement of published guidelines (Raghu et al., 2011). These criteria are:

1. Exclusion of other known causes of ILD (e.g. domestic and occupational environmental exposures, connective tissue disease, and drug toxicity).
2. The presence of a UIP pattern on HRCT in patients not subjected to surgical lung biopsy.
3. Specific combinations of HRCT and surgical lung biopsy pattern in patients subjected to surgical lung biopsy.

Beyond that, minor criteria have also been set for the diagnosis of IPF in the absence of a surgical lung biopsy (Raghu et al., 2011):

1. Age > 50 years.
2. Insidious onset of otherwise unexplained dyspnea on exertion.
3. Duration of illness being over 3 months.
4. Bibasilar inspiratory crackles (dry or ”Velcro” type).

Figure 2.4 shows the diagnostic workflow for adult patients with ILD and suspected IPF. If the high-quality HRCT evidence is sufficient enough for the recognition of histopathologic UIP pattern, surgical lung biopsy is not essential (Hunninghake et al., 2001; Raghu et al., 1999; Flaherty et al., 2003; Quadrelli et al., 2010). However,

a multidisciplinary discussion among experienced clinical, radiologic and histopathologic experts is particularly important when the radiologic and histopathologic patterns are discordant (e.g., HRCT is inconsistent with UIP and histopathology suggests UIP) (Raghu et al., 2011). Radiologic or pathologic UIP pattern is not 100% specific to IPF (Lynch et al., 2006; Trahan et al., 2008; Silva et al., 2008a).

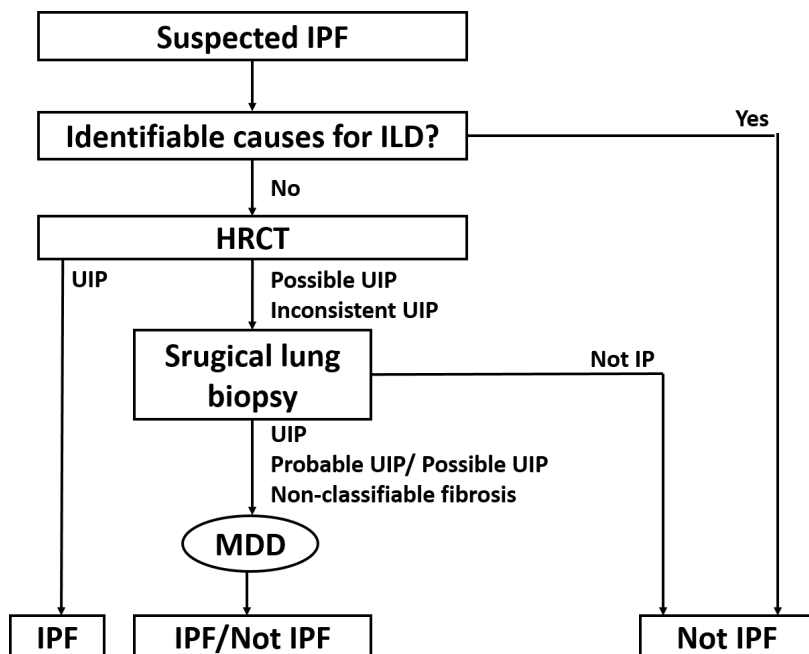


Figure 2.4: Diagnostic algorithm for IPF. Patients with suspected IPF (i.e., patients with unexplained dyspnea on exertion and/or cough with evidence of ILD) should be carefully evaluated for identifiable causes of ILD. In the absence of an identifiable cause for ILD, an HRCT demonstrating UIP pattern is diagnostic of IPF. In the absence of UIP pattern on HRCT, IPF can be diagnosed by the combination of specific HRCT and histopathological patterns. The accuracy of the diagnosis of IPF increases with multidisciplinary discussion (MDD) among ILD experts. Reproduced from (Raghu et al., 2011).

2.4 Clinical course

Some studies indicate that IPF patients have median survival time between two and three years from the time of diagnosis (Bjoraker et al., 1998; Flaherty et al., 2002; Nicholson et al., 2000; Rudd et al., 2007; King Jr et al., 001a, 2011). For most IPF patients, the clinical course has been described as a general decline in pulmonary function until eventual death from respiratory failure or complicating comorbidity (Carrington et al., 1978; Tukiainen et al., 1983; Gross and Hunninghake, 2001), however, the individual disease progression can be highly variable (Kim et al., 2006b; Meltzer and Noble, 2008). It appears that there are several possible clinical courses for patients with IPF (shown in Figure 2.5) (Raghu, 1987): slow and gradual progression over many years (the most common) (Ryu et al., 2014; Meltzer and Noble, 2008; Raghu et al., 2011); rapid and accelerated decline (Kim et al., 2006b; Selman et al., 2007); and acute exacerbations (King Jr et al., 2011; Xaubet et al., 2017). It is difficult to predict the natural history of disease progression for a given patient at the time of the diagnosis (Raghu et al., 2011). Whether the different clinical courses are influenced by geographic, ethnic, cultural, racial, or other factors remains unknown. But some evidence has been suggested that worsening prognosis may be associated with older people (> 70 years old), smoking history, low body mass index (BMI), severe physiological impairment, and large radiological extent of disease (Ley et al., 2011). Other comorbidities such as emphysema and pulmonary hypertension may also have an impact on the disease course (Mejía et al., 2009; Wells et al., 2003; Lettieri et al., 2006). While prediction of the likely course of disease is currently not possible, it would be very beneficial to enable clinicians to make an appropriate and optimal treatment plan as early as possible.

2.4.1 Slow and rapid progressive course

Most IPF patients deteriorate relatively slowly, and their pulmonary function usually decreases gradually over months to years after the first clinical symptoms (cough and progressive dyspnoea) (Ryu et al., 2014; Meltzer and Noble, 2008; Raghu et al., 2011). Patients usually experience reduction of lung volumes, and hypoxaemia at rest that worsens with exercise. This is accompanied by a decline of forced vital capacity (FVC) by a mean of 0.13 L to 0.21 L per year (Ley et al., 2011). In contrast, a subgroup of patients with IPF, mainly male cigarette smokers, experience a rapid worsening of symptoms, and insufficiency of pulmonary function (Kim et al., 2006b; King Jr et al., 2011), known as accelerated IPF. The patients with rapid progression have reduced survival time relative to those with a slowly progressive clinical course.

2.4.2 Acute exacerbations of IPF

“Acute exacerbation” was first proposed by Japanese physicians to describe acute, unexpected worsening of respiratory functions and severe hypoxaemia in patients with IPF, without a clear trigger (Kondoh et al., 1993; Gross, 1962). The rapid deterioration occurs in a small minority of patients with IPF (about 5-10%), with absence of infection, heart failure, pneumothorax, or pulmonary embolism (Azuma et al., 2005; King Jr et al., 2011; Raghu et al., 2011). The prognosis for patients with acute exacerbations is poor, and it may happen at any stage in the course of IPF (Kim et al., 2006a; Parambil et al., 2005; Sakamoto et al., 2009; Kondoh et al., 2010). Patients with acute exacerbation usually experience poor respiratory decline, worsened cough, fever and increased sputum production (Ambrosini et al., 2003; Kim et al., 2006a). The mortality rate for patients with acute exacerbations is over 60% (Wootton et al., 2011; Lettieri et al., 2006); for

cases requiring mechanical ventilation, the mortality is close to 100% (King Jr et al., 2011; Xaubet et al., 2017).

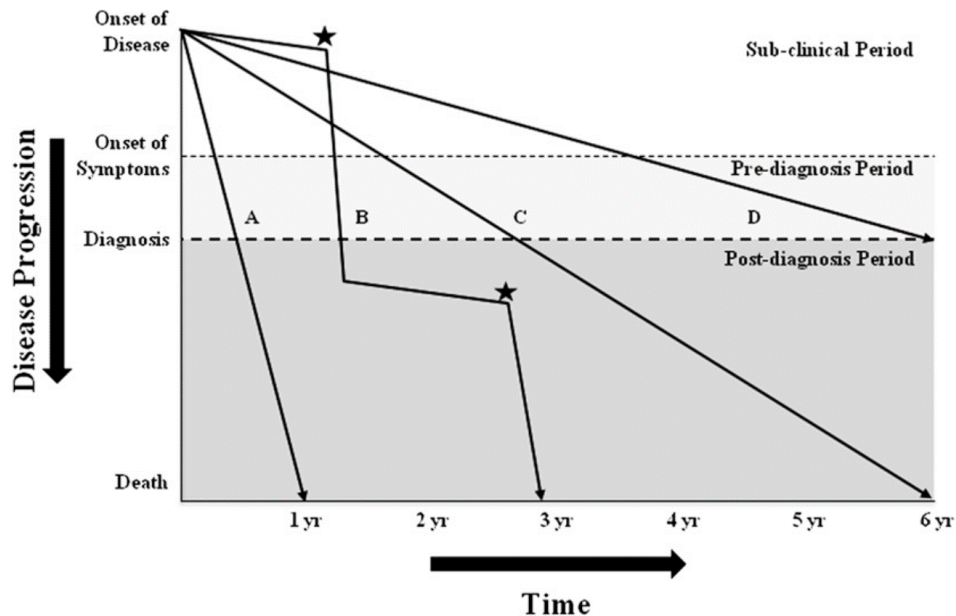


Figure 2.5: Schematic representation of potential clinical courses of IPF. A sub-clinical period of disease progression exists during which only radiographic evidence of disease may be noted. This is followed by a symptomatic phase comprising clinical stages (both pre-diagnosis and post-diagnosis). The rate of deterioration and progression to death may be fast (line A), mixed (line B), or slow (lines C and D), with phases of relative disease stability interspersed with acute decline (asterisks). Reproduced from (Ley et al., 2011).

2.5 Complications and comorbidities

Complications and comorbidities can occur in patients with IPF that may influence the clinical course and prognosis (Xaubet et al., 2017; King and Nathan, 2017; Martinez et al., 2017). It is reported that only 12% of patients with IPF have no comorbid illness, and most patients have comorbidities (Raghu et al., 2011; Kim et al., 2015b; Harari et al., 2016; Kreuter et al., 2016). Emphysema and pulmonary hypertension are both im-

portant comorbid conditions in IPF patients (Raghu et al., 2015; Martinez et al., 2017), and are briefly outlined here.

2.5.1 IPF and emphysema

Several research groups have described a syndrome in which IPF coexists with pulmonary emphysema (Wells et al., 1997, 2003; Cottin et al., 2005; Meltzer and Noble, 2008). In 2005, Cottin et al. (2005) presented a syndrome named "combined pulmonary fibrosis and emphysema" (CPFE). Both IPF and emphysema are associated with a significant smoking history, and CPFE is strongly associated with exercise hypoxaemia, severe dyspnea on exertion, upper lobe emphysema and lower lobe fibrosis, unexpected subnormal lung volumes, and severe reduction of carbon monoxide transfer (Silva et al., 2008b; Mejía et al., 2009; Cottin et al., 2010; King Jr et al., 2011; Lin and Jiang, 2015). Currently, whether CPFE is a distinct clinical entity or not remains unknown, i.e. whether this is just the presence of two different diseases running in parallel is unclear (King Jr et al., 2011; Lin and Jiang, 2015). Some researchers suggest that CPFE should be regarded as a distinct clinical entity, since it has a characteristic pulmonary function feature and unique natural history that is different from pure emphysema or IPF alone (Cottin et al., 2005; Lin and Jiang, 2015; Xaubet et al., 2017). CPFE occurs more frequently in males than in females and its prevalence is about 30% to 47% in patients with IPF (Xaubet et al., 2017). It is often associated with a significant drop of DLCO and severe hypoxaemia during exercise due to the additive effect of emphysema and fibrosis (Xaubet et al., 2017).

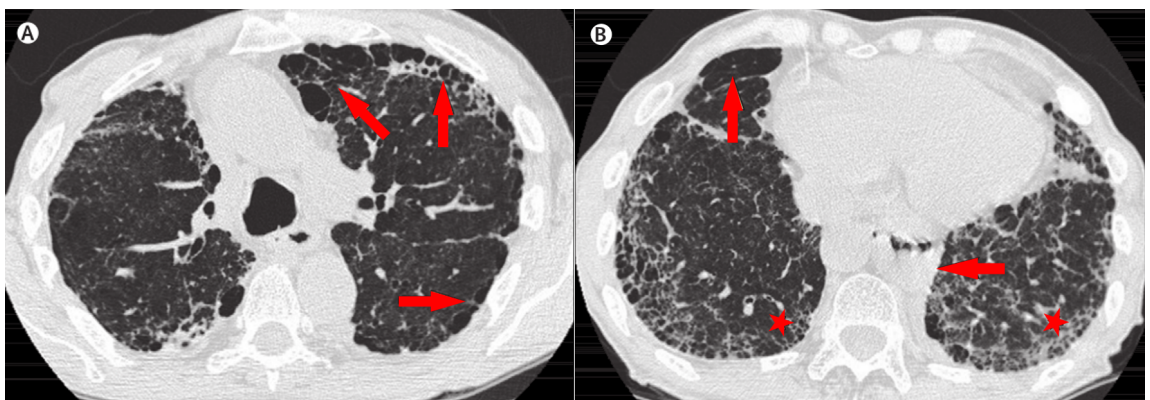


Figure 2.6: Combined pulmonary fibrosis and emphysema. High-resolution CT shows emphysematous lesions (arrows) in the upper lobes (in Figure A), emphysema (arrow) and usual interstitial pneumonia-like lesions (stars) in the lower lobes (in Figure B). Reproduced from (King Jr et al., 2011).

2.5.2 IPF and pulmonary hypertension

Pulmonary hypertension (PH), defined as a mean pulmonary artery pressure of > 25 mmHg at rest, is a frequent form of comorbid condition in patients with IPF and is the main determinant of poor prognosis (Raghu et al., 2011; Xaubet et al., 2017). It is estimated that the incidence of pulmonary hypertension is around 30% to 50% in IPF patients (King and Nathan, 2017). In general, pulmonary hypertension occurs due to several factors, with chronic hypoxia-induced vasoconstriction and destruction of the pulmonary capillary bed induced by fibrosis being the two main causes (Hayes Jr et al., 2016). The presence and development of pulmonary hypertension is associated with significant dyspnea, functional impairment (particularly in DLCO) and decreased exercise capacity, and may increase risk of mortality for patients with IPF (Mejía et al., 2009; Lettieri et al., 2006; Nadrous et al., 2005). Some studies have shown that combined pulmonary fibrosis and pulmonary hypertension has a significantly negative effect on the survival in patients with IPF alone, probably caused by the increased pulmonary

vascular resistance (Raghu et al., 2011; King Jr et al., 2011). Currently, whether IPF with pulmonary hypertension represents a distinct clinical entity (IPF–PH) is still unclear (Raghu et al., 2011).

2.6 Physiological alterations

The clinical presentation of IPF is related to a number of physiological alterations of the lung (Crystal et al., 1976; Plantier et al., 2018). These alterations have a complex and negative impact on all compartments of the respiratory system, from lung volume and compliance to gas exchange, from conducting airways to lung vasculature (Plantier et al., 2018). In general, patients with IPF usually have reduced lung volumes, reduced lung compliance, reduced diffusing capacity, increased ratio of the forced expiratory volume in the one second to the forced vital capacity of the lungs (FEV₁/FVC), and arterial hypoxaemia that worsens with exercise (Crystal et al., 1976; Society et al., 2000; Cortes-Telles et al., 2014; Plantier et al., 2018). These alterations in lung physiology are summarized in Table 2.1.

2.6.1 Alterations in the mechanical properties of the lung

Reduction in lung compliance

IPF disease often results in reduction in lung compliance (i.e. an increase in lung tissue stiffness). Studies have shown that the reduced lung compliance is caused by a reduction in the compliance of the lung extracellular matrix and by alterations in pulmonary surfactant (Plantier et al., 2018). In patients with IPF, surfactant shows alterations in its lipid profile (Gunther et al., 1999; Schmidt et al., 2002), which leads to severely im-

Table 2.1: Alterations of lung function tests in IPF. Reproduced from (Plantier et al., 2018)

	Mild IPF	Moderate to severe IPF
Static lung volumes		
- TLC	Normal	Decreased
- FRC	Normal	Decreased
Spirometry		
- FVC	Normal	Decreased
- FEV ₁ /FVC	Normal or increased	Normal or increased
Airways		
- Cough reflex	Increased	Increased
- Airway resistance	Decreased	Decreased
Blood gases at rest		
- P_aO_2	Normal	Decreased
- P_aCO_2	Normal	Decreased
Carbon monoxide transfer		
- DLCO	Decreased	Decreased
- V_A	May be normal	Decreased
- K_{CO}	May be normal	Decreased
Exercise physiology		
- Peak V_{O_2}	May be normal	Decreased
- V_D/V_T	Increased	Increased
- V_E/V_{CO_2}	Increased	Increased
- PAP at exercise	Increased	Increased
- $P_{A-a}O_2$ at exercise	Increased	Increased
Pulmonary haemodynamics at rest		
- PAP	May be increased	Frequently increased
- PCWP	Normal	May be increased

FVC: forced vital capacity; FEV₁ : forced expiratory volume in 1 s; TLC: total lung capacity; FRC: functional residual capacity; P_aO_2 : arterial oxygen tension; P_aCO_2 : arterial carbon dioxide tension; DLCO : diffusing capacity of the lung for carbon monoxide; V_A : alveolar volume; K_{CO} : transfer constant of carbon monoxide; PAP: pulmonary artery pressure; PCWP: pulmonary capillary wedge pressure; V_{O_2} : oxygen uptake; V_D/V_T : ratio of dead space volume to tidal volume; V_E/V_{CO_2} : ratio of minute ventilation to carbon dioxide elimination; $P_{A-a}O_2$: alveolar-arterial oxygen tension difference.

paired surface activity (Gunther et al., 1999). The reduction in lung compliance may happen from an early stage of IPF (Plantier et al., 2018). A study of 31 IPF patients from (Zielonka et al., 2010) showed that the static lung compliance was consistently and significantly reduced (by $44 \pm 6\%$). A similar result was found in another study (Orens et al., 1995), where all of the measured IPF patients had abnormal static lung compliance, which suggests that measurement of lung compliance could help with the early diagnosis of IPF.

The alterations of lung compliance in IPF patients appear to be strongly correlated with the degree of lung fibrosis as assessed by scoring of lung biopsies (Fulmer et al., 1979; Plantier et al., 2018). Nava and Rubini (1999) measured the dynamic lung compliance in seven patients with end-stage IPF, which showed that the reduction in lung compliance may be correlated with the progress of the disease. Currently, whether the reductions in lung compliance relate to clinical presentations (e.g. dyspnoea) remains unclear, but it is highly likely that the lung compliance has a strong relationship with the respiratory muscles and thus has an impact on the work of breathing (Plantier et al., 2018). In addition, as the distribution of disease is heterogeneous in IPF lungs, lung compliance is expected to be uneven between different lung regions (Organ et al., 2015), but more evidence is needed to understand the implications of disease distribution outcomes.

Reduction of lung volumes

The restriction of lung volumes (total lung capacity (TLC), functional residual capacity (FRC), forced vital capacity (FVC), and residual volume (RV)) is typical in patients with IPF. This restriction of lung volumes often occurs at some time point in the clinical course of IPF (Society et al., 2000; Plantier et al., 2018). However, sometimes lung vol-

umes may be normal in the early stage of IPF, especially for patients with superimposed chronic obstructive pulmonary disease (Martinez and Flaherty, 2006). Cherniack et al. (1995) studied 96 patients with biopsy-confirmed IPF. The range of TLC was from 42% to 125% predicted and the range of FVC was from 26% to 112% predicted. A reduction in lung volumes consistently relates to an increased risk of death (Martinez and Flaherty, 2006), and is weakly associated with dyspnoea or quality of life (Du Bois et al., 2011). However, whether the reduced lung volumes reflects the disease progression of IPF is still unknown (Plantier et al., 2018). Interestingly, patients with CPFE have higher RV and TLC compared to the patients with IPF alone (Mura et al., 2006), which may be caused by the effects of comorbid pulmonary emphysema on lung compliance (Doherty et al., 1997).

Alterations in the conducting airways

Some evidence suggests that alterations also occur in conducting airways in patients with IPF, including increased airway epithelial cell proliferation (Vuorinen et al., 2008) and differentiation (Plantier et al., 2016), and increased numbers of visible bronchioles in the distal regions (Chilosi et al., 2002). A reduction in conducting airway resistance was found in IPF lungs compared with normal, which may contribute to an increased ratio of FEV_1 to FVC (Pastre et al., 2015). Plantier et al. (2016) used volumetric capnography to estimate the volume of conducting airways in patients with IPF, patients with other ILDs, and healthy people. The results showed that conducting airway volume was significantly higher in IPF lungs in comparison with non-IPF ILD lungs and healthy lungs. However, this change in airway volume was not associated with the severity of alveolar lesions, dyspnea, cough or quality of life (Plantier et al., 2016). The increase in airway volume in IPF may reflect dilation of airways consistent with bronchiectasis that

can be characteristic of this disease, and a commonly accepted view is that bronchiectasis in IPF may be caused by fibrotic retraction of peribronchiolar alveolar attachments and subsequent airway dilation (Sumikawa et al., 2008). However, a recent study found that bronchiectasis had a weak relationship with total fibrosis extent observed from CT imaging (Walsh et al., 2015), which means the remodelling of conducting airways in IPF may be dissociated from alveolar fibrosis (Plantier et al., 2016). Patients with IPF usually have more rapid breaths with the progression of disease (Kornbluth and Turino, 1980; Renzi et al., 1982), and have a relatively increased flow rate in the conducting airways due to the increased static elastic recoil (Society et al., 2000). Additionally, it has been suggested that at least part of the ventilation abnormalities seen in IPF is associated with small airways disease with peribronchiolar fibrosis and inflammation, and 70% of IPF patients have narrowed small airways (Crystal et al., 1976).

Alterations in the lung vasculature

Vascular lesions are observed in the pulmonary vasculature in patients with IPF, and often lead to disproportionate increases in the pulmonary vascular resistance and pulmonary hypertension (Plantier et al., 2018). The tissues adjacent to the areas of fibrosis have been shown to have an increase in vessel profusion, whereas the fibrotic tissue itself demonstrates a reduced number of blood vessels (Cosgrove et al., 2004; Ebina et al., 2004). Jacob et al. (2016a) explored the relationship between pulmonary vessel volume (PVV) and ILD extent (includes ground glass, reticular and honeycomb patterns). It was found that PVV had a strong relationship with ILD extent ($R^2 = 0.73$, $P < 0.0001$) when using linear regression analysis. Furthermore, PVV was demonstrated to be an independent predictor of mortality, and a stronger predictor of mortality than all the other traditional CT features and pulmonary functional variables (Jacob et al., 2016a).

The increase in PVV seen in more advanced fibrosis may be caused by the vascular capacitance of spared lung (the upper and middle lobes in patients with IPF, which is a predominantly basal disease), and may also relate to the increased negative intrathoracic pressure which non-compliant fibrotic lungs need to generate during inspiration (Jacob et al., 2016b).

2.6.2 Alterations in pulmonary gas exchange

IPF is associated with multiple pathophysiological changes in pulmonary gas exchange. The lesions of the alveolar-capillary membrane in IPF lungs will impair both the diffusion capacity and ventilation/perfusion (V/Q) relationship, increase dead space ventilation and alveolar-arterial oxygen tension difference ($P_{A-a}O_2$), and finally cause chronic arterial hypoxaemia (Crystal et al., 1976; Plantier et al., 2018; Society et al., 2000).

Reduced diffusing capacity of the lung

The diffusing capacity of oxygen is considered to be reduced in almost all patients with IPF. However, in clinical examination, this diffusing capacity is technically very difficult to measure. Therefore, clinical tests actually measure the diffusing capacity of carbon monoxide (DLCO) which provides an estimate of the gas-exchange function of the whole lungs (Plantier et al., 2018). DLCO is a measure of the conductance of gas transfer from inspired gas to the red blood cells, and is usually tested in a single breath where the partial pressure difference between inspired and expired carbon monoxide is recorded (Rosenberg, 1996; Plantier et al., 2018). The carbon monoxide transfer coefficient (KCO) is an index of the efficiency of alveolar transfer of carbon monoxide. It can be referred to as DLCO/VA, where VA is the alveolar volume where gas exchange

takes place (Graham et al., 2017).

It has been shown that DLCO is reduced compared with normal values in 98% of IPF patients at initial diagnosis, although 27% of patients have normal TLC volumes, and 56% have normal FVC (Cortes-Telles et al., 2014). Interestingly, KCO is within the normal range in up to 30% of IPF patients (Wallaert et al., 2012), particularly in patients with moderately reduced DLCO (Pastre et al., 2015). But a normal KCO value in IPF patients does not mean that pulmonary gas exchange is normal (Plantier et al., 2018). It has been noted that both DLCO and KCO are significantly associated with the degree of IPF measured from CT scans (Wells et al., 1997), but DLCO correlates more strongly with exertional increases in $P_{A-a}O_2$ (Agustí et al., 1994) and highly relates to both dyspnoea (Swigris et al., 2012) and survival time (Hamada et al., 2007).

Dead space ventilation

Increased physiologic dead space ventilation (increased ratio of dead space volume to tidal volume V_D/V_T) is an important characteristic of lungs with fibrosis and happens in most IPF patients both at rest and at exercise (Fulmer et al., 1976; Crystal et al., 1976; Agustí et al., 1991; Miki et al., 2009). The increased dead space is mainly caused by two physiologic features: the first is the increased anatomical dead space, which is a result of the dilation of conducting airways in IPF as discussed in Section 2.6.1 (Plantier et al., 2016); the second is the regional ventilation-perfusion mismatch (increased variation in regional ventilation-perfusion ratio, V/Q), which increases the physiologic dead space. In IPF lungs, the fibrotic (i.e. honeycomb or reticular) areas that are not perfused or poorly perfused but still receive ventilation will have an increased regional V/Q ratio (Strickland et al., 1993; Plantier et al., 2018). An early paper indicated that patients with IPF will often have a V_D/V_T ratio of greater than 0.4 compared with a normal

person (approximate 0.3 for normal) (Crystal et al., 1976). In normal individuals the efficiency of ventilation improves with exercise (that is the V_D/V_T falls) (Jones et al., 1966; Wasserman and Whipp, 1975), but in more than 90% of IPF patients V_D/V_T stays constant or may increase (Crystal et al., 1976).

Ventilation-perfusion mismatching

It is generally thought that the hypoxemia of IPF is related to V/Q mismatching (Wagner et al., 1976; Crystal et al., 1976; Society et al., 2000). This V/Q mismatching may be associated with abnormalities both in ventilation and perfusion (Crystal et al., 1976; Strickland et al., 1993). Crystal et al. (1976) showed an equilibrium picture of ^{127}Xe distribution, which was used to determine regional ventilation, and showed that patients with IPF have patchy, non-segmental areas of decreased ventilation where airway obstruction or alveolar destruction occurred. As for perfusion, a shift of perfusion was observed to the upper lobes (reflecting pulmonary hypertension) due to the basal distribution of fibrotic lesions, so that areas of relatively low V/Q ratios mostly presented in the upper zones of the lung (Crystal et al., 1976). However, Strickland et al. (1993) indicated that the CT based cystic air spaces (i.e. honeycomb) were observed as poorly perfused (probably due to vascular obliteration) but were usually normally ventilated, which explains the increase in physiologic dead space seen at rest and with exercise. Thus, a higher V/Q ratio can be seen in areas where fibrosis and cystic air spaces are dominant, which could be used to distinguish IPF from emphysema (Strickland et al., 1993). In addition, an increased minute ventilation was found in most patients with IPF during exercise. This is mainly due to the increased respiratory frequency, and in part relates to an increase in dead space ventilation (Society et al., 2000).

Arterial hypoxaemia

Alterations in the mechanical properties of the lungs, impairment of diffusion capacity and ventilation-perfusion mismatch will finally lead to early-onset exertional chronic arterial hypoxaemia and later-onset resting chronic arterial hypoxaemia in IPF (Hempleman and Hughes, 1991; Hughes et al., 1991; Plantier et al., 2018). Some studies support that the major cause of arterial hypoxaemia in a large proportion of IPF patients is not the diffusion barrier to oxygen or the anatomic shunts, as was originally suspected, but is due to ventilation-perfusion mismatching (Finley et al., 1962; Wagner et al., 1976; Society et al., 2000). The alveolar-arterial oxygen gradient ($P_{A-a}O_2$), which is calculated from arterial oxygen tension (P_aO_2) and alveolar oxygen tension (P_AO_2) may increase, resulting from the reduced ventilation-perfusion ratio, right-to-left shunting, or impairment of oxygen diffusion (Plantier et al., 2018). The increase in $P_{A-a}O_2$ reflects hypoxaemia in IPF (Agustí et al., 1991). In a study of 29 IPF patients, the measured average resting P_aO_2 was 69.3 mmHg, and four patients had normal resting P_aO_2 . However, although the resting P_aO_2 can be normal in some IPF patients, the resting $P_{A-a}O_2$ is invariably abnormal (in about 97% of the patients with IPF) (Crystal et al., 1976).

2.7 Summary

IPF is a devastating lung disease characterized by an irreversible decline of lung function, and its incidence increases with years of age. The current efforts of studies in IPF mostly focus on the accurate identification and diagnosis of early IPF, underlying mechanisms of pathogenesis and potential bio-markers that can indicate the patient-specific clinical course. The presence of IPF is variable in most patients, but some common characteristics and progressions can be summarized, although this is challenging. The

clinical and physiological features of IPF reviewed in this chapter provides background information for further quantitative analysis (Chapter 4) and computational modelling of patients with IPF (Chapter 5).

Chapter 3

Pulmonary lobar segmentation from CT scans

Identification of pulmonary lobes is of great importance for image-based analysis of lung function and disease progression. Segmentation of lobes can facilitate intra-patient image registration for localizing and tracking fibrosis disease progression over time, since lobes are important structural landmarks (Lassen et al., 2011). Also, knowing the lobar distribution of pulmonary fibrosis disease is helpful to understand the pathophysiology of the disease and to guide a patient-specific functional simulation. However, the pulmonary lobar fissure is usually difficult to segment fully automatically, especially for diseased lungs, as fissures are thin, usually of fuzzy appearance and incomplete, and can be obscured by or confused with features of disease (Ukil and Reinhardt, 2009). The following chapter outlines the development of an automatic pulmonary lobar segmentation method using a statistical finite element shape model of the lungs and lobar fissures to guide segmentation. Unlike 'deep learning' methods, this approach requires relatively few subject images as a training set. Development of this method was motivated

by the poor reliability of existing methods for a guaranteed estimate of fissure location, particularly in volumetric images of IPF, or when only thin-slice CT (non-volumetric images) are available.

3.1 Background

3.1.1 Pulmonary lobar anatomy

Within the thorax, the lungs are enclosed by the ribs, and the base of the lungs rests on the diaphragm. The space in between the two lungs is called the mediastinum, and contains the heart, major blood vessels, the esophagus, the trachea, main bronchi, and several other thoracic structures. The airways, blood vessels and nerves enter the lungs from the mediastinum at the hilum. The lungs themselves comprise airways, vessels and a connective tissue framework referred to as the interstitium.

Human lungs are divided into five distinct anatomical regions, which are called pulmonary lobes. These lobes are each supplied by separate airway and vascular branches, and are largely anatomically independent regions. The separating junctions between these lobes are called the lobar fissures. The left lung consists of the left upper lobe and left lower lobe, which are separated by the left oblique fissure (major fissure). The right lung consists of the right upper lobe, right middle lobe and right lower lobe, which are separated by the right oblique fissure (major fissure) and right horizontal fissure (minor fissure). These fissures contain pleural fluid and provide separation between the lobes while permitting some movement relative to one another. In general, the functions of these lobes are relatively independent from each other since there are no major airways and vessels crossing the lobar fissures (Lassen et al., 2010; Doel et al., 2015; Ukil and

Reinhardt, 2009). Figure 3.1 shows a schematic diagram of the lungs. The lungs are bounded by two layers of membrane (pleura) separated by a thin layer of lubricating pleural fluid.

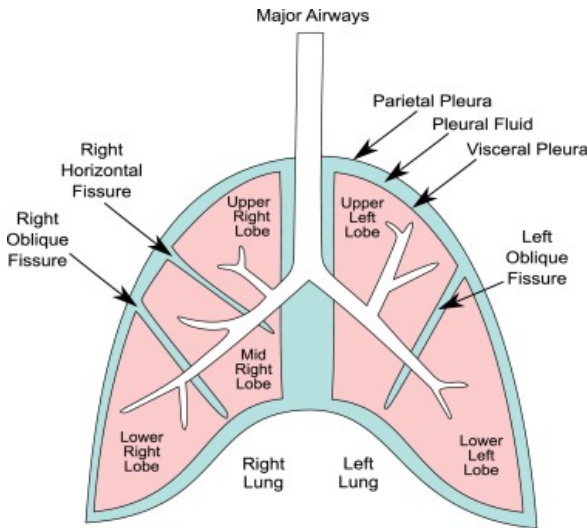


Figure 3.1: Schematic diagram of anatomical lung structure, showing the major airways, lobes and major fissures. The lungs are subdivided into the right upper (RU), right middle (RM), right lower (RL), left upper (LU), and left lower (LL) lobe. The pleural cavity which surrounds the lung consists of a double membrane layer (visceral pleura and parietal pleura) separated by a thin layer of pleural fluid. The inner membrane (visceral pleural) folds inwards between the lobes, creating fissures. Reproduced from (Doel et al., 2015).

3.1.2 High resolution computed tomography

Computed tomography (CT) imaging is a typical image modality used in diagnosis and management of IPF. It acquires multiple X-ray images at different orientations and reconstructs these images to obtain tomographic views in the region of interest (Zhang et al., 2011). This kind of imaging modality is typically used in clinical applications and research regarding pulmonary structure-function relationships (Hoffman and McLennan, 1997), including detection of both acute and chronic changes in the lung

parenchyma. It is particularly relevant here because normal two-dimensional X-rays can not show subtle defects. For evaluation of chronic interstitial processes (emphysema, fibrosis, and so forth), thin sections with high spatial frequency reconstructions are used (Coxson, 2007), and scans are often performed both in inspiration and expiration. This special technique is called high resolution computed tomography (HRCT). With the help of HRCT scans, a series of high-resolution chest sections can be acquired with slice thickness as low as 0.5 mm (Naidich, 2005), which can provide high visibility of the lung boundaries and pulmonary fissures. By making use of some advanced image processing technologies, a wide variety of features can be detected from these images such as density of the lung (Coxson, 2007), volumes of the lung (Hu et al., 2001), the regions of lung disease distributions (El-Baz et al., 2013; Ley-Zaporozhan et al., 2008), airway trees (Graham et al., 2010; Zhu et al., 2010; Diaz et al., 2010) and blood vessels (Shikata et al., 2009). CT images acquired at different stages in the breathing cycle can also be used to study lung mechanics and estimate regional lung ventilation (Hoffman et al., 2006; Yamamoto et al., 2011).

3.1.3 The importance of pulmonary lobar segmentation

The extraction of pulmonary lobes from CT scans is of great importance for lung disease assessment and treatment planning. For clinical applications, the distribution and location of pulmonary disease are beneficial information for doctors to recognize pathogenesis, guide therapy and have further value in surgical planning. That is, because many pulmonary diseases are more prevalent in specific anatomic regions of the lung, often acting at a lobar level. For example, emphysema (Jeffery, 1998), postprimary tuberculosis (Leung, 1999) and silicosis (Rees and Murray, 2007) usually affect the upper

lobes, while idiopathic pulmonary fibrosis is commonly present in the lower lobes (Lin and Jiang, 2015). However, there is currently a lack of quantitative and objective methods for the regional assessment of lung disease. Therefore, it is important to develop techniques that can identify the location, shape and volume of the lobes so that lung disease can be measured at a lobar level and the severity can be assessed accurately.

3.1.4 Challenges of automatic pulmonary lobar segmentation from CT scans

The most commonly used method to segment lobes from CT is through manual assessment by an experienced pulmonary radiologist. However, the process of determining the lobar boundaries is extremely laborious and a time-consuming task, typically taking hours for one patient. This is because a 3D HRCT image may contain a large number of axial slices which makes the manual segmentation very time consuming. Therefore, doctors rarely use manual lobe segmentation in clinical diagnosis and treatment in practice, and most clinicians use subjective visual observation. For this reason, an automatic (no user interaction) or semi-automatic (minimal user interaction) lobe segmentation technique is urgently needed in clinical applications and this has attracted great interest from researchers all over the world (Van Rikxoort and Van Ginneken, 2013; Pu et al., 2009a; Ukil and Reinhardt, 2009).

However, to find an effective and time-saving automatic lobe segmentation method is a challenging task because of anatomical variation and the possibility of incomplete fissures. Lobar structures vary significantly between subjects, and the anatomical variation in lobe structure is usually associated with age, sex and body type. Pathologies of diseased lungs usually deform the lobar shape abnormally and result in fuzzy appear-

ance of fissures on CT images, in particular when abnormalities are present near the fissures, which makes fissure segmentation challenging. Even in patients with healthy lung parenchyma, fissures are sometimes incomplete (Gülsün et al., 2006; Doel et al., 2015) (see Figure 3.2).

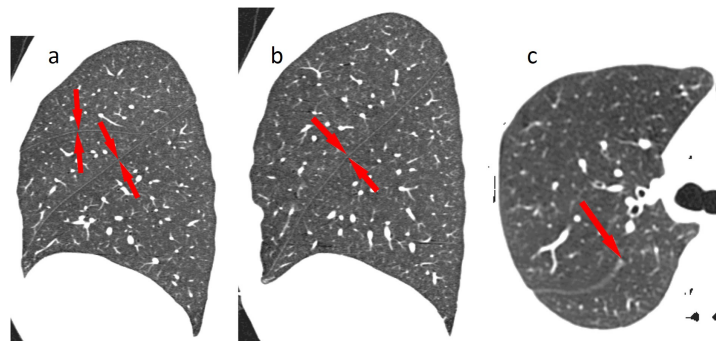


Figure 3.2: Slices of lung CT images illustrating the left and right fissures. Fissures are visible as white lines of high density tissue crossing the low density lung parenchyma. (a) Sagittal slice from the right lung showing the right oblique and horizontal fissures, the horizontal fissure is oriented horizontally. (b) Sagittal slice from the left lung showing the left oblique fissure. (c) Transverse slice from a different data set that show an incomplete right oblique fissure. Reproduced from (Ukil and Reinhardt, 2009).

3.2 Review of current published methods for pulmonary lobar segmentation

In a broad sense, existing lobe segmentation methods usually consist of two steps: the segmentation of lungs, and the detection of the three main pulmonary fissures (Van Rikxoort and Van Ginneken, 2013). Currently, a number of lung segmentation methods are available and most produce reliable results for normal lung at end-inspiration (Hu et al., 2001; Ukil and Reinhardt, 2005; Sun et al., 2006; Pu et al., 2008; Wang et al., 2009). In contrast, most challenges of automated lobar segmentation lie in the fissure detection,

and currently no method has yet been demonstrated to be robust and effective across a wide range of clinical imaging parameters and pathology experienced in clinical practice. Lung lobe segmentation is a complex multi-stage process that cannot be addressed by a simple algorithm (Van Rikxoort and Van Ginneken, 2013; Pu et al., 2009a; Ukil and Reinhardt, 2009). However, to some extent, lung segmentation and fissure detection are two independent parts and can be improved separately. That is, it should be possible to change lung segmentation in one way or another without affecting the fissure detection result dramatically. In the following section, existing work is discussed to highlight the key challenges of lobe segmentation algorithms, focusing on these two parts of the process. Then, a new approach to lung and lobe segmentation is presented.

3.2.1 Lung segmentation

Segmentation of lung is a prerequisite for the accomplishment of lobe segmentation, as it provides a boundary condition for subsequent fissure detection, allows estimation of lung volumes, and helps to detect and quantify abnormalities within the lungs. While not precisely defined, the lung region is usually considered to be the volume enclosed within the pleura, including the lung parenchyma, airways and vessels, but excluding those parts of the major airways and vessels which extend the pleural boundary. In this section, published methods for lung segmentation are briefly discussed. These methods are summarized in Table 3.1.

Conventional lung segmentation methods

In CT scans from healthy subjects, the air-filled lung parenchyma usually has a lower attenuation level compared to surrounding high-density tissue at the pleura. For this rea-

Table 3.1: Summary of lung segmentation methods

Authors	Algorithms	Notes
Kalender et al. (1991); Kemerink et al. (1998); Leader et al. (2003)	2D thresholding method	1. May cause discontinuity between slices; 2. Time consuming
Keller et al. (1981); Heddlund et al. (1982); Hoffman et al. (1983); Hoffman and Ritman (1985)	Early-stage 3D thresholding method combined with manual interaction	Causes too many intra-operator errors
Hu et al. (2001)	1. Automatically choose thresholding value; 2. Separate left and right lung 3. Morphological lung boundary smoothing	First group to apply fully automatic 3D thresholding method
Ukil and Reinhardt (2005)	1. Bounding box defined around mediastinum; 2. Extract left and right main stem bronchi; 3. 3D Morphological boundary closing	Automatic method using air-way tree information
Sun et al. (2006)	1. Anisotropic filtering; 2. Wavelet transform-based interpolation to construct 3D data; 3. Adaptive 3D region growing combined seed-locating to detect lung region; 4. Fuzzy logic algorithm and 3D morphological to fill hole	3D method using signal-to-noise ratio
Kitasaka et al. (2003)	1. Affine transformation to fit a contour shape model to individual images; 2. Active contour model to refine initial segmentations in 3D	Solves the problem of lesions adjacent to the chest wall and mediastinum
Pu et al. (2008)	1. 3D initial thresholding processing; 2. Adaptive border marching	Minimizes oversegmentation of adjacent regions such as abdomen and mediastinum
Pu et al. (2011)	1. Principal curvature analysis to eliminate noise; 2. Radius basis function to smooth lung in 3D	Solves the problems of disease, noise or artifacts
Prasad et al. (2008)	1. 3D thresholding algorithm; 2. Adapt lung curvature using rib curvature; 3. Morphologic operation	1. Uses rib curvature information to define lung borders; 2. Solves the problem of error detection for lung pathologies
Wang et al. (2009)	1. 3D thresholding processing; 2. Texture analysis to identify abnormal regions; 3. 2D hole filling	Texture feature analysis to segment ILD lungs
Sun et al. (2012)	1. Active shape model to roughly find lung outlines; 2. Optimal surface finding to adapt final segmentations	3D method using rib information

son, many conventional lung segmentation algorithms adopt a thresholding approach to search for a large connected region of the air-like values within the image. Threshold values are acquired from grey level histogram analysis and then an initial lung region is detected. A region growing method for the airways is usually applied subsequently to exclude the trachea and major airway branches. Some thresholding algorithms, especially older studies, were developed in 2D space, which means each axial section of CT imaging needs to be analysed separately (Kalender et al., 1991; Kemerink et al., 1998; Leader et al., 2003; Armato and Sensakovic, 2004). A 2-D method is a logical choice in the case of thick-slice CT data, but it may cause discontinuity between slices. Therefore, as higher resolution isotropic data became available, improved 3D processing methods were developed to avoid slice inconsistencies and reduce time for segmentation (Hu et al., 2001; Ukil and Reinhardt, 2005; Sun et al., 2006).

Most early 3D thresholding-based lung segmentation methods (Keller et al., 1981; Hedlund et al., 1982; Hoffman et al., 1983; Hoffman, 1985; Hoffman and Ritman, 1985) required significant manual interaction. This interaction included manually selecting threshold values or seed points for region growing, and separating left and right lungs manually. This leads to a process that is consuming and is subject to intra-operator errors. Hu et al. (2001) was the first group to apply a threshold-based algorithm in a fully automatic lung segmentation method. In their study, the lung region was firstly extracted from the CT images by gray-level thresholding processing. Instead of a fixed threshold value, an optimal thresholding method was used to automatically choose a threshold value that reflects the grey-scale characteristics of a specific dataset. The left and right lungs were then separated by identifying the anterior and posterior junctions by dynamic programming. Finally, a sequence of morphological operations was used to smooth the irregular boundary along the mediastinum.

Ukil and Reinhardt (2005) developed an improved automatic lung segmentation method to smooth lung boundaries in 3D using information from the segmented airway trees. A bounding box was first defined around the mediastinum for each lung using information from the segmented human airway trees, and all operations were then performed within the bounding box. After that, all generations of the airway distal branches were defined to the left and right main stem bronchi to be part of the respective lungs, and all the other segmented structures could be excluded. Finally, a fast morphological closing with an ellipsoidal kernel was performed to smooth the surface of the lung. This method solved the problem of irregular and inconsistent lung boundary of the regions near the mediastinum by using a common threshold algorithm.

Sun et al. (2006) presented a 3D-based method for segmenting lungs with improved accuracy. An anisotropic filtering method was first applied on CT slices to enhance the signal-to-noise ratio. A wavelet transform-based interpolation method was subsequently used to construct the 3D volumetric CT slice data with volume rendering. After that, an adaptive 3D region-growing algorithm was developed to detect the lung region, combined with automatic seed-locating methods. Fuzzy logic algorithms and 3D morphological closing approaches were finally used to refine the lung volume and fill the holes in it. The method was effective and, in general, robust with an average accuracy rate of 88.5%.

Specially designed lung segmentation methods for abnormal lungs

Although conventional threshold-based methods are fast, robust and typically accurate for healthy subjects, they may fail to perform well for scans containing physiologic abnormalities, which often results in segmentation errors and requires manual editing of the results (see in Figure 3.3). Currently, specially designed lung segmentation methods

mostly focus on a single lung disease and therefore can not get a good result across a large population (Kitasaka et al., 2003; Sluimer et al., 2005; Pu et al., 2008, 2011; Prasad et al., 2008; Korfiatis et al., 2008; Wang et al., 2009; van Rikxoort et al., 2009; Sun et al., 2012).

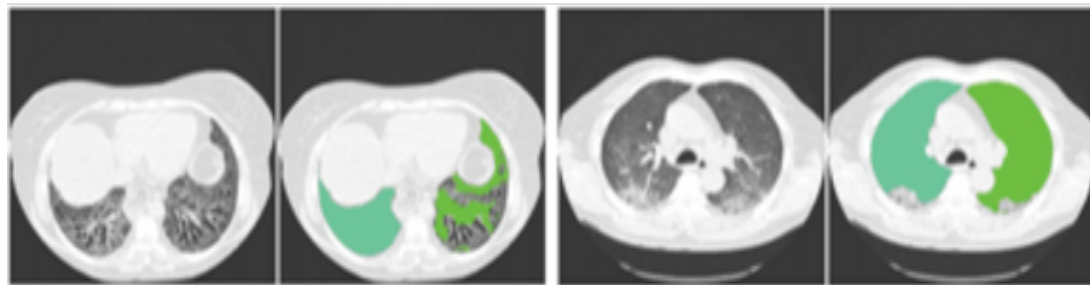


Figure 3.3: Illustration of the performance of conventional 3D thresholding lung segmentation methods on pathological lungs. Lung borders are not recognized accurately because of the higher densities of the abnormalities compared to the normal tissues. Reproduced from (Van Rikxoort and Van Ginneken, 2013).

To deal with the problem of lesions adjacent to the chest wall and mediastinum, (Kitasaka et al., 2003) developed a lung area extraction method using a shape model. A contour shape model using a Bézier surface was fitted to the contour surface of the individual input images with an affine transformation method. Then, an active contour model was utilized to refine the initial segmentation. The results showed that most lesions could be identified accurately using this method. However, as the lung apex and base were not included in the model, lesions adjacent to the lung apex or diaphragm could result in segmentation errors.

Pu et al. (2008) presented a lung segmentation algorithm based on adaptive border marching (ABM) to include juxtapleural nodules in the lung region since these nodules may be excluded from the results calculated by a conventional threshold-based algorithm. The adaptive border marching algorithm could smooth the lung borders after

an initial thresholding processing and minimize over-segmentation of adjacent regions such as the abdomen and mediastinum. The method was tested on 20 datasets and the results demonstrated that this method could re-include all juxtapleural nodules in the lung regions. An average over-segmentation ratio of this method was 0.43% which was lower than the reference standard average segmentation determined by an expert. In order to deal with the problem of different types of lung disease, image noise or artefacts, and individual anatomical variety, Pu et al. (2011) developed a shape analysis strategy termed "break-and-repair". A principal curvature analysis was applied to eliminate the problematic regions and then radial basis function (RBF) based implicit surface fitting was used to get a smooth lung surface.

To overcome the error in detection of the lung boundaries for lung pathologies, Prasad et al. (2008) made use of rib curvature information to help with finding the lung borders. The method was based on a threshold-based algorithm followed by a morphologic operation. The core principle of the method was to adapt the threshold value to an individual subject by making the curvature of lung along the ribs be similar to the curvature of the ribs. These curvatures were both represented by polynomial interpolation even though there was minimal deviation from this representation. The results showed that the performance of the rib segmentation method was better than the same method without guidance from rib segmentation.

Wang et al. (2009) proposed a texture analysis-based method to segment ILD lungs. The lung region including normal and mild ILD lung parenchyma was first segmented by a CT value thresholding technique and then texture-feature images derived from the co-occurrence matrix was used to identify abnormal lung regions with severe ILD from the initial results. 2D hole filling was applied to smooth the final lung segmentation. The overlap rate, volume agreement, mean absolute distance (MAD), and maximum

absolute distance between the automatically segmented lungs and the reference lungs (delineated manually by a medical physicist) were employed to evaluate the performance of the segmentation method, and showed accurate lung segmentation results for abnormal CT scans with severe ILD.

On the basis of the previous studies, (Sun et al., 2012) developed a further approach for segmentation of lungs with high-density pathologies. The method had two main steps. In the first step, a robust active shape model (RASM) matching method was utilized to roughly find the outline of the lungs. To initialize the shape model of RASM, detected rib information was used. In the second step, an optimal surface finding approach was applied to further adapt the initial segmentation result to the lung. The method was evaluated on both normal and abnormal subjects and had a better performance compared to two commercially available lung segmentation approaches.

3.2.2 Fissure detection

The currently published fissure detection methods can be, for the most part, classified into two categories: anatomical knowledge based analysis methods and shape based analysis methods. Anatomical knowledge based methods usually depend on either local or global knowledge of the anatomy of lung structure based on two pulmonary anatomical features. The first feature is the fact that there should not be any large vessels in the vicinity of lobar fissures, so fissures should locate in the gaps between airway and vessel trees. Another feature is that the airway bronchi can be classified into five lobar branches using an edge detection method (Figure 3.4). Shape based analysis methods commonly make use of gray-level information and shape information to detect the fissures. Published fissure detection methods are summarized in Table 3.2.

Table 3.2: Summary of fissure detection methods

Authors	Algorithms	Notes
Kuhnigk et al. (2003, 2005)	Watershed transformation method to analyze anatomical structures to help with fissure detection	First group to use lobar airways and vasculature into fissure detection ¹
Ukil and Reinhardt (2009)	1. Watershed transform guided cost image to define initial fissures; 2. Construct ROI; 3. Structure tensor analysis combined with optimal surface detection to find fissure surface; 4. Fast marching method to detect incomplete fissures	1. Improved on Kuhnigk's method; 2. Can detect incomplete fissures ¹
Lassen et al. (2010)	Watershed transformed anatomical structure based method	An extension of Kuhnigk's method ¹
Zhou et al. (2004); Saita et al. (2006)	1. Edge detection to class vessels and bronchi; 2. Hough transform to detect curve surface	Take advantage of linear appearance of fissures ¹
Wang et al. (2004, 2006)	1. Identify initial fissure ROI; 2. "Ridge map" based transformation to enhance initial fissure; 3. Shape-based curve growing to get the final fissures.	2D shape based method ²
Frangi et al. (1998)	Hessian matrix based analysis to extract local image structures	The first paper to apply Hessian matrix analysis on image segmentation in 3D ²
Wiemker et al. (2005)	Combine first derivative and second derivative of image gray values to find fissures	An early paper using Hessian matrix on fissure detection ²
Ochs et al. (2007); van Rikxoort et al. (2008)	Use pattern recognition approach and Hessian matrix and classification operation to detection fissure	An improved Hessian based method ²
Lassen et al. (2011, 2013)	1. Use anatomical structures to acquire initial fissure; 2. Hessian matrix surrounding initial guessing areas; 3. Morphological operations to filter noise	Combine both anatomical information and gray-level information ^{1,2}
Doel et al. (2012)	1. Use both anatomy knowledge and Hessian matrix to find fissure candidate points; 2. Multi-level B-spline curve to get the final fissure surface.	Combine both anatomical information and gray-level information ^{1,2}
Ross et al. (2010, 2013)	1. Particle system combined with Hessian matrix to get candidate fissure points; 2. Maximum a posterior method to remove noise points; 3. Thin plate spline to form final fissure surface.	Effective for lung lobe segmentation in absence of complete anatomical structures on CT imaging ²

¹ Anatomy knowledge based method.

² Shape based analysis method.

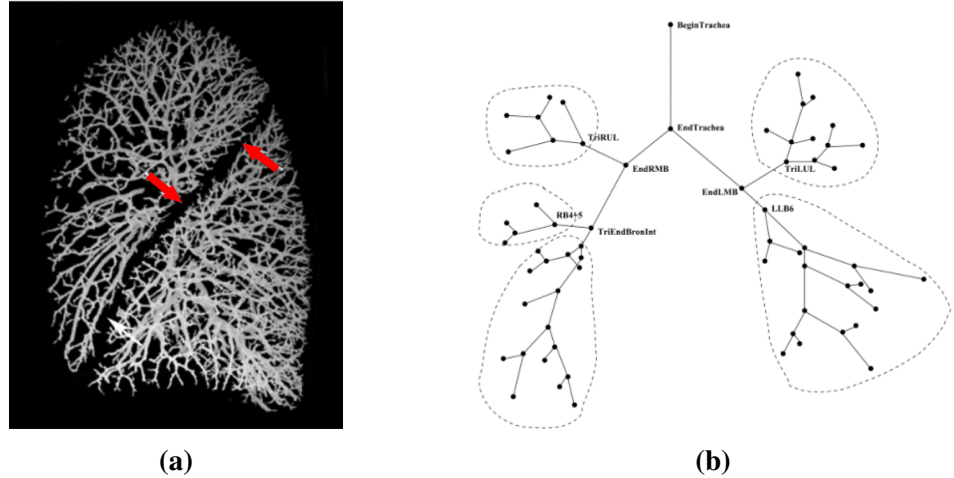


Figure 3.4: (a) Segmented volumes of the vascular tree. There are no large vessels in the vicinity of lobar fissures. (b) Anatomically labeled airway tree showing lobar subtrees. The airway tree can be classified corresponding to five lobes. Reproduced from (Ukil and Reinhardt, 2009).

Anatomical knowledge based method

Methods that aim to detect the lobar fissures usually start by finding an approximate location of the lobar borders based on prior anatomical knowledge of lung structures in order to narrow the search area for fissure detection (Kuhnigk et al., 2003, 2005; Zhou et al., 2004; Saita et al., 2006; Zhang et al., 2006; Ukil and Reinhardt, 2009; Pu et al., 2009a; Lassen et al., 2010; Doel et al., 2012). These methods are developed mainly based on two pulmonary anatomical features. A number of published papers use the segmentation results of airways and vessels to help localize fissures. Usually, the vascular segmentation provides more accurate estimation of lobar fissure locations than the airway trees, since more vessel generations can be detected from CT scans. These vessels span the entire lung volume which can help to find complete gaps between lobes. However, airways also play an important part in initial estimation of fissures, since airways trees can be more reasonably divided into lobes based on branching structure,

while the structure of vasculature branching is more complicated to extract from images and some connections are hard to separate accurately. Therefore, a lot of studies make use of both vessel and airway information to guide fissure detection (Ukil and Reinhardt, 2009; Lassen et al., 2010; Doel et al., 2012).

Kuhnigk et al. (2003, 2005) was an early group to present a framework of taking both lobar airways and vasculature into account for automatic fissure detection. A watershed transformation method has been used to take an analysis of these anatomical structures and this method was widely used and improved by other researchers, but the results calculated by this simple algorithm were not accurate enough even for some clearly visible fissures.

Ukil and Reinhardt (2009) developed Kuhnigk's fissure detection method which used a distance transform to combine segmented vessels, lobar airways, and original chest CT scan as a cost image to guide initial fissure guessing. They found that the improved watershed transform algorithm could provide a close initial approximation to the lobar fissures. Subsequently, a refinement method was used to construct a region of interest (ROI) which encompasses the fissures. A 3D optimal surface detection algorithm combined with a 'ridgeness' measurement was then applied to enhance the ROI, and find the optimal surface within the ROI. Finally, incomplete fissures were smoothly extrapolated using a fast-marching method based segmentation of a projection of the optimal surface. This method is able to segment incomplete fissures, and so significantly improved on prior methods.

Lassen et al. (2010) also described a fissure detection method by building a cost image for the watershed transformed segmentation which is an extension of the framework of Kuhnigk. The interactive segmentation method was tested on 25 CT scans comparing to a manual segmentation by a human observer and showed an average error

distance of 1.57 ± 0.3 mm. In addition, Zhou et al. (2004) and Saita et al. (2006) took advantage of the linear appearance of fissures to class the vessels and bronchi into five lobe regions using an edge detection method and used a Hough transform based curved surface detection method.

Shape based analysis method

Generally, lobar fissures can be regarded as bright planes crossing the pulmonary volume because of the higher density value of fissures compared to the surrounding tissues. Based on this information, quite a number of published methods use a local filtering algorithm to detect the voxels which lie on these planes, so that these detected voxel points can construct a continuous fissure surface. In 2D space, the fissure appears as a clear curve, therefore some early papers usually detected fissure points based on gray-level information in 2D space. For example, Wang et al. (2004, 2006) presented a 2D fissure detection method based on shape information. In this paper, the fissure was initially denoted as a curve based on the prior knowledge of the fissure shape to identify the surrounding region of fissure, called "fissure region" for subsequent automatic segmentation. Next an image transformation called "ridge map" was proposed for enhancing the appearance of initial fissures. A shape-based curve-growing method modeled by a Bayesian network could then be applied to this "map" to segment the fissure.

In 3D space, the most commonly used method to detect these pulmonary fissure plane structures is taking an eigenvalue analysis of the Hessian matrix (Frangi et al., 1998; Wiemker et al., 2005; Kitasaka et al., 2006; Ochs et al., 2007; van Rikxoort et al., 2008; Lassen et al., 2011, 2013; Ross et al., 2010; Doel et al., 2012). Frangi et al. (1998) was the first to present an eigenvalue analysis of the Hessian matrix to detect planar structures (fissures) and tube structures (vessels) on CT images. The relationship

between three eigenvalues of the Hessian matrix describes the local image structure and so can be used to determine a fissure probability. Wiemker et al. (2005) also used the Hessian matrix for fissure detection, proposing two 3D filter approaches in this paper. The first filter was based on the first derivatives of the image grey values and utilized the eigenvalues of the local structure tensor. The second filter was based on the second derivatives and utilized the eigenvalues of the local Hessian matrix.

Ochs et al. (2007) and van Rikxoort et al. (2008) used a pattern recognition approach to detect pulmonary fissures combined with eigenvalue analysis of the Hessian matrix as feature and classification was also performed on these fissures. Lassen et al. (2011, 2013) combined both anatomical based and shape based methods which successfully eliminated most false points (points identified as fissure but were not). The first anatomic-based method defined a region of interest, and then the Hessian matrix analysis was used only in this region of interest. The region of interest provides an initial guess for fissure locations. Subsequently, morphological operations such as direction-based connected component analysis were used to further reduce non-fissure points that are incorrectly identified as fissures. Doel et al. (2012) also made use of both an anatomical knowledge based method and the Hessian matrix to find fissure candidate points and constructed a multi-level B-spline smooth curve through the fissure points and extrapolated this curve to the lung borders to get complete fissure surfaces.

Ross et al. (2010, 2013) proposed a particle system that sampled the image domain combined with the Hessian matrix to get a set of candidate fissure locations. A maximum a posteriori (MAP) estimation was then used to eliminate false candidate points, and a post-processing operation was applied to remove remaining noise. A thin plate spline (TPS) interpolating surface fitting method was lastly performed to form the final fissure surfaces. This method is effective for lung lobe segmentation in the absence of

complete anatomical structures on CT imaging.

3.3 Methods: automatic statistical shape model based lobar segmentation method

Here, an SSM guided method is presented to segment pulmonary lobes from CT images.

A three-step approach is followed for the lobe segmentation (shown in Figure 3.5): in the first step, a threshold-based lung segmentation method defines the lung boundary; in the second step, an SSM is deformed to provide a "search region" for fissure locations; in the third step, fissures are located using a Hessian matrix protocol combined with connected component filters and a surface fitting algorithm. The new procedure does not depend on prior segmentation of anatomical structures (airway lobar classification) other than lung shape. A user-interactive interface was also developed for the user to control and visualize the whole segmentation process and to allow some manual correction on the segmented results, if required.

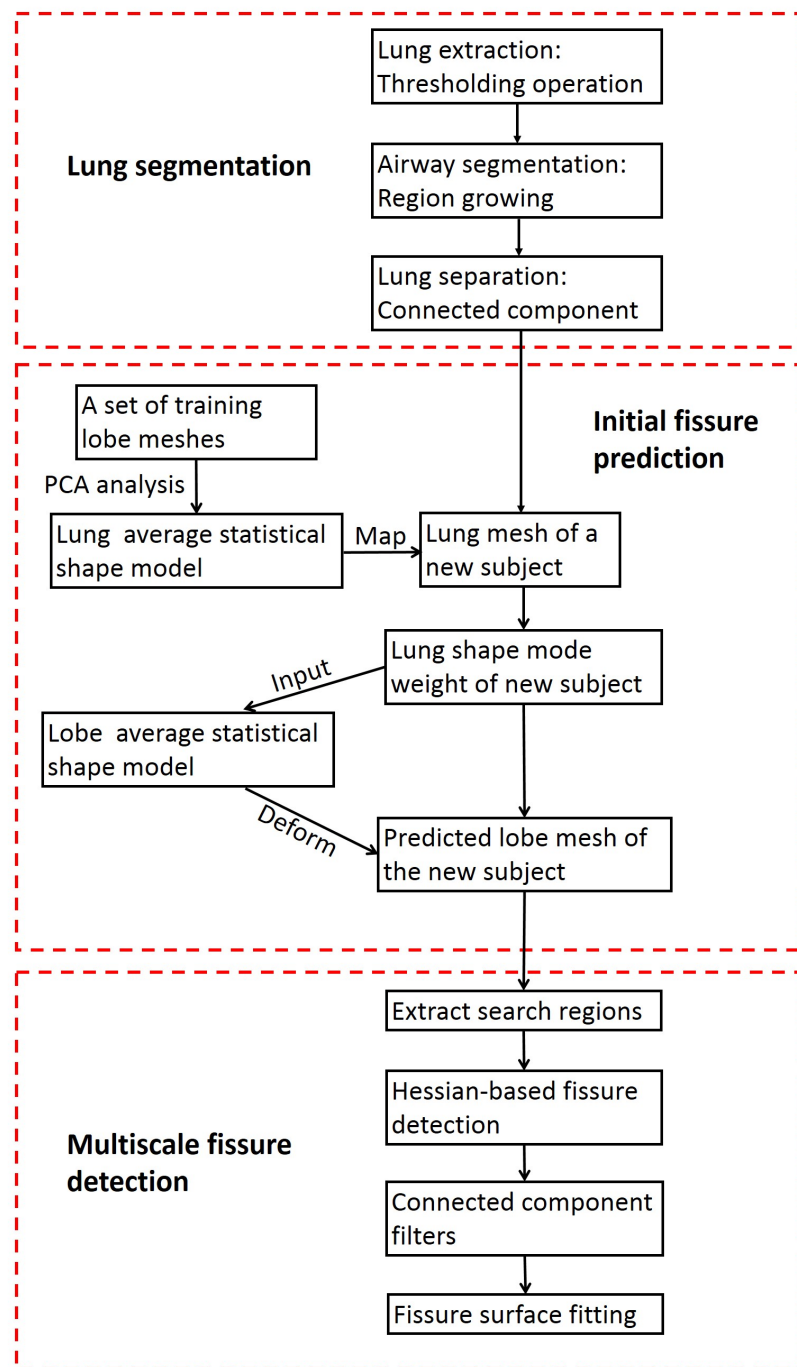


Figure 3.5: Flow diagram of the lobar segmentation process.

3.3.1 Lung segmentation

A good lung segmentation is a prerequisite for lobe segmentation, since all the other segmentations need to be performed inside the two lung regions. Here, a common thresholding method was used to segment the lungs (Ukil and Reinhardt, 2005). The procedure consists of the following steps: 1) uses a thresholding operation (-775 Hounsfield Units) and connected component identification to find the initial lung regions and trachea location, 2) by using the most apical point of the trachea as a starting point, a region growing technique is applied to detect the airway trees, and 3) left and right lungs are separated as the two largest connected components remaining after removing the trachea and main left and right bronchi. Figure 3.6 shows a typical lung segmentation result.

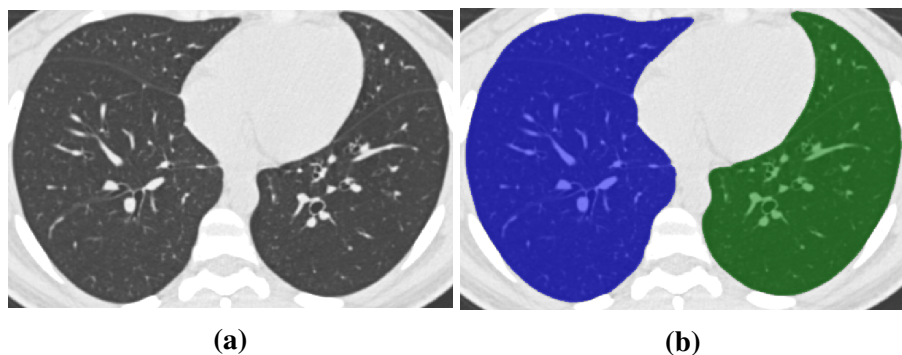


Figure 3.6: Lung segmentation result using the common thresholding method. (a) Raw CT image. (b) Segmented lungs.

3.3.2 Statistical finite element models of lung and fissure shape

For human organs, there is a significant difference in shape and anatomy between different groups of people, such as young and old, male and female, healthy and diseased (Krumpe et al., 1985; Crapo, 1993). This difference is caused by different functional signals and behaviours, leading to organ shape variation across populations. Shape

analysis provides a way to understand the underlying mechanisms of those variations in anatomical and physiological processes. The importance of statistical shape analysis in many kinds of biological studies has been well established (Dryden and Mardia, 1998; Stegmann and Gomez, 2002; Styner et al., 2003; Heimann and Meinzer, 2009), because of its potential to capture morphological variation within and between healthy and pathological structures.

Computational model-based approaches to solve problems in image segmentation have become increasingly popular in the last two decades (Taylor et al., 1995; Kelemen et al., 1999; Tsai et al., 2003; Okada et al., 2008). In these approaches, each new image set was matched to its expected shape of organ for that individual as a guide for segmentation. This potentially reduces the impact of image artefacts and other perturbations associated with traditional low-level algorithms (Ecabert et al., 2008; Zhang, 2013). To account for individual variations in lung shape and location of fissures (including how they vary with lung inflation), one can analyse a series of training shapes using statistical techniques, leading to a statistical shape model. Using this statistical definition of a cohort of individuals, one can begin to predict an individual's organ shape based on characteristics of that individual to help guide segmentation procedures.

Finite element lobar shape modeling

To guide a statistical shape model based segmentation, the first step is to generate a statistical lobar shape mesh using a set of training data. Here, we employ a Statistical Finite element analysis of Lobe (SFeaL) based on an active shape model (ASM) (Cootes et al., 1995). To do this, a training set of segmented lung and fissure surface locations was used to describe a cohort of adults with radiologically normal lungs. This approach employs a finite element shape mesh to specify pulmonary lobar shape which provides an efficient

parameterized representation of lobar boundaries and makes shape constraints available during image analysis. The training set consisted of data from 50 subjects. 35 subjects were selected from a study of healthy subjects aged 50 to 100 years, the human aging cohort (AGING) study and a further 15 subjects were selected from a separate study of younger healthy subjects, the Human Lung Atlas (HLA). All the AGING and HLA subjects are healthy non-smoking subjects including both males and females. In the AGING group, HRCT imaging was acquired at Auckland City Hospital using a Phillips Brilliance 16 scanner, with between 400-700 slices per volumetric image. The study was approved by the Northern A Health and Health and Disability Ethics Committees (HDEC), Ministry of Health on 29 April 2013 through the HDEC-Full Review Pathway - ethics reference 13/NT/41. The HRCT images from HLA cohort were obtained at the Iowa Comprehensive Lung Imaging Center (I-Clic) using a Siemens Sensation 64 MDCT scanner, with between 500-700 slices per volumetric image. The study was approved by the University of Iowa Institutional Review Board. A summarized population demographics of the subjects used for statistical shape model construction is listed in Table 3.3

Table 3.3: Summarized demographics for the AGING and HLA datasets.

	AGING (N=35)	HLA (N=15)
Age (years)	72.3 ± 11.41	22 ± 1.9
Sex(M/F)	18/17	5/10
Height(m)	1.66 ± 0.14	1.7 ± 0.1
Weight(kg)	70.6 ± 11.1	67.6 ± 12.2
BMI(kg/m^2)	25.6 ± 3.0	23.3 ± 2.2
Ethnicity		
- Caucasian	25	14
- Māori(AGING only)	1	N/A
- Asian	2	-
- African-American	-	1
- Unknown	7	-

To define the lung shape, volumetric CT images were segmented using the method described in Section 3.3.1. The segmented lung surface was then digitized into a set of data points as a 3D-space representation of lung shape (Figure 3.7a). Fissure surface segmentation was performed manually using the open-source visualization software CMGUI (<https://www.cmiss.org/cogui>) by an expert user, to provide a gold-standard definition of the fissure location for each subject in the training set (Figure 3.7b, 3.7c). A high order (bi-cubic Hermite) finite element template mesh with the same mesh connectivity for each subject was geometry fitted to the lung and fissure surface data for each subject. The current lung lobe mesh consists of two separate meshes which represent the left and right lung enclosing the lung parenchymal tissue volume.

An initial template mesh was created by selecting some data points to be nodes, and then creating two-dimensional surface elements by joining these node points appropriately. The template mesh for the left lung mesh has 35 nodes and 44 elements which described the left lung surface and left oblique fissure, while the right lung mesh has 50 nodes and 62 elements which defined right lung surface, right oblique fissure and right surface fissure. For fitting to lung and lobe shape data, the template mesh was modelled using bi-cubic Hermite basis functions with C1 continuity. This bi-cubic Hermite mesh has the same mesh connectivity as the template mesh, but it also contains nodal derivative information. Each node has 12 degrees of freedom (DoF)s which store the global coordinates (x, y and z) and first and second nodal derivatives ($\frac{\partial n}{\partial \xi_1}$, $\frac{\partial n}{\partial \xi_2}$, and $\frac{\partial^2 n}{\partial \xi_1 \xi_2}$), where n is x, y and z, and ξ is the local element coordinate. In this lung lobe model they are defined such that ξ_1 is in the anterior-posterior direction while ξ_2 is in the crano-caudal direction. ξ_1 and ξ_2 have values that range from 0 to 1. **There is actually no C1 continuity at certain regions such as the juction between fissure and surface. Some areas of the mesh required 'collapsing' either at the ends to close the mesh or at**

specific locations where additional directions were necessary to maintain the uniform ξ convention. In those regions, 'versions' were introduced to take care of sharp edges or where surface required edge or discontinuity. Versions can accommodate multiple derivatives for each x_i direction at one node. Each node of the fitted mesh is either an anatomical landmark (the left/right lung apex, the base vertex, the shape corner and the centre point of the middle line of fissure) or a pseudo-landmark (e.g. a specific proportion of the arc-length between two anatomical landmarks). These landmarks allow the coordinate of the control points to be defined in consistent positions registered to the geometry of the lung. A least squares fit of the mesh to the lung and fissure surface data was conducted using CMISS (<https://www.cmiss.org>), which is a finite element modelling environment. Specifically, the sum of the distances between each data point and its projection on to the nearest element was minimized during the fitting process. This distance is a function of the element location and shape parameters. In this procedure, the nodal parameters are interpolated to find the projected points. The global coordinates of the projected points are a function of local element coordinates, ξ_1 and ξ_2 , and nodal parameters. Some manual operations were involved to adjust the mesh nodal positions and derivatives to the data cloud, which can help to improve the speed and accuracy of fitting. The average root mean square (RMS) error of this fitting method was 4.79 mm for the 50 training subjects (Figure 3.7d). More details on the fitting procedure can be found in (Bradley et al., 1997; Tawhai and Burrowes, 2003; Fernandez, 2004).

PCA-based statistical shape model construction

A prerequisite of the construction of an SSM is object alignment to remove the orientation and scaling differences between shapes. Here a General Procrustes Alignment

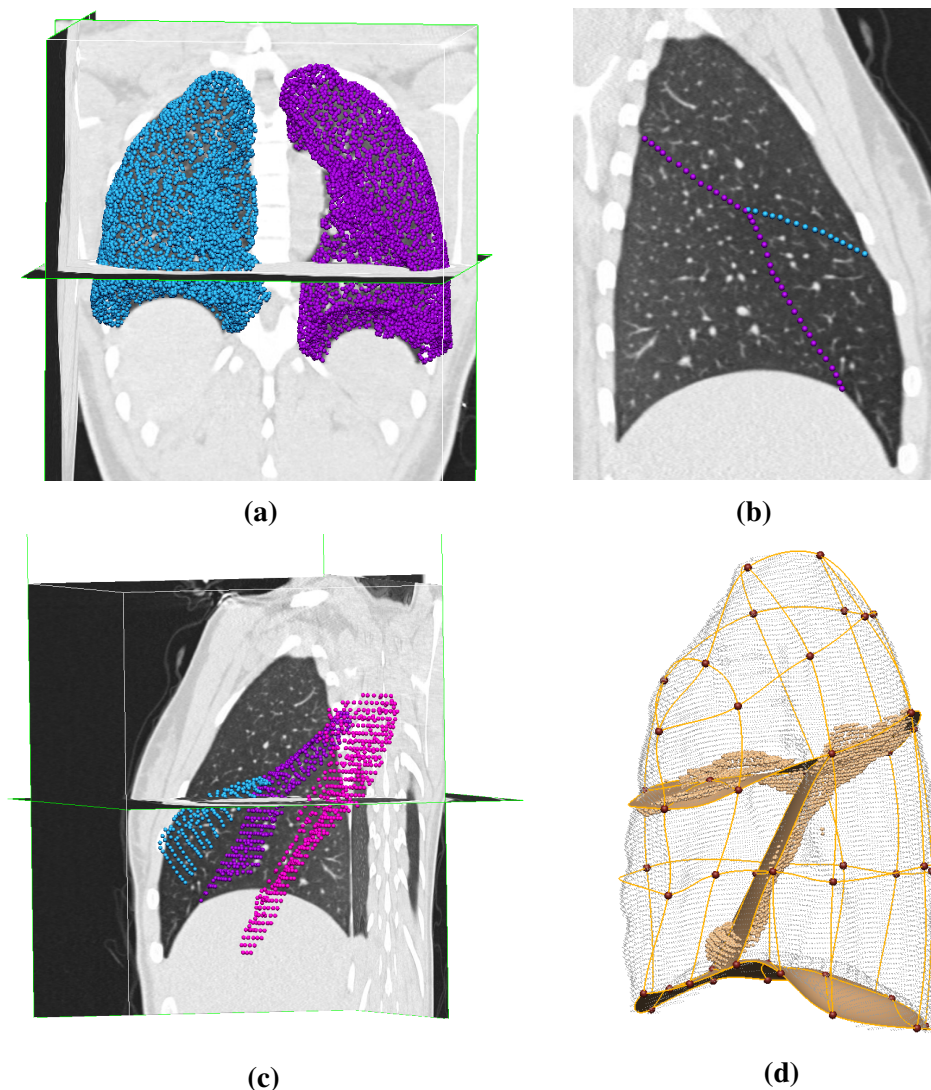


Figure 3.7: Finite element modeling of lung lobe shape. (a) Lung surface data extracted from segmented lung masks (purple points for left lung, blue points for right lung). (b) Manual digitized fissure points in 2D sagittal image of right lung (purple points for right oblique fissure, blue points for right horizontal fissure). (c) Manual digitized fissure points shown in 3D (pink points for left oblique fissure, purple points for right oblique fissure, blue points for right horizontal fissure). (d) Lobe shape fitting with lung surface data and digitized fissure data of right lung.

(GPA) was selected as a registration method (Dryden and Mardia, 1998; Rohlf, 1999). The GPA algorithm finds the optimal rotation matrix and translation vector which minimizes the overall distance between two sets of points with respect to the Euclidean norm. In this study, a reference lung model sample was randomly chosen from the training set. Then all the other training models were aligned to this reference model. In this process, the volumes of all subjects were normalized to 1 L and any residual rotation and translation were removed. The generalized procrustes alignment can be represented as an affine transformation in mathematical terms

$$\bar{S} = \alpha RS + T, \quad (3.1)$$

where \bar{S} represents the aligned shape vector to the reference shape from the subject shape vector S , R is the rotation matrix and T is the translation vector. Figure 3.8a shows the procrustes aligned meshes of all the 50 subjects. For each subject, the aligned lung shape can also be represented as

$$\bar{S} = [\bar{x}_1 \bar{x}_2 \bar{x}_3 \dots \bar{x}_{p-1}; \bar{x}_p], \quad (3.2)$$

where \bar{x} are the nodal parameters which contain coordinates and derivatives (12 DoFs), and p represents the number of nodes for both left and right lung ($p = 225$ in this study). The data vector \bar{S} of each lung was then assembled as the concatenation of all lungs, termed \bar{S}_{whole} . \bar{S}_{whole} is an $n \times N$ matrix, where n is the number of nodal parameters for each lung ($n = 12 \times 225 = 2700$ in this study), and N is the number of training subjects ($N = 50$). Thus, \bar{S}_{whole} can be regarded as a cloud of N points in the constructed n - N space. This matrix was decomposed into modes of variation using PCA. PCA is a commonly used technique in statistical feature space to reduce the dimension of

the dataset. It uses an orthogonal transformation to convert a number of (possibly) correlated variables into a set of values of linearly uncorrelated variables called principal components. The number of distinct principal components is equal to the smaller of the number of original variables or the number of observations minus one. The resulting vectors are an uncorrelated orthogonal basis set.

In order to perform PCA, each shape parameter was centred by subtracting the mean value \bar{x} . Then the covariance matrix was built based on the mean-centred matrix S by $C = SS^T$. After the PCA technique was performed on the covariance matrix C , we obtain a set of eigenvectors $\mathbf{u}_1, \mathbf{u}_2, \dots$, corresponding to a set of non-negative eigenvalues $\lambda_1, \lambda_2, \dots$. Each eigenvalue represents how much variation or variance in the data is captured by the corresponding eigenvector. Each lung shape variation $m_i(w)$ can be approximated by a linear combination of the eigenvector and its corresponding eigenvalue

$$m_i(w) \approx S_{mean} + \mathbf{u}_i w_i, \quad (3.3)$$

where w_i is a weight factor given to each mode of variation, and $i = 1, \dots, L$ ($L \leq 49$ in this study). S_{mean} is the average shape across all the subjects, which is obtained by

$$S_{mean} = \frac{1}{N} \sum_{i=1}^N s_i, \quad (3.4)$$

where s_i is the i th lung shape model from the training set, here $i = 1, \dots, N$ ($N=50$ in this study). The average shape model is shown in Figure 3.8b.

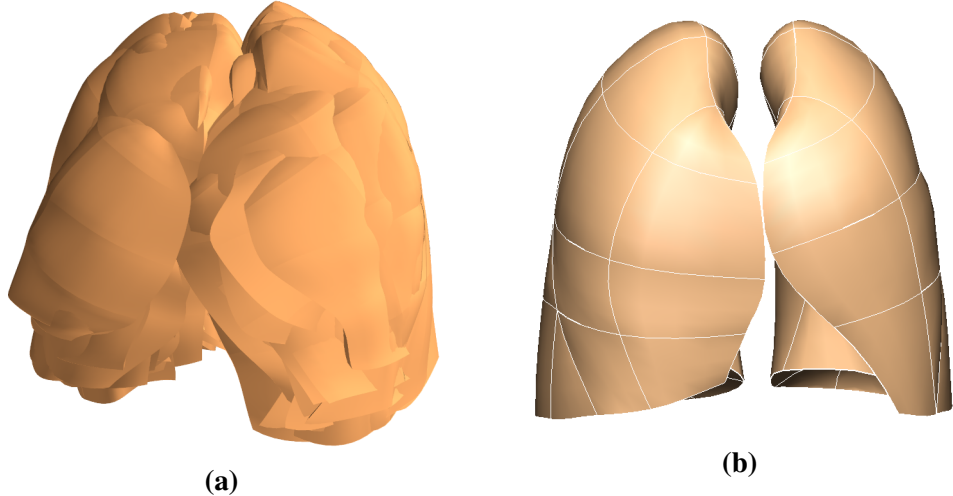


Figure 3.8: Statistical shape model construction based on principal component analysis. (a) Procrustes aligned meshes of 50 subjects. (b) Average shape model of 50 training subjects. All the weight values are zero for this shape model.

3.3.3 Initial prediction of lobar location in an individual

Using the method described in section 3.3.2, the lung shape variation across the training set can be decomposed into a series of modes, and each specific lung shape can be represented with the corresponding mode weight values. In this study each mode represents one type of lung and fissure surface shape variation. In order to predict the fissure location, two PCA-based SSMs were constructed using the same training dataset. The first lobe SSM was built using both the lung surface parameters and fissure surface parameters. The second lung SSM was derived for the same training set but did not include the fissure surfaces and so only described the shape of the lung surface.

The two SSMs were used to predict the fissure locations for subjects that were not part of the training set, using only the definition of the lung surface for the subject as input. A finite element mesh of the lung surface (without fissure information) was generated for each new subject. The new fitted lung mesh was procrustes aligned to the same

reference model as the training subjects were aligned to. Then this aligned lung surface mesh was projected on to the lung surface SSM (with no fissure surfaces). The principal component weight values were calculated from the projection, which was represented as $w_{new} = [w_{new1}, w_{new2}, \dots, w_{newL}]$ ($L \leq 49$) here. The first seven principal components accounted for over 90% of the total lung shape variation in the training set. Therefore, the first seven mode weights were used on the lobe SSM (which includes both lung and fissure surfaces) to reconstruct the projected lobe mesh for this new subject

$$S_{new} = S_{mean} + \sum_{i=1}^7 \mathbf{u}_i w_{newi}, \quad (3.5)$$

where S_{mean} is the average lobe shape model across all the subjects, \mathbf{u}_i is the first seven eigenvectors of the covariance matrix C corresponding to the lobe SSM, and w_{newi} is the projected weight values from the lung SSM. An initial estimation of fissure locations was then made (Figure 3.9). This initial prediction of lobar fissures provides a reduced search area for subsequent image analysis and ensures an estimation of complete lobar structures even if a fissure is incomplete or is difficult to detect.

3.3.4 Multi-scale Hessian-based fissure detection

The final fissure detection was accomplished using an enhancement filter. Conventional enhancement filters are typically based on first (structure tensor) or second (Hessian matrix) order image information (Frangi et al., 1998; Lorenz et al., 1997). This study used the Hessian matrix based on gray-scale curvature information combined with Gaussian smoothing as a basic operator to enhance the fissure structure. In 3D space, fissures are free-form surfaces in the lungs that locally resemble plate-like structures, since the grey-value increases rapidly from the structure border to the centre and decreases again

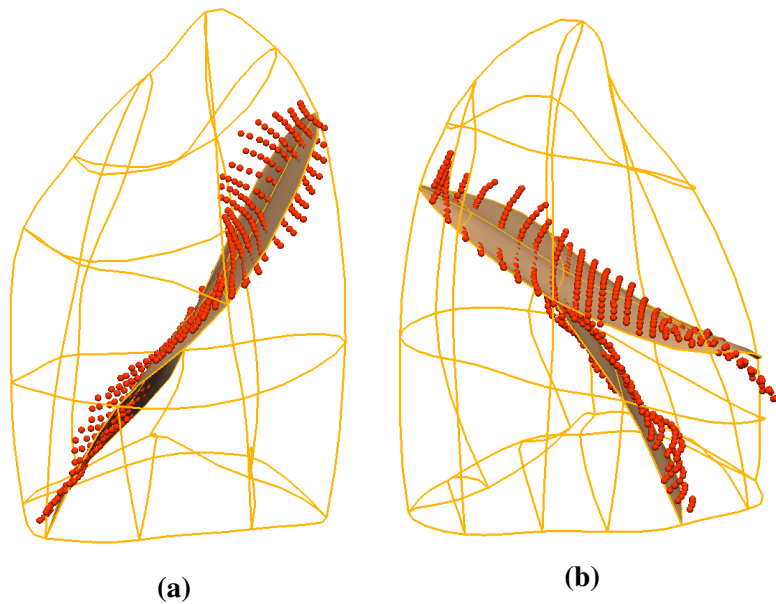


Figure 3.9: Fissure prediction results compared to ground truth fissure points for one subject. The fissure surface meshes are estimated fissure locations and the red points are manual tracing fissure points by an expert. (a) Left lung. (b) Right lung.

to the opposite border. Hessian-based filters are typically used to enhance and differentiate structures with specific shapes, i.e., blobs, sheets and tubes (Frangi et al., 1998; Lorenz et al., 1997).

A common approach to analyse the local behaviour of an image, L , is to consider the local grey-value variations in the neighbourhood of a point x_0 modelled by a Taylor expansion to the second order

$$L(x_o + \delta x_o, s) \approx L(x_o, s) + \delta x_o^T \nabla_{o,s} + \delta x_o^T H_{o,s} \delta x_o, \quad (3.6)$$

where $\nabla_{o,s}$ and $H_{o,s}$ are the gradient vector and Hessian matrix, respectively, of the image computed in x_o at scale s .

To calculate these differential operators of L , concepts of linear scale space theory are used (Koenderink, 1984; Florack et al., 1992). In this framework, differentiation is

defined as a convolution with derivatives of Gaussians

$$\frac{\partial L(x, s)}{\partial x} = s^\gamma L(x) * \frac{\partial G(x, s)}{\partial x}, \quad (3.7)$$

where the D-dimensional Gaussian is defined as

$$G(x, s) = \frac{1}{\sqrt{2\pi s^2}^D} e^{-\frac{\|x\|^2}{2s^2}}, \quad (3.8)$$

where s is the kernel size of the Gaussian. The second derivative of a Gaussian is in many cases a good approximation to the optimal filter for a plane-like structure. Through using the second derivative operator combined with Gaussian smoothing as the basic operator (Hessian matrix), we are able to make the non-supervised fissure filter scale-dependent (Lorenz et al., 1997; Li et al., 2003). In order to make sure a variety of sizes of fissures can be captured by the Hessian, a range of kernel sizes was implemented from 0.5 mm to 2.5 mm in 0.5 mm increments as the kernel size of the Gaussian to obtain a final estimate of 'fissureness'

$$F_{output} = \max_{s_{min} \leq s \leq s_{max}} F_0(s), \quad (3.9)$$

where s_{min} and s_{max} are the minimum scale (0.5 mm) and maximum scale (2.5 mm). Each scale s gets a response. In the final output of the multiscale enhancement filter, the maximum output over all scales is assigned to each voxel.

At each image voxel, the Hessian matrix was constructed from the six independent second order derivatives as a symmetric matrix

$$Hessian = \begin{bmatrix} H_{xx} & H_{xy} & H_{xz} \\ H_{yx} & H_{yy} & H_{yz} \\ H_{zx} & H_{zy} & H_{zz} \end{bmatrix}, \quad (3.10)$$

where $H_{ij} = \left| \frac{\partial^2 H}{\partial r_i \partial r_j} \right|$, and r represents the gradient direction.

The idea behind eigenvalue analysis of the Hessian is to extract the principal directions in which the local second order structure of the image can be decomposed. The eigenvalue decomposition extracts three orthonormal directions which are invariant up to a scaling factor when mapped by the Hessian matrix. In this chapter, λ_k will be the eigenvalue with the k -th smallest magnitude ($|\lambda_1| \leq |\lambda_2| \leq |\lambda_3|$). Under this assumption, Table 3.4 summarizes different structures distinguished by an analysis of the eigenvalues of the Hessian.

Table 3.4: Possible structures on images in 2D and 3D, and its corresponding eigenvalues λ_k . H and L describe the absolute value of λ_k , H is high, L is low, +/- indicate the sign of the eigenvalue. The eigenvalues relationship here is:
 $|\lambda_1| \leq |\lambda_2| \leq |\lambda_3|$.

2D		3D			Orientation structure
λ_1	λ_2	λ_1	λ_2	λ_3	
L	L	L	L	L	noisy structure
		L	L	H-	bright plane-like structure
		L	L	H+	dark plane-like structure
L	H-	L	H-	H-	bright tubular-like structure
	H+	L	H+	H+	dark tubular-like structure
H-	H-	H-	H-	H-	bright blob-like structure
H+	H+	H+	H+	H+	dark blob-like structure

As shown in Table 3.4, an eigenvector analysis of the Hessian matrix can thus be used to detect fissure-like structures, and the respective eigenvectors point out singular directions. In 3D space, a light plane on a dark background is characterized by one large

positive second derivative (λ_3) perpendicular to the fissure plane, since the grey-value increases rapidly from the plane-structure border to the centreline and decreases again to the opposite border. And two small second derivatives of either sign (λ_1 and λ_2) parallel to the plane should occur (shown in Fig 3.10). Thus, on the bright fissures, the ideal relationship is defined as $|\lambda_1| = |\lambda_2| = 0$ and $\lambda_3 \ll 0$, $|\lambda_1| \leq |\lambda_2| \leq |\lambda_3|$. From these characteristics, we can get a fissure probability of each voxel defined as

$$F_0(s) = \Theta S_{plane} S_{noise}. \quad (3.11)$$

The parameter Θ suppresses points whose largest eigenvalue λ_3 is positive, since fissures are locally bright, and is defined as

$$\Theta = \begin{cases} 1, & \lambda_3 < 0 \\ 0, & \lambda_3 \geq 0. \end{cases} \quad (3.12)$$

Since the largest eigenvalue $|\lambda_3|$ should be much larger than the other two eigenvectors, the second factor S_{plane} uses the ratio between $|\lambda_2|$ and $|\lambda_3|$ to search sheet-like structures, so that the voxels where $|\lambda_3|$ and $|\lambda_2|$ are significantly different. S_{plane} is defined as

$$S_{plane} = \exp\left(-\frac{R_{plane}^2}{2\alpha^2}\right), \quad (3.13)$$

$$R_{plane} = \frac{|\lambda_2|}{|\lambda_3|}, \quad (3.14)$$

where α was set to 0.5 in this study. The third factor S_{noise} aims to suppress noise voxels such as blob-like structures. Unlike plane-like structures which have relatively

large $|\lambda_2|$ and $|\lambda_3|$ ratio, the noise voxels usually have low $|\lambda_1|$, $|\lambda_2|$ and $|\lambda_3|$ (as shown in Table 3.4). Therefore, here we use

$$S_{noise} = 1 - \exp\left(-\frac{R_{noise}^2}{2\beta^2}\right), \quad (3.15)$$

$$R_{noise} = \sqrt{\lambda_1^2 + \lambda_2^2 + \lambda_3^2}, \quad (3.16)$$

with β set to 0.5 for thresholding. $F_0(s)$ then gives a high response to local plane-like structures (fissures) and suppresses other pulmonary structures (noise). An example of this enhancement filter applied in an individual is shown in Figure 3.12a.

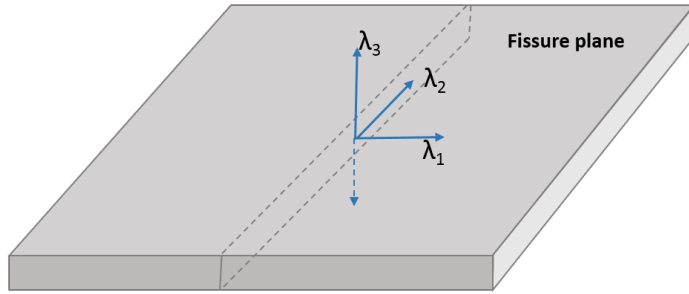


Figure 3.10: The three eigenvectors of the Hessian matrix representing plane-like structure (fissure). λ_1 and λ_2 are parallel to fissure plane, λ_3 is perpendicular to fissure plane.

Blood vessel voxels were subsequently filtered from the fissure enhanced result. The segmentation of vessels was achieved using a classical vessel segmentation method (Frangi et al., 1998). This method uses a multiple scale (from 0.5 mm to 3.0 mm in 0.5 mm increments as the kernel size of Gaussian) Hessian-based enhanced filter, which is similar to the fissure detection filter described previously. The main difference is here the aim is to search for the tube structure (vessels). In a 3D image, the relationship of Hessian eigenvalues λ_1 , λ_2 and λ_3 of an ideal bright tubular structure in a dark

background should be described as $|\lambda_1| \approx 0$, $|\lambda_1| \ll |\lambda_2|$, $\lambda_2 \approx \lambda_3$ (see Figure 3.11). Therefore, the following equations were used as the enhancement filter to detect vesselness structures

$$V_0(s) = \begin{cases} 0, & \text{if } \lambda_2 > 0, \\ (1 - \exp(-\frac{R_A^2}{a^2})) \exp(-\frac{R_B^2}{2b^2})(1 - \exp(-\frac{S^2}{2c^2})), & \text{otherwise} \end{cases} \quad (3.17)$$

where a and b were both set to 0.5, and c was set to 500 in this study. R_A , R_B and S are defined as

$$R_A = \frac{|\lambda_2|}{|\lambda_3|}, \quad (3.18)$$

$$R_B = \frac{|\lambda_1|}{\sqrt{|\lambda_2||\lambda_3|}}, \quad (3.19)$$

$$S = \|H\|_F = \sqrt{\sum_{j \leq D} \lambda_j^2}, \quad (3.20)$$

where D is the dimension of the image. $V_0(s)$ gives a probability of vesselness for each voxel. Then segmented blood vessels were selected through detecting the voxels whose vesselness value was larger than a specific threshold (threshold = 10 in this study (Frangi et al., 1998)). D_{vessel} was used to represent the distance transform to the segmented vessel line, thus the final fissureness after decreasing the values of vessel voxels was defined as

$$F_{final}(s) = F_0(s)S_{vessels}, \quad (3.21)$$

$$S_{vessels} = \exp\left(1 - \frac{D_{vessel}^2}{2d^2}\right), \quad (3.22)$$

where d was set to 5mm in this study. High vesselness voxels were therefore suppressed and not detected as fissure points in the final result. Fig ?? shows the result after eliminating the vessel voxels.

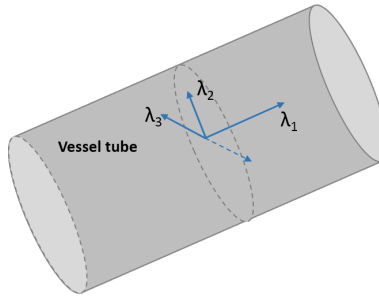


Figure 3.11: The three eigenvectors of the Hessian matrix representing tube-like structure (vessel). λ_1 is parallel to vessel tube, λ_2 and λ_3 are perpendicular to vessel tube.

The initial fissure location predicted by average SSM deformation gives a region of interest (ROI) for an accurate fissure detection, see Figure 3.12c. The candidate points are selected within a certain distance of the initial fissure approximation: the search distance was set to 20 voxels (default value) for the initially projected left and right oblique fissures and 15 voxels for the initially projected right horizontal fissure. To remove some spurious responses such as small plane-like structures on the result, a 2D 4-neighbourhood connected component filter and a 3D 6-neighbourhood vector-based connected component filter were employed successively to eliminate noise arising from small plane-like structures in this search region (Fig 3.12d). A 2D filter was used to eliminate 4-neighbour connected components that were smaller than a minimum small size (set to 10 voxels initially) slice by slice. The 3D vector-based connected component filter used the inner product of the normalized largest eigenvector of the Hessian matrix

in adjacent voxels. These largest eigenvectors are perpendicular to the fissure plane, and their inner product provides a criterion for component connection. As the curvature of a fissure is locally low, adjacent fissure voxels should have similar largest eigenvectors and thus the inner product value of their largest eigenvectors should equal to 1 or slightly smaller than 1. Connected boundary condition was set as an inner product ≤ 0.8 to connected component, then 3D 6-neighbour connected component with a volume less than 100 mm³ was removed as noise from the result.

The detected points were then divided into a set of small subsections corresponding to different x, y intervals. For each subsection, the point of the highest fissure probability (the highest S value) was selected as the final candidate fissure point (Fig 3.12e). Once the maximum fissureness candidates were found, a morphological dilation with a 3 × 3 × 3 voxel cube as structure element was applied iteratively until the largest connected fissure plane was big enough, so that all the other unconnected outliers could be filtered subsequently. Finally, a continuous smooth fissure surface was generated based on the maximum fissure points using a β -spline method with a thin-plane spline (Lee et al., 1997) and extrapolated to the lung boundaries, see Fig 3.12f.

3.3.5 Interactive user control interface

As discussed above, a series of parameter values need to be chosen correctly to ensure a successful lobar segmentation. However, a fixed parameter value is usually not suitable for all the subjects due to a wide variation of lung tissue and fissure appearances across the population. Therefore, a fast and convenient manual interaction to control the segmentation procedure is reasonable and acceptable. Based on an open source software, Pulmonary Toolkit (PTK, <https://github.com/tomdoel/pulmonarytoolkit>), an improved

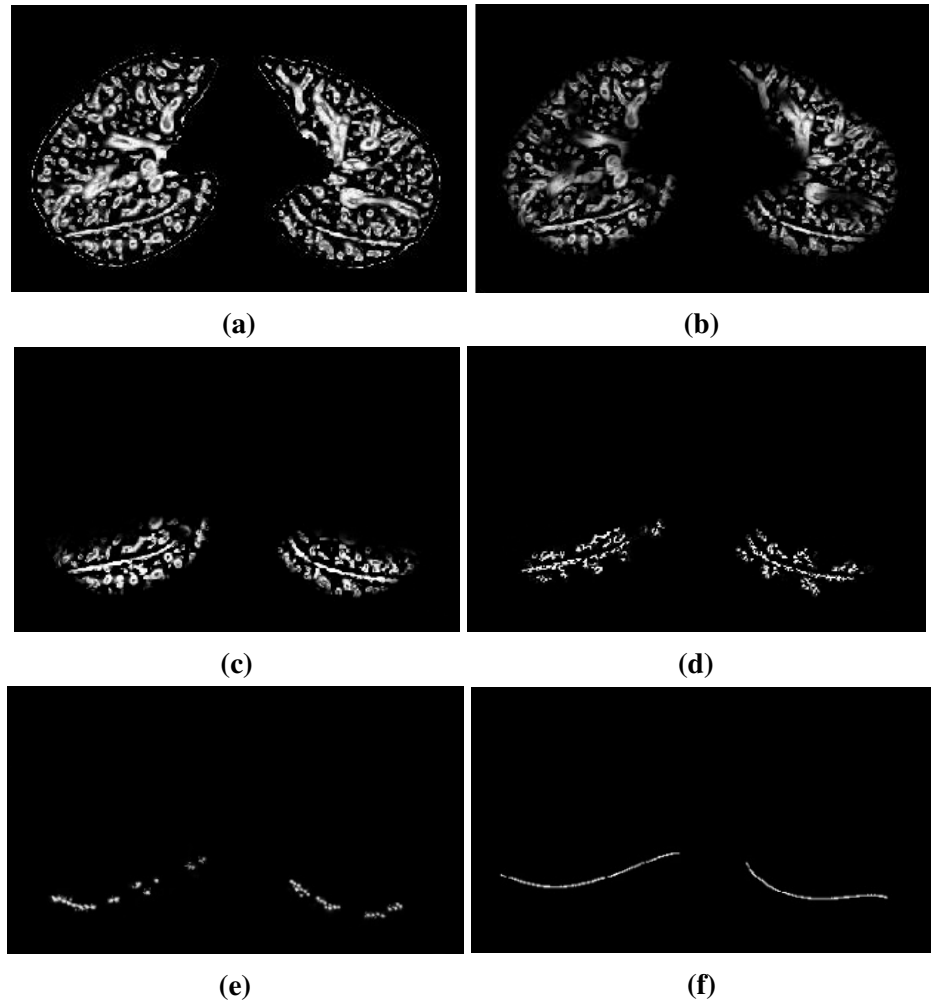


Figure 3.12: Hessian-based multiscale fissure detection results. (a) Hessian-based plane-like structure enhancement filter. (b) Remove vessel voxels (tube-like structures). (c) Selected search regions for fissure detection based on SSM initial fissure prediction. (d) 2D and 3D eigenvector based connected component filter. (e) Fissure candidate points. (f) β -spline curve fissure surface fitting.

user-friendly interactive interface was developed to control the segmentation parameters as input (improved version: <https://github.com/qiuyufly/pulmonarytoolkit/tree/yuwen>). PTK is a software developed on Matlab for the analysis of 3D medical lung images for academic research use. It comprises a library of lung analysis algorithms, a GUI application for visualising and analysing clinical lung images and a rapid prototyping framework for users to develop their new algorithms in an easy way. By making use of some built-in objects and the visualisation system of PTK, the lobar segmentation algorithm was added into the algorithm package and parameter control buttons were made available on the interface. Table 3.5 summarises the interactive user control parameters.

Figure 3.13 shows the user interface of PTK.

Table 3.5: Summary of interactive user control parameters

Parameters	Default values	Notes
Search region for left oblique fissure	20 voxels	Increase the value if there are not enough positive candidate points; decrease the value if there is too much noise
Search region for right horizontal fissure	20 voxels	
Search region for right oblique fissure	15 voxels	
Connected component size for left oblique fissure	30 voxels	Decrease the value if there are not enough positive candidate points; increase the value if there is too much noise
Connected component size for right horizontal fissure	30 voxels	
Connected component size for right oblique fissure	30 voxels	
Total connected component size	300 voxels	

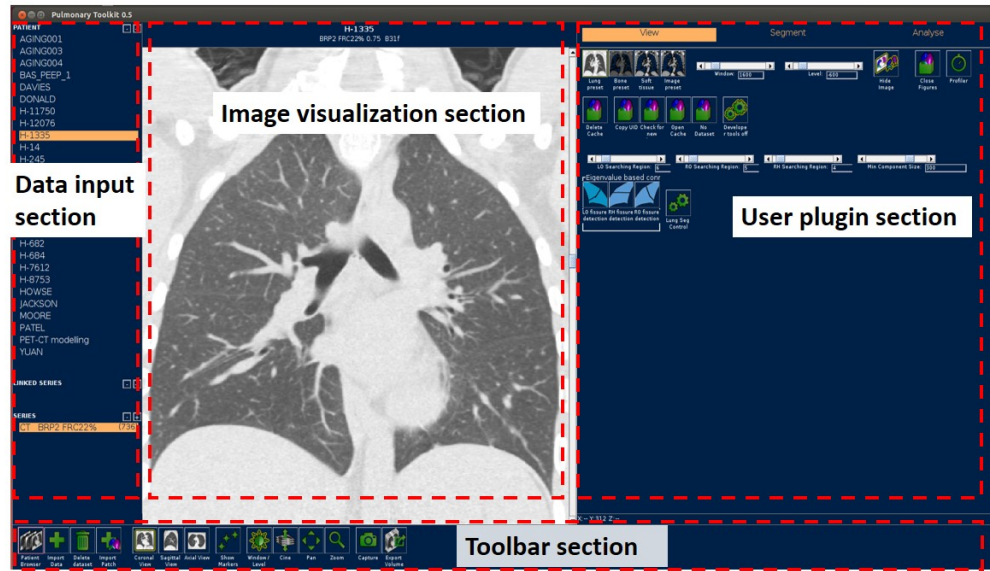


Figure 3.13: PTK User interactive interface. It consists of data input section, image visualization section, user plugin section and toolbar section.

Search region control

Fissure candidate points were detected within a certain distance of the initial fissure approximation. The default distance was set to 20 voxels for left and right oblique fissures and 15 voxels for right horizontal fissure. However, with a fixed search distance, fissure detection sometimes could not be implemented efficiently and accurately. The probability of error detection may increase if the search distance is too large, as more noise will be included in the initial search region. In contrast some positive fissure points will be missed if the search distance is too small. Accurate fissure candidate points are an important prerequisite for good fissure surface fitting. Therefore, user interactive slide buttons were developed on the PTK interface to control the search distance. Through inputting SSM based initial fissure prediction mesh, the estimated fissures can be visualized to overlap on the raw images in the PTK visualization section. Then it is possible

for users to select a suitable search region for each fissure depending on the accuracy of the initial fissure estimate. The better the initial fissure approximation, the lower the search region that should be selected. Figure 3.14 shows the lobe segmentation result before and after change to the search region.

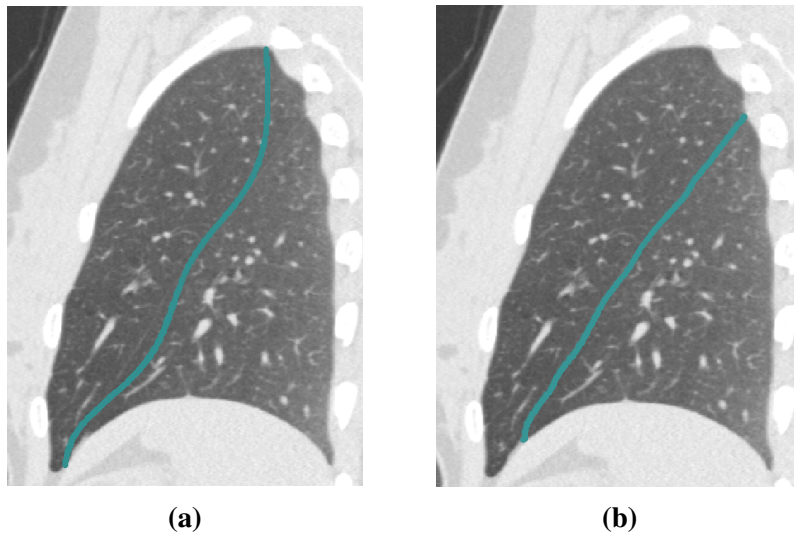


Figure 3.14: Fissure detection results before and after control the search regions. (a) Fissure detection result with a search distance of default 20 voxels. (b) Fissure detection result after setting a specific search distance depending on the accuracy of initial fissure guessing.

Connected component analysis filter control

Connected component analysis is an important operation to help with noise elimination during fissure detection. A suitable connected component size is able to remove most of the small connected structures as outliers and in the meantime retain true fissure structures as much as possible. In order to improve the filter performance, a slide button was used to control the connected component size on the PTK user interface. Through changing the component size threshold, it is possible for us to find a balance between spurious response elimination and target points retention.

Manual correction

Manual correction remains an essential part of lobe segmentation processing. A manual correction tool was available in the PTK software, but in this method only one correct landmark could be selected at a time. Here, a multiple landmark correction method was developed based on PTK built-in packages, and the improved correction tool allows users to modify three fissure points at the same time. By selecting a series of correction landmarks, the corresponding fissure plane is deformed to a new curved surface which passes through all the correct landmarks. The correction region was calculated based on the distance between the landmark and its corresponding fissure plane, and a 3D Gaussian filter with the landmark as the centre was also used to specify the corrected boundary. The correction happens in 3D space so that users don't need to do the correction slice by slice. The whole correction can be finished in a few minutes even when automatic fissure is not complete. Figure 3.15 shows the fissure detection results before and after manual correction.

3.4 Results for SMM segmentation

3.4.1 Testing CT dataset

The semi-automatic SSM lobe segmentation method was tested on two datasets: 1) CT images from five young normal subjects taken at different lung volumes (end inspiration and end expiration), in the supine posture, from the HLA dataset (introduced in Section 3.3.2). The selected dataset consists of five end expiration images and five end inspiration images, which were not part of the SSM training set; 2) CT images from older patients (slice thickness 1.25-3.00 mm) acquired during routine diagnostic inspection

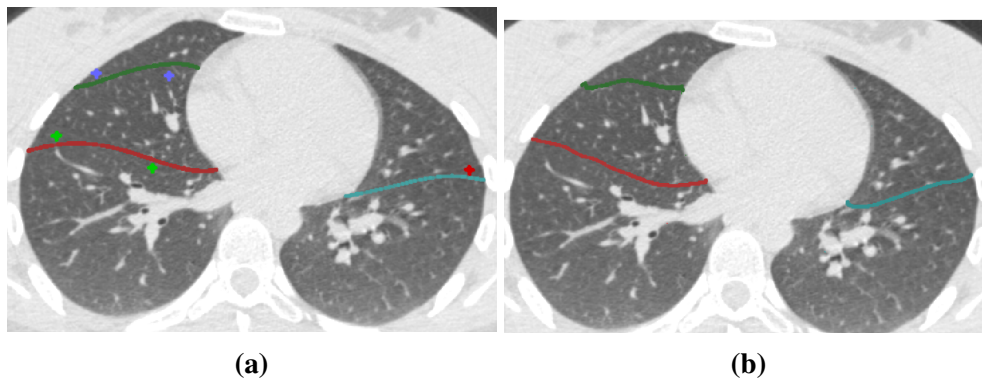


Figure 3.15: Manual correction on automatic fissure detection results (a) Manually select a set of landmarks on real fissure lines shown in raw images to correct automatic fissure detection results (red landmarks are for left oblique fissure, green landmarks are for right oblique fissure, blue landmarks are for right horizontal fissure). (b) Corrected fissure detection results shown with raw images. The corrected fissure lines can match the real fissure locations.

for idiopathic pulmonary fibrosis (IPF). Data from these subjects were acquired from the Auckland District Health Board (ADHB). Access to clinical data was approved by the Southern Health and Disability Ethics Committee.

3.4.2 Test and results

Figure 3.16 shows raw images, initial SSM based fissure predicted locations, and the final automatic SSM-based lobar segmentation results (no manual correction) for a normal healthy subject. Figure 3.17 shows the results for an IPF subject.

To evaluate the performance of the automatic SSM lobe segmentation, the SSM based method was compared with two anatomical-based lobar segmentation methods. A "gold-standard" manual segmentation of the fissures was used for a quantitative evaluation of the performance. The efficiency of manual correction on the segmentation result was also tested.

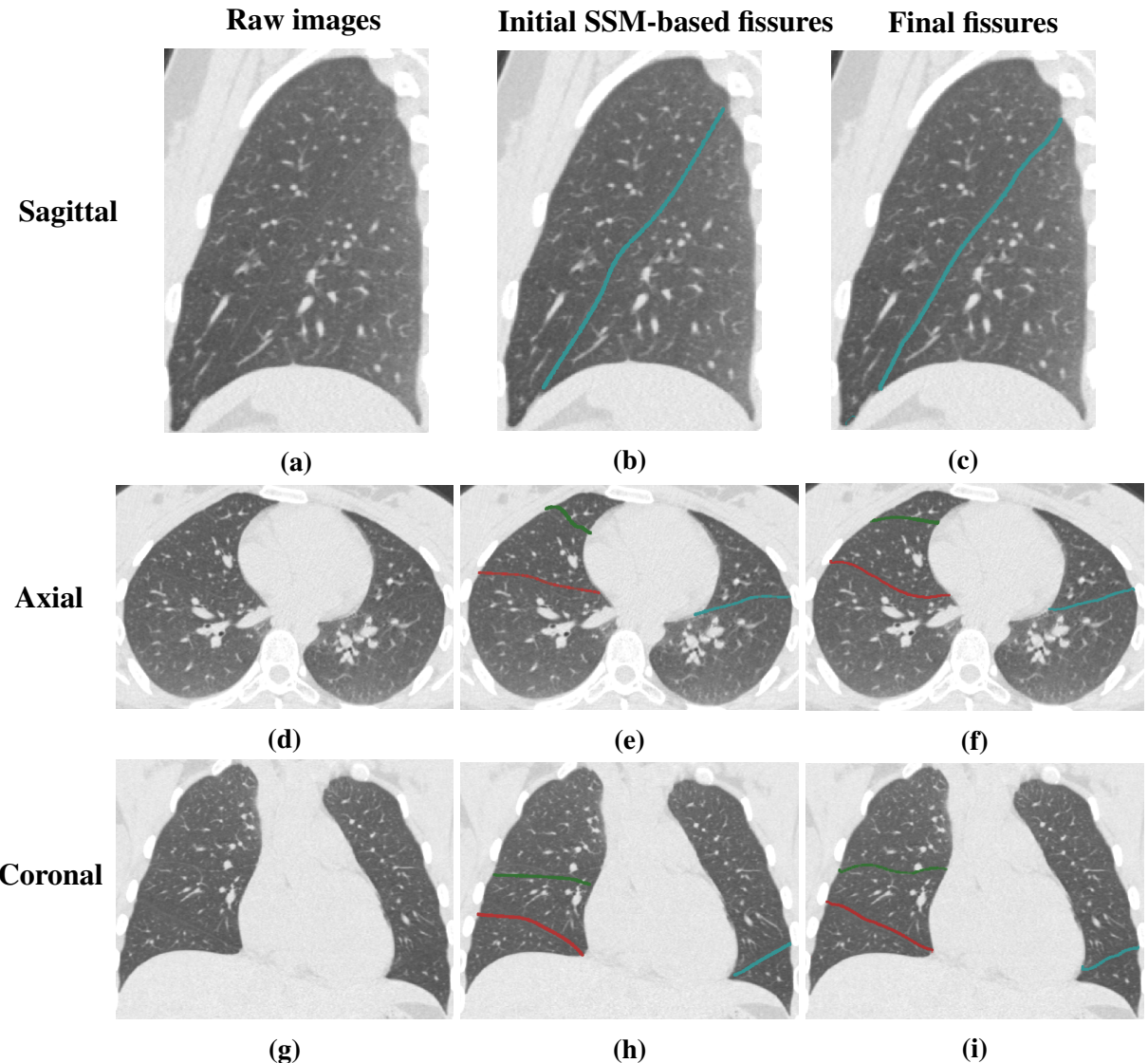


Figure 3.16: Sagittal, axial, and coronal views illustrating raw image, SSM based initial fissure guessing and final automatic fissure detection results of a normal healthy subject. (a), (d), (g) are sagittal, axial and coronal raw images. (b), (e), (h) are sagittal, axial and coronal SSM based initial fissure guessing results. (c), (f), (i) are sagittal, axial and coronal automatic fissure detection results.

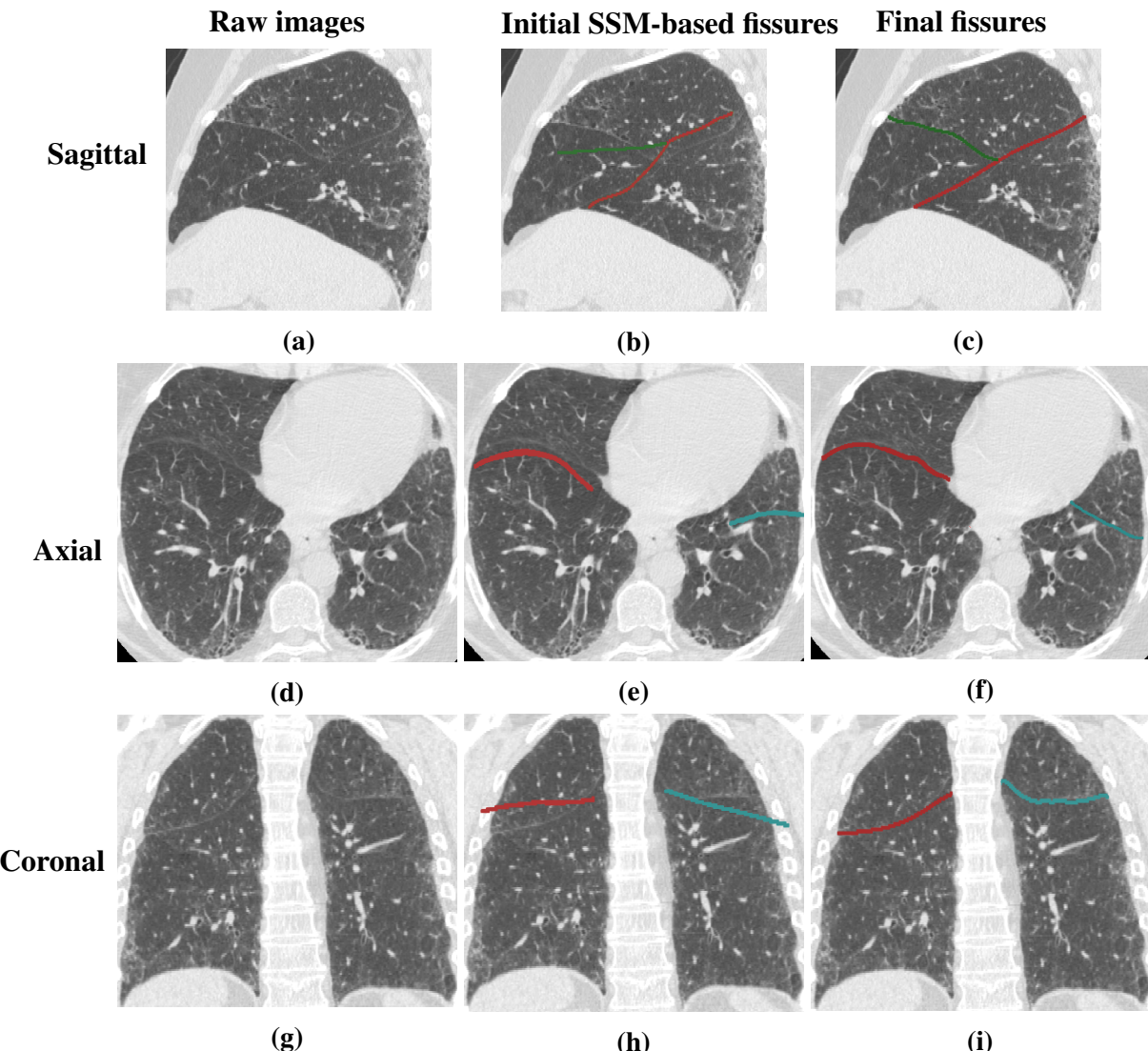


Figure 3.17: Sagittal, axial, and coronal views illustrating raw image, SSM based initial fissure guessing and automatic fissure detection results of an IPF subject. (a), (d), (g) are sagittal, axial and coronal raw images. (b), (e), (h) are sagittal, axial and coronal SSM based initial fissure guessing results. (c), (f), (i) are sagittal, axial and coronal automatic fissure detection results.

The gold standard and quantitative evaluations

To allow for a quantitative evaluation of the performance in a healthy normal dataset and an IPF dataset, the automatic segmentation results were compared with "gold-standard" manual segmentations of the fissures. The "gold-standard" segmentations were acquired by an experienced researcher manually tracing all the three fissures for each subject by digitizing a series of points. The tracing was done on transverse, sagittal and coronal slices to maximise visualisation of the fissures using a custom-written configuration of the open source visualization software CMGUI. The observer can select any of the slice section when digitizing the fissure which can give the best contrast, see Figure 3.7 in section 3.3.2. Fissure detection accuracy was assessed by computing the mean distance between manually-defined fissures points and automatic segmented fissures (with a few manual parameter controls, but without manual correction). For each point in the manual "gold-standard" segmentations, the distance was defined between this point and its closest point in the automatic segmentations as follows:

$$d_i = \min_j \left\{ \sqrt{(x_j^A - x_i^M)^2 + (y_j^A - y_i^M)^2} \right\}, \quad (3.23)$$

where (x_i^A, x_i^M) is the manually traced fissure point, and (x_j^A, x_j^M) is the automatic segmented fissure point. Then the mean error was calculated as:

$$d_{mean} = \frac{\sum_{i=1}^N d_i}{N}, \quad (3.24)$$

where N is the number of points in the manually traced fissure. In addition, the accuracy of the algorithm was evaluated using a percentile measurement. The percentile accuracy is defined as the percentage of the distance between manual and automatic points under

a 3 mm criteria, following the equation:

$$\sqrt{(x_i^A - x_i^M)^2 + (y_i^A - y_i^M)^2} \leq 3 \text{ mm}, \quad (3.25)$$

since 3 mm approximates the thickness of clinical CT images that surgeons and radiologists read in clinical settings (Wei et al., 2009).

For normal subjects, the average mean differences (and accuracies) were 1.76 mm (81%), 3.66 mm (65%), and 2.55 mm (74%), for left oblique, right horizontal and right oblique fissures, respectively. For IPF subjects, the average mean differences (and accuracies) were 2.82 mm (70%), 5.39 mm (59%), and 4.71 mm (63%), for left oblique, right horizontal and right oblique fissures, respectively (shown in Table 3.6).

Table 3.6: Mean error and percentile accuracy of normal healthy and IPF subjects (mean value \pm standard deviation).

	Normal healthy subjects		IPF subjects	
	Mean error (mm)	Accuracy (%)	Mean error (mm)	Accuracy (%)
Left oblique	1.76 \pm 0.68	81.19 \pm 6.61	2.82 \pm 0.71	70.26 \pm 9.10
Right horizontal	3.66 \pm 1.37	64.81 \pm 13.19	5.39 \pm 1.90	58.43 \pm 14.53
Right oblique	2.55 \pm 0.90	73.81 \pm 7.96	4.71 \pm 1.60	62.86 \pm 11.21

Figure 3.18 shows the spatial distribution of error for three representative subjects. Error was highest in regions close to the hilum (where the anatomical structures are complex, and/or the fissure is often incomplete), and where the right fissures meet.

Comparison to anatomical based lobar segmentation method

A marker-based interactive watershed transformation algorithm is a commonly used lobe segmentation method in the current literature (Ukil and Reinhardt, 2009; Pu et al., 2009b; Lassen et al., 2011, 2013). This method mainly relies on anatomical information of the lung which integrates fissures, bronchi and vessels into a cost image

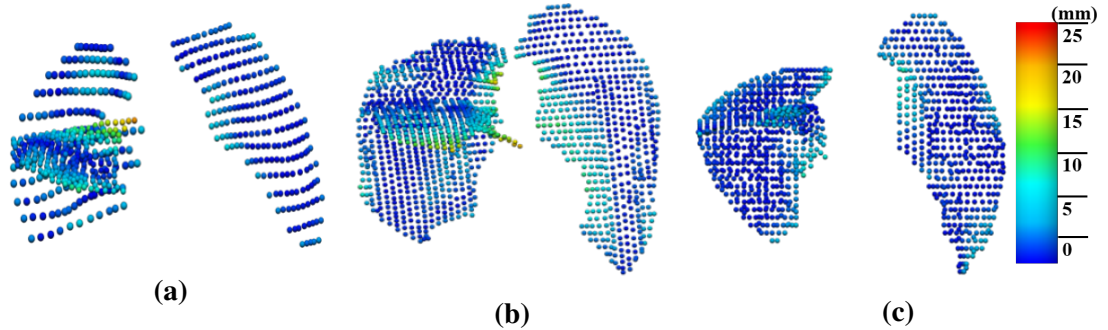


Figure 3.18: The spatial distribution of error between the gold-standard and semi-automatic methods for three representative subjects, highlighting localized regions of low accuracy.

to obtain the lobar boundaries. In the current method, a lobar statistical shape model constructed based on principal component analysis was used to provide an initial estimation of fissure locations. This method gets rid of the dependence on prior segmentation of anatomical structures. To investigate the contribution of using the approximated lobe borders from the deformation of SSM, here the method is compared to two interactive watershed-based pulmonary lobe segmentation softwares: 1. Pulmonary Toolkit, PTK, <https://github.com/tomdoel/pulmonarytoolkit> (introduced in Section 3.3.5); 2. Pulmonary Analysis Software Suite, PASS (Guo et al., 2008). PASS is custom-written software developed at the University of Iowa, that integrates quantitative measurements of lung function and structure analysis. Both of these softwares have a built-in lobe segmentation method which is guided by vessel tree and airway tree.

The two segmentation softwares PASS and PTK tested for comparison were unable to segment the lobes for 9/20 and 7/20 subjects respectively (1/10 and 1/10 normal and 8/10 and 6/10 IPF subjects). In contrast, the model-based method gave an initial estimate for all subjects at all volumes. The main reason for the failure of segmentation is that the airway trees can't be segmented or labelled as lobar branches correctly. Figure

3.19 shows an example of an IPF subject in which airway branches are mislabelled.

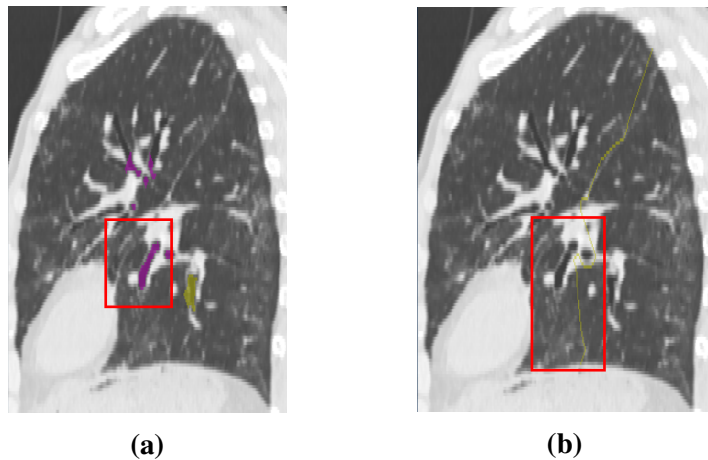


Figure 3.19: An inaccurate initial fissure estimate for an IPF subject caused by mislabeling of lobular airway branches using marker-based interactive watershed transformation algorithm (sagittal view, left lung). (a) The mislabeling of lobular airway branches. Purple is for left upper branches and yellow is for left lower branches. The lower branches in the red box are mis-detected as upper branches. (b) The initial fissure guessing based on the erroneous airway branch labelling result. The approximate fissure has a significant erroneous shift in the red box where mislabelling of lobular airway branches occurs.

The mean square error and percentile accuracy of each fissure for each subject segmented using PTK, PASS and the new method are listed in Table 3.7, 3.8 and 3.9. Although the SSM-based method was able to segment all the subjects (whereas PASS and PTK can't), PASS could sometimes perform better on some young healthy subjects. That is probably because in the healthy lungs, it is possible to extract airways and vessels accurately, therefore these structures are able to provide reliable anatomical information. The SSM-based method had lower error and higher percentage accuracy than PTK for all three fissures for both IPF and normal. Error and accuracy for the SSM-based method were similar to PASS for the healthy subjects, whereas error was much lower and accuracy higher for the SSM-based method applied to IPF data.

Table 3.7: Mean error and percentile accuracy of left oblique fissure for each subject .

Subject	SSM-based		PTK		PASS	
	Mean error (mm)	Accuracy (%)	Mean error (mm)	Accuracy (%)	Mean error (mm)	Accuracy (%)
HLA1	0.96	91.3	1.98	77.3	1.14	89.7
HLA2	1.17	85.6	1.58	82.7	0.57	95.9
HLA3	1.74	79.8	3.18	72.9	0.93	92.2
HLA4	2.61	81.2	Fail	Fail	2.65	82.0
HLA5	1.44	81.6	1.25	90.7	Fail	Fail
HLA6	3.31	68.1	3.78	53.6	0.92	96.0
HLA7	1.67	80.2	1.75	77.0	3.54	66.4
HLA8	1.52	83.3	2.99	66.2	2.68	68.0
HLA9	1.20	88.7	5.69	44.3	2.61	70.6
HLA10	2.03	72.2	5.55	49.6	1.89	77.1
Mean ± Std (HLA)	1.76±0.68	81.2±6.6	3.08±1.56	68.2±15.0	1.88±0.98	82.0±11.3
IPF1	1.91	82.0	Fail	Fail	Fail	Fail
IPF2	3.15	62.3	17.90	22.9	Fail	Fail
IPF3	2.71	79.0	Fail	Fail	Fail	Fail
IPF4	3.21	61.8	Fail	Fail	4.21	56.2
IPF5	1.93	78.7	Fail	Fail	Fail	Fail
IPF6	3.27	63.2	6.71	39.2	4.54	58.8
IPF7	4.24	57.7	4.97	44.7	Fail	Fail
IPF8	2.65	62.8	Fail	Fail	Fail	Fail
IPF9	3.27	73.0	Fail	Fail	Fail	Fail
IPF10	1.91	82.1	3.13	71.5	2.96	73.3
Mean ± Std (IPF)	2.82±0.72	70.3±9.1	8.18±5.76	44.6±17.5	3.90±0.68	62.8±7.5

Table 3.8: Mean error and percentile accuracy of right horizontal fissure for each subject .

Subject	SSM-based		PTK		PASS	
	Mean error (mm)	Accuracy (%)	Mean error (mm)	Accuracy (%)	Mean error (mm)	Accuracy (%)
HLA1	2.61	72.8	2.32	73.7	1.77	81.6
HLA2	1.55	84.1	3.21	58.3	1.59	86.7
HLA3	3.34	60.9	2.68	72.6	1.31	88.3
HLA4	1.67	84.9	Fail	Fail	1.61	88.6
HLA5	4.89	57.9	10.01	41.7	Fail	Fail
HLA6	3.57	62.6	2.64	65.4	6.38	56.2
HLA7	6.02	39.0	4.20	54.1	Fail	Fail
HLA8	4.09	69.9	6.61	22.8	4.48	39.2
HLA9	5.02	52.9	21.74	21.9	Fail	Fail
HLA10	3.86	63.3	18.04	11.6	13.11	14.5
Mean ± Std (HLA)	3.66±1.37	64.8±13.2	7.94±6.85	55.5±16.8	4.32±3.99	65.0±27.1
IPF1	3.91	75.1	Fail	Fail	Fail	Fail
IPF2	4.99	67.0	10.60	12.2	Fail	Fail
IPF3	2.19	82.1	Fail	Fail	Fail	Fail
IPF4	4.95	58.7	Fail	Fail	10.09	19.2
IPF5	6.99	49.2	Fail	Fail	Fail	Fail
IPF6	6.21	38.5	41.01	0.5	Fail	Fail
IPF7	6.47	53.6	9.2	19.6	Fail	Fail
IPF8	8.04	41.2	Fail	Fail	Fail	Fail
IPF9	7.52	45.4	Fail	Fail	Fail	Fail
IPF10	2.67	73.6	9.31	34.9	7.56	49.4
Mean ± Std (IPF)	5.39±1.90	58.4±14.5	17.53±13.57	16.8±12.4	8.83±1.26	34.3±15.1

Table 3.9: Mean error and percentile accuracy of right oblique fissure for each subject .

Subject	SSM-based		PTK		PASS	
	Mean error (mm)	Accuracy (%)	Mean error (mm)	Accuracy (%)	Mean error (mm)	Accuracy (%)
HLA1	1.99	79.9	2.54	69.9	1.12	87.7
HLA2	2.03	75.1	2.98	58.1	0.64	96.0
HLA3	1.64	82.4	2.48	72.3	0.66	96.5
HLA4	2.15	82.2	Fail	Fail	1.37	96.4
HLA5	2.07	78.5	3.23	61.4	Fail	Fail
HLA6	4.98	75.7	8.31	45.4	4.93	94.5
HLA7	3.02	55.3	3.17	57.1	3.47	57.8
HLA8	2.33	74.0	3.97	58.9	2.40	71.3
HLA9	3.01	66.6	5.72	50.4	2.89	73.5
HLA10	2.32	68.4	8.61	35.4	2.53	70.7
Mean ± Std (HLA)	2.56±0.91	73.8±7.9	4.56±2.78	56.5±10.9	2.23±1.35	82.7±13.7
IPF1	2.52	81.7	Fail	Fail	Fail	Fail
IPF2	2.94	82.5	3.56	55.4	Fail	Fail
IPF3	3.68	59.5	Fail	Fail	Fail	Fail
IPF4	6.23	59.0	Fail	Fail	49.16	6.1
IPF5	4.14	62.0	Fail	Fail	Fail	Fail
IPF6	5.43	48.4	15.88	23.7	6.86	41.6
IPF7	5.07	57.0	11.66	19.3	Fail	Fail
IPF8	7.33	47.8	Fail	Fail	Fail	Fail
IPF9	6.69	63.5	Fail	Fail	Fail	Fail
IPF10	3.06	67.3	4.53	47.8	3.57	67.1
Mean ± Std (IPF)	4.71±1.60	62.9±11.2	8.91±5.10	36.6±15.4	19.87±20.76	38.3±25.0

Manual correction

In order to test the efficiency of manual correction for segmented fissures, three students (who were able to recognize lobe fissures on raw images accurately) were asked to perform manual corrections on an automatic segmented fissure result, spending no more than ten minutes per subject. Table 3.10 lists the comparison of the segmentation accuracy before and after the ten-minute manual correction.

Table 3.10: Mean square error (MSE) (mm) and percentile accuracy(%) of segmented left oblique (LO), right horizontal (RH), and right oblique (RO) fissures before and after manual correction

	Before correction		After correction					
	MSE	Accuracy	Student 1		Student 2		Student 3	
			MSE	Accuracy	MSE	Accuracy	MSE	Accuracy
LO	3.19	57.55	1.35	89.59	1.21	91.84	1.17	93.47
RH	5.02	39.09	1.85	85.28	1.61	90.36	1.64	87.31
RO	4.83	47.80	1.37	92.67	1.18	89.52	0.98	96.88

In addition, for normal healthy subjects, it is most likely to get an accuracy greater than 90% within a few manual corrections. For some abnormal subjects, especially for some severe diseased lungs or some datasets with low quality imaging, over 90% accuracy is possible but needs more time.

3.5 Discussion

In this chapter, a novel pulmonary lobar segmentation method was presented and compared against two existing softwares (PTK and PASS). Results show that the method outperforms both PTK and PASS with respect to the proportion of subjects for whom a segmentation was possible, and the new method had lower error and higher percentage accuracy than both comparison softwares for IPF data. Segmentation error and accu-

racy for data from healthy subjects was similar to PASS, but outperformed PTK. Due to lower imaging resolution and tissue abnormalities, the accuracy of the method was lower for the IPF subjects than the healthy subjects. However, the method was able to detect a fissure in each case, whereas existing research-focussed software can not, especially for the abnormal subjects. Automated segmentation of anatomical structures is still challenging in cases with abnormalities, however, the method did not fail, and it provides a robust basis for segmentation even in abnormal cohorts.

For fissure detection, there are usually two types of errors, false negative detection and false positive detection. False negative detection indicates the leak detection of some true fissure points where fissures are incomplete or have fuzzy appearance. False positive detection indicates the mis-detection of some false fissure points where tissues with small plane-like structures are incorrectly identified as fissures. For IPF subjects, both of the errors may occur during fissure detection. The first type of error exists for most of the subjects, since CT-visualized complete pulmonary fissures are rare, especially for IPF CT imaging, which makes automatic lobe segmentation challenging due to the absence of a physical border. In the current method, the β -spline method with thin plane spline-based surface fitting is able to provide an automated correction of the first type of error, since the fitting operation may help to estimate "incomplete" fissures in the correct direction through extrapolating "complete" fissures to lung borders. This fissure fitting method is a commonly used fitting algorithm (Lee et al., 1997; Doel et al., 2012), however the accuracy of the fitting performance is heavily reliant on the correct detection of complete fissures and a good initial approximation of fissure. Therefore, for some IPF subjects with lower fissure completeness, more manual operations may be needed.

For the second type of error, incorrect detection is usually caused by accessory fis-

sures and interstitial lung disease tissues such as scarring or fibrosis. The 2D connected component filter and 3D eigenvector based connected component filter are able to eliminate most of the non-fissure structures within the search region. However, for IPF subjects, it is still difficult to remove all the noise, since fibrosis usually appears surrounding the fissures and may even be connected to the main fissure plane. For some terminal stage IPF patients, severe honeycomb and reticular regions make lung parenchyma really fuzzy and low contrast from the fissures which increases the difficulty of avoiding mis-detection.

The new SSM-based method performed better on the left oblique fissure than the other two fissures, likely because the left lung has a simpler anatomic structure with only one fissure. In contrast, error detection happens more often in the area of the right lung where the two fissures come into contact. This is illustrated in Figure 3.18, which shows the error distribution over the three fissures for three subjects. It can be seen that the method results in higher error in the lung boundary area, since the fissures here are commonly incomplete on CT scans, thus few fissure candidate points can be detected accurately. There is also a high error around the junction area of the right oblique fissure and right horizontal fissure, since the two fissures are too closed in this region and the search regions may overlap with each other.

In the new method, a statistical shape model was used to provide an initial fissure estimate. Compared to the current published anatomical structure-based methods, the model-based method can predict the fissure location without requiring a preliminary analysis of other anatomical features other than lung shape. For example, traditional anatomical knowledge-based methods such as the watershed-based lobar segmentation relies on the success of the automatic segmentations of the vessel and airway tree and need to label the airway trees to the five main lobar bronchi to get an initial fissure

approximation. When one of those segmentations fails, the method is likely to perform worse (as shown in Figure 3.19). Vessels are distributed all over the lung and due to the high contrast to the lung parenchyma a good segmentation of the vessels is feasible. But in some cases vessels cross the lobar boundaries. Thus, the assumption that there are no vessels at the lobar boundary is not always correct (Pu et al., 2009b). On the other hand, due to the complex radiological appearance of pathological lungs, it is usually difficult to get a reliable airway and vessel tree segmentation (Lassen et al., 2011, 2013). In the current method, no watershed-based lobe segmentation can be performed in the case of a failed bronchi segmentation because the required lobe markers are generated from the labelled bronchi tree. In those cases, the approximated lobar borders might be at the wrong location in the scan. In contrast, the new method is largely independent of the knowledge of lung anatomy, so in the comparison of the model-based estimation of fissure location with a watershed-based method, the latter failed for nearly half of the subjects.

The accuracy of the initial fissure prediction is a very important basis for a good segmentation. However, the model-based fissure prediction method still has some limitations. A main disadvantage is that it can only produce lobar shapes close to the shapes represented in the training set, which leads to a larger error in cases where pathological processes had altered the lobe shapes. As shown in Figure 3.16 and 3.17, the SSM based initial fissure estimate usually performs worse in IPF subjects than in normal healthy subjects. In the following chapters, a statistical shape analysis shows that there is a significant shape difference of right middle lobe and right upper lobe between IPF lungs and normal old lungs. That would be a reasonable explanation for the poor estimation of right horizontal fissure and right oblique fissure of the IPF subject shown in Figure 3.17. In the future, a statistical lobar shape model dataset for a variety of pathologies

could be developed. A dataset containing a wide range of statistical models for different ages, sexes, lung volume or diseases would be able to help predict a more accurate ROI for fissure detection.

Due to variation in lung anatomy and pulmonary disease, no automatic segmentation method can ensure a satisfying lobe segmentation result for all cases. Even for a widely used robust lobe segmentation method, it may be impossible to get a highly accurate segmentation result for all subjects, especially for some abnormal subjects. Therefore, manually interactive operation is usually acceptable and involved in a lot of lobe segmentation processing. A combination of an automatic algorithm and manual interaction is an effective way to obtain accurate segmentation. On the one hand, an automatic segmentation algorithm would help researchers save considerable time from laborious and time consuming manual tasks. On the other hand, a fast and intuitive correction is able to improve the automatic segmentation performance within a few minutes.

3.6 Summary

In this chapter, an SSM based lobe segmentation method was developed. **In addition to producing a result for all subjects, the segmentation accuracy is decent.** The method can provide a relatively accurate result for most IPF subjects, although manual interaction is still needed for some subjects. The method is at least as good as existing methods when segmenting healthy lung, but is considerably more accurate for IPF. It is also more robust than the tested watershed methods, as it does not "fail". In the next chapter, the segmented lobe results will be used to construct an FE mesh to describe the lobe shape for each IPF subject. The patient-specific lobe mesh will work as a basic geometry structure to guide a further disease distribution analysis and functional simulation.

Chapter 4

Quantitative computerized analysis of idiopathic pulmonary fibrosis

As introduced in Chapter 2, the natural history of IPF is poorly understood, and the clinical course for a given patient is unpredictable. Currently, there is a shortage of accepted bio-markers that can indicate the likely progression of IPF (Bartholmai et al., 2013). A successful quantification scheme that allows for recognition of disease across radiology, pulmonary and pathology disciplines still remains difficult. Development of accurate and automatic tools for quantitative assessment of alterations in the lung with IPF will be essential for a rapid patient-specific diagnosis and treatment. To date, the shape of the lungs and lobes in IPF has not been quantified, and nor has the spatial distribution of tissue abnormalities. This chapter describes a study of quantitative analysis of IPF disease based on HRCT scans, including both assessment of tissue abnormalities and lung lobe shape analysis.

4.1 Background

4.1.1 Challenges of IPF diagnosis

Managing patients with IPF presents a substantial health-care burden, due to short survival time and lack of effective treatments (with associated morbidity) (Olson et al., 2007; Raghunath et al., 2014). Accurate assessment and diagnosis of IPF is very challenging, since there is significant individual radiological and physiological variability among patients (Devaraj, 2014). The progression of disease varies considerably, ranging from rapid worsening of symptoms to relatively slow deterioration over several years (King Jr et al., 2011; Richeldi et al., 2017). The American Thoracic Society (ATS) and European Respiratory Society (ERS) has developed diagnostic criteria and schema for adult patients with IPF, and this criteria strongly recommends a multidisciplinary discussion between pulmonologists, radiologists and pathologists for an accurate diagnosis (Raghu et al., 2011; Travis et al., 2013). However, a successful classification and quantification tool that allows recognition of disease consistently across radiology, pulmonary and pathology disciplines still remains difficult.

The appearances of IPF abnormalities are complex and keep changing in extent over time is difficult to assess by traditional methods. Traditional radiological observation to distinguish disease patterns is tedious and not reproducible, and this manual evaluation is not consistent due to variation of inter- and intra-assessment (Flaherty et al., 2007; Watadani et al., 2013). Specifically, the difference in perception and interpretation of visual features of disease, which is associated with the experience and skills of clinical doctors, may lead to variable description of the same patient or even cause "reader error". However, this "error" can not be fully solved by training or improvement of imaging technologies (Kundel, 2006; Bartholmai et al., 2013). More importantly,

the final decision of clinical diagnosis is often based on independent evaluation from the radiologist, clinician and pathologist, which makes it hard to ensure consistency and dependability of results (Flaherty et al., 2004; Sverzellati et al., 2011). Another challenge of diagnosing IPF is the clinical problem of how to consistently detect and discriminate IPF from other idiopathic interstitial pneumonias (IIPs). These distinctive diseases usually have similar clinical presentations or indeterminate pathologic and radiographic appearances. Some cases may even have mixed restrictive/fibrotic and destructive/obstructive processes (Bartholmai et al., 2013). For example, non-specific interstitial pneumonia (NSIP), a pathological subtype of IIPs, appears to behave similarly to those with IPF/UIP patterns, especially for the cases with coexisting UIP and fibrotic NSIP patterns (Monaghan et al., 2004; Flaherty et al., 2001). All of these various IIPs have distinctly different prognosis, and specific therapy that is targeted to a particular pathological process is becoming necessary (Lynch et al., 2005). Therefore, non-IPF IIPs must be discriminated from IPF (Bjoraker et al., 1998).

4.1.2 Advantages of quantitative analysis using HRCT

Recent development in radiological imaging techniques offers exciting opportunities to develop radiological patient-specific biomarkers as important indicators of specific phenotypes (Devaraj, 2014; Gotway et al., 2007). HRCT has played an essential role in evaluating lung disease through recognizing visual patterns and features of disease regions such as ground-glass opacities, reticular patterns and honeycombing (Mueller-Mang et al., 2007). HRCT is also a useful diagnostic tool to differentiate between IPF and other pathologies. It is generally believed that the extent of visual lesion present on HRCT strongly relates to the severity of pathology, and therefore can be used to

monitor the progression of disease and then response to therapy (Kazerooni et al., 1997; Kim et al., 1999; Wells et al., 2003; Saketkoo et al., 2011). In addition, it has been noted that the use of HRCT can actually decrease the need for surgical lung biopsy which is risky for older patients with comorbidities (Bartholmai et al., 2013). As a non-invasive tool for visualizing abnormal parenchymal densities, HRCT has its own advantage in IPF diagnosis even for the cases where HRCT fails to show enough specific features to reflect typical UIP pattern, since HRCT can provide guidance for optimizing the site to obtain a surgical lung biopsy (Kazerooni, 2001; Diette et al., 2005; Misumi and Lynch, 2006; Costabel et al., 2007).

Currently, how the changes of disease can be consistently characterized and quantified over time and how these changes can predict disease progression are still challenging problems. Manual classification and subjective evaluation are usually complicated and not accurate enough. Image-based quantitative analysis is therefore strongly needed for developing a robust and consistent IPF assessment system (Gotway et al., 2007; Lynch et al., 2005). A number of studies have indicated that the quantification of abnormalities on thoracic HRCT has potential to determine the extent of disease. Moreover, it can help with stratifying different types of disease with numerous imaging features in variable distribution (Best et al., 2008; Wells et al., 2003; Sumikawa et al., 2008; Bartholmai et al., 2013). The hypothesis is that through quantifying abnormalities from radiological images, robust objective bio-markers can be developed to drive a patient-specific prediction based on specific phenotypes. This will be important for facilitating individualized clinical management and identifying specific phenotypes linked to clinical disease presentations or therapeutic responses (Raghunath et al., 2014).

4.1.3 Review of current published methods of quantitative analysis of lung disease

In the past few years, there has been considerable effort to provide quantitative analysis of lung parenchymal abnormalities on HRCT scans. Fortunately, quantitative methods to analyse disease patterns of chronic obstructive pulmonary disease (COPD) such as emphysema have been well developed over the last 20 years, and have been able to provide reproducible bio-markers used in sub-clinical diagnosis and assessment (da Silva Felix et al., 2008; Gietema et al., 2011; Galbán et al., 2012; Wang et al., 2013; Castaldi et al., 2013). However, quantification of disease patterns of lung fibrosis or other interstitial lung disease is more challenging, since the appearances and changes of these abnormalities are even more complicated than the characteristics seen with emphysema (Lynch, 2007; Delorme et al., 1997; Galbán et al., 2012; Depeursinge et al., 2010). In the early days, first-order textural analysis methods such as mean lung density (MLD) and histogram analysis (HIST) were used to analyse radiological lung imaging (Gilman et al., 1983; Gould et al., 1988; Müller et al., 1988; Kinsella et al., 1990; Knudson et al., 1991; Behr et al., 1992). These approaches to assess CT data are automatic and objective, but they simply examined a single parameter for the whole lung. The measurement of attenuation (which relates to density) is highly dependent upon lung volume and can be significantly affected by beam-hardening effects, scatter and drifts in scanner calibration. Therefore, these methods are difficult to apply in the presence of mixed disease.

Uppaluri et al. (1999b,a) was an early group to present a multiple feature based method to automatically quantify and classify pulmonary parenchyma of interstitial lung disease based upon HRCT. An adaptive multiple feature method (AMFM) which combined statistical texture measures with a fractal measure was developed to initially

assess the emphysema regions of the lung, and subsequently extended to study subjects with IPF or sarcoidosis. AMFM was further improved to assess as many as 22 independent texture features which enabled classification of pulmonary parenchymas into six tissue patterns, including: honeycombing, ground-glass, broncho-vascular, nodular, emphysema-like, and normal. These 22 texture features consist of statistical features (grey level distribution features, run-length features and co-occurrence matrix features) and fractal features (geometric fractal dimension and stochastic fractal dimension). The lung slices were divided regionally into 31×31 pixel regions of interest (ROI). In each ROI, an optimal subset of texture features was evaluated to determine which of the six patterns in the region could be characterized. A non-linear statistical classifier, the Bayesian classifier, was built to do the classification through calculating the probability that the ROI belongs to each tissue pattern. The whole algorithm contains two stages: the first stage involves training AMFM to recognize different HRCT based tissue patterns using a preselected dataset; the second stage involves a new CT data to be analysed using the above introduced method. This multiple textural feature based method established the foundation and framework for subsequent studies on quantitative assessment of lung imaging. Xu et al. (2006b,a) enhanced the ability of AMFM based on the work of Uppaluri et al. (1999b,a). In this study, the 2D textural feature-based tissue analysis method was extended to 3D space for quantifying emphysema and early smoking related lung pathologies. The extracted features involved both first-order features (mean, variance, kurtosis and entropy of grey level distribution) and second-order features (run-length and co-occurrence measurements). The results showed that 3D AMFM analysis of lung parenchyma improved discrimination compared to 2D AMFM of the same volumes of interest (VOIs).

In the past 15 years, AMFM has been widely used to quantify and classify lung dis-

ease from CT imaging (Van Ginneken et al., 2002; Chabat et al., 2003; Best et al., 2003; Uchiyama et al., 2003; Kim et al., 2005; Zavaletta et al., 2006; Arzhaeva et al., 2007; Best et al., 2008; Kim et al., 2010, 2011, 2015a). A general workflow of texture analysis is: 1. preset several types of tissue patterns; 2. divide lung slices into a set of ROIs with a square shape; 3. use texture analysis to extract multiple features for each ROI; 4. select representative expert-labelled ROIs as a training set for a classifier; 5. use the features of ROIs from a new set as input to the classifier to find the corresponding tissue pattern. Currently, most of the published CT based lung tissue analysis methods were developed based on this framework. Different textural features, ROI sizes or classifier types were specifically selected to target different lung disease or clinical requirement. Best et al. (2003, 2008) used mean lung attenuation (MLA), skewness (asymmetry) and kurtosis (peakedness) as features combined with a further univariate and multiple correlation and regression statistical analysis to determine relationships between histogram signals and results of PFTs in patients with IPF. The result showed that CT histograms of the lungs were correlated with PFT measurements, therefore the visual disease extent on CT images can be used as a strong independent predictor of mortality in IPF. Chabat et al. (2003) used similar textural features and classifier to the method of Best et al. (2003, 2008) for differentiating centrilobular emphysema, panlobular emphysema, constrictive obliterative bronchiolitis and normal lung tissue. Zavaletta et al. (2007) trained and tested three classifiers which included 10 nearest neighbour classifier, fisher linear discriminant analysis, and Parzen windowing to classify normal and abnormal structures in lungs with IPF.

Uchiyama et al. (2003) and Kim et al. (2005) employed multi-layered artificial neural networks (ANNs) with a back-propagation algorithm as a classifier to distinguish between different tissue patterns which includes both normal and diffuse lung disease

slices. ANNs, using their simplest definition, are the modelling of the human brain, and their building blocks are neurons. They are excellent tools for finding patterns which are too complex or numerous for a human programmer to extract and teach the classifier to recognize, therefore will increase the accuracy of classification. In addition, Kim et al. (2010, 2011, 2015a) published a series of papers presenting a texture-based computer-aided diagnosis (CAD) scoring system to assess quantitative lung fibrosis (QLF) as a measurement of lung disease severity and as a surrogate imaging marker. The QLF score (a texture feature-based measure) was compared to the CT histogram metric (a global statistical measure), and the baseline severity and early change within 7 months in patients with IPF was assessed. The result concluded that classifier-model-derived scores (QLF scores) were associated with baseline disease extent and were also a sensitive measure of change over time, and a QLF score could be used for measuring the extent of disease severity and longitudinal changes.

Most published methods focus on texture-based classification of lung parenchyma or the severity and volumetric quantification of disease for the whole lung (such as the QLF score). Currently, very few studies attempt to quantitatively characterize the spatial distribution of each disease pattern or describe how each tissue pattern changes or converts over time. Moreover, many of the existing methods are time consuming and sometimes even require several hours. These real-world limitations present difficulties when translating these techniques into clinical applications (Bartholmai et al., 2013).

In addition, it has been generally believed that there is a decrease in lung volume (both FRC and TLC) in patients with IPF, but up to now, few studies have been presented to explore the lung and lobe shape alteration in IPF lungs compared to normal ones. It is a reasonable assumption that shape changes will be observed in IPF lungs due to physiologic alterations and disease progression over time.

4.1.4 Computer-Aided Lung Informatics for Pathology Evaluation and Ratings

CALIPER (Computer-Aided Lung Informatics for Pathology Evaluation and Ratings) is a computational image analysis platform developed by the Biomedical Imaging Resource Laboratory at the Mayo Clinic (Rochester, MN, USA) for the characterization and classification of lung parenchymal findings on HRCT (Maldonado et al., 2013; Bartholmai et al., 2013; Raghunath et al., 2014). The data processing step includes lung segmentation and classification of the remaining pulmonary parenchyma on the CT dataset. Briefly, CALIPER isolates the lung parenchyma by extracting central airways and vascular structures, and then classifies every parenchymal voxel into the following characteristic CT patterns: normal (N), reticular (R), honeycomb (HC), ground-glass (GG), and mild low attenuation areas (LAA), moderate LAA, and severe LAA (including emphysema). This novel computer-aided method for analysing pulmonary tissue features provides a consistent and reproducible quantification of lung disease that relates to the semi-quantitative assessment from radiologists(Maldonado et al., 2013). Figure 4.1 shows visual appearance of each characteristic CT pattern.

Pre-processing is conducted before the eventual classification of the pulmonary parenchyma. This requires segmentation of anatomic lung regions. The lungs are initially segmented using an adaptive density-based morphology (thresholding) method (Hu et al., 2001). Airways are segmented by thresholding combined with a 3D region growing algorithm and vessels are segmented by an enhancement filter based on Hessian matrix (Sato et al., 2000), then the final lung segments are extracted.

The volumetric detection and classification of pulmonary parenchyma by CALIPER uses a sliding window supervised classification scheme based on histogram signature

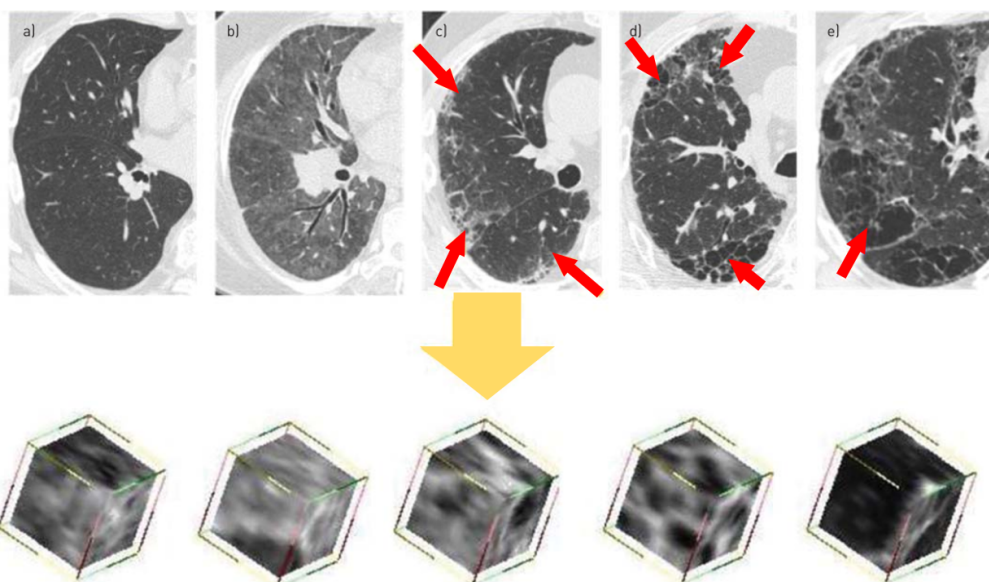


Figure 4.1: Computed tomography images demonstrating appearance and various visual manifestations of idiopathic pulmonary fibrosis: a) normal, b) ground glass, c) reticular changes (arrows), d) honeycombing (arrows) and e) emphysema (arrow). In training datasets, the consensus of four thoracic radiologists was used to identify multiple volumes of interest (VOIs) corresponding to normal, ground-glass density, reticular abnormalities, honeycombing and emphysema. Reproduced from (Maldonado et al., 2013).

mapping techniques (Zavaletta et al., 2007). This classification technique was trained by expert radiologists via consensus assessment of pathologically confirmed datasets, which were obtained from the Lung Tissue Research Consortium (LTRC). LTRC is a resource program sponsored by the NIH/NHLBI that provides clinical and physiologic data of human lung tissues to qualified investigators for use in their research and to help investigators develop a better understanding of lung disease. The central part of the classification scheme is the selection of a set of expert-labelled volumes of interest (VOIs) as the training data for a classifier. The training data used in CALIPER comprises $15 \times 15 \times 15$ -voxel VOIs acquired from HRCT scans of subjects with proven pathological diagnosis of interstitial lung disease (ILD) or emphysema from the LTRC repository. These VOIs were selected from CT scans through independent analysis by four experienced thoracic radiologists, with instructions and criterion to determine if the visual appearance should represent normal, emphysema or one of the characteristic lung fibrosis CT patterns: honeycomb, reticular or ground-glass (Maldonado et al., 2013; Bartholmai et al., 2013).

The VOIs with agreement by all four radiologists on the class of abnormality were used as exemplars to determine canonical histogram signatures of the CT patterns of visual abnormality by automatic cluster affinity techniques. Quantitative discriminability of a series of pairwise dissimilarity metrics based on the VOI histograms was tested using multi-dimensional scaling (MDS). The Cramer Von Mises Distance (CVM), which was found to be most consistent with the expert groupings, was selected as the dissimilarity metric to train CALIPER. For each of the parenchymal voxels needing to be classified, the local histograms of its neighbouring $15 \times 15 \times 15$ voxels were compared against the histograms of the exemplars identified in the training phase. A CVM dissimilarity measure was used in the comparison and the fundamental type of the exemplar

(N,R,H,G or emphysema) with the lowest CVM was assigned as the parenchymal CT pattern to this classified voxel. The parenchymal voxels identified as vessel structures were classified as normal pattern. Figure 4.2 shows a representative dataset with axial, coronal and sagittal sections of a CT lung volume where every voxel of the parenchyma is characterized and colour coded into one of the parenchymal patterns (N, R, H, G, and mild, moderate and severe LAA).

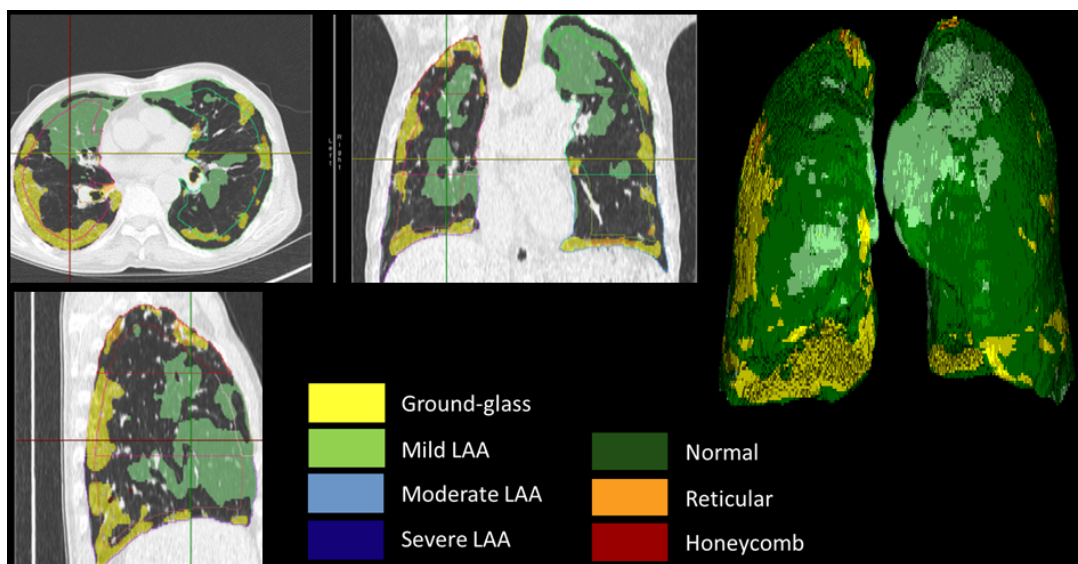


Figure 4.2: Colour labelled classification result from CALIPER of one subject diagnosed with IPF. (a) Transverse plane. (b) Coronal plane. (c) Sagittal plane. (d) 3D colour labelled lung.

4.2 Methods: quantitative analysis of IPF lungs

This section describes the quantitative methods used in this chapter to analyse and characterize IPF tissue abnormalities and lung lobe shape, longitudinally and in comparison to normal subjects. In summary, HRCT imaging was classified by pattern using a validated image analysis process (CALIPER) (Maldonado et al., 2013; Bartholmai et al.,

2013; Raghunath et al., 2014). The tissue classification data was mapped to a mean statistical shape model (SSM) allowing a quantitative approach to analyse tissue pattern density, tissue pattern volume, spatial distribution of abnormalities, and regional changes in tissue abnormalities over time. In the shape analysis, lobar finite element meshes for both IPF and normal subjects were projected to the SSM, and lobe shape differences in IPF were then quantitatively characterized.

4.2.1 Tissue classification of IPF lungs

Imaging and clinical data

Data used in this study was acquired as part of routine clinical diagnosis or follow up. Data use was approved by the Southern Health and Disability Ethics Committee. Data include volumetric HRCT and PFTs from 13 patients who were diagnosed with or suspected to have IPF. All patients were under clinical care at Auckland City Hospital, Auckland, New Zealand. Volumetric HRCT images (slice thickness 1.25-5.00 mm) were acquired at the end of inspiration during routine diagnostic inspection and/or monitoring for IPF disease. Eleven of the subjects had more than one serial CT scan within a 5-79 month interval, representing different time points (7 subjects had 3 time points, 4 subjects had 2 time points). The population demographics for these subjects is shown in Table 4.1.

Table 4.1: Demographic data.

Description	
Age (years)	43-83
Females/Males	3/10
Slice thickness	1.25-5.00 mm
Scan month interval	5-79 month
Slice resolution	512 × 512 mm
Number of slices	68-227

Normalization of classified data

Tissue CT patterns for each patient at each time point were classified using the CALIPER software introduced in Section 4.1.4. Then, lung surface data and fissure surface data were acquired using the lobe segmentation method introduced in Chapter 3. A bi-cubic Hermite finite element surface mesh was fitted to the shape of the lung and its fissures via a least squares fit using the CMISS software package (<https://www.cmiss.org>). The details for the generation of lobe data and the lobe mesh are given in Chapter 3, Section 3.3.2.

There is lung shape variation between different subjects and often between clinical images obtained at different times, as well as variation in the extent to which a patient inhales during imaging, even with careful training. Thus, the classified volumetric lung data was then mapped to a statistical shape model (SSM) of the "normal" older human lung to provide a consistent mapping of tissue abnormalities in individuals to a consistent lung shape. The steps for the construction of the SSM were introduced in Chapter 3, Section 3.3.2, which described an SSM for a cohort aged 21-83. In this chapter, data from 35 normal subjects aged 50 years and older were used to derive an SSM because this is consistent with the typical age of onset of IPF. The SSM used for mapping data is

the average mesh of the lung lobes which was derived from these 35 training subjects, and it provides a description of a statistical mean lung and fissure surface shape for a cohort of normal adults aged > 50 years.

In order to map the individual classified data to the SSM mesh, the bi-cubic Hermite finite element mesh of the lung surface was converted to a tri-cubic Hermite volumetric mesh which describes not only the lung surface but also the internal anatomy (Tawhai and Burrowes, 2003). The volumetric mesh has 40 nodes and 30 elements for left lung, and 56 nodes and 38 elements for right lung. Each node has 24 DOFs which store the global coordinates (x , y and z) and the first, second and third nodal derivatives ($\frac{\partial n}{\partial \xi_1}$, $\frac{\partial n}{\partial \xi_2}$, $\frac{\partial n}{\partial \xi_3}$, $\frac{\partial^2 n}{\partial \xi_1 \xi_2}$, $\frac{\partial^2 n}{\partial \xi_2 \xi_3}$, $\frac{\partial^2 n}{\partial \xi_1 \xi_3}$ and $\frac{\partial^3 n}{\partial \xi_1 \xi_2 \xi_3}$), where n is x , y and z , and ξ is the local element coordinate.

During the data mapping, all of the classified data should be completely enclosed inside its lobe volume mesh. The position of each point within the finite element mesh was defined locally in each element of the mesh by ξ_i , for $i=1,\dots,3$ with $0 < \xi_i < 1$. The ξ_i location denotes the local coordinates of the data point with respect to its element. The local coordinate ξ_i was then used to calculate the global coordinates of the mapped data points using

$$u(\xi_i) = \sum_{n=1}^N \psi_n(\xi_i) u_n, \quad (4.1)$$

where u_n is a vector of N element nodal parameters of the SSM lobe mesh associated with the interpolation functions ψ_n .

In order to force a uniform data point distribution throughout each lung, the gaps in the mapped data caused by the mapping deformation from individual shape to SSM (shown in Figure 4.3a) were "filled" by matching the classification of their closest

neighbour point among the classified data. Uniform data point distribution facilitates further density and spatial distribution analysis of abnormalities. Briefly, the gaps in the mapped data were filled using the following steps:

1. Mapped data were cut into a series of axial slices (shown in Figure 4.3a).
2. The lung mesh of average SSM was used as a mask to define the lung boundary. (shown in Figure 4.3b).
3. Morphological operations were applied to smooth the lung boundary, then a lung mask was generated (shown in Figure 4.3c).
4. The gaps enclosed inside the lung mask were filled with the CT pattern color of its closest point among the classified data (shown in Figure 4.3d).

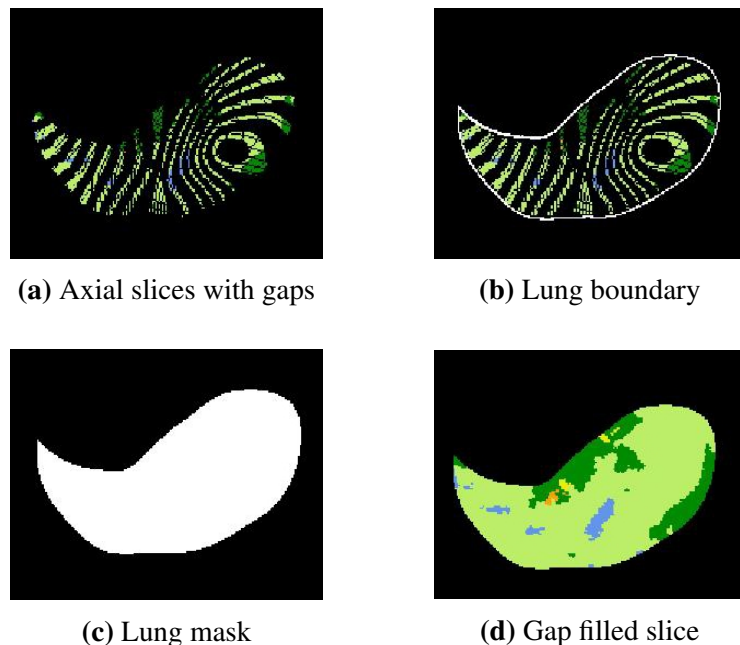


Figure 4.3: Diagram of gap filling steps within the mapped data. (a) Get axial slices of mapped data (with gaps). (b) Define lung boundary (SSM defined). (c) Get lung mask. (d) Fill the gaps within lung mask.

4.2.2 Tissue quantification of IPF lungs

Density analysis

The average density value of each classified CT pattern was calculated. In a typical CT image, intensity is measured in Hounsfield units (HU) which corresponds linearly to the actual density of the imaged tissue. HU was calculated with the segmentation software PTK calibrated to values of -1024 for air density, zero for water density, and over 40 for blood, bone, and other non-parenchymal tissue. The tissue density (ρ , g/cm^3) was then acquired at each voxel using

$$\rho = \frac{HU}{1024} + 1. \quad (4.2)$$

The average density of each CT pattern was then calculated from individual voxel density.

Spatial distribution analysis

Based on the criteria of IPF defined by the ATS and ERS, the diagnosis of IPF is usually associated with the presence of a UIP pattern in HRCT (see details in Chapter 2, Section 2.3.4). The distribution of UIP on HRCT is characteristically basal and peripheral (subpleural), though often patchy. Therefore, in order to quantitatively analyse the spatial distribution of IPF abnormalities, the percentage of honeycomb, reticular, emphysema and ground-glass which represent typical UIP disease patterns on HRCT were calculated in basal-to apical sections, dorso-to-ventral sections, from subpleural to internal, and by lobe:

Basal-to-apical: In the direction from base to apex, the volume percentage of each disease region was averaged in bins representing 5% of lung height (along the crano-caudal axis).

Dorso-to-ventral: In the direction from posterior to anterior, the volume percentage of each disease region was averaged in bins representing 5% of distance along the crano-caudal axis.

Subpleural to internal: The distance from the abnormalities to the boundary of the lung and to the centre of the lung were measured to analyse the location of disease with respect to the lung surface. To be specific, the centre location of each connected cluster of disease area was firstly extracted, and the subpleural to internal distance percentage $R_{subpleural}$ of each connected cluster, which described how far the connected cluster was from the lung surface, was then calculated as in Figure 4.4.

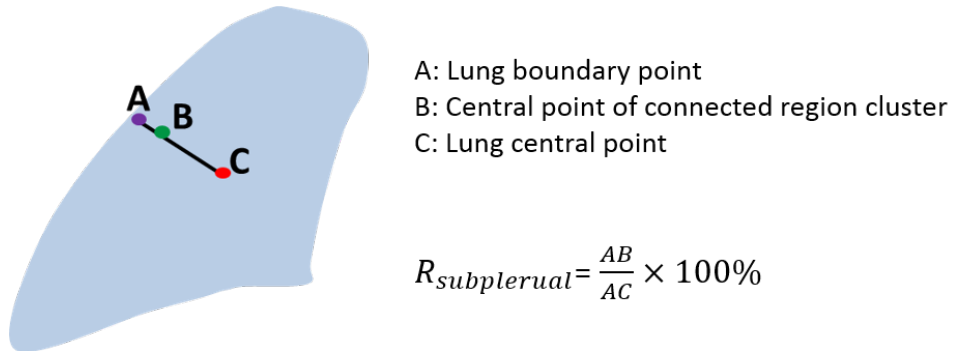


Figure 4.4: Diagram of subpleural-to-internal percentage measurement. $R_{subpleural}$ is the subpleural-to-internal percentage measurement, AB and AC are linear distance between A and B, and A and C, respectively.

The coordinate of the lung central point $P_{centre}(x, y, z)$ was calculated as

$$P_{centre}(x, y, z) = \frac{\sum_{i=1}^N P_{surface}(x, y, z)}{N}, \quad (4.3)$$

where $P_{surface}(x, y, z)$ is the coordinate of the lung surface data point, and N is the number of lung surface data points.

Lobar distribution: In order to analyse the lobar distribution of disease, the volume percentage of each disease CT pattern located in each lobe was calculated.

Change in classification of tissue pattern over time

Median survival time of patients with IPF is generally from 3 to 5 years from time of diagnosis. However, individual progression of disease is variable and how the characteristic disease pattern changes over time (e.g. whether a disease region deteriorates and changes to other tissue patterns or stays the same over time) still remains elusive. In this study, the classified data of all subjects and time points have been normalized to a standard lung shape (SSM, as introduced in Section 4.2.1), thus making it possible to detect the disease change in specific regions over time, by extracting the CT pattern of each voxel at different time points.

4.2.3 Volume analysis of IPF lungs

The change in whole lung volume over time

The volume of each classified tissue pattern in both left and right lung was calculated using:

$$V_{Region} = N \times R_x \times R_y \times R_z, \quad (4.4)$$

where N is the number of voxels of each tissue pattern, R_x , R_y are the x, y resolution of the CT scan, and R_z is the thickness of the CT scan. Then the whole volume of left and

right lung was calculated as the sum of the volume of each CT pattern.

Lobe volume difference between old normal lungs and IPF lungs

The lobe volume of the IPF cohort was compared with the older normal cohort described in Section 4.2.1. In order to quantitatively analyse the lobe volume difference between the two groups, the volume proportion of each lobe was calculated as:

$$P_i = \frac{V_i}{\sum_{i=1}^5 V_i}, \quad (4.5)$$

where V_i is the volume of each lobe with $i=1$ corresponding to left lower lobe, $i=2$ corresponding to left upper lobe, $i=3$ corresponding to right lower lobe, $i=4$ corresponding to right middle lobe and $i=5$ corresponding to right upper lobe. The differences in lobe volume proportions between IPF subjects and normal subjects were compared statistically using a t-test. In order to further compare lobe volumes between these two groups, the average lobe volume proportion among IPF subjects and among the normal subjects were then calculated.

4.2.4 SSM based shape analysis of IPF lungs

The SSM was used to quantitatively analyse the alterations in lung lobe shapes of patients with IPF. As previously described in Section 4.2.1, 35 normal subjects aged > 50 years were used as training data to construct the SSM which contained both lung surface and fissure surface. PCA was used to decompose the shape variation of the lung lobe into a set of modes, and each mode represented one type of lung and fissure surface shape variation. Thus, each lung lobe shape was described by a linear combination of the mode vector and its corresponding weight by

$$S_{new} = S_{mean} + \sum_{i=1}^L \mathbf{u}_i w_i, \quad (4.6)$$

where S_{mean} is the average lobe shape model across all the training subjects, $\mathbf{u}_i (i = 1, 2, \dots, L, L = 34$ in this study) is the mode vector of shape variation which corresponds to the i^{th} largest principal component from PCA, and w_i is a weight factor given to each mode of variation.

The lung lobe FE mesh of each IPF subject was then procrustes projected on to the average SSM after alignment to the reference model (details can be seen in Chapter 3, Section 3.3.3). The new weight values of all shape modes $w_{new} = [w_{new1}, w_{new2}, \dots, w_{newL}]$ ($L = 35$) were calculated from the projection. These mode weights can be used as quantitative indexes to analyze and compare the shape variation and difference between IPF and the control group.

Shape difference between IPF lungs and normal control lungs

For the SSM of the control group, the first three shape modes explained over 30% of the total variation in the training set. Therefore, the weight values of the first three modes were used as the measurement to compare the shape difference of lung lobe between controls and IPF. The p-values of the first three shape modes between the two groups were calculated using a t-test.

Relationship between lung lobe shape and fibrosis and low attenuation area extent

In order to quantitatively investigate the association between fibrosis extent and lung shape variation, the association of the first three mode weightings with the overall volume percentage of fibrosis and low attenuation area (LAA) was estimated using linear

regression. Total fibrosis extent was estimated as the sum of reticular, honeycomb and ground-glass opacification of both lungs, and total LAA extent was estimated as the sum of mildLAA, moderateLAA and severeLAA of both lungs. The behaviour of the first three modes with respect to overall fibrosis percentage and LAA percentage was analysed using linear regression.

4.3 Results

4.3.1 Normalization of classified data

The data classified using the CALIPER software were mapped to the SSM using the method introduced in 4.2.1. Figure 4.5 shows the mapped classification data for a single subject. The mapped data for the other subjects can be found in Appendix A.

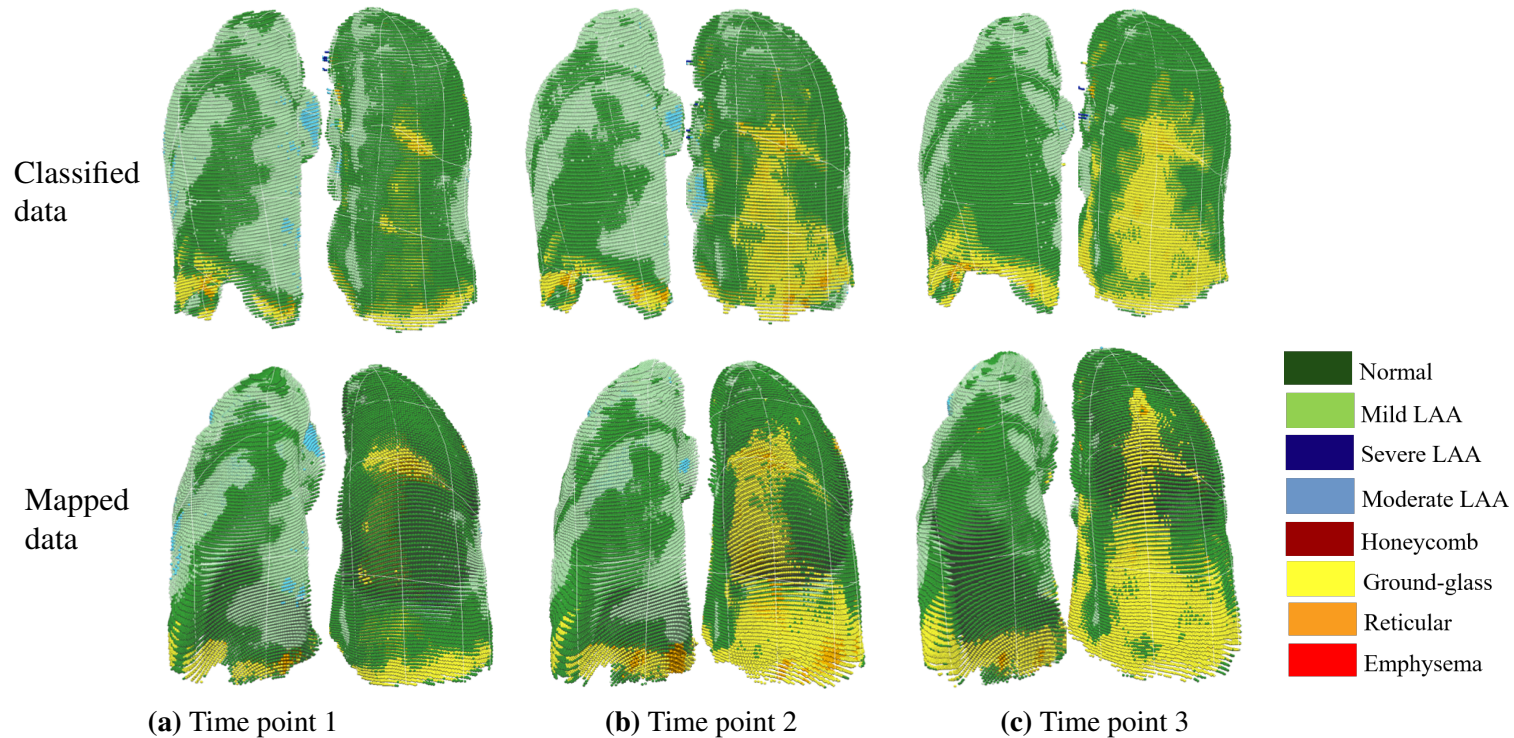


Figure 4.5: Classified data (top row) and mapped data (bottom row) for three time points from one subject diagnosed with IPF. (a) The first time point, scan time: 0 months. (b) The second time point, scan time: 15 months. (c) The third time point, scan time: 20 months.

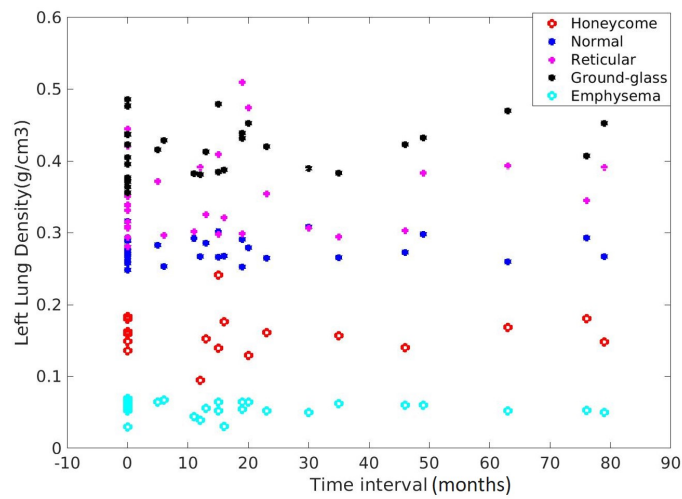
4.3.2 Tissue quantification of IPF lungs

Density analysis

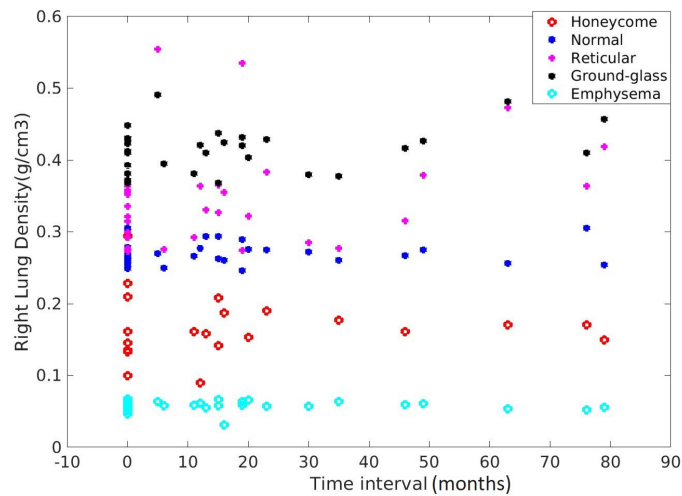
The density analysis result is shown in Figure 4.6 and Table 4.2. It can be seen that the average density of each CT pattern remains consistent and fluctuates only within a specific range over time in both left and right lung. The ground-glass region has the highest average tissue density and emphysema has the lowest average tissue density. This supports that the CALIPER tissue type classification is robust and repeatable.

Table 4.2: Mean tissue density (g/cm^3) of each CT pattern for left and right lung (mean value \pm standard deviation)

	Mean tissue density (left lung)	Mean tissue density (right lung)
Normal	0.28 ± 0.02	0.27 ± 0.01
Honeycomb	0.15 ± 0.04	0.15 ± 0.03
Reticular	0.35 ± 0.05	0.32 ± 0.04
Ground-glass	0.42 ± 0.05	0.40 ± 0.02
Emphysema	0.08 ± 0.01	0.08 ± 0.02



(a) Left lung tissue density



(b) Right lung tissue density

Figure 4.6: Average tissue density (g/cm^3) of each CT pattern in IPF lungs. Each data point represents the tissue density of one time point from one patient. X axis represents the month interval of scan time for each patient, and "0" represents the first scan for this patient. (a) Tissue density of left lung. (b) Tissue density of right lung.

Spatial distribution analysis

Basal-to-apical distribution Figure 4.7 shows the percentage distribution (the average volume percentage of all time points from all patients) against lung height (cranio-caudal axis) of four characteristic CT patterns: ground-glass, reticular, honeycomb and emphysema for left and right lung. It can be seen from the result that ground-glass mainly locates in the basal part of the lung. The percentage of ground-glass decreases gradually with increasing lung height, and the distribution of ground-glass is quite similar in left and right lung. In contrast, the percentage of emphysema trends toward increasing from lung base to apex. The reticular tissue is mainly located in the most basal and apical areas: it is much lower in the middle part of the lung. The distribution of honeycomb does not have a relationship with lung height.

Figure 4.8 shows the percentage distribution at month 0 (the average volume percentage of the first time point from all patients) against lung height (cranio-caudal axis) of four characteristic CT patterns (ground-glass, reticular, honeycomb and emphysema) in left and right lung at month 0. From the result, the cranio-caudal distribution of the four CT patterns at month 0 are quite similar to the total average distribution shown in Figure 4.7, but the absolute percentages of the abnormalities at month 0 are lower than the total average values. That is, as expected, the volume of disease increases over time as a whole in the IPF lung.

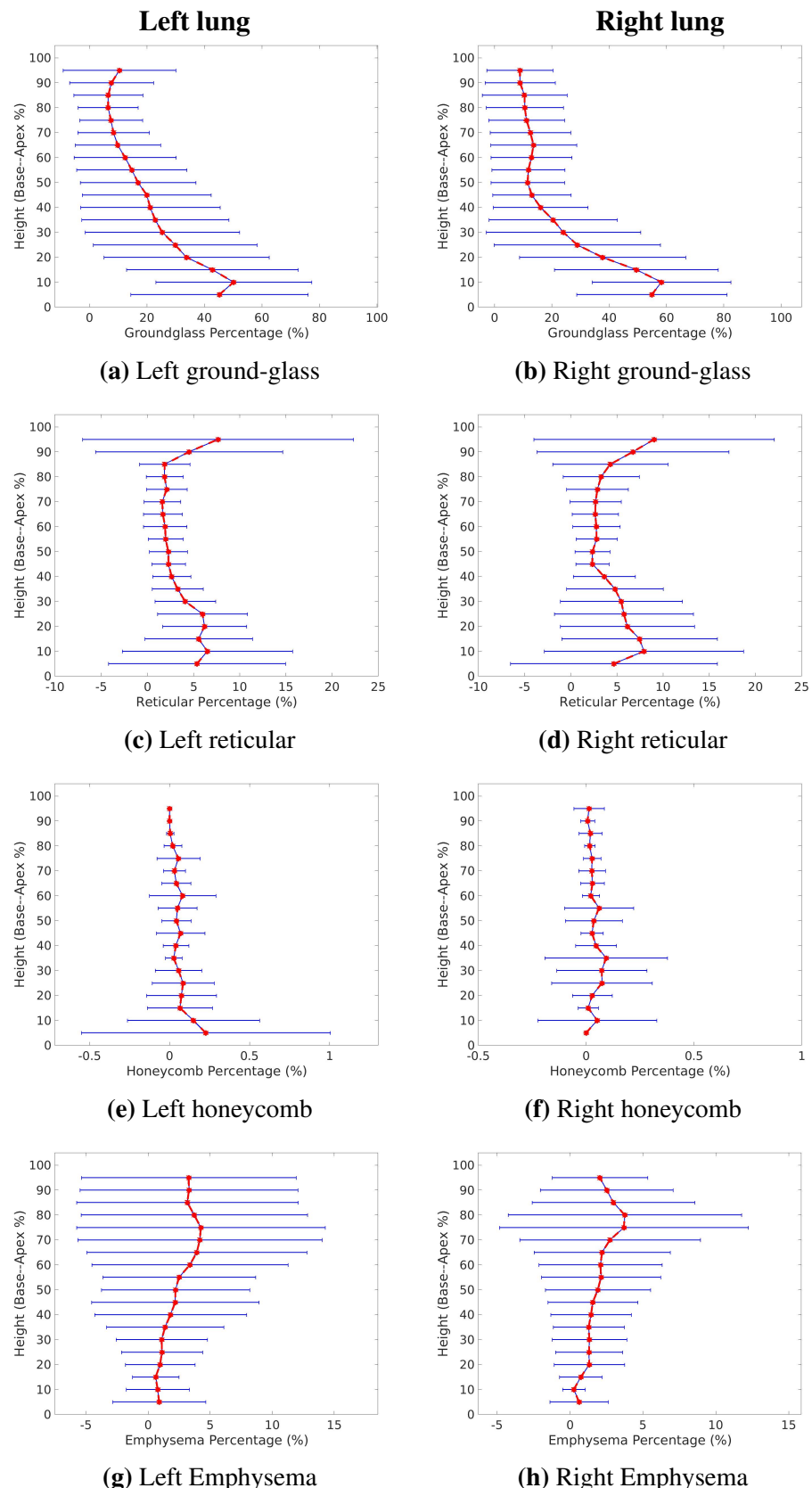


Figure 4.7: Volume percentage of each tissue classification plotted against lung height (cranio-caudal axis) in IPF left and right lungs. The average percentage was calculated within 5% sections of the lung height from the base to apex. Red shows the average value at each position across all patients, and blue shows the standard deviation. (a) (b) is ground-glass distribution. (c) (d) is reticular distribution. (e) (f) is honeycomb distribution. (g) (h) is emphysema distribution.

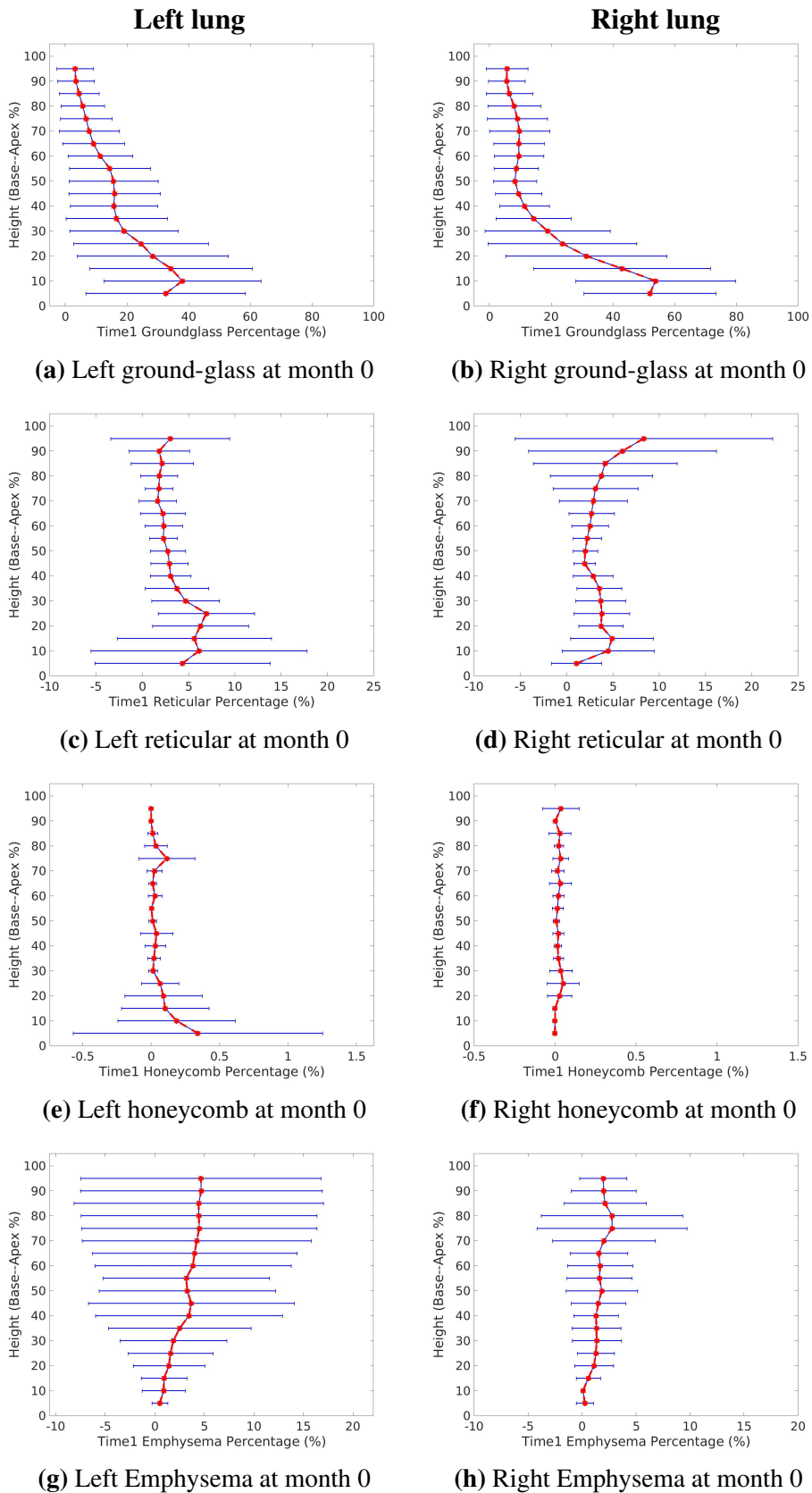


Figure 4.8: Volume percentage of each tissue classification plotted against lung height (cranio-caudal axis) in IPF left and right lungs at month 0. The average percentage was calculated within 5% sections of the lung height from the base to apex. Red shows the average value at each position across all patients, and blue shows the standard deviation. (a) (b) is ground-glass distribution. (c) (d) is reticular distribution. (e) (f) is honeycomb distribution. (g) (h) is emphysema distribution.

Figure 4.9 shows (for a single representative patient) the percentage distribution against lung height (cranio-caudal axis) of the four characteristic CT patterns in the left and right lung over time. From time point 1 to time point 3, an overall increase of the disease regions can be observed, even though the percentage of some tissue pattern may fall during this time. The distribution of ground-glass and reticular in base-to-apex does not change quantifiably over time, however, there are some fluctuations for honeycomb and emphysema (but the amount of honeycomb is very small). Results are only shown for one representative subject here, because the number of months between imaging is quite variable between subjects which makes it difficult to graphically present the spatial distributions for the entire cohort except for at time 0 or for all time points and subjects simultaneously. The percentage distribution against lung height over time for other patients can be found in Appendix B.

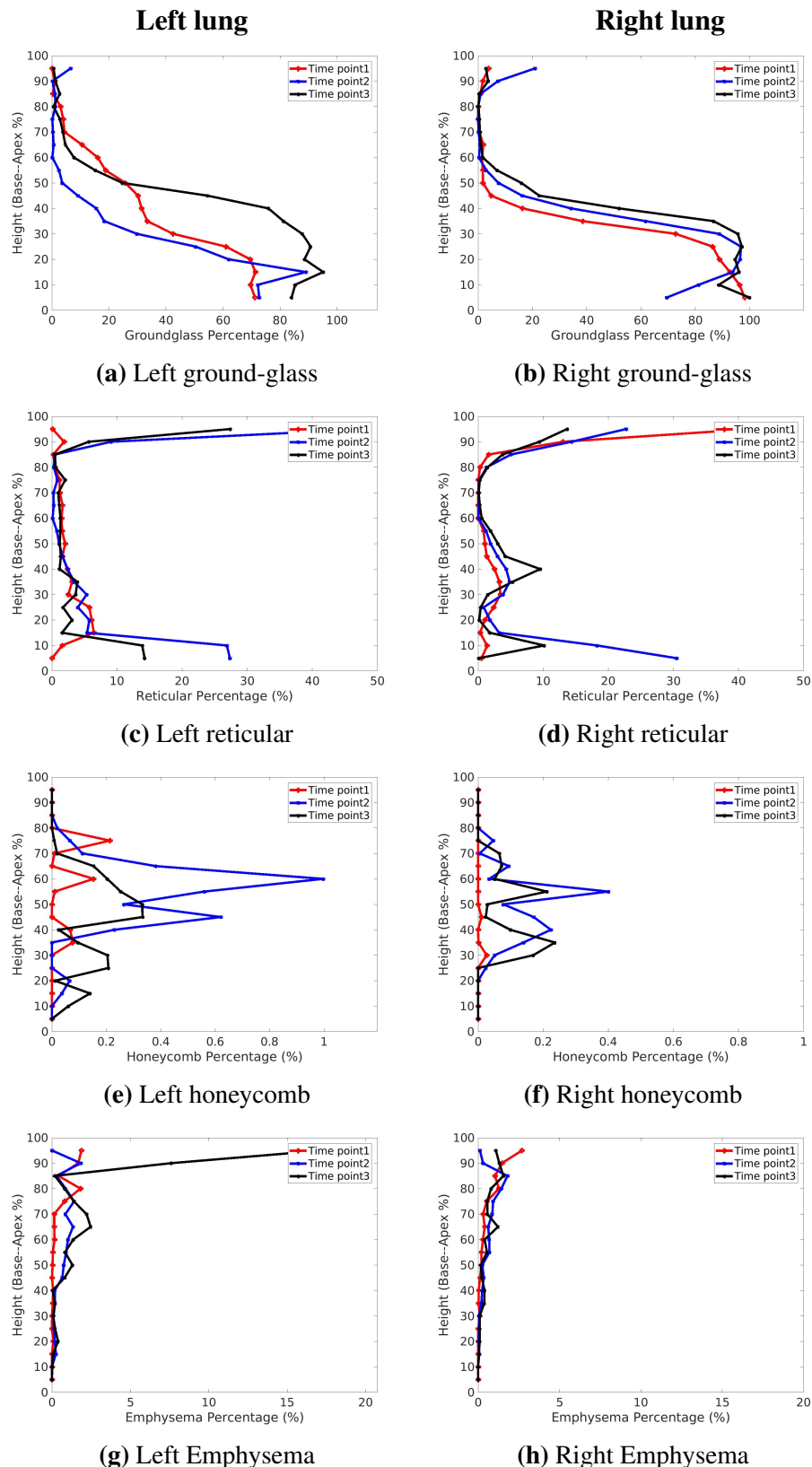


Figure 4.9: Volume percentage of each tissue classification plotted against lung height (cranio-caudal axis) of one patient diagnosed with IPF in left and right lungs over time. The average percentage was calculated within 5% sections of the lung height from the base to apex. (a) (b) is ground-glass distribution. (c) (d) is reticular distribution. (e) (f) is honeycomb distribution. (g) (h) is emphysema distribution. **The time interval from time point 1 to time point 2 is 63 months, from time point 1 to time point 2 is 16 months, from time point 1 to time point 3 is 79 months.**

Dorso-to-ventral distribution Figure 4.10 shows the percentage distribution (the average volume percentage of all time points from all patients) from posterior to anterior of the lung (dorso-ventral axis) for the four characteristic CT patterns for left and right lung. This illustrates that the percentage of ground-glass and reticular keep decreasing from back to front, and they mostly locate in the dorsal part of the left and right lungs. Honeycomb and emphysema are both relatively constant along the dorso-ventral axis, but for the honeycomb pattern, there are relatively more abnormalities appearing in the dorsal and ventral regions compared to the middle area.

Figure 4.11 shows the percentage distribution (the average volume percentage of the first time point from all patients) from posterior to anterior of the lung (dorso-ventral axis) for the four characteristic CT patterns in left and right lung at month 0. It can be seen that, like the crano-caudal distribution, the distribution of the diseases in the dorso-ventral direction at the first time point are almost the same as the distribution in Figure 4.11, and the disease percentage at month 0 is slightly lower than the total time averaged value.

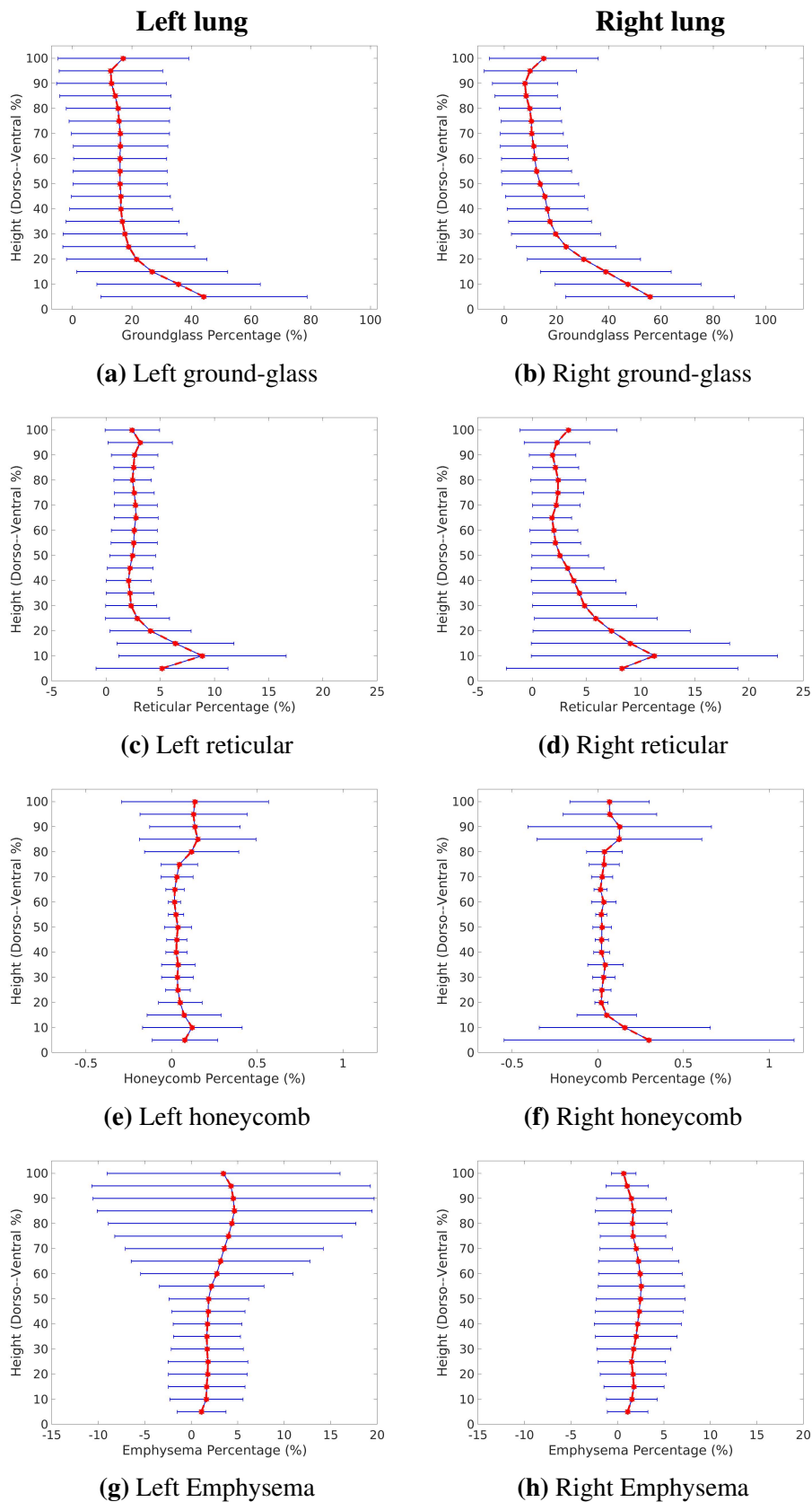


Figure 4.10: Volume percentage of each tissue classification plotted in the direction of dorso-ventral axis in IPF left and right lungs. The average percentage was calculated within 5% sections along the axis from posterior to anterior. Red shows the average value at each position across all patients, and blue shows the standard deviation. (a) (b) is ground-glass distribution. (c) (d) is reticular distribution. (e) (f) is honeycomb distribution. (g) (h) is emphysema distribution.

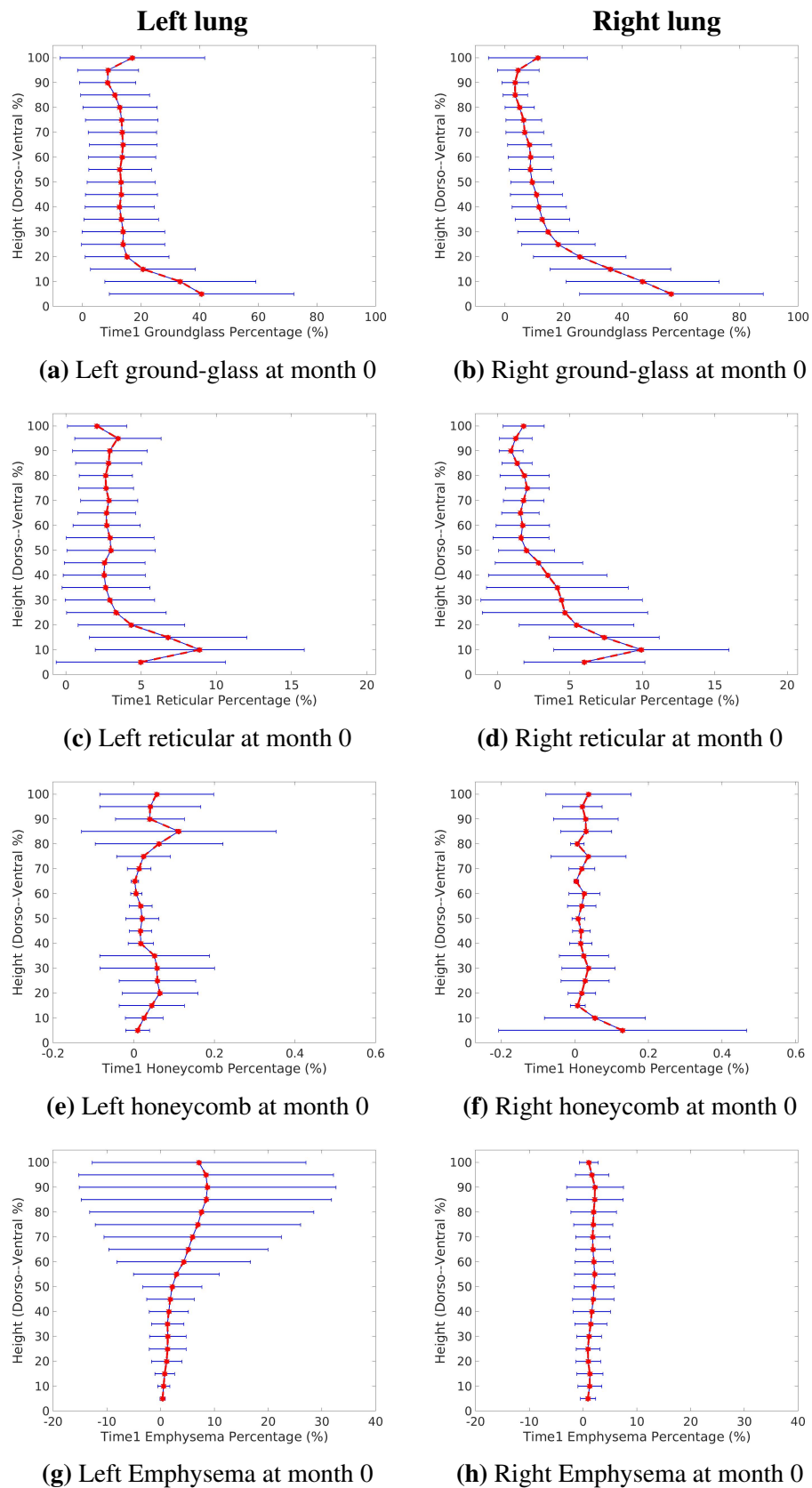


Figure 4.11: Volume percentage of each tissue classification plotted in the direction of the dorso-ventral axis in IPF left and right lungs at month 0. The average percentage was calculated within 5% sections along the axis from posterior to anterior. Red shows the average value at each position across all patients, and blue shows the standard deviation. (a) (b) is ground-glass distribution. (c) (d) is reticular distribution. (e) (f) is honeycomb distribution. (g) (h) is emphysema distribution.

Figure 4.12 shows the percentage distribution from the posterior to anterior of the lung (dorso-ventral axis) of the four characteristic CT patterns from an individual patient diagnosed with IPF in left and right lung over time. For ground-glass, emphysema and left honeycomb, an increase in the volume percentage over time can be seen and the dorso-ventral distribution does not change quantifiably during this period of time. However, the spatial location of reticular and honeycomb (in the right lungs) redistributes in the dorso-ventral direction over time, and no consistent trend is observed. The percentage distribution in this axis over time for all patients can be found in Appendix B.

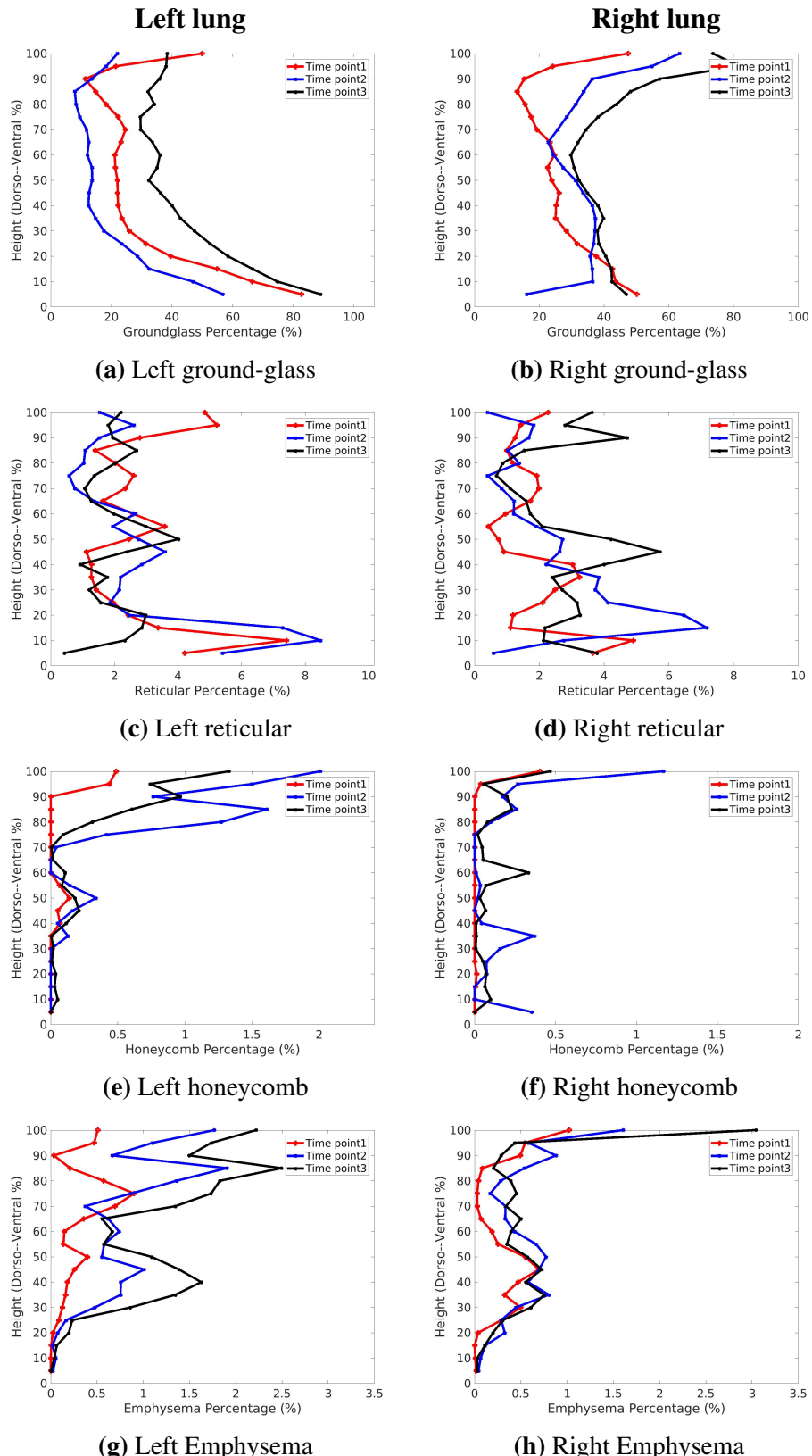


Figure 4.12: Volume percentage of each tissue classification plotted in the direction of dorso-ventral axis from one patient diagnosed with IPF in left and right lungs over time. The average percentage was calculated within 5% sections along the axis from posterior to anterior. (a) (b) is ground-glass distribution. (c) (d) is reticular distribution. (e) (f) is honeycomb distribution. (g) (h) is emphysema distribution. The time interval from time point 1 to time point 2 is 63 months, from time point 1 to time point 2 is 16 months, from time point 1 to time point 3 is 79 months.

Subpleural to internal distribution Figure 4.13 plots the subpleural-to-internal distance percentage of each connected cluster of three fibrosis CT patterns: ground-glass, reticular and honeycomb. The result shows that the subpleural-to-internal percentage of most connected disease clusters are < 20% for both left and right lungs. That is, the fibrosis is located preferentially within 20% of the distance from the lung surface. Reticular and ground-glass abnormalities are distributed throughout the centre to surface, whereas honeycomb is mostly not observed in the central core of the lungs in these subjects.

Lobar distribution Figure 4.14 shows the average volume percentage (across all time points from all patients) of ground-glass, reticular, honeycomb and emphysema in the five lobes (left upper, left lower, right upper, right middle, right lower). Fibrosis is located predominantly in the lower lobes (53.9%, 57.6%, 64.4% for honeycomb, reticular, ground-glass) compared to the other two lobes. For reticular pattern, the percentage in the middle lobe is much lower than the percentage in other lobes. Emphysema predominantly presents in the upper lobes (69.5%) and may also appear in the middle lobe of the right lung. Figure 4.15 shows the volume percentage of the four tissue patterns in the five lobes at each time point from an individual patient diagnosed with IPF. As shown in the figures, the lobar distribution of the fibrotic disease remains almost the same at different time points (except for reticular at time point 3), with more fibrosis appearing in the lower lobes and emphysema presenting mainly in upper lobes. The lobar distribution over time for other patients can be found in Appendix B.

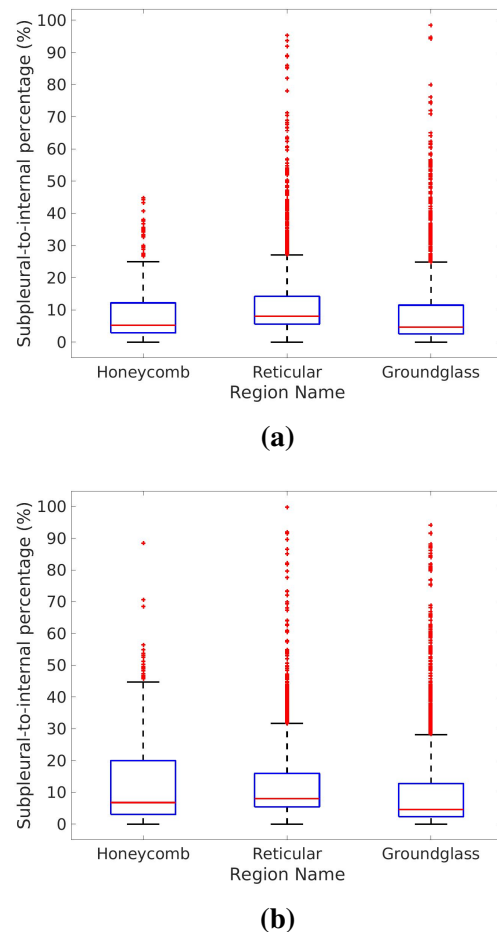


Figure 4.13: Subpleural-to-internal percentage of connected cluster of disease in IPF left and right lung. (a) Left lung. (b) Right lung.

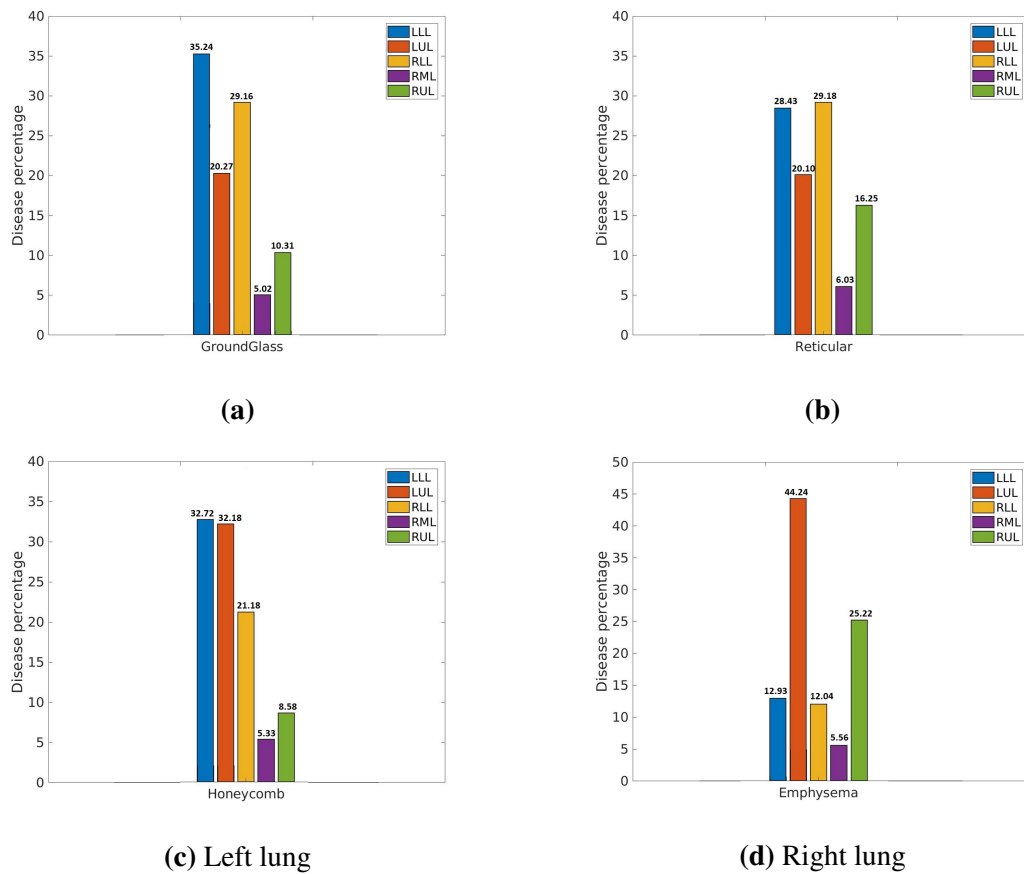


Figure 4.14: Average lobar distribution of abnormal tissue. The tissue percentage in different lobes is shown by color, and each bar represents the volume percentage of the CT pattern for one lobe across all the subjects. The black line shows the standard deviation. (a) Ground-glass lobar distribution. (b) Reticular lobar distribution. (c) Honeycomb lobar distribution. (d) Emphysema lobar distribution.

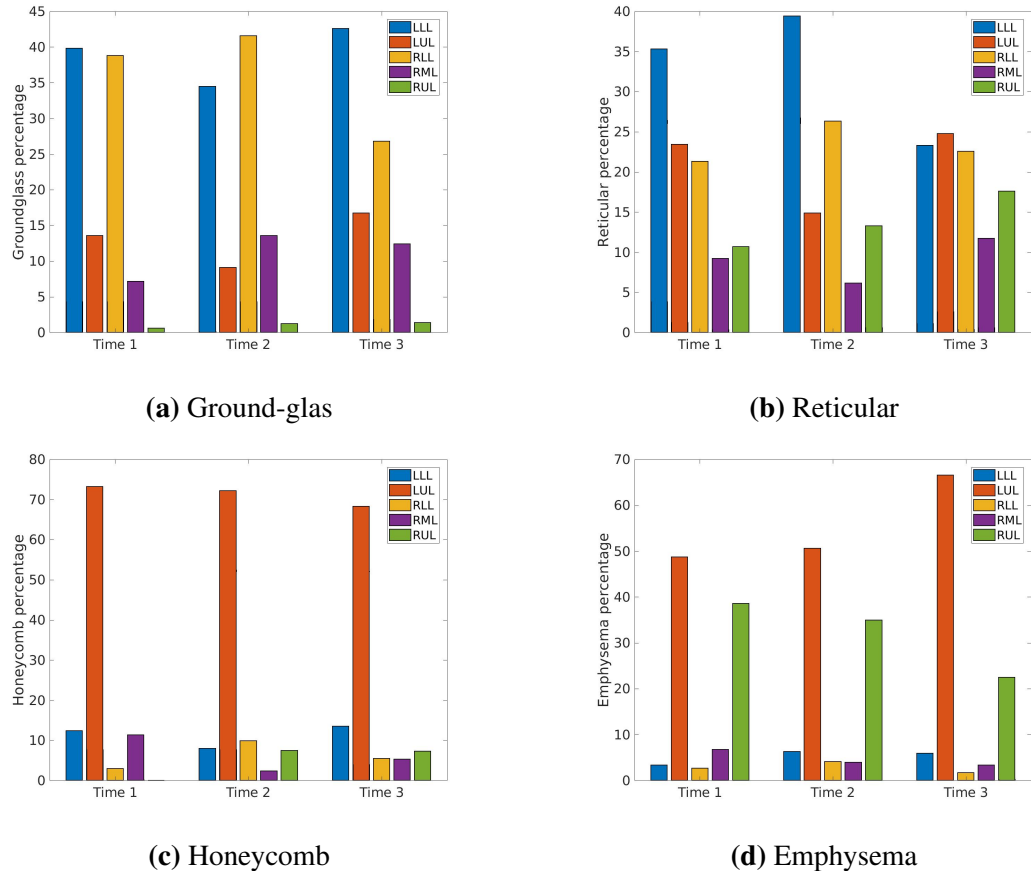


Figure 4.15: Lobar distribution of abnormal tissue for one patient diagnosed with IPF over time. The tissue percentage in different lobes is shown by colour, and each bar represents the volume percentage of the CT pattern for one lobe. (a) Ground-glass lobar distribution. (b) Reticular lobar distribution. (c) Honeycomb lobar distribution. (d) Emphysema lobar distribution. **The time interval from time point 1 to time point 2 is 63 months, from time point 1 to time point 2 is 16 months, from time point 1 to time point 3 is 79 months.**

Change in classification of tissue pattern over time

Table 4.3 and Table 4.4 show quantitative results for the change in classification of tissue pattern (ground-glass and reticular) for one patient with IPF between time points. The change in volume percentage of classified tissue CT patterns between time points is

given (for ground-glass or reticular pattern to the other tissue CT patterns). Over 50% of areas initially identified as ground-glass remain classified the same over time in both left and right lung, whereas other parts of ground-glass are subsequently classified as reticular or normal tissue. For the reticular region, although a high percentage doesn't change between time points, a large proportion is recognized as ground-glass at the second and third time point, especially in right lung (more than 50% on average).

In this subject and others in the cohort, some disease areas are classified back to normal tissue at later time points, although a decline in lung function can be observed during this period. Around 10%-30% of reticular and ground-glass areas are identified back to normal region during this time. This is clearly an artefact of analysis of the IPF patient, which may be explained by the two following reasons: 1. Error caused by the lung surface fitting and classified data mapping. As introduced in Chapter 3, Section 3.3.2, the average RMS error of the fitting method for 50 subjects was 4.79 mm, and this error was inevitable. The accuracy of the classified data mapping to the mean SSM partly relied on the accuracy of lung surface fitting, as the local coordinate within the corresponding element was used during the mapping. 2. Error caused by the CALIPER tissue classification. The distribution of abnormalities in IPF lung is mainly patchy, and the regions of fibrosis and emphysema are not always large connected areas. Figure 4.16 shows the CALIPER tissue classification overlapping on a raw image. As shown in Figure 4.16, different tissue patterns in most of the lung region are mixed and interlaced, which increases the difficulty of identifying tissue pattern in these parts accurately.

Table 4.3: Change in classification of tissue CT pattern (volume percentage) over time of left lung from one subject diagnosed with IPF (subject 6 with three time points) (%).

		Ground-glass	Mild-LAA	Moderate-LAA	Normal	Reticular	Honeycomb	Severe-LAA
Time1 - Time2	Ground-glass	53.65	0.36	0	37.31	8.65	0	0.03
	Reticular	29.76	3.01	0	28.41	38.82	0	0
Time2 - Time3	Ground-glass	71.61	0.13	0.03	15.41	12.82	0	0
	Reticular	39.94	0.83	0	16.59	42.56	0.07	0
Time1 - Time3	Ground-glass	70.01	0.83	0	20.80	8.35	0.01	0
	Reticular	37.97	4.73	0	15.49	41.81	0	0

The time interval from time point 1 to time point 2 is 15 months, the time interval from time point 1 to time point 2 is 5 months, the time interval from time point 1 to time point 3 is 20 months.

Table 4.4: Change in classification of tissue CT pattern (volume percentage) over time of right lung from one subject (subject 6 with three time points) diagnosed with IPF (%).

		Ground-glass	Mild-LAA	Moderate-LAA	Normal	Reticular	Honeycomb	Severe-LAA
Time1 - Time2	Ground-glass	61.76	4.15	0.92	7.14	25.92	0	0.11
	Reticular	47.61	6.88	0.01	11.10	34.37	0	0.03
Time2 - Time3	Ground-glass	78.16	0.08	0.01	18.51	3.23	0	0.05
	Reticular	55.74	0.44	0	31.46	12.35	0.01	0
Time1 - Time3	Ground-glass	79.98	1.82	1.63	12.82	3.45	0	0.30
	Reticular	65.80	3.28	0.02	19.40	11.33	0	0.16

The time interval from time point 1 to time point 2 is 15 months, the time interval from time point 1 to time point 2 is 5 months, the time interval from time point 1 to time point 3 is 20 months.

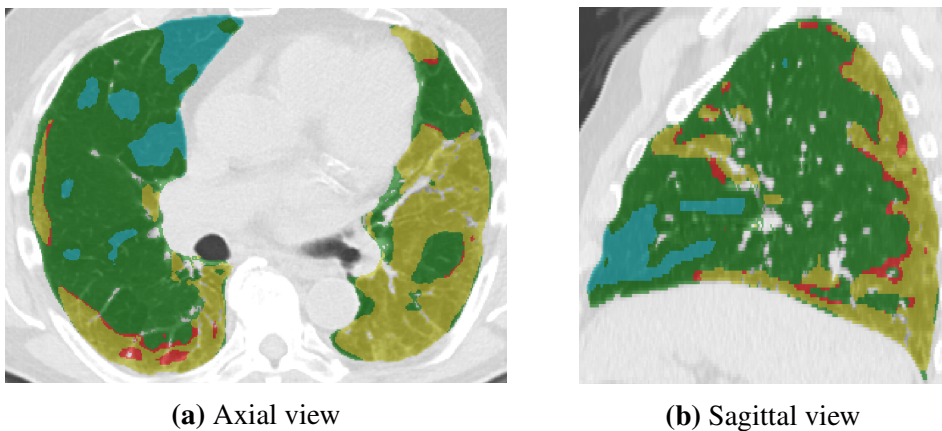


Figure 4.16: CALIPER tissue classification overlapping on raw image. Green is the normal region, red is the reticular region, yellow is the ground-glass region, and blue is the mild LAA region. (a) Axial view. (b) Sagittal view.

4.3.3 Volume analysis of IPF lungs

The change of whole lung volume over time

Table 4.5 shows the imaged volume of left and right lung (the first two columns) of all subjects for each time point. It can be seen that although the imaged lung volumes of most (9) patients decrease over time, some subjects (4 patients) do exhibit an increase in lung volume as time goes by. Interestingly, for most of the (9) patients, the changes of lung volume (decrease or increase) are consistent with the changes of the percentage of LAA over time.

Lobe volume difference between old normal lungs and IPF lungs

The average lobe volume proportion among IPF subjects and among normal subjects (the control group) are shown in Table 4.6 (the first two columns). It can be seen that the IPF group has a lower average volume proportion for left lower lobe and right lower

Table 4.5: Imaged volume of each lung (L) and the percentage of LAA area (%) in both lungs for each time point.

Sub No.	Time point	Scan time	Left lung	Right lung	LAA percentage
IPF2	Time point1	0 month	1.39	2.04	4.41
	Time point2	15 month	1.88	2.72	37.49
	Time point3	35 month	1.83	2.68	25.00
IPF3	Time point1	0 month	1.55	2.34	6.80
	Time point2	11 month	1.38	2.11	5.84
	Time point3	30 month	1.28	2.05	4.75
IPF5	Time point1	0 month	1.73	1.49	19.64
	Time point2	12 month	1.58	1.31	16.41
	Time point3	23 month	1.67	1.43	31.54
IPF6	Time point1	0 month	2.41	3.47	81.27
	Time point2	15 month	2.13	3.01	73.79
	Time point3	20 month	2.06	3.09	59.76
IPF9	Time point1	0 month	1.35	1.49	7.69
	Time point2	7 month	1.22	1.43	4.43
	Time point3	20 month	1.23	1.53	8.64
IPF10	Time point1	0 month	1.34	1.66	35.76
	Time point2	14 month	1.01	1.25	1.03
IPF13	Time point1	0 month	1.94	1.58	22.62
	Time point2	16 month	1.85	2.40	23.04
IPF14	Time point1	0 month	2.45	2.74	54.43
	Time point2	46 month	2.16	2.33	32.36
IPF15	Time point1	0 month	3.72	3.37	73.90
	Time point2	13 month	2.86	3.38	69.51
	Time point3	76 month	3.04	3.72	72.03
IPF21	Time point1	0 month	2.24	2.31	29.38
	Time point2	63 month	1.88	1.86	29.04
	Time point3	79 month	1.73	1.85	23.21

lobe compared to the value of the control group. Smaller lower lobe volume would be consistent with increase in stiffness of the lower lobes in IPF lungs, which relates to the basal appearance of fibrosis. The difference in lobe volume proportions between IPF subjects and the control group were compared statistically using a Student t-test. Table 4.6 (the third column) shows the p-values for this test when comparing volumes of the five lobes between the two groups. The result shows a significant difference in the volume proportion for both right lower lobe and right middle lobe between IPF subjects and the controls ($p < 0.001$), but not for the left lower lobe. That is, the right lower lobe is significantly smaller in IPF, and this is at the expense of a significant increase in right middle lobe size.

Table 4.6: Lobe volume proportion comparison between IPF subjects and older normal subjects.

Lobe	IPF	Older normal	P-value
Left lower lobe	0.205	0.211	0.532
Left upper lobe	0.251	0.242	0.352
Right lower lobe	0.210	0.254	$\ll 0.001$
Right middle lobe	0.119	0.087	$\ll 0.001$
Right upper lobe	0.214	0.207	0.559

4.3.4 SSM - shape analysis of IPF lungs

Shape difference between IPF lungs and normal lungs

Figure 4.17 shows the weight value distribution of the first three principal shape modes for IPF and the control subjects.

There is a significant difference of the first mode weight between IPF and controls ($p \ll 0.001$). However, for mode 2 and mode 3, no significant shape difference was observed between the two groups ($p = 0.017$ and $p = 0.641$, respectively). Figure 4.18

illustrates overall shape variation of the first mode with added different values of standard deviation to the mean shape model. The first shape mode accounts for over 20% of the entire shape variation in normal control lungs. It is seen in Figure 4.18 that the first mode relates to the largest change in the anterior-posterior diameter of the lung with a lateromedial tilt towards both apices, and is also associated with the ratio of apical to basal diameters. With the positive or negative standard deviation added to the mean shape model, there is a variation in the right anterior edge, the inferior lingular segment of the left superior lobe, the medial basal segment of the right middle lobe, and the left oblique fissure. In addition, there is a shape change in the "roundness" of the lateral surface in both left and right lung, and the variation in the distance of left and right lungs in the apex and base is also observed. As shown in Figure 4.17a and Figure 4.18, the weight values of Mode 1 for IPF subjects are distributed across negative values except for one data point (with an average value lower than -1), where the negative weight corresponds to a larger ratio of anterior-posterior diameter to lung height compared to control lungs. While mode 3 was not statistically different between the IPF and normal cohorts, the range of mode 3 values was far smaller for the IPF subjects ($\sim -0.8 - 0.75$) than the normals ($\sim -1.75 - 2.5$). This suggests a restriction on shape associated with this mode.

The values of the first three shape modes of IPF subjects for each time point are listed in Table 4.7. As can be seen from the table, the first three shape modes did not change significantly between time points (with all the p-values > 0.1 between time point 1 and time point 2, time point 1 and time point 3, time point 2 and time point 3). There were no regular trends in any of the three shape modes over time.

Table 4.7: Values of the first three shape modes of IPF subjects for each time point.

Sub No.	Time point	Scan time	Mode 1	Mode 2	Mode 3
IPF2	Time point1	0 month	-1.42	0.92	-0.83
	Time point2	15 month	-0.31	0.38	-0.90
	Time point3	35 month	-0.57	0.52	-0.54
IPF3	Time point1	0 month	-2.69	0.60	-0.17
	Time point2	11 month	-2.45	0.09	-0.04
	Time point3	30 month	-2.36	0.47	0.43
IPF5	Time point1	0 month	-1.23	-0.83	0.26
	Time point2	12 month	-1.28	-0.70	-0.12
	Time point3	23 month	-0.65	0.47	0.56
IPF6	Time point1	0 month	-1.05	-0.12	-0.35
	Time point2	15 month	-1.50	0.47	0.16
	Time point3	20 month	-1.56	0.16	0.38
IPF9	Time point1	0 month	-0.75	0.83	-0.18
	Time point2	7 month	-0.51	0.96	-0.43
	Time point3	20 month	-0.59	1.16	-0.63
IPF10	Time point1	0 month	-2.45	1.10	0.42
	Time point2	14 month	-2.20	1.56	-0.04
IPF13	Time point1	0 month	-2.32	0.75	-0.03
	Time point2	16 month	-2.15	-0.04	0.51
IPF14	Time point1	0 month	-1.56	-0.46	-0.30
	Time point2	46 month	-2.21	-0.08	-0.83
IPF15	Time point1	0 month	-1.29	1.41	-0.27
	Time point2	13 month	-0.58	1.15	-0.19
	Time point3	76 month	-1.64	0.91	-0.82
IPF21	Time point1	0 month	-0.60	0.76	-0.02
	Time point2	63 month	-1.93	0.63	0.55
	Time point3	79 month	-1.43	1.41	0.73

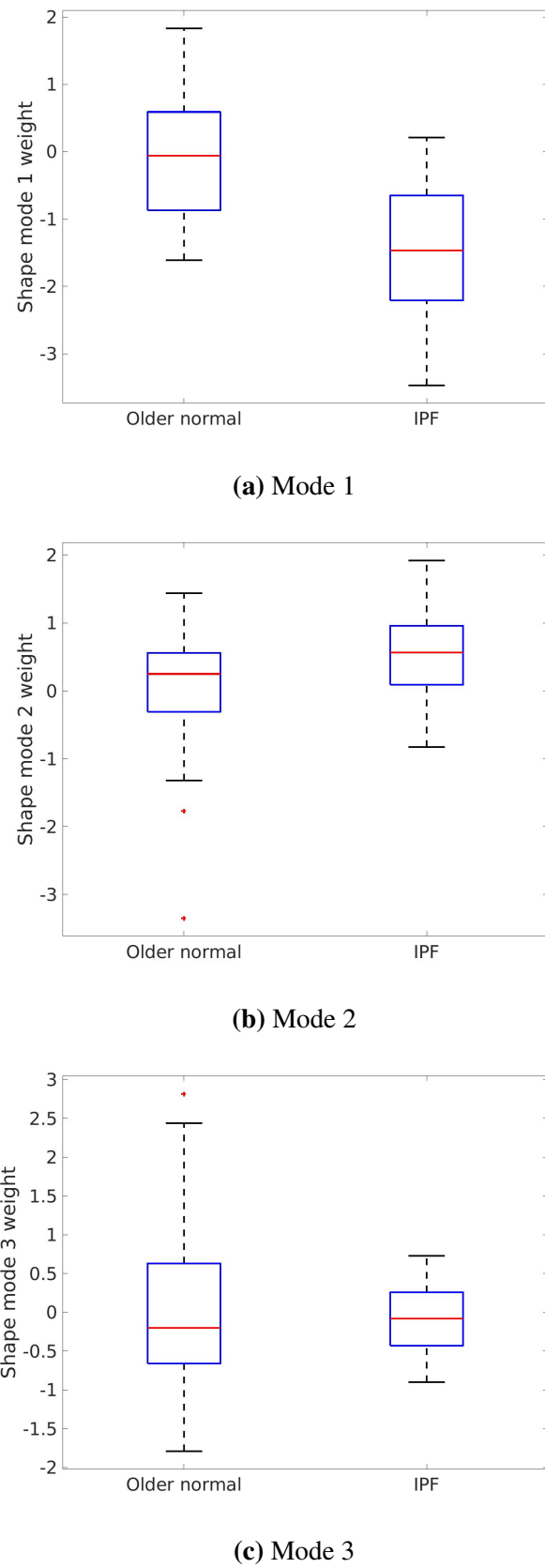


Figure 4.17: Shape differences between IPF subjects and old normal subjects of the first three modes (shown with different time point). (a) Mode 1 weight. (b) Mode 2 weight. (c) Mode 3 weight.

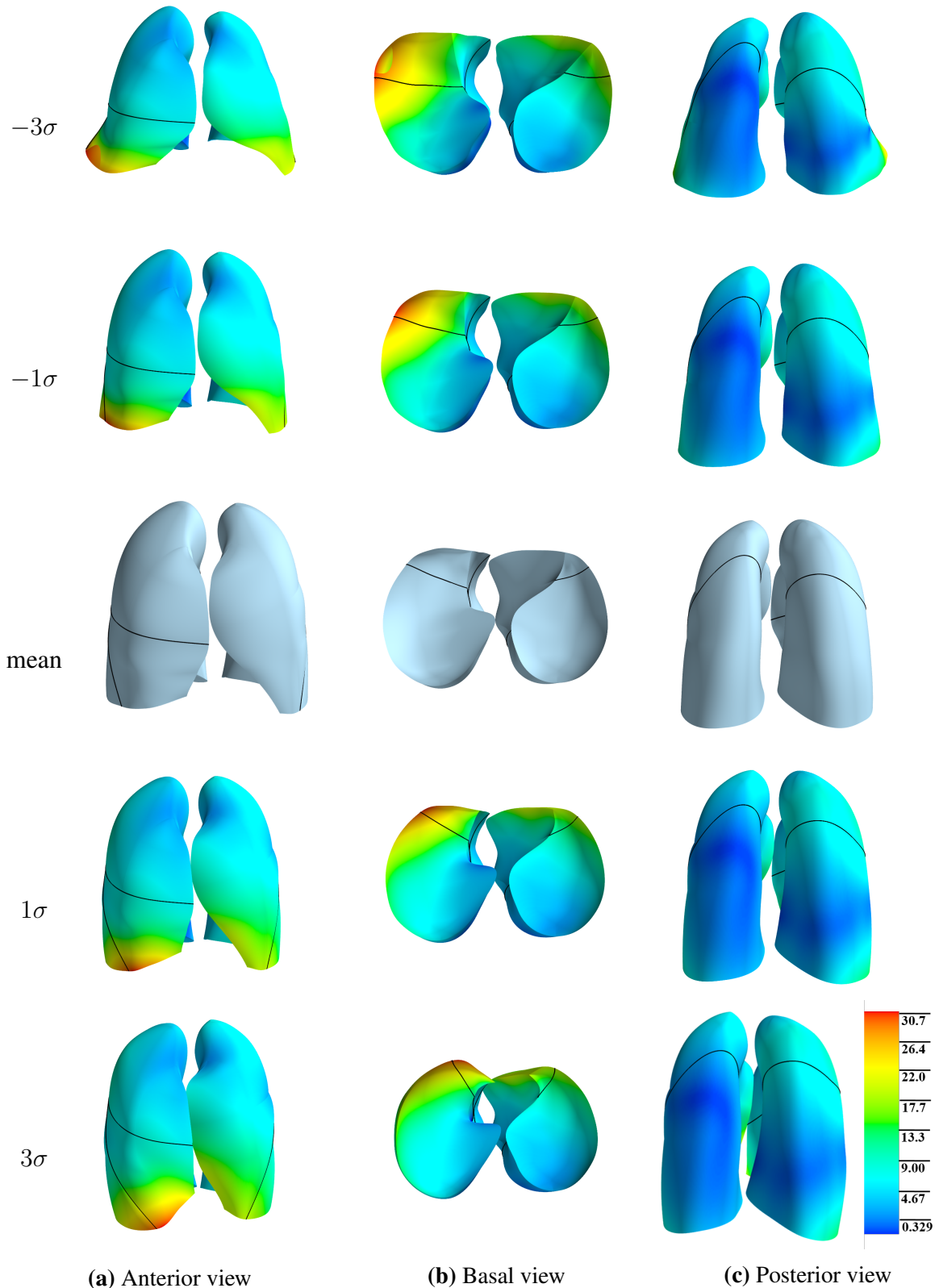


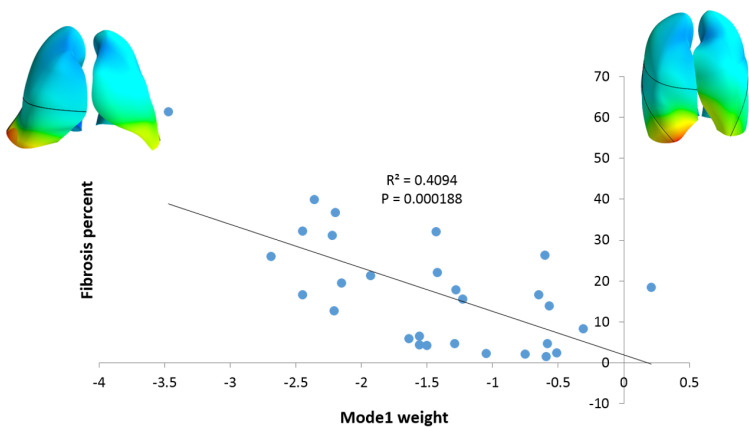
Figure 4.18: PCA-derived shape variation of the first shape mode, with different values of standard deviation ($-3\sigma, -1\sigma, \mu, 1\sigma, 3\sigma$) added to the mean shape model. (a) Anterior view. (b) Basal view. (c) Posterior view. The colormap shows the extent of shape variation from the mean shape model.

Relationship between lung lobe shape and fibrosis and low attenuation area extent

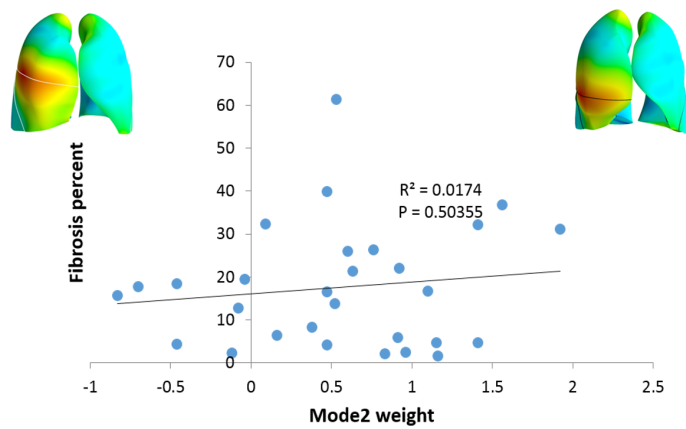
Table 4.8 lists the p-values and R values from linear regression for the correlation of the first three modes with fibrosis and LAA percentage. Figure 4.19 shows the relationship of the first three modes to overall fibrosis percentage. No correlations were found between the three shape modes and LAA extent. The first shape mode shows a significant relationship with the percentage of fibrosis ($p < 0.0001$). With an increase of the percentage of fibrosis, the weight value of mode 1 becomes increasingly negative which corresponds to a larger shape difference from the mean control lung shape. Negative weighting of mode 1 is also associated with increased ratio of anterior-posterior diameter to the height of the lung, which makes the lung appear 'fatter' and 'shorter'. Therefore in general, the lung shape difference in patients with IPF is strongly associated with the fibrosis extent, and the more extensive the fibrosis, the more 'abnormal' the lung shape is.

Table 4.8: Results for linear regression of shape mode weighting against extent of fibrosis.

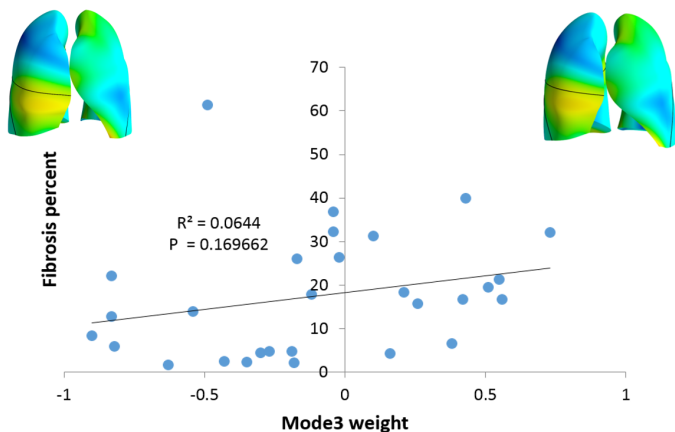
Mode	Fibrosis		LAA	
	P-value	R	P-value	R
Mode 1	$\ll 0.001$	0.640	0.168	0.265
Mode 2	0.504	0.132	0.578	0.110
Mode 3	0.170	0.254	0.796	0.047



(a) Mode 1



(b) Mode 2



(c) Mode 3

Figure 4.19: A Linear regression of the PCA-derived first three modes with respect to overall fibrosis percentage. (a) Mode 1 weight. (b) Mode 2 weight. (c) Mode 3 weight.

4.4 Discussion

Individualized treatment strategies are urgently needed in clinical applications and are the ultimate goal of modern pulmonary medicine. A quantitative analysis of IPF based on HRCT images has the potential to build a reliable relationship between imaging tissue-level bio-markers and clinical endpoints. In this chapter, data from IPF patients are quantitatively analysed and compared between time points and individuals.

Quantitative analysis of density and spatial distribution of tissue patterns in IPF a consistent understanding of IPF disease

As imaging data acquired in different patients and at different time points has been mapped to a consistent geometrical framework, the analysis presented here allows a more direct comparison between tissue identified as pathological, than if images were simply compared side-by-side, or registered to a single arbitrary image for each subject. From the quantitative analysis results, the mean density of each tissue pattern remains consistent over time in both lungs, and ground-glass has highest average tissue density whereas emphysema has the lowest average tissue density. Ground-glass mainly locates in the basal and dorsal part of the lung, and reticular is throughout the entire lung with a greater percentage basally, apically and posteriorly, while emphysema presents predominantly around the apex region of the lung. Fibrosis (ground-glass, reticular and honeycomb) is highest in the two lower lobes and preferentially appears near the lung surface; in contrast, more emphysema presents in the upper lobes. These quantifications of tissue abnormalities are consistent with the clinical radiological findings of IPF discussed in Chapter 2. While fibrosis is highest in the lower lobes, it is still significant in the upper lobes. For example, in Figure 4.14, the proportion of ground-glass in the LUL

(20%) is only 10% less than the proportion in the RLL.

The density analysis shows consistent average tissue density for each CT pattern at different time points, which suggests that CALIPER is consistent and robust with its identification of each abnormality type over time. This means that the normalized tissue classification error noted in Section 4.3.2 is likely to mainly come from the lung surface fitting, conversion of the surface mesh to a volume mesh, and classified data mapping procedures.

There appears to be consistency between subjects in the spatial distribution of ground-glass (which accounts for the largest proportion of fibrosis), both apical-basally and dorso-ventrally. This consistent trend can be observed across all time points and subjects (Figure 4.7 and 4.10) and also at time 1 across all subjects (Figure 4.8 and 4.11). The analysis suggests that ground-glass locates predominantly in the basal and posterior region, particularly in the right lung. That is the right lower lobe seems to be more affected, which is consistent with larger decreases in right lower lobe volume across the cohort (as shown in Table 4.6, there is a significant decrease in the right lower lobe of IPF lung). While the literature suggests that IPF predominantly appears in the lower lobes (King Jr et al., 2011; Raghu et al., 2011; Richeldi et al., 2017), no prior study has highlighted differences in disease distribution difference between the two lungs, or between lobes.

No substantial shifts (redistributions) in spatial distribution of the tissue abnormalities were found over time on a population level (trends at time 1 are similar to the trends across all time points on average) (Figure 4.7, 4.8, 4.10 and 4.11), and the amount of disease exhibits an overall increase during the clinical course. However, some individuals do show larger shifts in distribution of the disease than others (see Appendix B). The subject in Figure 4.12 and 4.9, for example, shows an increase in ground-glass in

left lung over time (throughout the lung but particularly in the basal region). In the right lung, however, most changes occur just in the anterior area.

Moreover, in the subpleural to internal axis, all the three tissue patterns for fibrosis are on average within 10% distance from the pleural surface to the centre of the lung. However, reticular and ground-glass can appear anywhere through the lung volume. This has been qualitatively described in the literature (King Jr et al., 2011), but now has been quantitatively measured.

As shown here, tissue density, tissue volume, and spatial distribution of abnormalities could all be important indexes for succinctly describing IPF disease. Through quantifying these features in addition to standard qualitative evaluation, subjective errors could be avoided to offer a more consistent assessment of individual patients.

Average statistical shape model provides a consistent measurement to quantify disease among different people and over the whole clinical course

The SSM provides a consistent geometric viewpoint through which to assess changes in lung tissue features as illustrated in Figure 4.5. IPF is a progressive lung disease that has a variable presentation between different patients. In this study, the spatial distribution of CALIPER-classified data in the IPF lung were quantified along crano-caudal, dorso-to-ventral, and subpleural-to-internal directions over time. Currently, few published studies have quantitatively analysed the spatial distribution of IPF abnormalities, especially for the progression and change of disease over time. The SSM-based quantitative method used here normalized a set of lungs of different shapes into a standard shape model, thus providing a convenient way to make a comparison between different patients or within one patient at different time points. This method makes it possible to capture the disease variation across a population and describe the difference using

objective indexes. Furthermore, the progression of disease over time can be analysed. The goal is that this contributes to helping describe the clinical course of disease.

It is widely acknowledged that typical symptoms occur on average 1-2 years before a definite clinical diagnosis of IPF, and some radiographic evidence of IPF may even be found before symptoms occur (Raghu et al., 2011; Devaraj, 2014). Understanding this 'sub-clinical' period of disease is very important for developing an early diagnosis of IPF disease. The SSM-based method makes it possible to compare the IPF lung with a normal cohort. However, while the IPF lung was shown to have significantly different shape to the normal lung (primarily with respect to mode 1), its shape did not change significantly over time. Remodelling of the chest wall and lung shape therefore appears to occur primarily before the initial imaging. The structural changes during this pre-clinical time period have a relatively small impact on function, whereas the increase in fibrosis that occurs following initial imaging has a much greater impact on lung function. In mode 1, the primary shape mode, although there was overlap with the normal cohort, all IPF subjects at all but one time point had a negative weight value, while the normal subjects we considered had values between -2 and 2. In a previous SSM analysis that included the older normal cohort (Osanlouy, 2018), mode 1 was strongly associated with age. This association is not as strong for the > 50 cohort used here. However, the negative shape weighting tends to be for the older subjects, so the lung shape of IPF the subject has an "older" appearance. Lung shape, as quantified by the SSM here, reflects both changes in chest wall shape and in fissure location (lobe shape). The differences between normal and IPF therefore reflect some abnormal and quantifiable chest wall remodelling as well as changes to mechanical properties of the tissue that affect the fissure locations.

The shape of the basal part of IPF lung is significantly different to the normal lung and correlates with fibrosis extent

The first shape mode of the SSM is significantly different between IPF and normal, and strongly correlates with the percentage of fibrosis. The first shape mode corresponds mainly to the anterior-posterior diameter of the lung which is associated with a variation of diaphragm location. This shape change of the diaphragm is potentially explained by the spatial distribution of tissue abnormalities. The basal and peripheral location of disease is very likely to increase the stiffness of the lower part of the lung, thus it could impact on the movement of the diaphragm when breathing. Furthermore, fibrosis extent in IPF is found to be related to the ratio of anterior-posterior diameter to the height of lung (as the first mode relates to the largest change in the anterior-posterior diameter of the lung, see Section 4.3.4). A larger proportion of fibrosis is usually correlated with a larger ratio of anterior-posterior diameter to the height of lung. This "compression effect" on the lung shape may be associated with the reduction in tissue compliance caused by fibrosis. Specifically, since the IPF subject and control imaging used in this chapter were all acquired at the end of inspiration, the lower tissue compliance caused by fibrosis will influence the expansion of the lung during inhalation if inhalation is driven by a normal muscle pressure, and therefore this may have an effect on the lung shape. In addition, it is demonstrated in the lobe volume analysis that the IPF lung has a lower average volume proportion for the left lower lobe and right lower lobe, which may be also caused by the "compression effect" of the lower lobe in IPF lungs. These features provide a potential way to indicate if the 'lung function' is deteriorating before PFTs can show any abnormalities as a shape difference of IPF patient may be observed when comparing with older normal lungs.

In addition, the restriction of chest wall would have an impact on the lung shape changes in IPF. When inhale, the diaphram contracts and moves downward, and this increases the space in the chest cavity, into which the lung expands. We breath primarily from the diagphram but the chest wall does inflate and makes some contribution, particularly when moving towards full inspiration (how the subjects used in this study were imaged). With damage to the lung tissue (such as IPF lungs), there would likely be an increase in the work of breathing, which would lead to subtle changes in an individual mode of breathing. If this persists, there would be a remodeling of the chest wall over months or years. In addition, on a breath by breath basis, a restriction of the chest wall would most likely make it harder to breath, therefore would restrict lung volumes. In the future studies, the modeling of chest wall in normal and IPF subjects could help to investigate the impact of the restriction of chest wall on the lung shape changes in IPF.

4.5 Summary

In this chapter, IPF classified tissue was analysed and characterized over time using quantitative methods. The results show that fibrosis presented predominantly basally and peripherally. In contrast, emphysema was mostly located in upper lobes. The first principal SSM mode ($> 20\%$ of the shape variation in normal lungs) was significantly different between IPF and normal and strongly correlated with fibrosis extent in IPF lungs. This quantitative analysis provides consistent potential tissue-level markers which will be used to guide the computational modelling of IPF lungs in the next chapter.

Chapter 5

Functional modelling of idiopathic pulmonary fibrosis

In Chapter 4, HRCT based quantitative analysis and shape analysis methods were developed to provide a consistent way of describing the features and progressions of IPF disease. However, it is not clear how - or whether - the spatial distribution of tissue abnormalities in IPF (including classifications of tissue type) correlate with lung function and their change over time. Translating these imaging and shape bio-markers into functional bio-markers to directly help with clinical diagnosis and treatment is still a challenge in progress. For the patient with IPF, V/Q mismatching and hypoxaemia are frequent occurrences. Computational modelling provides a novel way to understand how changes to the lung tissue contribute to observed decline in lung function, therefore modelling can potentially be used to build a relationship between image-based bio-markers and functional presentations. This chapter outlines an approach to functional modelling of IPF. The quantitative tissue-level and shape-level features described in previous chapters were combined with pulmonary function tests (PFTs) to guide a patient-specific

computational model of lung function in IPF. The lung function of healthy older adults was also modelled for comparison with the IPF models. This chapter therefore aims to integrate data from volumetric imaging, PFTs, and computational models of lung function, to understand differences between IPF and normal older lungs. Hypoxaemia in IPF has been suggested to be caused by either increased V/Q mismatch, anatomical shunts, or thickening of the gas exchange barrier. Swan (2010) showed that whole lung gas exchange is more sensitive to tissue stiffness (i.e. via V/Q mismatch) than gas exchange barrier thickness. Therefore, this chapter seeks to confirm whether stiffening-induced V/Q mismatch is sufficient to explain hypoxaemia in IPF. Lung function in IPF has been described in Chapter 2, and lung function in healthy older people will be introduced in Section 5.1. However, lung function is expected to decline with age even in normal individuals. Therefore, expected respiratory function in older people is first introduced, and then computational models aiming to reproduce this function are described.

5.1 Respiratory structure and function in older people

The respiratory system of the human keeps developing throughout life, with the peak-point of pulmonary function achieved before 30 years of age (Janssens et al., 1999; Sprung et al., 2006). For most people, respiratory performance begins to gradually decline after reaching this maximal status. The ability of the lung to deliver more oxygen to tissues than they require ("reserve capacity") decreases by about four-fold from age 20 to age 70 in healthy people (Smith, 1986; Zaugg and Lucchinetti, 2000). Even in older athletes who experience vigorous endurance exercise and have better aerobic ability, the functional capability of the lung will progressively deteriorate over time (Mittman et al., 1965; Pollock et al., 1997; McClaran et al., 1995).

Ageing-related changes in respiratory physiology are usually associated with structural alterations in both lungs, dilatation of alveoli, enlargement of airspaces, a decrease in gas exchange surface area, and increased residual volume (RV) and functional residual capacity (FRC) (Sprung et al., 2006; Lalley, 2013). There is a reduction in chest wall compliance and the static elastic recoil of the lung, which will lead to static air-trapping, a decrease in vital capacity (VC), a decrease in expiratory flows and an increasing work of breathing compared with younger individuals (Sprung et al., 2006). The strength of respiratory muscles decreases with age, and this is strongly correlated with nutritional status (lean body mass, body weight) and cardiac index (Janssens et al., 1999). The V/Q ratio heterogeneity tends to increase because of closing of dependent airways, and carbon monoxide transfer capability also decreases which is associated with the reduced alveolar surface area (Janssens et al., 1999). Interestingly, despite these changes, some research indicated that gas exchange may be preserved both at rest and during exertion, with only a slight reduction in arterial oxygen tension, and no significant change in arterial carbon dioxide tension, but pulmonary reserve is diminished (Janssens et al., 1999; Sprung et al., 2006). These age-associated changes are summarized in Table 5.1.

5.1.1 Ageing-associated alterations in the chest wall and respiratory muscle function

Several morphological changes occur in chest wall and diaphragm in older people that reduce the efficiency of the respiratory system. One of the most important changes is a progressive decline in chest wall compliance, which relates to a decrease in cross sectional area of the intercostal muscles, calcification of costal cartilage and rib-vertebral articulations, and narrowing of intervertebral disk spaces (Murray, 1986; Crapo, 1993).

Table 5.1: Age-associated changes in respiratory function and their relationships to clinical presentations (Reproduced from (Sprung et al., 2006; Lalley, 2013))

Measurements	Changes, ≥ 60 yrs.	Clinical presentations
Static lung volumes		
- TLC	Unchanged	
- FRC	Increase	
- IRV	Modest increase	
- ERV	Increase	
- V_T	Modest increase	
- VC	Decrease	
- IC	Increase	
- RV	Increase	Impaired gas exchange
Dynamic lung volumes		
- FVC	Decrease	
- FEV ₁	Decrease	
- FEV ₁ /FVC	Decrease	
- Peak expiratory flow	Decrease	
Resistance and compliance		
- Respiratory system resistance	Increase	
- Small airways closure	Increase	Impaired gas exchange
- Chest wall compliance	Decrease	Increase in work of breathing
- Lung compliance	Increase	Decrease in ventilatory response to exercise
Respiratory (muscle) pressures		
- Mean pleural pressure	Unchanged	
- Respiratory muscle strength	Increase	
Gas transfer		
- Ventilation-perfusion mismatch	Increase	Impaired gas exchange
Altered control of breathing		
- Responsiveness to imposed respiratory loads	Decrease	Hypoventilation
- Responsiveness to hypoxemia and hypercarbia	Decrease	Hypoxemia and hypercarbia
- Sensitivity to anesthetic agents and opioids	Increase	Respiratory failure in early postoperative period

TLC: total lung capacity; FRC: functional residual capacity; IRV: inspiratory reserve volume; ERV: expiratory reserve volume; V_T : tidal volume; VC: vital capacity; IC: inspiratory capacity; RV: Residual volume; FVC: forced vital capacity; FEV₁ : forced expiratory volume in 1 s; FEV₁/FVC : the ratio of the forced expiratory volume in the first one second to the forced vital capacity of the lungs.

The structural changes that occur in the chest wall are associated with a reduction in the curvature of the diaphragm and in the maximal transdiaphragmatic pressure, however the thickness of the diaphragm seems not to change significantly in older adults (Zaugg and Lucchinetti, 2000; Sprung et al., 2006). It is noted that age-associated osteoporosis results in a shape change of the thorax geometry; that is, an increase in dorsal kyphosis and anterior-posterior chest diameter (Janssens et al., 1999; Sprung et al., 2006).

The reduction in respiratory muscle strength that leads to age-related decrease of maximal static inspiratory and expiratory pressures will lead to lower efficiency of respiratory muscle activity (Wijesinghe and Dow, 2005; Sprung et al., 2006; Lalley, 2013). It has been shown that the reduced respiratory muscle strength is associated with a deficient nutritional status in older people, and a strong relationship has been found between maximal inspiratory/expiratory pressure and lean body mass (Arora and Rochester, 1982; Janssens et al., 1999). The electromyographic signal produced by twitch stimulation decreases by around 50% in 70-year-olds compared with young subjects, and this reduction is attributed to the loss of type II fast-twitch muscle fibres (Larsson, 1983).

5.1.2 Ageing-associated alterations in pulmonary mechanics and lung volumes

Although the chest wall becomes stiffer in older people, their lung parenchyma actually becomes more compliant (Mittman et al., 1965; Turner et al., 1968; Zaugg and Lucchinetti, 2000). The elastic recoil pressure of lung tissue gradually reduces with ageing, at a rate of around 0.1 to 0.2 cmH₂O on average every year (Turner et al., 1968), and this reduction is attributed to the alterations in the spatial distribution of the elastic

fibre network in the lung parenchyma (Sprung et al., 2006). In older people, the static pressure-volume curve of the lung is shifted to the left; in contrast, the pressure-volume curve of the thorax is shifted to the right (Zaugg and Lucchinetti, 2000; Sprung et al., 2006).

The tidal volume also experiences a slight decrease with age, whereas the respiratory rate gradually increases (Sprung et al., 2006). As mentioned in Section 5.1.1, the chest wall becomes stiffer with age, while the lung tissues become more compliant. These changes will lead to an increase in RV and a decrease in VC (Lalley, 2013). Some research has indicated that RV increases by approximately 50% from a 20-year-old to a 70-year-old on average, and VC will drop to around 75% of its peak value during this period, with a decrease of 20 to 30 ml per year (Janssens et al., 1999; Sprung et al., 2006). The TLC, which is the air volume in the lungs during a maximum inspiratory effort, remains unchanged with age, as the effect of the decreased inward elastic recoil of the lung is offset by the reduction in the outward elastic recoil of the chest wall (Sprung et al., 2006). However, FRC increases by 1 to 3% per decade, since the rate of decrease in lung recoil exceeds the rate of decrease in chest wall compliance (Janssens et al., 1999; Lalley, 2013). Forced vital capacity (FVC) and forced expiratory volume in one second (FEV_1) have been demonstrated to decrease progressively with ageing in both men and women (Knudson et al., 1976), but these measurements decrease more rapidly in males than in females (Crapo, 1993). FEV_1 decreases by approximately 20 ml per year in subjects aged 25 to 29 years, but for people more than 65 years old, the average annual rate of reduction is more dramatic: up to 38 ml (Brandstetter and Kazemi, 1983).

5.1.3 Ageing-associated alterations in gas exchange

The inhomogeneity or "mismatch" in ventilation and perfusion increases with age, especially in the gravitationally dependent regions of the lung where intrapleural pressure becomes higher with age, and as the lung tissues become less elastic, they fail to keep small airways open (Holland et al., 1968; Paoletti et al., 1985; Lalley, 2013). The increased ventilation-perfusion heterogeneity results in a reduction in P_aO_2 , with a progressive drop from approximate 95 mmHg at 20 years to about 75 mmHg at 70 years. However, $PaCO_2$ remains almost unchanged with increasing age, although PaO_2 declines (Wahba, 1983; Sprung et al., 2006). This can possibly be explained by a decreased rate of basal metabolism and a higher diffusive capability of CO_2 across the alveolar-capillary membrane (Levitzky, 1984). Local pulmonary perfusion can also reduce with age in some regions that are well ventilated as a result of reduced cardiac output (Levitzky, 1984; Lalley, 2013). The alveolar-arterial pressure difference for oxygen ($P_{A-a}O_2$) increases with ageing due to the increased heterogeneity of V/Q, and this change is probably also related to the increase in closing volume during breathing (Janssens et al., 1999). It can be observed that PaO_2 reduces at a rate of approximately 5 mmHg per decade from the age of 20 years. Additionally, the diffusing capacity of the lungs for carbon monoxide (DLCO) decreases with age (Guenard and Marthan, 1996), with loss of about $0.3 \text{ mL}\cdot\text{min}^{-1}\text{mmHg}^{-1}$ and $0.2 \text{ mL}\cdot\text{min}^{-1}\text{mmHg}^{-1}$ per year for men and women, respectively (Murray, 1986). The reduction is more significant after 40 yrs of age, and the increased mismatch in V/Q, a decline in the alveolar surface area (Verbeken et al., 1992; Thurlbeck and Angus, 1975), the decreased density of lung capillaries (Butler and Kleinerman, 1970) and the reduction in pulmonary capillary blood volume (Guenard and Marthan, 1996) are all potential factors that may cause a reduced

diffusion capacity.

5.1.4 Relationship between lung function and lung shape

There is strong evidence that age-related changes in lung structures are associated with a series of alterations in respiratory function (introduced in Section 5.1). For example, the reduction in chest wall compliance of older people leads to a decrease in VC, while an increased RV in the elderly usually results in impaired capability of gas exchange which relates to a lower measured DLCO. In a previous study (Osanlouy, 2018), several lung structure-function relationships were analysed through quantifying the correlations between the first three PCA-based mode weights calculated for a SSM of a healthy cohort aged 20-90 years with age, BMI, lung volume and some pulmonary function measurements. For each training subject of this SSM, the individual weight scores for each of the first three shape modes (which captures most shape variation) were examined. An ordinary least squares regression was applied to test the associations, and the P-value was used to quantify the strength of each association, with an alpha level of 0.05 considered statistically significant. Analysis showed that Mode 1 is positively correlated with FEV₁, FEV₁/FVC, Maximal mid-expiratory Flow (FEF25%-75%), BMI and DLCO, whereas it is negatively correlated with age, RV and RV/TLC. For Mode 2, only BMI is found to be correlated with the shape variation, whereas quite a number of lung volume measurements (including FRC, TLC ,VC and RV) showed strong relationships with Mode 3.

5.2 Methods: Patient-specific modelling of IPF lung function

In this section, a patient-specific computational model of lung function is proposed to explore V/Q matching and whole lung gas exchange for patients with IPF. In order to make a comparison of lung function between the IPF patient and older normal people, for each patient, a subject-specific lung mesh that represents the statistical lung shape of a normal individual of the same age, BMI and pulmonary function data was predicted using an SSM. Anatomically-based airway and blood vessel trees were generated from HRCT images of IPF subjects, and for the corresponding normal lung mesh. Ventilation, perfusion, and gas exchange were simulated in the IPF and control models under baseline healthy conditions, and with constriction of airways and/or blood vessels in tissue regions classified as abnormal. To achieve this, the individual's lung parenchymal tissue classification and quantification data was mapped to their spatial model, with fibrosis assumed to reduce tissue compliance and narrow vessels. Data from PFTs were used to parameterize the models and set the boundary conditions for simulation. The modelling framework is illustrated in Figure 5.1.

5.2.1 Clinical data

Two patients diagnosed with IPF were selected from the clinical data used in Chapter 4 as representative subjects for functional modelling. Patient 1 is female with three imaging time points at 0, 12 and 23 months, and Patient 2 is a male with two time points at 0 and 46 months. The clinical data for each patient includes both HRCT images and PFT results, with less than 3 months between the scan date and the PFT date.

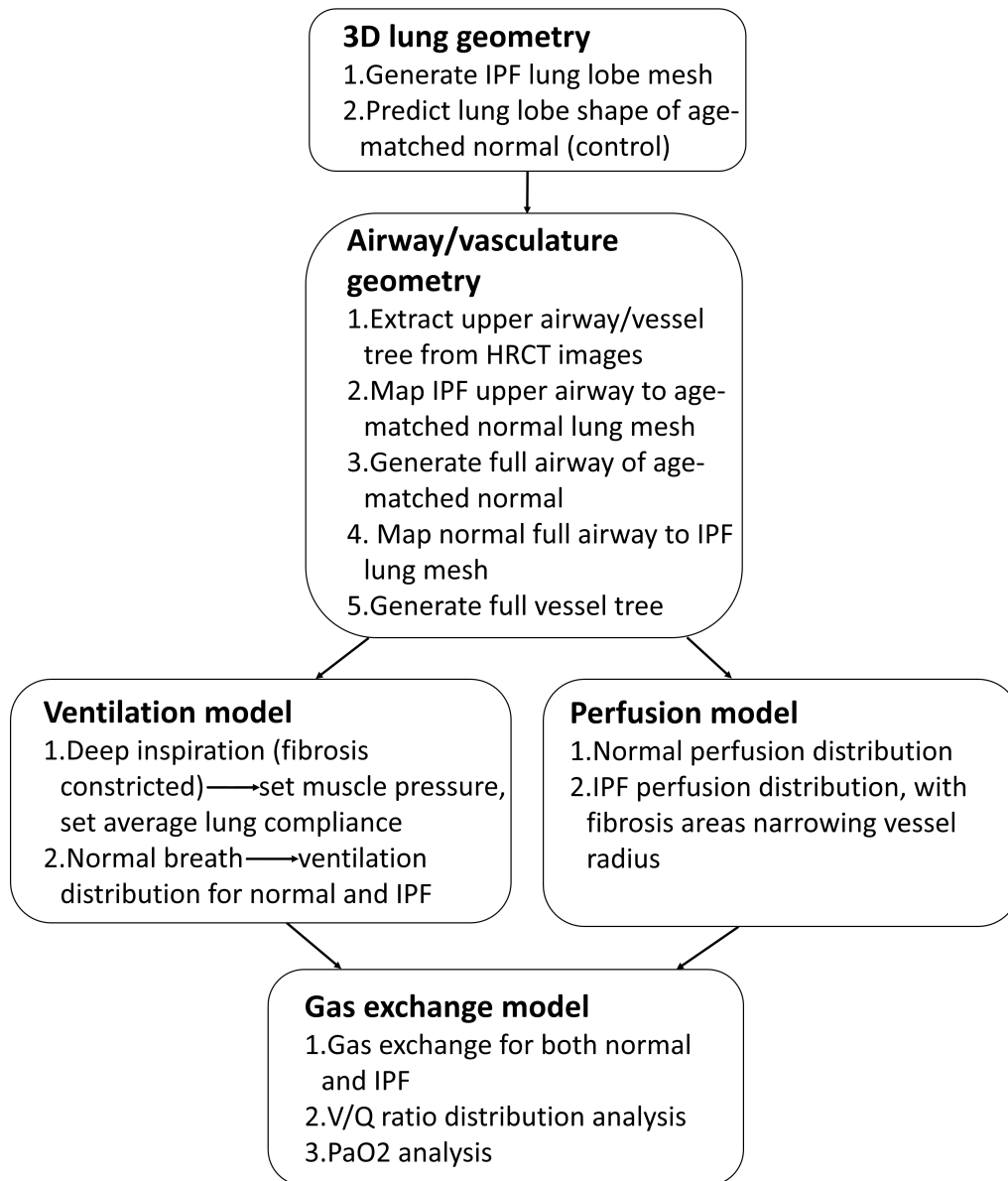


Figure 5.1: Computational modeling framework for IPF and older normal lung function.

5.2.2 Construction of lung lobe geometry

In Chapter 4, Section 4.3.3 and 4.2.4, the lung lobe shapes and volumes of an IPF cohort were compared with a normal older (control) cohort with a similar age range. It was shown that there is a significant difference in lung lobar geometry between IPF and older controls. This alteration in lung shape is mainly basal (lower lobe), and is strongly associated with the distribution of fibrosis in IPF. In order to include the impact of shape change into the modelling of lung function, the SSM of a normal older cohort and the IPF patient's individual information were combined to predict a lung lobe shape of an age-matched normal as a control model to compare to each IPF patient. The lung lobe mesh of each IPF patient was generated using the method introduced in Chapter 3, Section 3.3.2.

The SSM used to predict the age-matched control model in this chapter is different from Osanlouy (2018), because it only includes subjects aged 50 years and over. Underlying relationships with lung function are still expected to be present, however.

Shape prediction of a normal lung to correspond to each IPF patient

A lung shape prediction model for a healthy cohort aged ≥ 50 years was developed based on a previous analysis of lung structure-function relationships (Osanlouy, 2018). Age, BMI, FVC, FEV₁, FRC, TLC, VC, RV, RV/TLC and DLCO were selected as the individual functional measurements to train the lung shape predictive model, as these parameters have been shown to have relatively strong correlations with the first three shape modes. The training process for the lung shape predictive model was to find optimized equations that best describe the relationship between the functional measures and the mode weights. For each shape mode, a multivariate regression model was con-

structed as:

$$w_i = \alpha_{0i} + \alpha_{1i}m_1 + \alpha_{2i}m_2 + \dots + \alpha_{ni}m_i + \varepsilon, \quad (5.1)$$

where w_i is the weight score of the i th shape mode, n is the number of functional measures, $\alpha_{0i}, \alpha_{1i}\dots\alpha_{ni}$ are the regression coefficients (in which α_{0i} is the intercept) m_i is the tested value of the i th functional measure, and ε is a random error.

Using Equation 5.1, a set of possible regression models can be developed for each shape mode (with different regression coefficients $\alpha_{0i}, \alpha_{1i}\dots\alpha_{ni}$). In order to find the best predictive model from all possible models, the two most common criterion for model selection - the Akaike information criterion (AIC) and the Bayesian information criterion (BIC) - were used to deal with the trade-off between the goodness of fit of the model and the simplicity of the model (Aho et al., 2014). Both AIC and BIC are founded on information theory, with each calculated by

$$AIC = 2k - 2\ln L(\theta), \quad (5.2)$$

$$BIC = \ln(n)k - 2\ln L(\theta), \quad (5.3)$$

where k is the number of the estimated parameters (that is the number of functional measures in this study) in the model, **n is the number of subjects**, $L(\theta)$ is the maximized value of the likelihood function of the model and θ are the parameter values that maximize the likelihood function.

The multivariate regression models with the lowest values of AIC and BIC were selected as the best predictive models, then the models of the first three PCA modes

were constructed in the form of Equation 5.1, as

$$\begin{aligned} w_1 &= 1.38 + (-0.04 \times \text{Age}) + (0.38 \times \text{FVC}) + (-0.04 \times \text{DLCO}), \\ w_2 &= 3.49 + (-0.16 \times \text{BMI}) + 0.02 \times \text{RV/TLC}, \\ w_3 &= 4.90 + (-0.02 \times \text{Age}) + (-0.45 \times \text{TLC}) + (-0.05 \times \text{DLCO}), \end{aligned} \quad (5.4)$$

where w_1 , w_2 and w_3 are the weight scores of the first three shape modes. By inputting the individual functional measures into the regression models, the weights of the first three modes are calculated. Then the subject-specific predicted shape of the control lung model is reconstructed by adding the linear combination of the first three modes to the average SSM

$$S_{pred} = S_{mean} + \sum_{i=1}^3 \mathbf{u}_i w_i, \quad (5.5)$$

where S_{mean} is the mean of the SSM for the older normal cohort, and S_{pred} is the subject-specific predicted lung shape.

5.2.3 Construction of airway/vascular geometry

Subject-specific conducting airway trees and pulmonary vasculature trees were constructed for both the actual shape of the IPF patient's lung and control model with the same characteristics of that subject. The geometry of the pulmonary airway and vessels are important subject-specific features. In this study, airway/vessel trees were first generated for the predicted control model, which represents a healthy lung matched to the IPF subjects. The models were then deformed to the shape of the IPF lung mesh which has quantifiable shape differences as described in Chapter 4. The airway/vasculature

diameters were assigned to each branch as a postprocessing step, with values appropriate for a healthy lung and for IPF. In this way, the branches for the IPF and control airway/vascular models retain the same geometric connectivity and same lobar distribution, but have different radius and length.

Airway tree

In order to generate an airway tree in the lung shape, the bi-cubic Hermite finite element mesh of the lung surface was converted to a tri-cubic Hermite volumetric mesh (introduced in Chapter 4, Section 4.2.1). An anatomically-based structure of the bronchial airways (from trachea to terminal bronchioles) was generated using the methods described in detail by Tawhai et al. (2004). In brief, the centrelines of the largest airways (trachea, and left and right branches of the first 6 generations of airways) were manually segmented from the subject's HRCT images. This provides an incomplete description of the airway tree. Then, the larger airways were used as an initial condition to generate the remaining branches down to the level of the terminal bronchioles within the subject's lung mesh using a volume-filling branching algorithm. The steps to generate patient-specific airways in IPF and old normal lungs are summarized as follows:

1. 1-D finite element mesh of the centerlines of IPF larger airways were created manually from HRCT raw images of the IPF patient (shown in Figure 5.2a).
2. The 1-D tree of central airways was mapped to the volumetric mesh of the control model. The nodal positions inside the control mesh were mapped by calculating the local coordinate ξ_i with respect to its element (details in Chapter 4, Section 4.2.1). The branches outside the mesh were then scaled to match the target lung volume, followed by a manual adjustment. The element connectivity remained the same during mapping.
3. The mapped larger airways in step 2 was used as a starting geometry for gen-

erating a full airway tree by using a volume-filling branching algorithm (Tawhai et al., 2004), to fill the shape of the control mesh. Briefly, a uniformly-spaced grid of seed points was created within the 3D volumetric lung mesh. The number of seed points was ~ 32000 (45% for left lung and 55% for right lung) which approximates the number of pulmonary acini in the lung (Haefeli-Bleuer and Weibel, 1988). The branching algorithm was designed to generate a branching structure recursively towards the center of mass of seed point groupings, until each seed point was assigned to a terminal bronchiole (shown in Figure 5.2b).

4. The generated linear mesh of the full airway tree in step 3 was mapped back to the volumetric lung mesh of the IPF patient using the same method as in step 2.

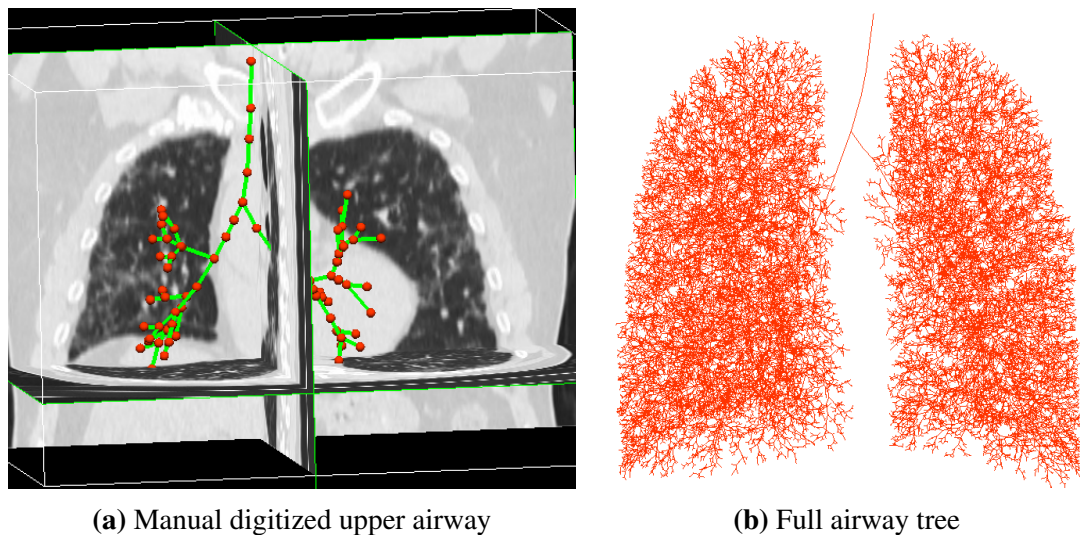


Figure 5.2: Generation of airway tree. (a) Manual digitized upper airway tree from HRCT images in 3D. Green lines are the centerlines of upper airway tree, and red points represent airway nodes. (b) Geometry of full conducting airway tree generated using volume-filling algorithm. The model is shown from the anterior view, with the left lung on right, and right lung on left.

In the next stage, the diameters of the airway branches were assigned for both IPF and control models. The method was:

1. The trachea radius for IPF was measured from segmented HRCT images (based on the segmented cross-section of larger airway branches) at 25%, 50%, and 75% along the centreline of the trachea. The trachea radius was defined as the average of the three measurements.
2. The radius of the terminal bronchioles in the control models were assumed to be 0.2mm (Horsfield et al., 1976). The airways in the IPF lung have been found to be narrowed in 70% of patients (Crystal et al., 1976). The terminal bronchiole radius for the IPF models was therefore scaled to a smaller value. The scaling was assumed to be in proportion to the ratio of IPF to control model volumes, as:

$$R_{TB_{IPF}} = R_{TB_{Control}} \times \sqrt[3]{\frac{FRC_{IPF}}{FRC_{Control}}}, \quad (5.6)$$

where FRC_{IPF} is the measured FRC volume for the IPF patient and $FRC_{Control}$ is the reference FRC volume for the control model, $R_{TB_{IPF}}$ is the terminal bronchiole radius in the IPF models, and $R_{TB_{Control}} = 0.2\text{mm}$ is the terminal bronchiole radius in the reference (i.e. control) model.

3. The radii of the other airway branches for the IPF models were calculated by assuming a constant Horsfield diameter ratio (R_dH) for each IPF subject. R_dH is the rate of reduction of diameter (or radius) with reduction in Horsfield order, with R_dH calculated by:

$$R_dH = \frac{10 \times (\log_{10} R_{TB} - \log_{10} R_{Trachea})}{1 - H_{Trachea}}, \quad (5.7)$$

where R_{TB} is the terminal radius, $R_{Trachea}$ is the trachea radius, and $H_{Trachea}$ is the Horsfield order of the trachea.

4. While the R_{TB} is expected to be smaller in IPF (Crystal et al., 1976), the anatom-

ical deadspace (V_D) is actually larger (Plantier et al., 2016). $R_{Trachea}$ and R_dH for the control models were therefore set such that V_D (control) < V_D (IPF), for $R_{Trachea}$ within the normal published range for men (6.5-12mm) and women (5-11mm) (Breatnach et al., 1984). V_D (control) was initialized using V_D (control) = V_D (IPF) \times (34.2/45.3), which is a relationship measured by Plantier et al. (2016) for IPF and controls. $R_{Trachea}$ and R_dH were adjusted until $R_{Trachea}$ was within the normal size range.

Using the above steps, a patient-specific pulmonary airway geometry for IPF and the control lung was constructed.

Vascular tree

The centerlines of the first two generations of vessel trees were manually segmented from HRCT images, and represented as a 1-D finite element mesh. In this thesis, the pulmonary arterial and venous trees of other generations were assumed to be approximate replicas of the airway tree. Using the airway tree to approximate vessel geometry is a reasonable assumption, as the conventional pulmonary arteries generally follow the same branching pattern as the airways trees, and the airways and blood vessels have similar lengths and orientations. The airway and vasculature have been observed to bifurcate in union from larger branches to the bronchiole level, and the veins to divide at the approximate midpoint between adjacent airway bifurcations (Weibel, 1984; Hsia et al., 2016). The manually-segmented larger vessel branches plus the finite element model of the airway tree provided a full pulmonary blood vessel geometry for the IPF patient (the larger vessels and larger airways have the same topology). The vascular structure for the control model was obtained using the same mapping procedure used for the airways as described previously. The microcirculatory model of Clark et al. (2010, 2011) was appended to each terminal arteriole, to supply a corresponding ter-

minal venule. This model is a symmetric-branching system of arterioles and venules that are connected (from arteriole to venule) at each generation by a recruitable and distensible "capillary sheet".

The unstrained (zero transmural pressure (P_{tm})) radius of the main pulmonary artery ($R_{mArtery}$) and vein (R_{mVein}) were assigned based on the patient-specific (measured) trachea radius and data from morphometric studies (Equation 5.8and 5.10) (Horsfield, 1978; Horsfield and Gordon, 1981; Huang et al., 1996). The radius of all other arteries and veins down to the distal level were calculated based on a defined rate of increase in diameter with vessel Strahler order, the Strahler diameter ratio for artery and vein (R_dS_{Artery} and R_dS_{Vein}). The value of R_dS for the arterial tree and venous tree were specified according to the radius of the main artery and vein, and aiming for consistency with published human data (Horsfield et al., 1971; Horsfield, 1978; Horsfield and Gordon, 1981; Huang et al., 1996):

$$R_{mArtery} = \frac{k_{Artery} \times R_{Trachea}}{R_{Trachea_{ref}}}, \quad (5.8)$$

$$R_dS_{Artery} = \frac{10 \times (\log_{10} R_{sArtery} - \log_{10} R_{mArtery})}{1 - S_{mArtery}}, \quad (5.9)$$

$$R_{mVein} = 10 \times \log_{10} \left(\frac{k_{Vein} \times R_{Trachea}}{\log_{10} R_{Trachea_{ref}}} \right), \quad (5.10)$$

$$R_dS_{Vein} = \frac{10 \times (\log_{10} R_{sVein} - \log_{10} (k_{Vein} \times R_{Trachea}))}{3 - S_{mArtery}}, \quad (5.11)$$

where k_{Artery} is constant artery radius (equals to 11.53), k_{Vein} is a constant for vein radius (equals to 6.3), $R_{Trachea_{ref}}$ is a statistical reference trachea radius (equals to 9

mm), $R_{sArtery}$ is the target for smallest arteries (equals to 0.125 mm), R_{sVein} is the target for smallest veins (equals to 0.125 mm), and $S_{mArtery}$ is the Strahler order of the artery model. The vessel radius for the IPF models and the control models were then calculated.

5.2.4 Construction of computational models

In this chapter, computational modelling of lung function integrates previously published models of ventilation (Swan et al., 2012), perfusion (Clark et al., 2010, 2011) and gas exchange (Clark et al., 2014) to simulate \dot{V}/\dot{Q} distribution and oxygen and carbon dioxide exchange during tidal breathing in the upright posture. The patient-specific geometry of airways and vessels were used as input for these models. A brief introduction of the model components is summarized below, and details can be found in the referenced papers.

Ventilation model

The ventilation model developed by Swan et al. (2012) was used to predict the time-averaged topological distribution of inhaled air in the upright human lung, governed by local tissue deformation, elastic recoil pressure, airway resistance and acinar compliance. Each of the acini in the tree model subtending each terminal bronchiole are assumed to function as compliant compartments. The acinar volume and compliance were initialised at FRC using a distribution of tissue strain along the gravitational direction that was consistent with strain computed by a tissue mechanics model (Tawhai et al., 2009). The acinus volumes were perturbed around these values to provide variability as observed in the lung (a coefficient of variation of 0.1). Compliance of each

acinus was calculated using a relationship between volume and compliance for isotropically expanding units of tissue in the Tawhai et al. (2009) tissue mechanics model. Compliance C, is defined by

$$C = \left[\frac{\xi e^\gamma}{6V_0} \left(\frac{3(3a+b)^2(\lambda^2 - 1)^2}{\lambda^2} + \frac{(3a+b)(\lambda^2 + 1)}{\lambda^4} \right) \right]^{-1}, \quad (5.12)$$

where λ is the (isotropic) stretch, V_0 is the undeformed volume, and $\gamma = \frac{3}{4}(3a+b)(\lambda^2 - 1)^2$. The movement of air into each acinar unit was determined by expansion of the alveolar tissue and airway resistance.

In this model, the flow through the conducting airways was assumed to be Poiseuille with a "correction factor" to account for additional energy losses that occur in branching airways (Pedley et al., 1970). Additional energy losses caused by flow disturbances are created at the airway bifurcations and contribute to the calculation of pressure drop across the junction. A correction term, Z_{Pe} , was used to define the ratio of actual energy dissipation to Poiseuille flow dissipation, then the ratio of actual airway resistance (R_{aw}) to its Poiseuille flow equivalent (R_P) can be calculated by (ignoring kinetic energy changes):

$$Z_{Pe} = \frac{R_{aw}}{R_P} = \frac{K_{Pe}}{4\sqrt{2}} \left(R_e \times \frac{2r}{l} \right)^{0.5}, \quad (5.13)$$

where R_e is the Reynolds number, r and l are the radius and length of the airway, respectively. $R_e = \frac{2Q\rho}{\pi r \mu}$, where ρ and μ are the density ($1.51 \times 10^{-6} g.mm^{-3}$) and viscosity ($1.92 \times 10^{-5} Pa.s$) of air, respectively. K_{Pe} is a constant, set to 1.85. Then, the resistance of each airway branch was calculated as the Poiseuille resistance (R_{aw}) multiplied by the term Z_{Pe} , and the Poiseuille flow through each conducting airway was acquired by the following equation:

$$P_{aw_2} - P_{aw_1} = R_{aw} \dot{V} = Z_{Pe} R_P \dot{V} = Z_{Pe} \frac{8l\mu}{\pi r^4} \dot{V}, \quad (5.14)$$

where P_{aw_1} , P_{aw_2} are the air pressures at the start and end of a branch, and \dot{V} is the air flow through the airway. The air flow into the acinus (modelled as a compliant unit subtending the terminal bronchiole) was determined by an equation of motion that relates airway resistance, air flow, tissue compliance and the rate of change of internal and external pressures:

$$P_{aw} = \frac{V_A}{C_A} + R_{aw} \dot{V} + I \frac{d\dot{V}}{dt} - P_l, \quad (5.15)$$

where P_{aw} , R_{aw} and \dot{V} are the pressure, Poiseuille resistance and flow in the terminal bronchiole, V_A and C_A are the volume and compliance of the acinar unit, I is inertance of the unit, and P_l is an external driving pressure (varied sinusoidally) working to expand the unit and drive air flow through the conducting airways to the terminal units.

Here, we assumed that the rate of change of airflow \dot{V} is small enough, that the term $I \frac{d\dot{V}}{dt}$ in Equation 5.15 can be neglected. A suitable small time interval, $\Delta t = t_n - t_{n-1}$, was defined, and the flow at the end of the time period $\dot{V}_n = \dot{V}(t_n)$ is:

$$\dot{V}_n = C_A(\nu - \beta) + \dot{V}_{n-1} - C_A(\nu - \beta) \exp\left(-\frac{\Delta t}{R_{aw} C_A}\right), \quad (5.16)$$

where $\dot{V}_{n-1} = \dot{V}(t_{n-1})$ is the flow at the end of the previous time period. $\nu = dP_{aw}/dt$, and $\beta = dP_l/dt$ are the change of bronchiole pressure and driving pressure with respect to t , respectively. This equation is derived from Equation 5.15. The detailed description can be found in Swan et al. (2012).

Perfusion model

The pulmonary perfusion model developed by Clark et al. (2011) was used to simulate a time-averaged distribution of blood flow, capillary blood volume and average red blood cell (RBC) transit time for each acinus unit. The full vascular structure (including arteries, veins, intra-acinar arterioles and venules, and capillaries) generated in Section 5.2.3 was the geometric domain for this model. Distension of blood vessels and hydrostatic effects were also included in the model, with arterial and venous diameter and the thickness of the capillary sheet assumed proportional to the transmural pressure (P_{tm}). The intra-acinar (extra-capillary) blood flow was modeled in the symmetric ladder structure introduced previously. The microcirculatory model relates the vessel diameter, length and the thickness of capillary sheet.

Similarly to air flow, the flow through pulmonary arteries and veins was predicted using a Poiseuille equation, with an additional term for gravitational effects acting on blood in the vessels. The relationship is given by

$$\Delta P = P_{b2} - P_{b1} = \frac{128\mu_b L \dot{Q}}{\pi D^4} + \rho_b L g \cos\theta, \quad (5.17)$$

where P_{b1} and P_{b2} are the blood pressures at the beginning and end of the vessel element, μ_b and ρ_b are the viscosity and density of the blood in the vessel, L and D are the vessel length and radius, \dot{Q} is the volumetric flow rate in the vessel, g is the gravitational acceleration ($9.81 m/s^2$), and θ is the angle between the vessel and the direction of gravity.

The term $\rho_b L g \cos\theta$ in Equation 5.17 represents the effect of gravity on blood in the vessels. In the microcirculatory model, an arteriole and venule were joined at each generation by a capillary bed, forming a "ladder-like" structure, to construct the intra-

acinar circulation. Therefore, the term $\rho_b L g \cos\theta$ was considered negligible because the length of acinar arterioles and venules was assumed to be small enough, and

$$\Delta P = \frac{128\mu_b L \dot{Q}}{\pi D^4}. \quad (5.18)$$

The strained diameter D in Equation 5.18 was assumed to have a linear relationship with the transmural pressure P_{tm} as

$$\frac{D}{D_0} = \alpha P_{tm} + 1, \quad (5.19)$$

where D_0 is the unstrained vessel diameter, α is the vessel compliance constant. The relationship between transmural pressure and blood vessel diameter represents the passive response of the pulmonary blood vessels to changes in blood and tethering pressure. It is actually not completely linear. Specifically, it represents the non-linearity in blood vessel wall compliance with a piecewise linear function (it does not increase beyond a maximum transmural pressure of 32cmH₂O). However, at this level, a linear relationship assumption is accurate enough for the modeling procedure. The tethering pressure acting on the blood vessel in the radial direction was assumed to be equal and opposite to the local tissue elastic recoil pressure (P_e), therefore $P_{tm} \approx P_b - P_e$, where P_b is the average blood pressure along the vessel. Then, the blood flow through a capillary sheet (\dot{Q}) was modelled using the classic sheet flow theory developed by Fung and Sobin (1969) as

$$\dot{Q} = \frac{SA}{\mu_c f l_C^2} \int H^3 dP_{tm}, \quad (5.20)$$

where A is the alveolar surface area, S is the proportion of alveolar surface area (A)

composed of capillaries, μ_c is the apparent viscosity of blood in the capillaries, f is the numerical friction factor, l_C is the average path length through the capillary network between arteriole and venule. H is the thickness of the capillary sheet which was assumed to be approximately linearly dependent on P_{tm} similar to Equation 5.19

$$\frac{H}{H_0} = \alpha_C P_{tm} + 1, \quad (5.21)$$

where H_0 is the unstrained sheet thickness. In both Equation 5.19 and Equation 5.21, maximum P_{tm} was assumed to be $32\text{cmH}_2\text{O}(3.1\text{kPa})$. α_C is the compliance of the capillary sheet, which was assumed to reduce linearly with increase of transpulmonary pressure (P_{tp})

$$\alpha_C(P_{tp}) = a + bP_{tp}, \quad (5.22)$$

where a and b are constants, P_{tp} is assumed to be equal and opposite to P_e . The values of a and b were firstly measured for dogs by Glazier et al. (1969), then scaled for human as $a = 0.165\mu\text{m}/\text{cmH}_2\text{O}$, $b = -2.58\mu\text{m}/(\text{cmH}_2\text{O})^2$.

Gas exchange model

The ventilation and perfusion distribution predicted by the ventilation and perfusion models described in the previous section were used as inputs in a whole lung model of gas transport and exchange. The ventilation model provided the volume change in each acinus during inspiration and expiration. The perfusion model determined the acinar capillary blood volume and average RBC transit time. The modelling was based on the assumption that the acinus was well-mixed, and the ventilation and perfusion distributions were time-invariant. Then the rate of O_2 removal from the alveolar air and

the rate of CO_2 transferred to the well-mixed alveolar compartment of the acinus were determined. The steady-state gas transfer model developed by Kapitan and Hempleman (1986) and used by Clark et al. (2014) was used to predict the partial pressure of oxygen in alveolar air ($P_{A_O_2}$) and in arterial blood (P_{aO_2}).

In each gas exchange acinar unit, the steady-state blood and gas compositions are related by conservation of mass. The equilibrium oxygen partial pressure was described through the relationship

$$\dot{V}_I P_{I_{O_2}} - \dot{V}_E P_{A_{O_2}} = k \dot{Q}_C (C_{C_{O_2}} - C_{\bar{V}_{O_2}}), \quad (5.23)$$

where \dot{V}_I is the unit's inspired ventilation (L/min), $P_{I_{O_2}}$ is the oxygen partial pressure (mmHg) of the humidified inspired air, \dot{V}_E is the expired (alveolar) ventilation (L/min), $P_{A_{O_2}}$ is the oxygen partial pressure (mmHg) of the alveolar air, k is a constant that accounts for differences in temperature and pressure between body and the atmosphere as well as allowing consistency between the units of the left and right hand side of Equation 5.23, \dot{Q}_C is the capillary blood flow, $C_{C_{O_2}}$ is the oxygen content in the end-capillary blood (ml gas/100 ml blood), and $C_{\bar{V}_{O_2}}$ is oxygen content entering the lungs from mixed venous blood (ml gas/100 ml blood). The O_2 and CO_2 contents are associated with the corresponding partial pressure of O_2 and CO_2 by the appropriate dissociation curve. The left-hand side of Equation 5.23 represents the volume rate of gas uptake from the compartment by the air, and the right-hand side represents the volume rate of gas uptake from the compartment by the blood. The rates are equal at steady-state.

The non-linear Monod-Wyman-Changeaux model (Monod et al., 1965) is used to solve the relationship between oxygen content and partial pressure. The oxygen content in the end-capillary blood $C_{C_{O_2}}$ in each acinus unit is related to the end-capillary oxygen

partial pressure (P_cO_2) as

$$C_{CO_2} = \frac{15 \times 1.34 \times \rho(P_cO_2) + 0.03 \times P_cO_2}{100}, \quad (5.24)$$

where $\rho(P_cO_2)$ is the oxygen saturation, and it is a function of P_cO_2 . The oxygen binding capacity with haemoglobin is 1.34 mL oxygen per gram of hemoglobin, and around 15 g of hemoglobin per 100 mL of blood. Therefore, the term $15 \times 1.34 \times \rho(P_cO_2)$ expresses oxygen bound to haemoglobin. The term $0.03 \times P_cO_2$ expresses the oxygen dissolved in blood plasma, which gives 0.03 mL of oxygen per 100 mL of whole blood for each mmHg of partial pressure.

The oxygen saturation $\rho(P_cO_2)$ was calculated from Monod-Wyman-Changeaux model (Monod et al., 1965) as

$$\rho(P_cO_2) = \frac{LK_T\sigma P_cO_2(1 + K_T\sigma P_cO_2)^3 + K_R\sigma P_cO_2(1 + K_R\sigma P_cO_2)^3}{L(1 + K_T\sigma P_cO_2)^4 + (1 + K_R\sigma P_cO_2)^4}, \quad (5.25)$$

where K_R (equals to $3.6 \times 10^6 L/mol^{-1}$) and K_T (equals to $10 \times 10^3 L/mol^{-1}$) are the microscopic dissociation constants of a single ligand bound to a stereospecific site, in the two states (R and T), respectively. L (equals to 171.2×10^6) is the equilibrium constant for the state R to T transition, and σ (equals to $1.4 \times 10^{-6} mol \cdot L^{-1} mmHg^{-1}$) is the oxygen solubility.

In this model, it is assumed that the blood stays in the capillaries long enough to achieve equilibrium between the alveolar air and capillary blood, and P_AO_2 can equilibrate with P_cO_2 at the end of each inspiration. Therefore, P_AO_2 and P_cO_2 can be solved from Equation 5.23 using Newton's method. The ventilation-weighted sum of P_AO_2 was calculated as an estimate of expired oxygen partial pressures from the full

lung, and the perfusion-weighted sum of C_cO_2 was used to estimate the P_aO_2 .

The predicted acinus ventilation and perfusion were used as input into the gas exchange model, and carbon dioxide transport was also simulated using the same assumption of equilibration between air and blood similar to the oxygen transfer model (Kapitan and Hempleman, 1986). In each acinus unit, equilibration of carbon dioxide between air side and blood side was represented through a mass balance equation

$$\dot{V}_A P_A CO_2 = k\dot{Q}_C (C_{CO_2} - C_{\bar{V}CO_2}), \quad (5.26)$$

where \dot{V}_A is the expired or alveolar ventilation, C_{CO_2} is the carbon oxygen content in the end-capillary blood, and $C_{\bar{V}CO_2}$ is carbon oxygen content entering the lungs from mixed venous blood. As in the calculation for oxygen exchange, the assumption that transport time is sufficient to equilibrate between blood and air for carbon dioxide exchange was used, so that $P_A CO_2$ can be predicted by solving Equation 5.26. P_cCO_2 in each acinus unit was calculated from C_{CO_2} using Henry's law

$$C_{CO_2} = \frac{M \cdot P_cCO_2}{1 + M \cdot P_cCO_2} (P_cCO_2 - P_vCO_2), \quad (5.27)$$

where M (equals to $23.86 ml \cdot mmHg^{-1}$) is the transfer factor for carbon oxygen across the capillary-alveolar membrane (Chakraborty et al., 2004), and P_vCO_2 is the partial pressure of oxygen in mixed venous blood.

Some parameter values used in the ventilation, perfusion and gas exchange models are listed in Table 5.2. More details of the models are given in Swan and Tawhai (2010), Swan (2010), Clark et al. (2011), and Swan et al. (2012).

Table 5.2: Parameter values and their source used in computational models

Parameter	Description	Value	Source
K_{Pe}	Pedley correction factor	1.85	Pedley et al. (1970)
p	Air density	$1.15 \times 10^{-6} g.mm^3$	Ideal gas law (37C)
μ	Air viscosity	1.92×10^{-6}	Sutherland's formula (37C)
α	Vessel compliance	$1.49 \times 10^{-4} Pa^{-1}$	Krenz and Dawson (2003)
μ_b	Blood viscosity	$3.36 \times 10^{-3} Pa/s$	Pries et al. (1996)
p_b	Blood density	$1.05 \times 10^{-6} kg/mm^3$	Pries et al. (1996)
μ_c	Apparent viscosity of blood in capillary bed	$1.92 \times 10^{-3} Pa/s$	Fung (2013)
f	Numerical friction factor	21.6	Fung (2013)
α_c	Compliance of capillary sheet	$1.30 \times 10^{-9} Pa/s$	Fung and Sabin (1969)
l_c	Pathlength from arteriole to venue	$11.86 \times 10^{-6} m$	Clark et al. (2010)
K_R	microscopic dissociation constant	$3.6 \times 10^6 L/mol^{-1}$	Monod et al. (1965)
K_T	microscopic dissociation constant	$10 \times 10^3 L/mol^{-1}$	Monod et al. (1965)
L	equilibrium constant	171.2×10^6	Monod et al. (1965)
σ	oxygen solubility	$1.4 \times 10^{-6} mol \cdot L^{-1} mmHg^{-1}$	Monod et al. (1965)
M	transfer factor for carbon oxygen across the capillary-alveolar membrane	$23.86 ml \cdot mmHg^{-1}$	Chakraborty et al. (2004)

5.2.5 Modelling lung function

Ventilation, perfusion and gas exchange models were solved under normal conditions (using lung and airway geometry for older normal people) and diseased conditions (using lung and airway geometry of IPF patients). Individual subject tissue classification from CALIPER was projected to the IPF airway/vessel trees as labelled disease regions to drive the patient-specific functional modelling of IPF, with fibrosis reducing tissue compliance and narrowing vessel radius. The subject-specific tidal volume, cardiac output, oxygen consumption (VO_2) and carbon dioxide consumption (VCO_2) were estimated based on the patient's individual information. Data from PFTs (introduced in Section 5.2.1) were used as boundary conditions to control the simulations.

Disease region labelling

The different tissue patterns classified by CALIPER were mapped to the individual airway/vessel trees of each subject. For each airway/vessel terminal node, the corresponding tissue pattern it belonged to (is surrounded by) was extracted through finding the tissue pattern of the closest voxel to the node, so that each terminal node can be indexed to a particular tissue pattern. The percentage distribution of each tissue pattern against gravitational height (cranio-caudal axis) quantified in Chapter 4 was also used in the labelling. If the initial labelled amount of disease nodes was less than the cranio-caudal percentage, additional disease regions were added until the cranio-caudal distribution of disease matched the CALIPER classified data. Figure 5.3 shows the disease labelled airway nodes of one patient diagnosed with IPF. Table 5.3 lists the volume percentage of fibrosis (honeycomb + reticular + ground-glass) and emphysema classified by CALIPER software for each time point of these two patients.

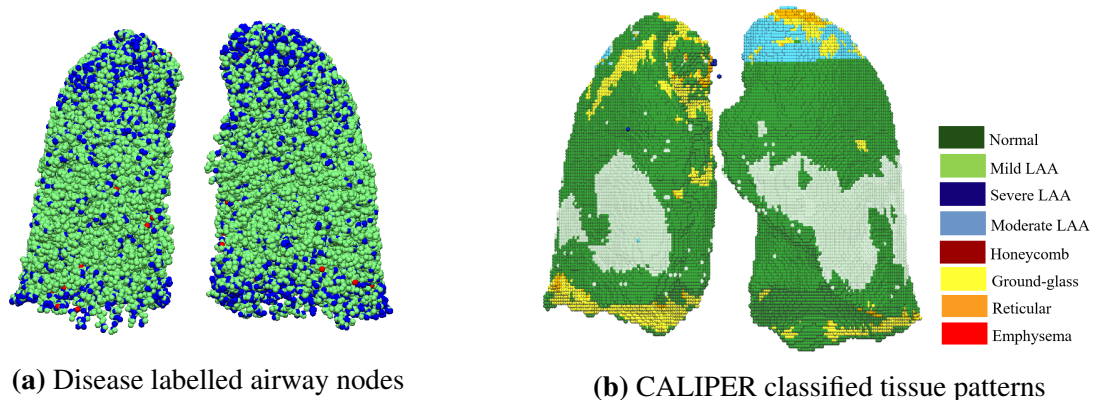


Figure 5.3: Disease labeled airway nodes. For the model in (a), green is classified as normal tissue, blue is fibrosis, and red is emphysema. For the classified data in (b), the colour scheme indicates the tissue classification type

Table 5.3: The volume percentage of CALIPER classified disease tissues for each time point of these two patients (%).

Patient No.	Time point	Honeycomb	Reticular	Ground-glass	Total fibrosis	Emphysema
Patient 1	Time point 1	< 1%	6.78	8.84	15.62	< 1%
	Time point 2	< 1%	4.13	13.62	17.77	< 1%
	Time point 3	< 1%	3.53	13.05	16.60	< 1%
Patient 2	Time point 1	< 1%	1.96	2.42	4.38	< 1%
	Time point 2	< 1%	4.12	8.58	12.72	< 1%

Deep inspiration model

To determine an appropriate total compliance for the IPF model, the model was required to predict the patient's forceful inhalation from FRC to TLC. Inhalation muscle pressure was assumed to be the same in normal and IPF, therefore an appropriate muscle pressure was estimated for the normal model and used in the IPF model. A deep inspiration model was constructed based on the ventilation model (introduced in Section 5.2.4) to simulate a deep inspiration from FRC to TLC. For simulation in the control models, the reference FRC volume (that is the patient-specific predicted normal volume as reference) from PFTs was used as an initial volume to start inspiration, and a subject-specific muscle pressure was solved to drive the lung expansion to the target reference TLC volume (the predicted TLC for the patient). Under the assumption that inspiratory muscle strength does not change with IPF disease (De Troyer and Yernault, 1980), the same driving pressure was used to simulate a deep inspiration in the corresponding IPF model. The IPF models started from their measured FRC. The modelling for IPF patients was divided into two separate stages:

1. The compliance of acini in labelled fibrosis regions (sum of honeycomb, reticular and ground-glass) was reduced to a very low value (less than $0.001 \text{ L/cmH}_2\text{O}$) to represent stiffness due to fibrosis. Then, inspiration was modelled under this initial fibrosis condition.
2. The deep inspiration volume for IPF models acquired in Step 1 was used as the target volume, and the tissue compliance of every acinar unit was scaled down together until the simulated inspiration volume can hit the target, then the corresponding scale factor of total tissue compliance was acquired.

Passive ventilation model

Time-averaged passive ventilation to each acinus over four breathing cycles was predicted using the previously described ventilation model. Acinar volumes in the control and IPF models were initialized to FRC, using the reference normal value and measured disease value, respectively. The scale factor for acinar tissue compliance identified in Step 2 (above) was applied in the simulation for the IPF patient. Patient-specific tidal volume was estimated based on the patient's weight, gender and height (Gilbert et al., 1972; Pelosi et al., 1998).

Perfusion model

The perfusion model introduced in Section 5.2.4 was used to estimate the distribution of blood. The individual age, weight, height and gender were used to predict the cardiac output for each patient (Brandfonbrener et al., 1955; Miyamura and Honda, 1973; Stelfox et al., 2006), and the inlet and outlet pressure were adjusted in order to match the estimated cardiac output. Based on previous observations of reduced perfusion in regions of fibrosis (Crystal et al., 1976; Strickland et al., 1993; Plantier et al., 2018), the blood vessel radius in the fibrosis labelled regions were narrowed for IPF models, so that the blood flow would be reduced to the abnormal tissue.

Gas exchange model

The gas transport and exchange were simulated using the gas exchange model introduced in Section 5.2.4. The ventilation and perfusion distribution predicted by the ventilation and perfusion model were used as inputs in the normal and disease condition. Patient-specific oxygen consumption (VO_2) and carbon dioxide consumption (VCO_2)

were estimated using the following equations (Kwan et al., 2004; Coelho-Ravagnani et al., 2013):

$$VO_2 = P_{VO_2} \times W, \quad (5.28)$$

$$VCO_2 = VO_2 \times 0.8, \quad (5.29)$$

where P_{VO_2} is the oxygen consumption at rest ($P_{VO_2} = 2.84 \pm 0.34 \text{ml/kg}^{-1}/\text{min}^{-1}$ for male and $P_{VO_2} = 2.82 \pm 0.37 \text{ml/kg}^{-1}/\text{min}^{-1}$ for female), and W is the weight of the patient (kg).

Using the patient-specific (or control-specific) tidal volume and dead space, and patient- (or control-) specific distribution of \dot{V} and \dot{Q} , the partial pressure of oxygen in alveolar (P_{AO_2}) and in arterial blood (P_{aO_2}) can be predicted using the Kapitan & Hempleman gas transfer model (Kapitan and Hempleman, 1986).

5.3 Results

5.3.1 Construction of lung lobe geometry

Table 5.4 lists the age, BMI and functional measures used for normal control lung shape prediction for one patient with IPF. The values for FVC, TLC, RV/TLC, and DLCO were predicted reference values from the patient's individual information. Figure 5.4 presents the lung mesh of the IPF patient and its corresponding predicted control lung mesh for the matching normal.

The lobe volume proportions for IPF lung meshes and predicted control meshes are

shown in Table 5.5. As discussed in Chapter 4, Section 4.2.4, the shape change in IPF usually relates to a relatively larger anterior-posterior diameter and smaller height of the lung. The IPF lung has a lower average volume proportion for the left lower lobe and right lower lobe compared with normal older subjects. The results illustrated in Figure 5.4 and Table 5.5 are consistent with these previous findings, with the predicted lung mesh for normal controls showing a "thinner" and "elongated" shape and lower average volume of left and right lower lobes compared with the IPF mesh generated from CT imaging.

Table 5.4: Predicted reference values used as input to predict a shape model for a normal control.

Parameters	Age	BMI	FVC(L)	TLC(L)	RV/TLC	DLCO(mL/mmHg/min)
Values	82	32.77	3.87	7.22	46	25.1

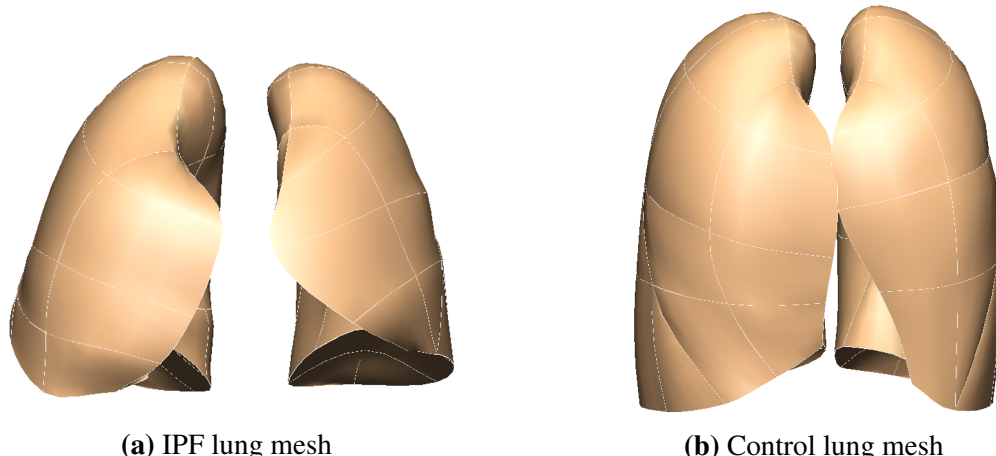


Figure 5.4: Lung mesh for IPF subject and the predicted lung mesh for a normal control with same characteristics. (a) IPF lung mesh generated from CT imaging of a patient with IPF. (b) Control mesh predicted using the reference values for the same patient.

5.3.2 Construction of airway/vasculature geometry

Airway tree

Figure 5.5 illustrates the generated airway trees of one IPF patient and its corresponding predicted airway tree for the control.

Table 5.5: Average lobe volume proportion of IPF lung mesh and predicted control lung mesh.

Patient No.	Time point	LLL		LUL		RLL		RML		RUL	
		Control	IPF								
Patient 1	Time point 1	0.249	0.253	0.222	0.287	0.277	0.214	0.079	0.144	0.173	0.102
	Time point 2	0.248	0.257	0.222	0.287	0.277	0.211	0.079	0.144	0.174	0.102
	Time point 3	0.249	0.265	0.221	0.286	0.278	0.187	0.079	0.143	0.172	0.119
Patient 2	Time point 1	0.231	0.194	0.238	0.287	0.262	0.213	0.081	0.105	0.188	0.201
	Time point 2	0.234	0.186	0.236	0.302	0.265	0.201	0.080	0.112	0.186	0.199
Average		0.242	0.231	0.228	0.290	0.272	0.205	0.078	0.130	0.179	0.144

For Patient 1, the time interval from time point 1 to time point 2 is 12 months, from time point 1 to time point 2 is 11 months, from time point 1 to time point 3 is 23 months. For Patient 2, the time interval from time point 1 to time point 2 is 46 months.

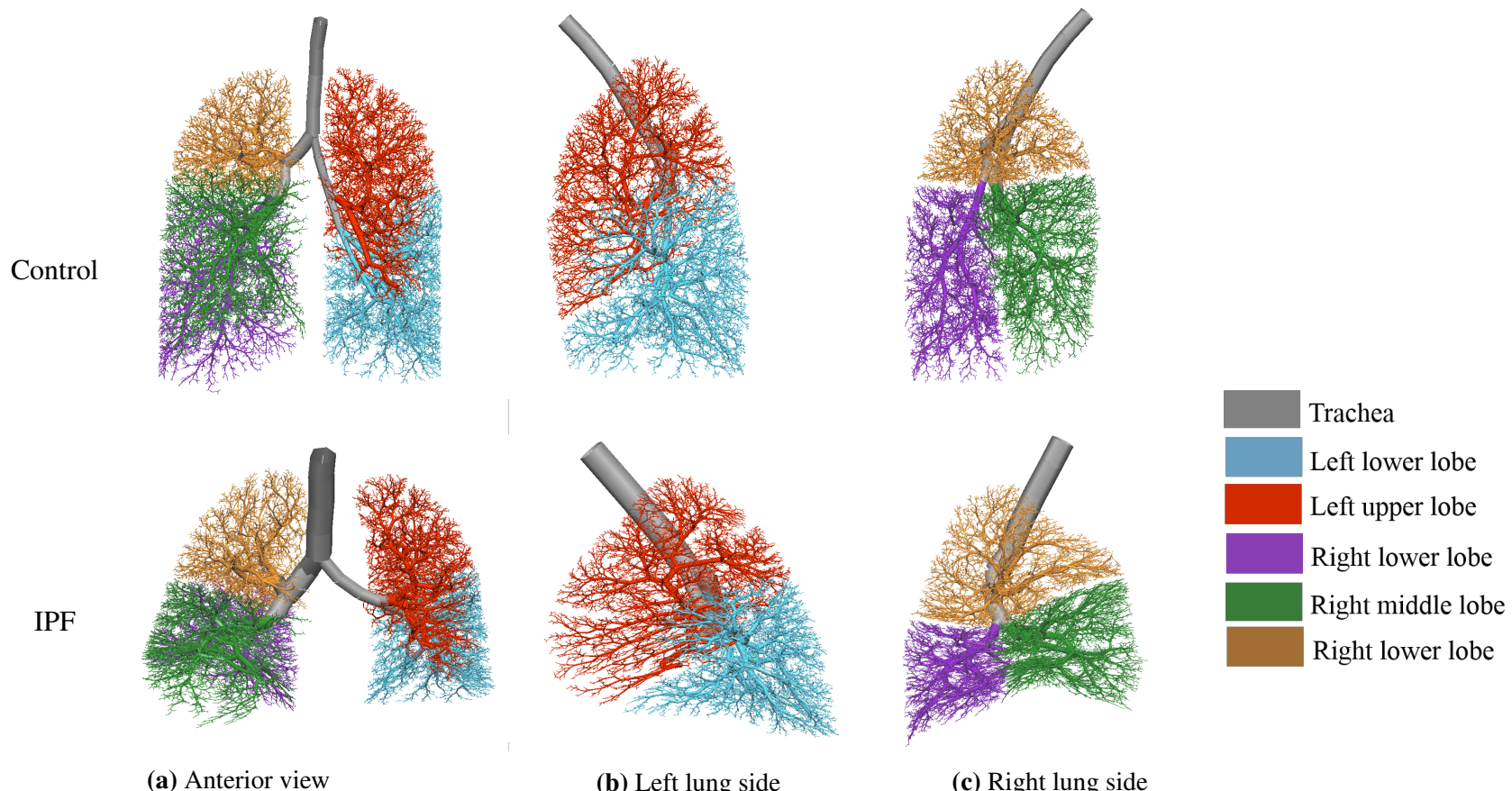


Figure 5.5: Generated normal control airway tree (top row) and IPF airway tree (bottom row) for one patient diagnosed with IPF. (a) Anterior view. (b) Left lung side. (c) Right lung side.

From Figure 5.5, it can be seen that compared with the control airway tree, the IPF airway tree has a larger trachea radius (which is associated with the dilation of the conducting airway in the IPF lung), a relatively smaller lower lobe and a larger anterior-posterior diameter with respect to the cranio-caudal length. These features are consistent with the SSM based analysis result of IPF lung shape in Chapter 4.

Vascular tree

The generated IPF and control artery trees are shown in Figure 5.6. Table 5.6 lists the parameters used for generating the airway tree. Table 5.7 lists the parameters for generating vessel trees.

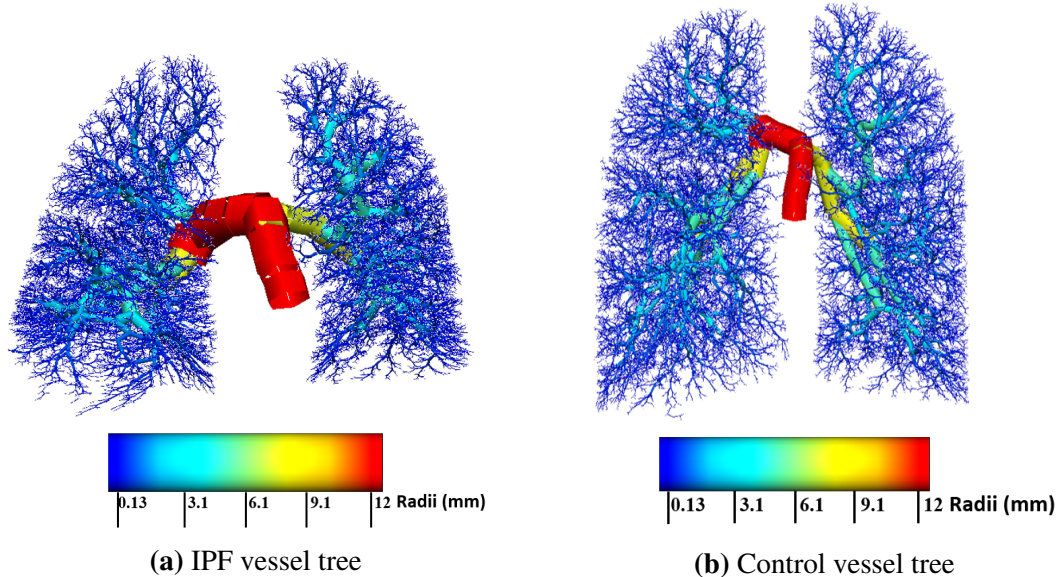


Figure 5.6: Generated geometry of the vessel trees. (a) IPF vessel tree. (b) Control vessel tree. The radius of branches are visualized as shown by the colour bars.

Table 5.6: Parameters of control and IPF airway tree

Patient No.	Time point	Trachea radius (mm)		Horsfield diameter ratio(R_dH)		Terminal radius (mm)		Airway volume (ml)	
		Normal	IPF	Normal	IPF	Normal	IPF	Normal	IPF
Patient 1	Time point 1	6.00	8.81	1.14	1.16	0.20	0.18	76.14	99.80
	Time point 2	6.00	9.82	1.14	1.17	0.20	0.18	75.53	123.87
	Time point 3	6.00	10.03	1.14	1.16	0.20	0.18	74.17	134.84
Patient 2	Time point 1	6.50	9.678	1.14	1.16	0.20	0.18	87.70	110.99
	Time point 2	6.50	8.71	1.14	1.15	0.20	0.18	88.85	111.15

For Patient 1, the time interval from time point 1 to time point 2 is 12 months, from time point 1 to time point 2 is 11 months, from time point 1 to time point 3 is 23 months. For Patient 2, the time interval from time point 1 to time point 2 is 46 months.

Table 5.7: Parameters of control and IPF vessel tree

Patient No.	Time point	Main artery radius (mm)		Artery R_{dS}		Main vein radius (mm)		Vein R_{dS}	
		Normal	IPF	Normal	IPF	Normal	IPF	Normal	IPF
Patient 1	Time point 1	7.69	11.28	1.45	1.51	9.17	14.66	1.48	1.54
	Time point 2	7.69	12.58	1.45	1.52	9.17	16.75	1.48	1.56
	Time point 3	7.69	12.86	1.45	1.52	9.17	17.20	1.48	1.56
Patient 2	Time point 1	8.33	12.40	1.52	1.58	11.18	18.38	1.57	1.65
	Time point 2	8.33	11.16	1.52	1.57	11.18	16.11	1.57	1.63

For Patient 1, the time interval from time point 1 to time point 2 is 12 months, from time point 1 to time point 2 is 11 months, from time point 1 to time point 3 is 23 months. For Patient 2, the time interval from time point 1 to time point 2 is 46 months.

5.3.3 Deep inspiration modelling

Table 5.8 lists the deep inspiration volumes (from FRC to TLC) for the reference values, simulated, and measured values (from the PFT report). In Table 5.8, the simulated inspiration volume (with CT-based abnormality labelling) at all time points for the two patients are higher than the measured values. That is, loss of compliance in the abnormal (fibrosis) regions on the volumetric CT is not sufficient to explain the reduction in inspiration volume from FRC to TLC in the model, except at time point 3 in patient 1.

Table 5.8: Reference normal, simulated and PFT measured inspiration volume (L).

Patient No.	Time point	Ref. normal	Simulated	PFT measured
Patient 1	Time point 1	1.93	1.26	1.16
	Time point 2	1.93	1.27	1.12
	Time point 3	1.84	1.15	1.14
Patient 2	Time point 1	3.4	2.58	2.37
	Time point 2	3.36	2.37	1.93

For Patient 1, the time interval from time point 1 to time point 2 is 12 months, from time point 1 to time point 2 is 11 months, from time point 1 to time point 3 is 23 months. For Patient 2, the time interval from time point 1 to 2 is 46 months.

Additional "fibrosis" was added to the CALIPER classified "normal" tissues until the modelled inspiration volume matched the measured one (as in the last column of Table 5.8). The percentages of CT-based fibrosis (CALIPER classified) and PFT-based fibrosis (CALIPER classified + additional labelled) are listed in Table 5.9.

The respiratory system compliance (including the chest wall compliance in parallel with the lung) and the total lung compliance predicted from control, CT-based and PFT-based models for each time point are presented in Table 5.10. From Table 5.9 and 5.10, the total compliances experience a drop with increasing fibrosis percentage. Total lung compliance decreases to less than half the control value in Patient 1, and about half the control value in Patient 2 in the PFT-based model.

Table 5.9: Percentage of CT-based fibrosis from CALIPER classification and PFT-based fibrosis (CT-based plus additional fibrosis required to limit inspiration from FRC to TLC).

Patient No.	Time point	CT-based fibrosis (%)	PFT-based fibrosis (%)
Patient 1	Time point 1	17.6	23.7
	Time point 2	18.9	28.9
	Time point 3	22.1	22.9
Patient 2	Time point 1	4.3	11.9
	Time point 2	12.5	29.1

For Patient 1, the time interval from time point 1 to time point 2 is 12 months, from time point 1 to time point 2 is 11 months, from time point 1 to time point 3 is 23 months. For Patient 2, the time interval from time point 1 to 2 is 46 months.

5.3.4 Perfusion modelling

Table 5.11 lists the mean pulmonary artery pressure (mPAP), pulmonary vascular resistance (PVR) and pulmonary blood vessel volume (PVV) of control, CT-based and PFT-based models for each time point of these two patients. From the table, the CT-based model has a consistently lower mPAP value compared with the PFT-based model which has more "fibrosis" constriction. That is, there is an increase in mPAP when occluding more small vessels in IPF lungs. For PVV, disease models (both CT-based and PFT-based) have a higher value than the normal control model, but most of the increase in PVV probably comes from the larger pulmonary artery size set for disease vessel models. In spite of this, the PVV of the PFT-based model is also slightly higher compared with the CT-based model. This result is consistent with the observation of Jacob et al. (2016b,a), which indicated that an increase in PVV can be seen in lungs with more advanced fibrosis. Moreover, when comparing PFT and CT models, it can be seen that the former exhibits a larger value of PVR, which leads to a dilation of arteries and an increase in PVV.

Table 5.10: Values of total respiratory system and total lung compliance (L/cmH₂O) of normal control, CT-based and PFT-based modelling results.

Patient No.	Time point	Total respiratory system			Total lung		
		Control	CT-based	PFT-based	Control	CT-based	PFT-based
Patient 1	Time point 1	0.108	0.070	0.064	0.235	0.108	0.094
	Time point 2	0.108	0.070	0.060	0.235	0.108	0.086
	Time point 3	0.106	0.067	0.066	0.226	0.101	0.099
Patient 2	Time point 1	0.120	0.099	0.089	0.300	0.196	0.160
	Time point 2	0.120	0.090	0.069	0.300	0.164	0.105

For Patient 1, the time interval from time point 1 to time point 2 is 12 months, from time point 1 to time point 2 is 11 months, from time point 1 to time point 3 is 23 months. For Patient 2, the time interval from time point 1 to time point 2 is 46 months.

Table 5.11: Values of mPAP (mmHg), PVR (MPa·/mm³) and PVV (ml) of normal control, CT-based and PFT-based modelling results.

Patient No.	Time point	mPAP			PVR			PVV		
		Control	CT-based	PFT-based	Control	CT-based	PFT-based	Control	CT-based	PFT-based
Patient 1	Time point 1	14.46	14.68	14.93	15.91	16.59	17.31	260.16	410.43	411.30
	Time point 2	14.51	14.54	14.92	15.23	15.36	16.48	260.99	550.82	552.57
	Time point 3	14.66	14.43	14.47	17.90	17.40	17.52	272.38	583.91	584.11
Patient 2	Time point 1	14.96	14.59	14.93	12.97	12.35	12.92	509.49	886.57	889.38
	Time point 2	14.66	15.10	16.02	12.64	13.36	14.88	515.30	798.78	804.67

For Patient 1, the time interval from time point 1 to time point 2 is 12 months, from time point 1 to time point 2 is 11 months, from time point 1 to time point 3 is 23 months. For Patient 2, the time interval from time point 1 to time point 2 is 46 months.

5.3.5 Gas exchange model

Figure 5.7 illustrates the distribution of control, CT-based and PFT-based simulated V/Q ratio and arterial oxygen at one time point for one IPF patient. The figures are shown with V/Q plotted on a logarithmic scale, which is consistent with the presentation of V/Q measurements using the multiple inert gas elimination technique (MIGET). From the results, the simulation for the control model (the first row) predicts a normal V/Q ratio distribution with PaO_2 of 89.33 mmHg; this slightly low PaO_2 is typical for the normal older adult (Wahba, 1983; Sprung et al., 2006). In the control model, most of the alveoli are in the $P_a\text{O}_2$ range of 80-100 mmHg. The model labelled with CT-based fibrosis predicts a characteristic (for IPF) bimodal V/Q distribution (the second row), and PaO_2 considerably decreased (71.63 mmHg) from the control. The higher proportion of alveoli appears at high $P_a\text{O}_2$ because of the high \dot{V} compared with \dot{Q} . It can be observed that about 10% of alveoli have $P_c\text{O}_2$ lower than 63 mmHg which has a net effect of the reduction in total $P_a\text{O}_2$. Also, in the CT-based model, there are more low $P_c\text{O}_2$ acinus units with relatively high perfusion. A slight shift to the left hand side is observed for the highest peak of the V/Q ratio curve compared with the control model. The smaller peak of the V/Q ratio appears around $\text{V}/\text{Q} = 5$ (larger than 1), as there is a decrease in perfusion in fibrotic regions due to the narrowed vessel radius. The model with additional fibrosis (with appropriate patient-specific inspiration from FRC to TLC) predicts further decrease in PaO_2 to 67.85 mmHg. There is an increase in the proportion of well-perfused but less ventilated units, which leads to more alveoli at low $P_c\text{O}_2$. Meanwhile, the proportion of ventilation also increases at very high $P_c\text{O}_2$ units in the PFT-based model compared with the other two models.

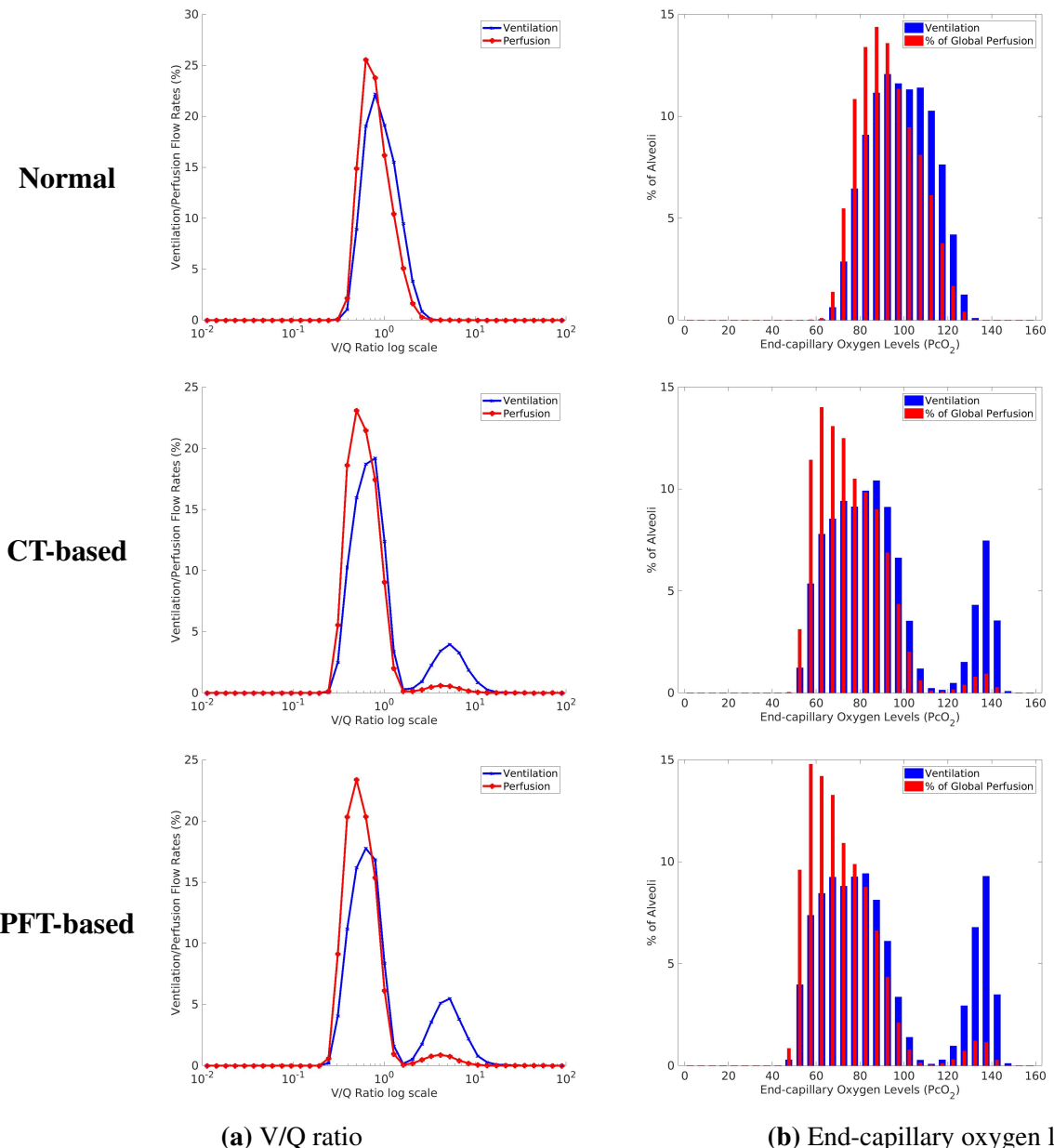


Figure 5.7: V/Q ratio distribution and end-capillary oxygen distribution of control, CT-based and PFT-based simulation result at one time point for one patient diagnosed with IPF). (a) V and Q with respect to V/Q ratio. (b) Distribution of end-capillary oxygen levels amongst alveoli.

Figure 5.8 shows the \dot{V} , \dot{Q} and V/Q ratio distributions against lung height (cranio-caudal axis) simulated in the control, CT-based and PFT-based models. For the upright models, \dot{V} is higher in the lung base than apex (Figure 5.8a). The main difference between the control and fibrosis models is a left-wards shift of the \dot{V} curves because of lower total ventilation. The CT- and PFT-based models have very similar \dot{V} . Differences in \dot{Q} are mainly in the basal part of the lung, where more fibrosis appears in the fibrosis models. The two fibrosis models have much higher variability of \dot{Q} within iso-gravitational slices (the error bars in Figure 5.8a and 5.8b) than the control model, particularly in the basal region. For the control model simulation, V/Q ratio is ~ 1 , with a slight increase moving apically.

The measured DLCO values for each time point of these two patients, and the values of PaO_2 and PaCO_2 for control, CT-based and PFT-based models for each time point are listed in Table 5.12. For CT-based and PFT-based simulation, PaO_2 experiences an overall decrease over time for both of these two patients, corresponding to the gradual increase of fibrosis. The reduction of PaO_2 and $P(A - a)\text{O}_2$ predicted by the PFT-based model follows the reduction in measured DLCO (and $P(A - a)\text{O}_2$, which has an opposite trend), with the first patient decreasing from time point 1 to time point 2 but slightly increasing from time point 2 to time point 3, and the second patient decreasing from time point 1 to time point 2. MIGET plots of V/Q ratio and arterial oxygen distribution, plots of cranio-caudal distribution of V, Q and V/Q ratio for other subjects and time points can be found in Appendix C.

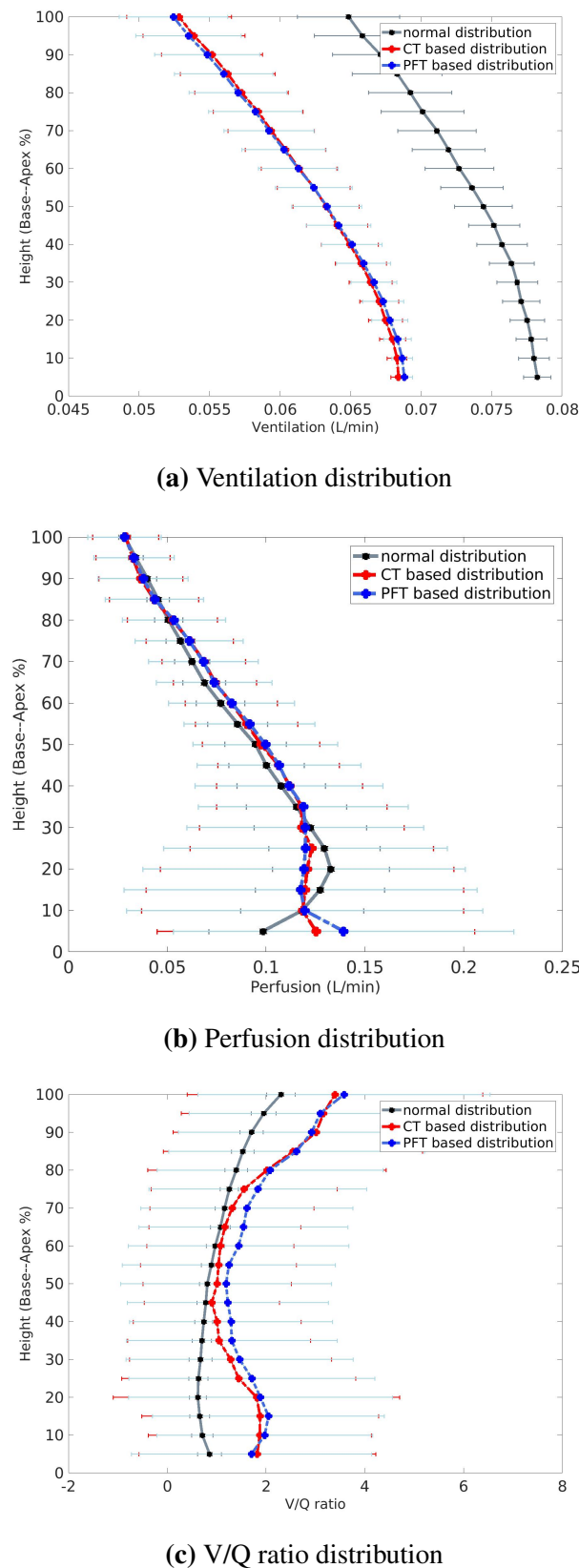


Figure 5.8: Ventilation, perfusion and V/Q ratio distribution against lung height (cranio-caudal axis). (a) Ventilation distribution against lung height. (b) Perfusion distribution against lung height. (c) V/Q ratio distribution against lung height.

Table 5.12: Measured DLCO (mL/mmHg/min) for each time point, and values of PaO₂ (mmHg), PaCO₂ (mmHg) and P(A – a)O₂ (mmHg) of normal control, CT-based and PFT-based modelling results.

Patient No.	Time point	DLCO	PaO ₂			PaCO ₂			P(A – a)O ₂		
			Control	CT-based	PFT-based	Control	CT-based	PFT-based	Control	CT-based	PFT-based
Patient 1	Time point 1	11.8	89.33	71.63	67.85	41.87	52.73	53.97	8.59	17.09	20.79
	Time point 2	9.8	95.37	64.56	58.72	37.81	57.48	59.58	7.69	18.13	23.87
	Time point 3	10.12	87.92	60.43	60.00	42.76	59.83	59.97	9.01	20.85	21.29
Patient 2	Time point 1	16.20	92.31	88.52	85.13	39.80	41.74	42.86	9.90	10.06	13.35
	Time point 2	14.50	91.72	83.70	75.35	39.09	43.77	46.76	9.75	14.29	22.94

For Patient 1, the time interval from time point 1 to time point 2 is 12 months, from time point 1 to time point 3 is 11 months, from time point 1 to time point 3 is 23 months. For Patient 2, the time interval from time point 1 to time point 2 is 46 months.

5.4 Discussion

This chapter sets out to determine whether, based on structural parameters, one can use computational models to predict function in the normal older lung, and in individuals with characteristics of IPF lung disease. The models that have been applied in this chapter demonstrate a good prediction of function in the normal older lung, as has been previously assessed in younger adults (Tawhai et al., 2004; Swan et al., 2012; Clark et al., 2011). In the IPF case, model predictions suggest that there must be disease present that is radiologically silent, as mapping disease labelled regions directly to models of lung expansion shows that, in the subjects assessed, the lung of patients is consistently less compliant than the simulated lung. For gas exchange, the IPF models (based on degradation in structure) give reasonable reductions in gas exchange function, solely through V/Q disturbances.

SSM based lung shape prediction provides a way to compare lung function of IPF patient with older normal people

An SSM was used to make a prediction of older normal lung shape for each patient. The SSM based lung shape prediction provides a way to make a comparison of the lung function between a patient-specific lung and its corresponding normal equivalent. The patient-specific shape prediction was achieved based on the patient's individual information which shows significant correlations with older normal lung shape, therefore the estimated lung shape is able to represent the statistical lung shape of older normal people as a control group. Through modelling the airway/vessel tree and lung function with the predicted normal lung mesh, it is possible to quantitatively describe the change of respiratory geometry in IPF lung, the decline of lung function, the severity of dis-

ease and the prediction of progression. This could be a promising direction for clinical applications in the future.

Volumetric CT imaging may not provide sufficient information to explain the stiffness of the IPF lung

The computational modelling in this chapter suggests that radiologically-identified tissue abnormalities from volumetric CT imaging may be not sufficient to explain the increase in lung stiffness and the decline of lung function in IPF patients. Under the assumption that inspiratory muscle pressure does not change in IPF, ascribing only "abnormal" tissue to be highly stiffened could not fully explain the reduction in TLC-FRC volume. Additional tissue (up to 10% in patient 1 and 17% in patient 2) was required to be stiffened to achieve a correct prediction of volume change from FRC to TLC. The proportion of fibrosis increased in both patients over time, and the additional fibrosis in the PFT model increased this further except for time point 3 in patient 1, where no "additional" fibrosis was needed. Total respiratory system compliance was about 30-40% lower in the IPF models compared with their controls. All models assumed a chest wall compliance of $0.2\text{L}/\text{cm} \cdot \text{H}_2\text{O}$. Total lung compliance in the control models was higher than the $0.2\text{L}/\text{cm} \cdot \text{H}_2\text{O}$ expected for the young adult lung, reflecting the higher tissue compliance for these older subjects. Total lung compliance in the two patient models was about half of "normal", with the PFT-based models up to 35% lower compliance than the CT-based models. The method used here to parameterise the compliance of the tissue units assumes that the IPF subject can generate the same driving pressure for inspiration as the control. While the literature suggests that muscle pressure does not change in IPF (De Troyer and Yernault, 1980), it is possible that the change in lung and chest wall geometry reduces the transfer of the driving pressure to the lung. Regardless,

it is reasonable to expect that tissue with normal appearance on CT has already **under-gone** remodelling that affects its function. Extension of this method and validation in a larger number of subjects could provide an estimate of the proportion of visually normal but functionally abnormal tissue.

V/Q mismatch (impaired gas exchange) is present in CT-based abnormal tissue as well as in regions that are classified as 'normal'. Additional V/Q mismatch emerges in the PFT-based model due to tissue unit stiffening and artery constriction, which results in a reduction in P_aO_2 and increase in P_aCO_2 . Blood gas data was not available for any subjects in this thesis to compare with the model predictions; however, DLCO reduced over time and was consistent with the model's prediction of gas exchange impairment. Several potential mechanisms have been proposed important in the development of hypoxaemia in IPF: gas exchange barrier thickening, anatomical shunts, and V/Q mismatch. Results from this study suggests that V/Q mismatch in regions of radiologically-identified tissue abnormality (plus additional regions in the PFT-based model) is sufficient to predict a major reduction in P_aO_2 . Gas exchange barrier thickening could have an additional effect, however Swan (2010) showed that gas exchange was more sensitive to changes in tissue elasticity than barrier thickness.

The predicted ventilation, perfusion and gas exchange distribution can be explained by the background knowledge of IPF

The physiological alterations in IPF (discussed in Chapter 2, Section 2.6.1) are supportive of the modelling results. First, it has been found that IPF disease often results in reduction in total lung compliance (an increase in lung tissue stiffness), and the alterations of total lung compliance in IPF patients appear to be strongly correlated with the degree of lung fibrosis (Fulmer et al., 1979; Plantier et al., 2018). As should be expected,

the total compliance predicted by the ventilation (deep inspiration) model (Table 5.9 and 5.10) decreases with more fibrosis added into the model lung tissues. Second, although the fibrotic tissue is associated with a reduced number of blood vessels (Cosgrove et al., 2004; Ebina et al., 2004), Jacob et al. (2016b,a) has demonstrated that pulmonary vessel volume (PVV) increases with fibrosis, and can be used as an independent predictor of mortality. Similarly, the predicted PVV in the PFT-based model is higher than the CT-based model, despite having additional vessel occlusions. The larger PVR in the PFT-based model results in slightly higher mPAP which distends the arteries and increases PVV. It should be noted that the assumed tissue tethering pressure (from tissue to blood vessels) was the same in both models. If this were increased in the PFT-based model, it would further increase PVV. In addition, in the perfusion model, the predicted PVV of disease models are higher than the normal control model, but this might be caused by the larger vessel radius assigned to the disease vessel geometry. Third, the predicted P_aO_2 (which decreases in IPF lung model) and $P_{A-a}O_2$ (increases in the IPF lung model) from the gas exchange model presents a consistent trend with the change of measured DLCO (from PFTs) over time. DLCO is an important index to measure the gas exchange function of the lung, therefore while the simulated P_aO_2 and $P_{A-a}O_2$ cannot be compared directly against data for these subjects, it is reassuring that the model gas exchange follows the DLCO trend. Collection of blood gas data is not standard during lung function testing, whereas measurement of DLCO is. It would therefore be appropriate in future studies to model DLCO (as a surrogate of gas exchange) and compare directly against data. The preliminary outcomes of the modelling framework demonstrated in this chapter suggest that a model-based approach that combines simulation of abnormal mechanics (from FRC to TLC) and gas exchange could be used to estimate the amount of abnormally-functioning lung tissue that appears radiologically

normal.

Limitations of modelling procedure

There are some limitations of the modelling procedure introduced in this chapter. First, in the IPF lung, there is a dilation in trachea, but a constriction in small airway. In this chapter, the trachea radius of normal lung was scaled from the trachea radius of the IPF lung using a statistically measured ratio which represents the conducting airway volume difference between normal and IPF. The main limitation of this method is that the measured ratio may be not accurate enough for all the subjects even though the standard deviation has been taken into consideration here. A potential approach in future work could be to use the change of dead space to tidal volume ratio in IPF lung in the construction of the airway geometry.

Second, regions of tissue classified as emphysema or low attenuation area (LAA) were not taken into consideration in this model. Although emphysema classified by CAPLIPER only covers a small proportion of the lung (usually less than 1%), it is believed to have an impact on the deterioration of lung function together with fibrosis in IPF (Cottin et al., 2005; King Jr et al., 2011; Lin and Jiang, 2015). LAA (mild, moderate and severe) can account for a sizable proportion of the lung; both emphysema and LAA are associated with air trapping at the end of inspiration (Slebos et al., 2015; Hoesein and De Jong, 2017), which will influence the lung volume at FRC and the change of tissue compliance during breathing. Therefore emphysema and LAA should be accounted for in future extensions of this work.

Third, for some end-stage subjects with a large proportion of fibrotic lesion and a small constricted FRC volume, a larger driving pressure may be needed to drive the expansion of the stiffer lung to TLC, because the deep inspiration volume won't be

estimated accurately with a "normal" driving pressure. For future studies, this could require explicitly modelling the chest wall in normal and IPF subjects, to understand how chest wall shape change affects chest wall mechanics and the pressures developed during deep inspiration.

5.5 Summary

In this chapter, a preliminary patient-specific computational modelling method was developed to investigate the association between lung structure and lung function in IPF patients. In order to make a comparison between IPF patients and older normal people, an SSM was used to make a prediction of the lung shape of an equivalent older normal for each patient, and the V/Q distribution and gas exchange were then simulated in normal and IPF conditions, respectively, with CALIPER tissue classification data and PFT data as input. The results show that the computational model can predict a reasonable level of abnormality in ventilation, perfusion and gas exchange in the IPF lung, and suggests a predictable difference of lung function between IPF and older normal people based on lung structure. Moreover, the model results suggest tissue based abnormalities do not fully explain the change in lung function in IPF. These preliminary results suggests that a model-based approach could be developed to estimate the amount of "normal" appearing tissue with abnormal function, by considering both lung mechanics (expansion from FRC to TLC) and gas exchange.

Chapter 6

Conclusion

This thesis aimed to develop a consistent method with which to integrate volumetric CT data, quantitative analysis, pulmonary function test data and computational modelling to investigate structure-function relationships in IPF. This chapter provides a summary of the important outcomes of the research, how the thesis addressed the objectives set out in Chapter 1, Section 1.2, and makes some suggestions for future work.

6.1 Thesis Summary

Objective 1: *Develop an automatic lung lobe segmentation method based on HRCT images that can consistently estimate lobar boundaries even if the boundary is not clear along its entire length. The method needs to be tested on both healthy subjects and IPF subjects. Ideally the algorithm will be automatic , or semi-automatic.*

A PCA-based statistical shape model guided method was developed to segment pulmonary lobes from HRCT images in Chapter 3. The method was tested on 20 inspi-

ratory and expiratory CT scans: 10 healthy young subjects and 10 older subjects diagnosed with IPF. Results show that the method can perform well to detect the location of the fissures over most of the fissure surfaces on CT images from normal subjects, and provides a relatively accurate result (compared with some existing tools) for IPF (abnormal) subjects although manual interaction is still needed for a few subjects. The method provided a more accurate result on the left oblique fissure than the other two fissures, because the left lung has a simpler anatomic structure with only one fissure. The ability of the method to provide an initial estimate of the fissure locations was compared with two other segmentation softwares which use watershed-based (anatomical knowledge-based) methods. The two segmentation softwares PASS and PTK were unable to segment 9/20 and 7/20 subjects respectively. In contrast, our model-based method can estimate the fissure location for all subjects at all volumes. Although PASS can provide a more accurate segmentation for some young healthy subjects, the new method was on average as accurate as PASS, and more accurate than PTK. This new procedure does not depend on prior segmentation of anatomical structures (airway lobar classification) and has promising potential as a clinically useful semi-automatic lobe segmentation procedure.

Objective 2: *Classify and quantify tissue abnormalities from HRCT scans of IPF lungs. Analyse the density, volume, spatial distribution, and their change over time.*

The tissue abnormalities of IPF lungs were classified and analysed at several time points using quantitative methods based on HRCT imaging in Chapter 4. Tissue regions of HRCT images were classified using CALIPER software. The classified data was mapped to a statistical shape model, and quantitative approaches were used to analyse tissue density, tissue volume, the spatial distribution of abnormalities, and regional

changes in tissue over time. Spatial distribution of tissue abnormalities was quantitatively described in apical-basal, anterior-posterior, internally-to-externally, and by lobe. The distributions of fibrosis were generally consistent between subjects and did not change over time (although the amount of fibrosis increased somewhat).

Objective 3: *Quantify the difference of lung shape between IPF and older normal lungs, and explore the correlation of lung shape change in IPF with the extent of fibrosis.*

In Chapter 4, the geometric mesh of IPF lung and lobes were compared with a statistical shape model of old normal to quantify the lung lobe shape difference between IPF patients and healthy subjects aged > 50 years, and the impact of fibrosis extent on lung shape variation was also investigated. It was found that the first shape mode of the SSM (based on PCA) is significantly different between IPF subjects and normal subjects and strongly correlates with the percentage of fibrosis. The first shape mode corresponds mainly to the anteroposterior diameter of the lung. While there is a difference in the shape of the IPF lung compared with normal, the shape does not appear to change with progression of the disease.

Objective 4: *Integrate the image-based tissue quantification, pulmonary function tests and computational modelling to simulate lung function in IPF, and compare with simulated lung function in older normal people, and use these tools to estimate the impact of radiological features of IPF on lung function.*

In Chapter 5, a multiple time point patient-specific computational modelling method was developed using CT and PFT data as input to investigate the lung geometry and lung function in two IPF patients. The simulated V/Q distribution and gas exchange, as a result of abnormal tissue function, were compared between IPF patients and normal

"control" models. Compared with the control models, the IPF models had a lower PaO₂ and increased V/Q mismatch. V/Q mismatch and decrease in PaO₂ increased for successive imaging time points. The modelling results suggest that the abnormalities on volumetric CT imaging are not sufficient to explain the decline of lung function (decrease in tissue compliance) in IPF patients, and the impaired gas exchange (V/Q mismatch) will appear in not only abnormal regions but also in CT-classified 'normal' tissues. The results also suggest that V/Q mismatch as a direct result of abnormally stiff and underperfused tissue results in progressive worsening of gas exchange that mirrors the decline in DLCO. That is, thickening of the gas exchange barrier or increase in anatomical shunts are not necessary to explain gas exchange abnormality in IPF.

6.2 Future directions

6.2.1 Improvement of the statistical shape model

The SSM used in this thesis was generated using 35 healthy subjects aged > 50 years. In order to capture more kinds of components of shape variation, a larger number of subjects with a wider range of age should be added into the SSM in the future work. With adding more subjects, it could be possible to generate a more sophisticated model describing a continuous shape variation with age, which may increase the accuracy for estimating the initial fissure locations. Furthermore, the construction of an SSM of the IPF lung could also be taken into consideration for future work. In Chapter 4, it was shown that there is a significant shape difference between IPF and older normal lungs. Therefore, a SSM specific to IPF patients may provide a better way to identify shape features of IPF patients, and would be able to provide a better fissure estimation for IPF

subjects and further help with statistical analysis of IPF lung function.

6.2.2 Involvement of diffusing capacity for carbon monoxide in the lung functional model

It has been found that DLCO is reduced in 98% of IPF patients at the initial diagnosis (Cortes-Telles et al., 2014), and some studies indicate that the impairment of diffusion capacity is one cause of chronic arterial hypoxaemia in IPF (Plantier et al., 2018). DLCO is an important measurement in the PFT report that can help clinicians to make a diagnosis of IPF, thus could be used as a bio-marker in our computational modelling of the IPF lung function in future work. The value of DLCO is determined by the structural and functional properties of the lung (Graham et al., 2017). The structural properties includes lung gas volume, thickness and area of the alveolar capillary membrane, and the volume of haemoglobin in capillaries. The functional properties are mainly related to absolute levels of ventilation and perfusion, the uniformity of the distribution of ventilation relative to the distribution of perfusion, and the concentration and binding properties of haemoglobin in the alveolar capillaries (Graham et al., 2017). In the IPF lung, there will be a reduction in the surface area for diffusion, and an increase in the thickness of the alveolar capillary membrane due to fibrosis. Therefore, through developing a DLCO calculation component in the model, the patient-specific properties of the alveolar capillary membrane could be parameterized for fibrosis and emphysema areas by fitting to the measured DLCO.

Appendices

Appendix A

Mapped classification data for each patient

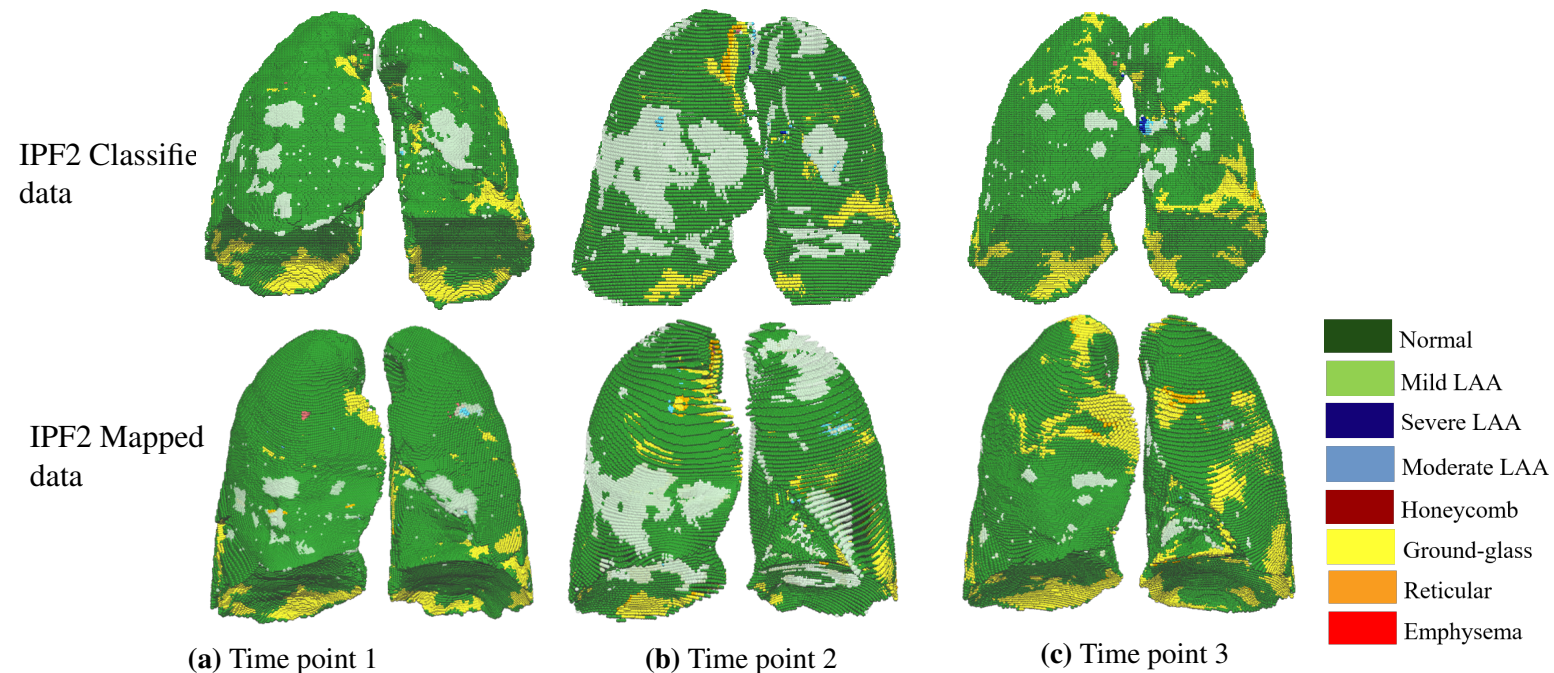


Figure A.1: Classified data (top row) and mapped data (bottom row) of three time points of case IPF2. (a) The first time point, scan time: 0 month. (b) The second time point, scan time: 15 months. (c) The third time point, scan time: 35 months.

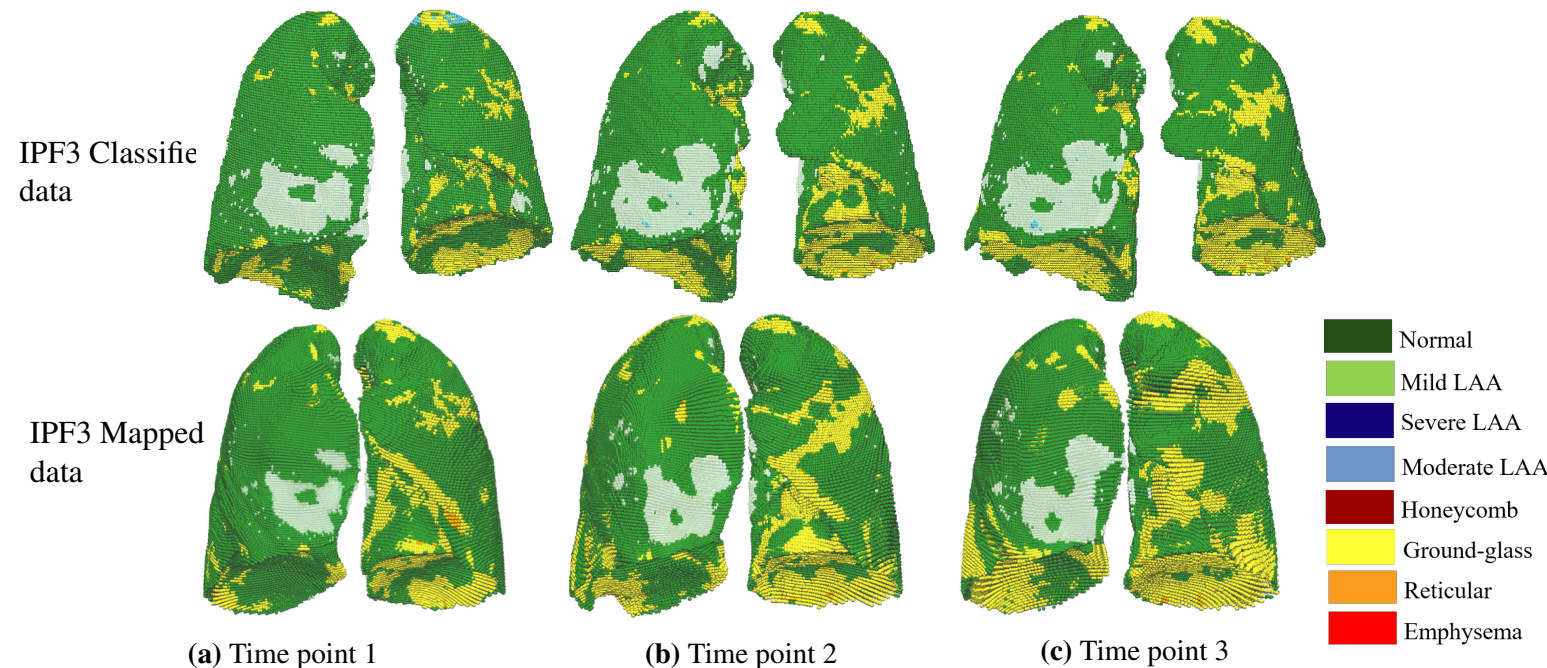


Figure A.2: Classified data (top row) and mapped data (bottom row) of three time points of case IPF3. (a) The first time point, scan time: 0 month. (b) The second time point, scan time: 11 months. (c) The third time point, scan time: 30 months.

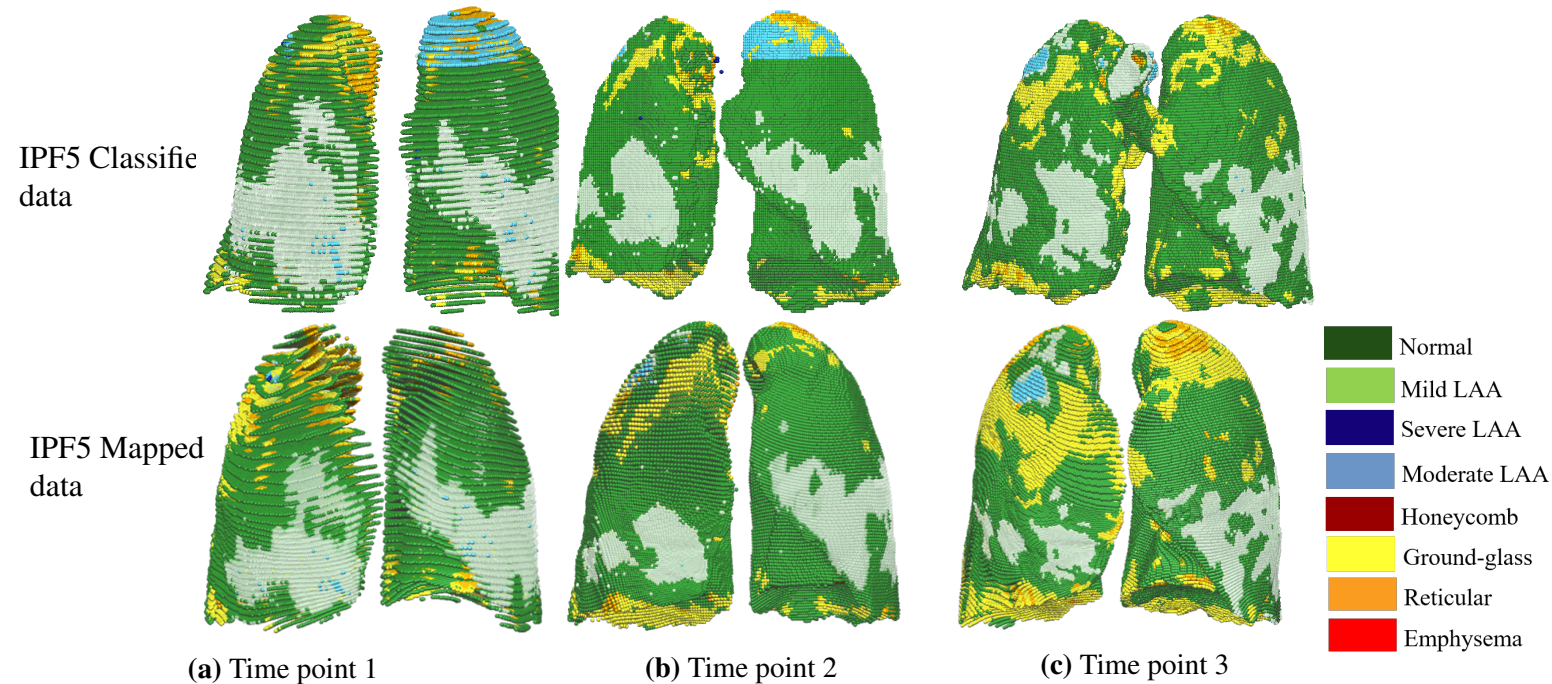


Figure A.3: Classified data (top row) and mapped data (bottom row) of three time points of case IPF5. (a) The first time point, scan time: 0 month. (b) The second time point, scan time: 12 months. (c) The third time point, scan time: 23 months.

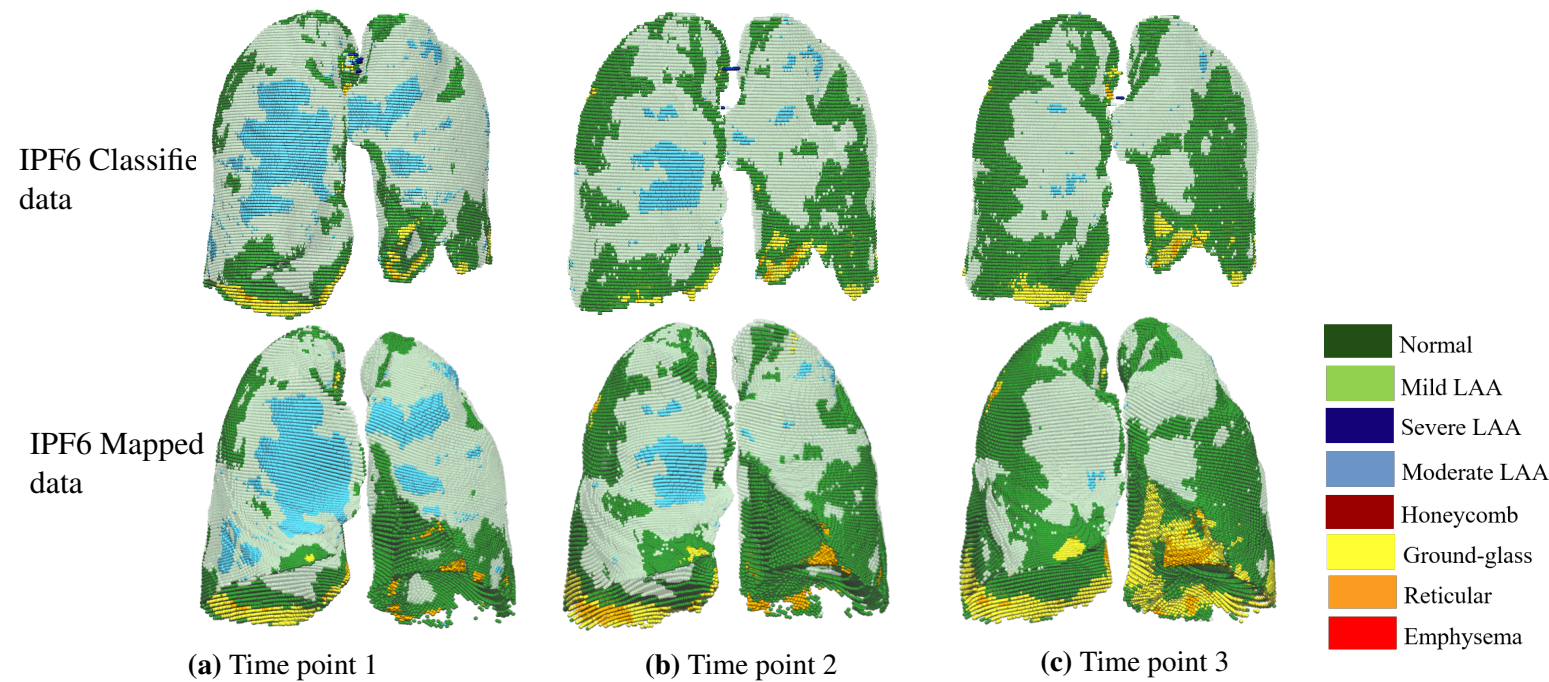


Figure A.4: Classified data (top row) and mapped data (bottom row) of three time points of case IPF6. (a) The first time point, scan time: 0 month. (b) The second time point, scan time: 15 months. (c) The third time point, scan time: 20 months.

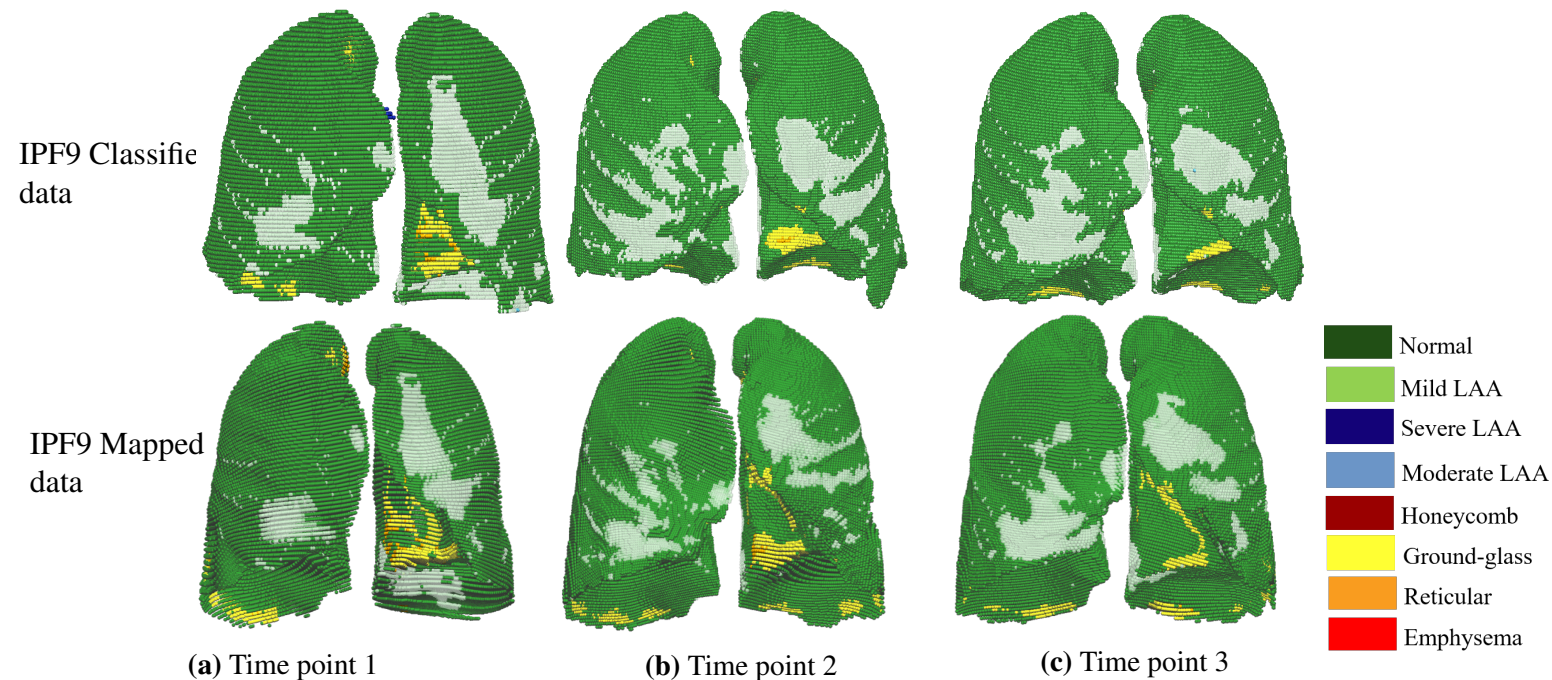


Figure A.5: Classified data (top row) and mapped data (bottom row) of three time points of case IPF9. (a) The first time point, scan time: 0 month. (b) The second time point, scan time: 6 months. (c) The third time point, scan time: 19 months.

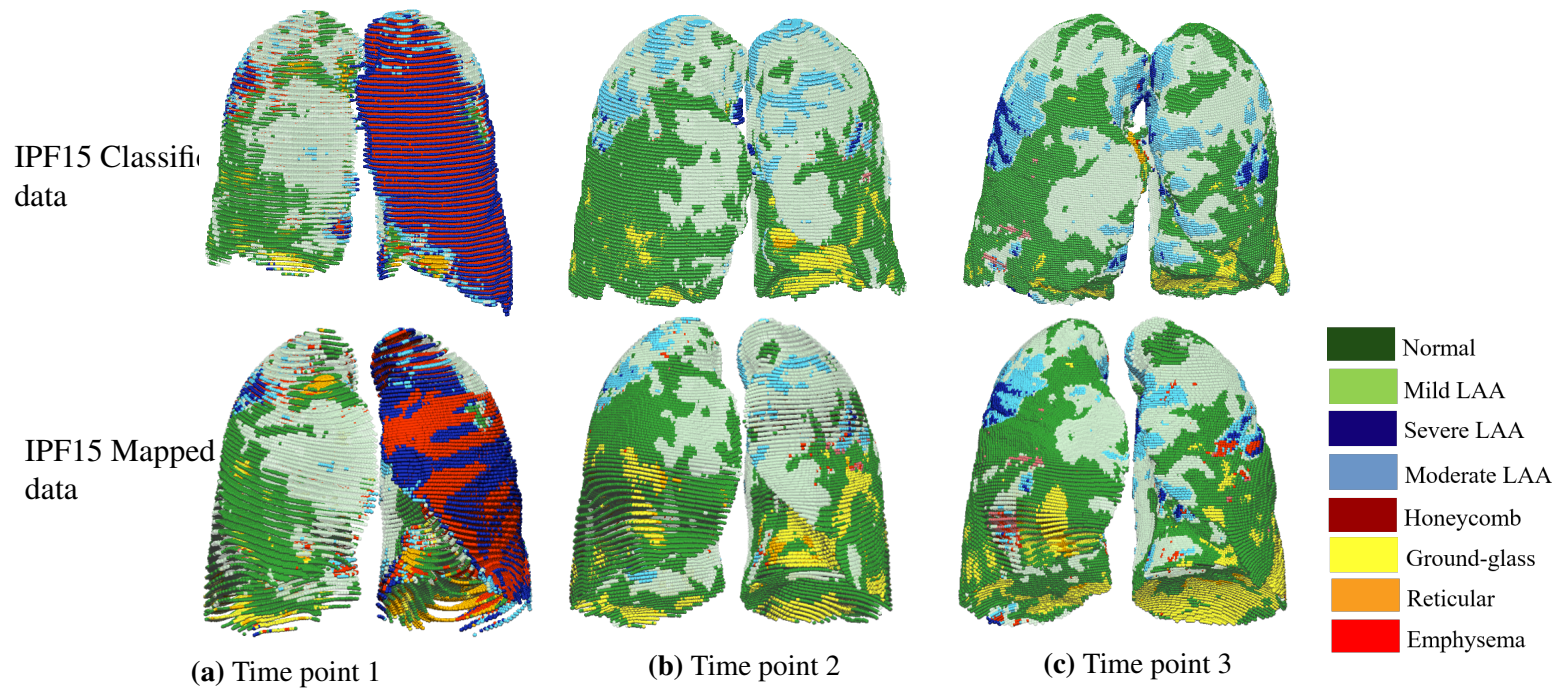


Figure A.6: Classified data (top row) and mapped data (bottom row) of three time points of case IPF15. (a) The first time point, scan time: 0 month. (b) The second time point, scan time: 13 months. (c) The third time point, scan time: 76 months.

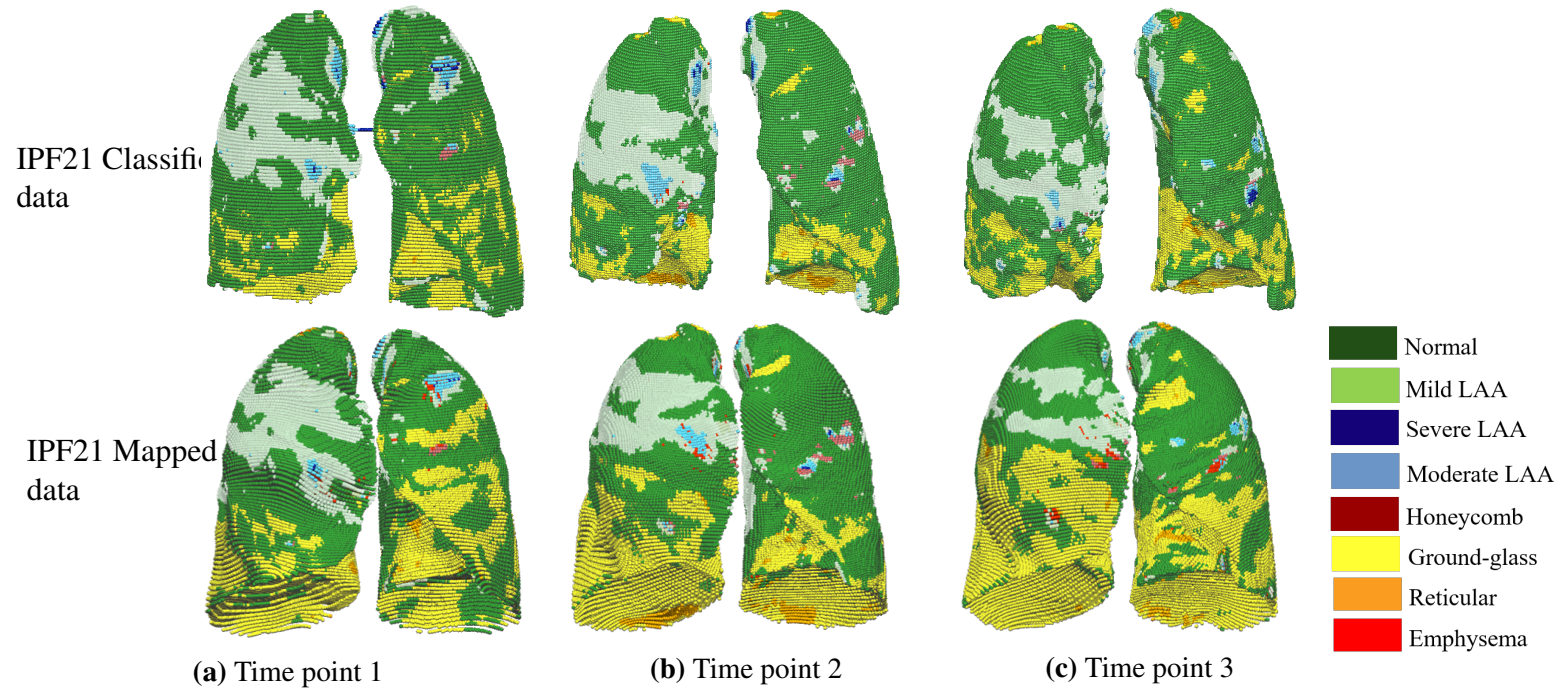


Figure A.7: Classified data (top row) and mapped data (bottom row) of three time points of case IPF21. (a) The first time point, scan time: 0 month. (b) The second time point, scan time: 63 months. (c) The third time point, scan time: 79 months.

Appendix B

Spatial distribution of abnormalities for each patient

B.1 Basal-to-apical distribution over time for each pa- tient

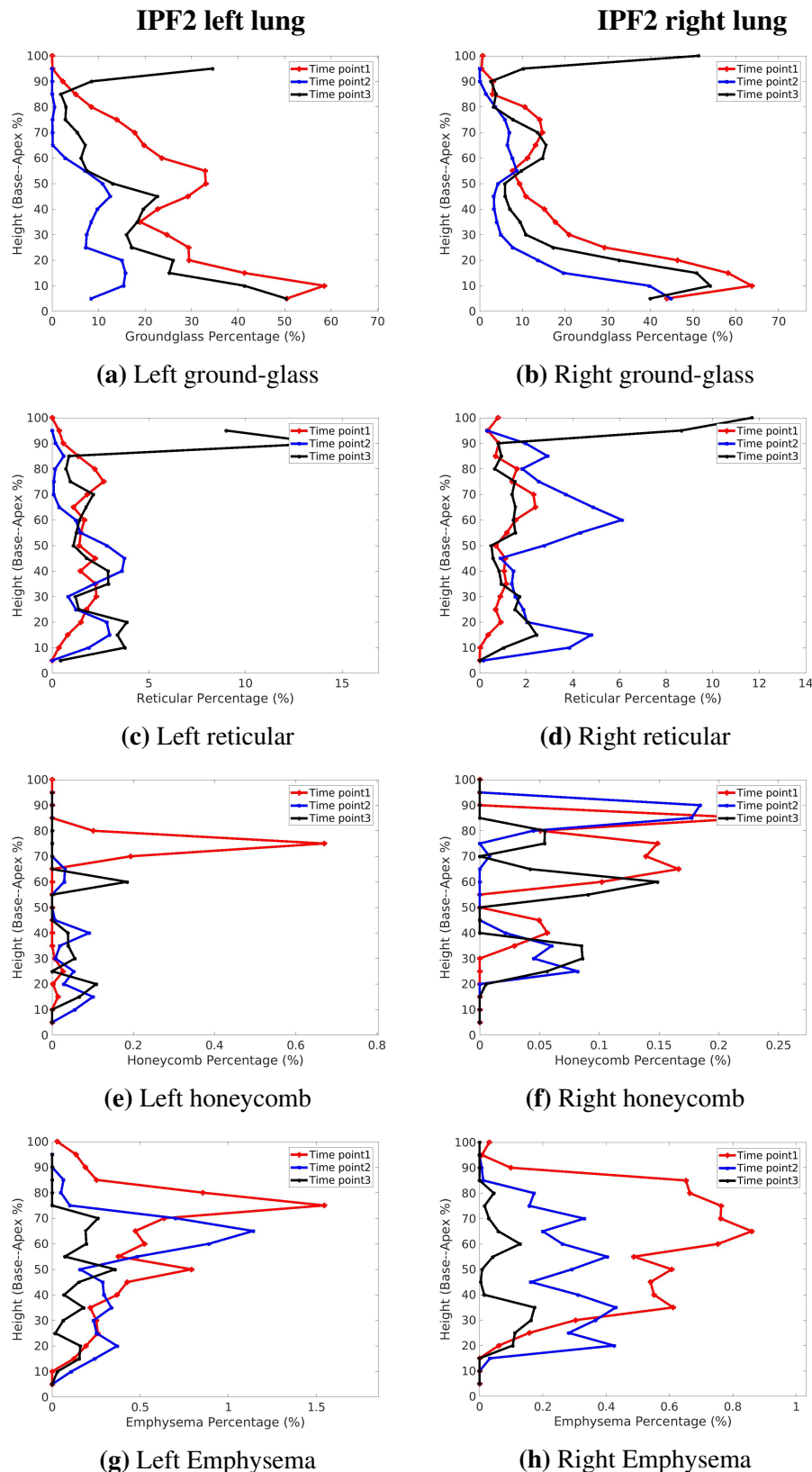


Figure B.1: Volume percentage of each tissue classification plotted against lung height (cranio-caudal axis) of case IPF2 in left and right lungs over time. The average percentage was calculated within 5% sections of the lung height from the base to apex. (a) (b) is ground-glass distribution. (c) (d) is reticular distribution. (e) (f) is honeycomb distribution. (g) (h) is emphysema distribution.

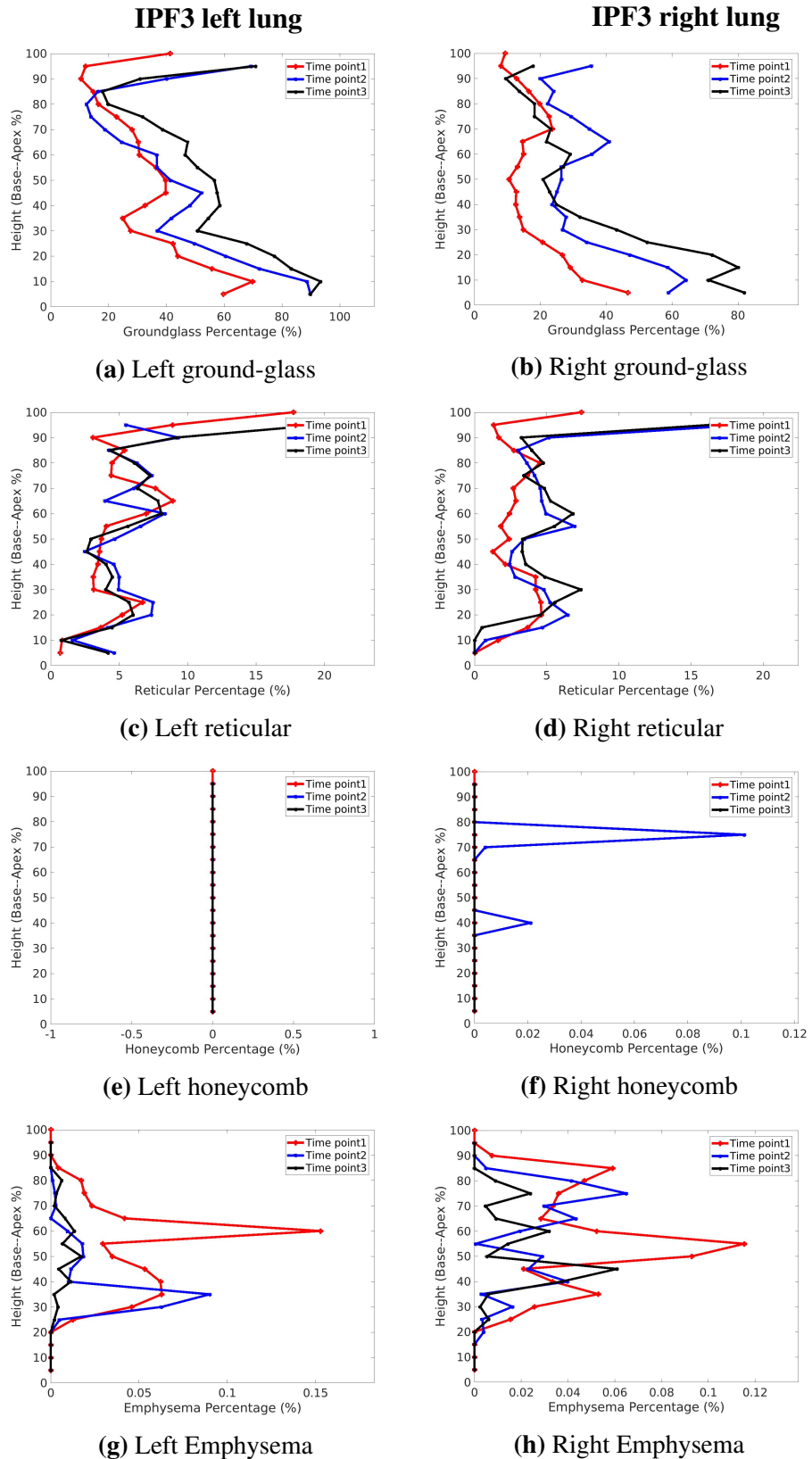


Figure B.2: Volume percentage of each tissue classification plotted against lung height (crano-caudal axis) of case IPF3 in left and right lungs over time. The average percentage was calculated within 5% sections of the lung height from the base to apex. (a) (b) is ground-glass distribution. (c) (d) is reticular distribution. (e) (f) is honeycomb distribution. (g) (h) is emphysema distribution.

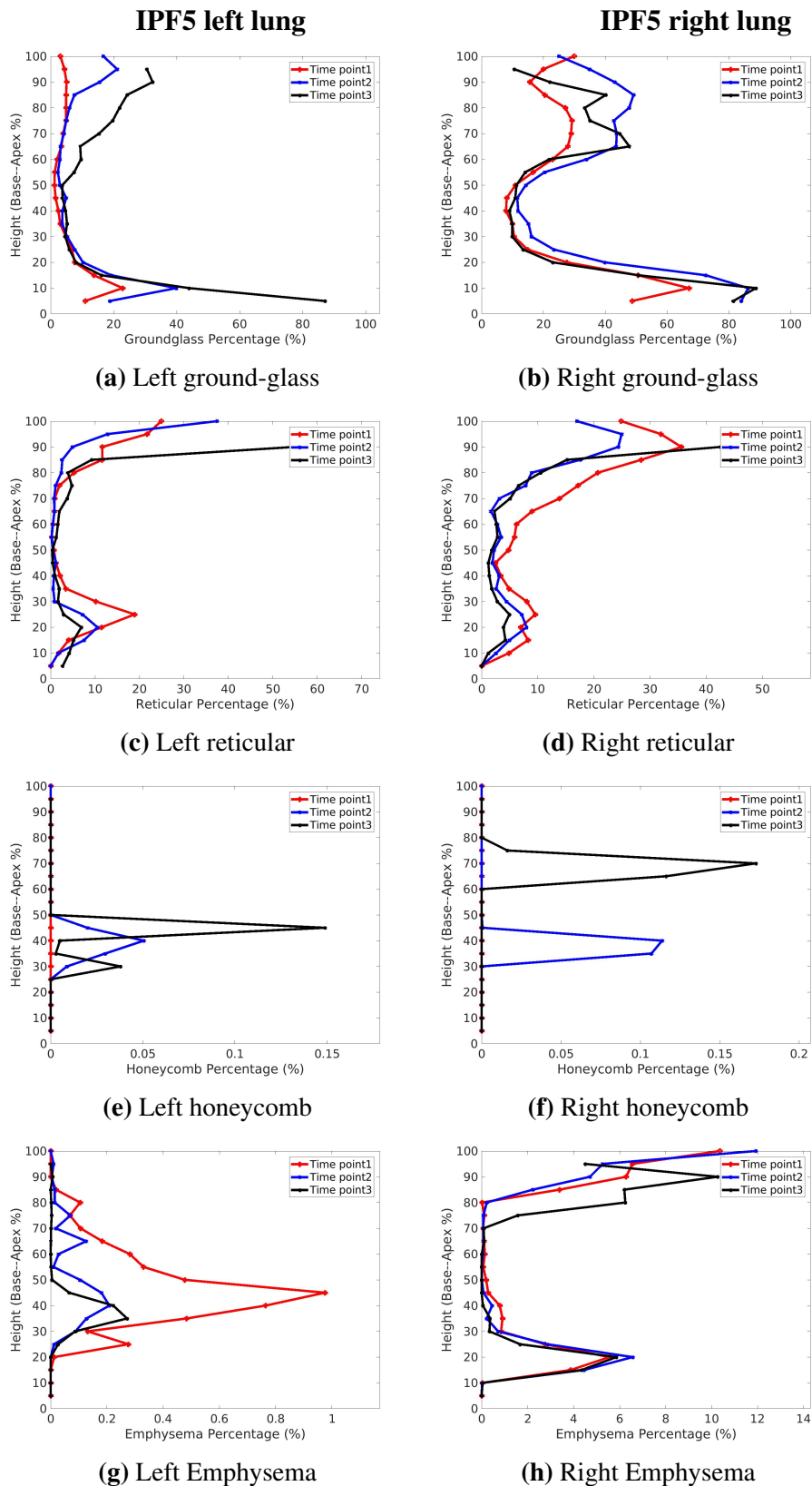


Figure B.3: Volume percentage of each tissue classification plotted against lung height (cranio-caudal axis) of case IPF5 in left and right lungs over time. The average percentage was calculated within 5% sections of the lung height from the base to apex. (a) (b) is ground-glass distribution. (c) (d) is reticular distribution. (e) (f) is honeycomb distribution. (g) (h) is emphysema distribution.

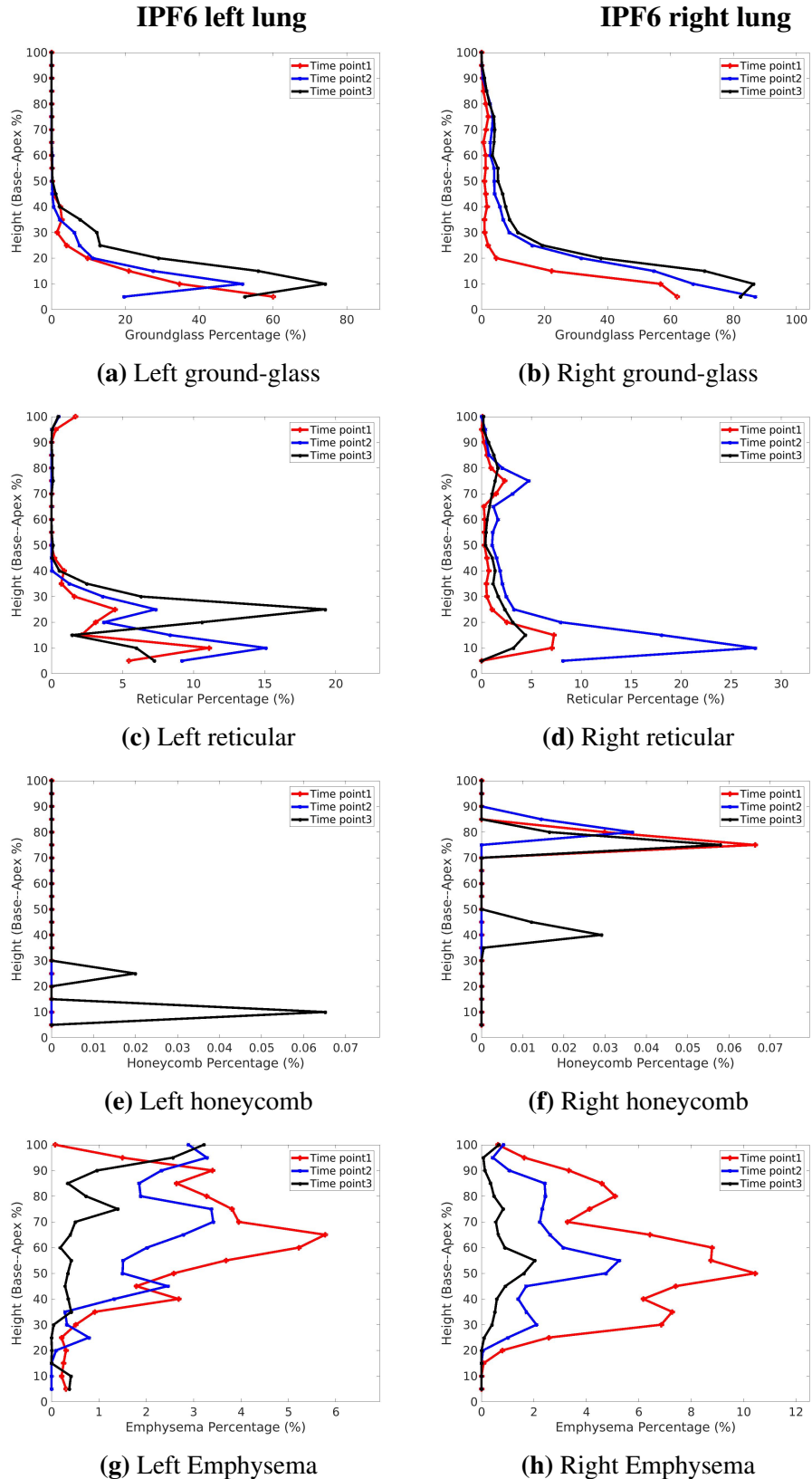


Figure B.4: Volume percentage of each tissue classification plotted against lung height (crano-caudal axis) of case IPF6 in left and right lungs over time. The average percentage was calculated within 5% sections of the lung height from the base to apex. (a) (b) is ground-glass distribution. (c) (d) is reticular distribution. (e) (f) is honeycomb distribution. (g) (h) is emphysema distribution.

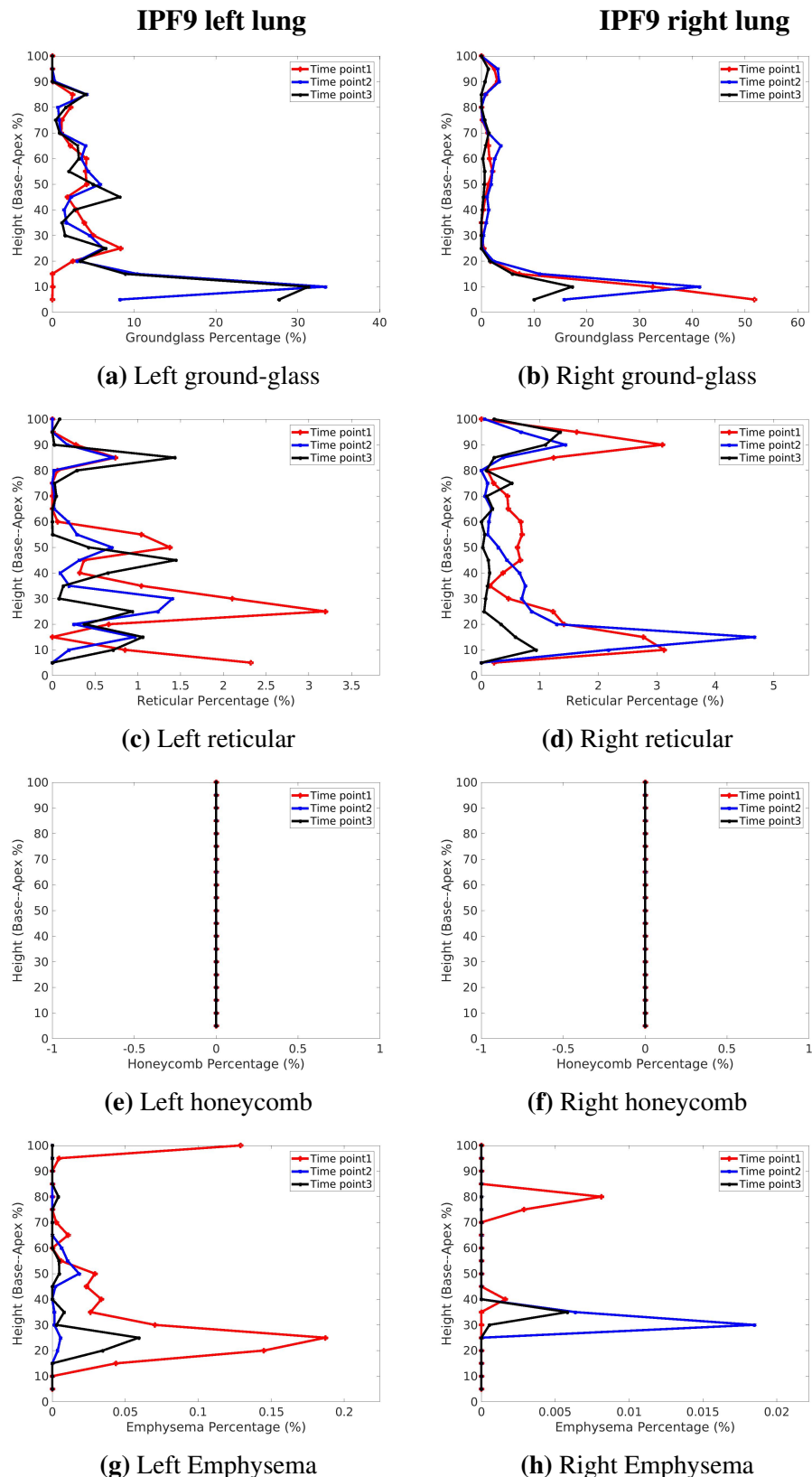


Figure B.5: Volume percentage of each tissue classification plotted against lung height (cranio-caudal axis) of case IPF9 in left and right lungs over time. The average percentage was calculated within 5% sections of the lung height from the base to apex. (a) (b) is ground-glass distribution. (c) (d) is reticular distribution. (e) (f) is honeycomb distribution. (g) (h) is emphysema distribution.

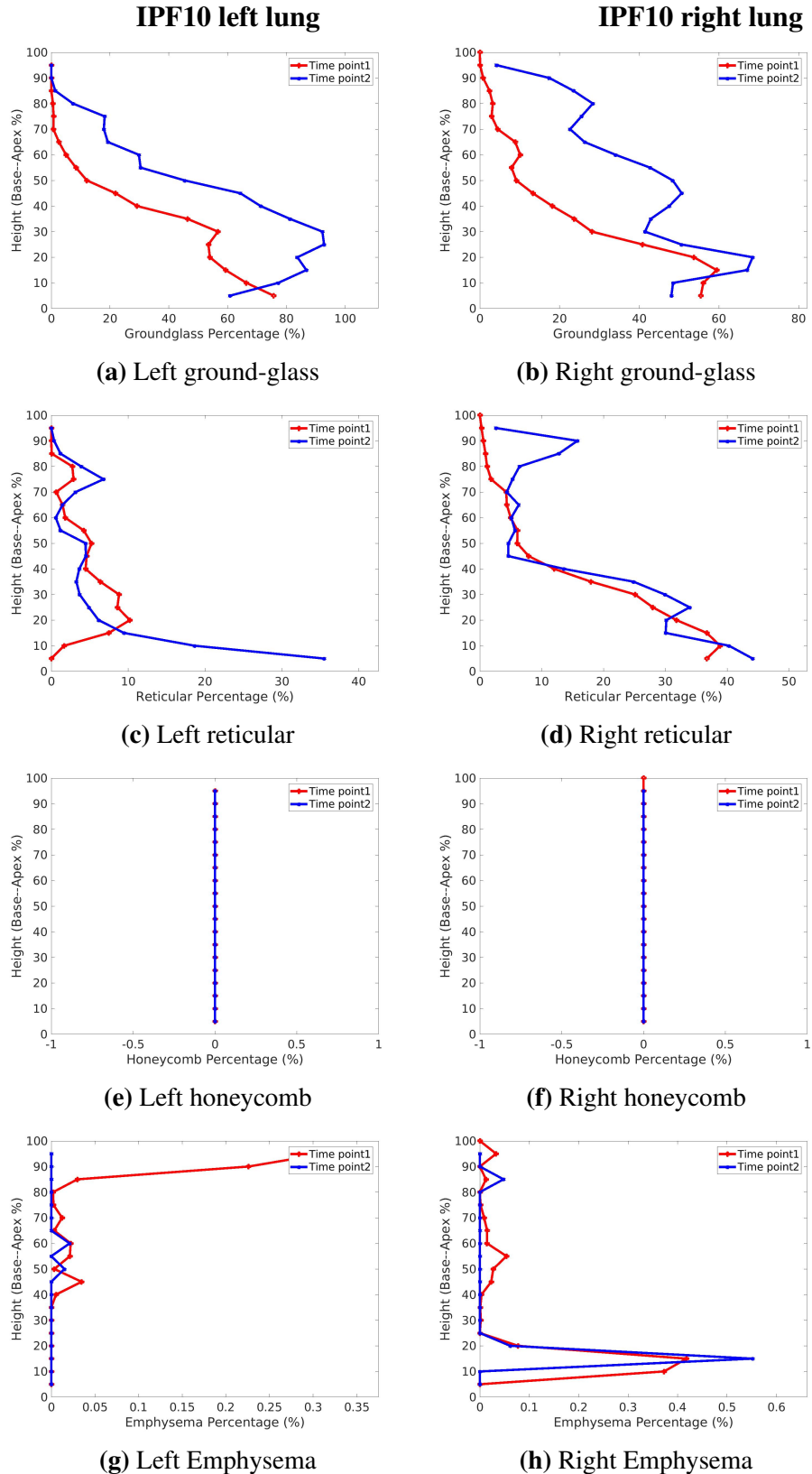


Figure B.6: Volume percentage of each tissue classification plotted against lung height (cranio-caudal axis) of case IPF10 in left and right lungs over time. The average percentage was calculated within 5% sections of the lung height from the base to apex. (a) (b) is ground-glass distribution. (c) (d) is reticular distribution. (e) (f) is honeycomb distribution. (g) (h) is emphysema distribution.

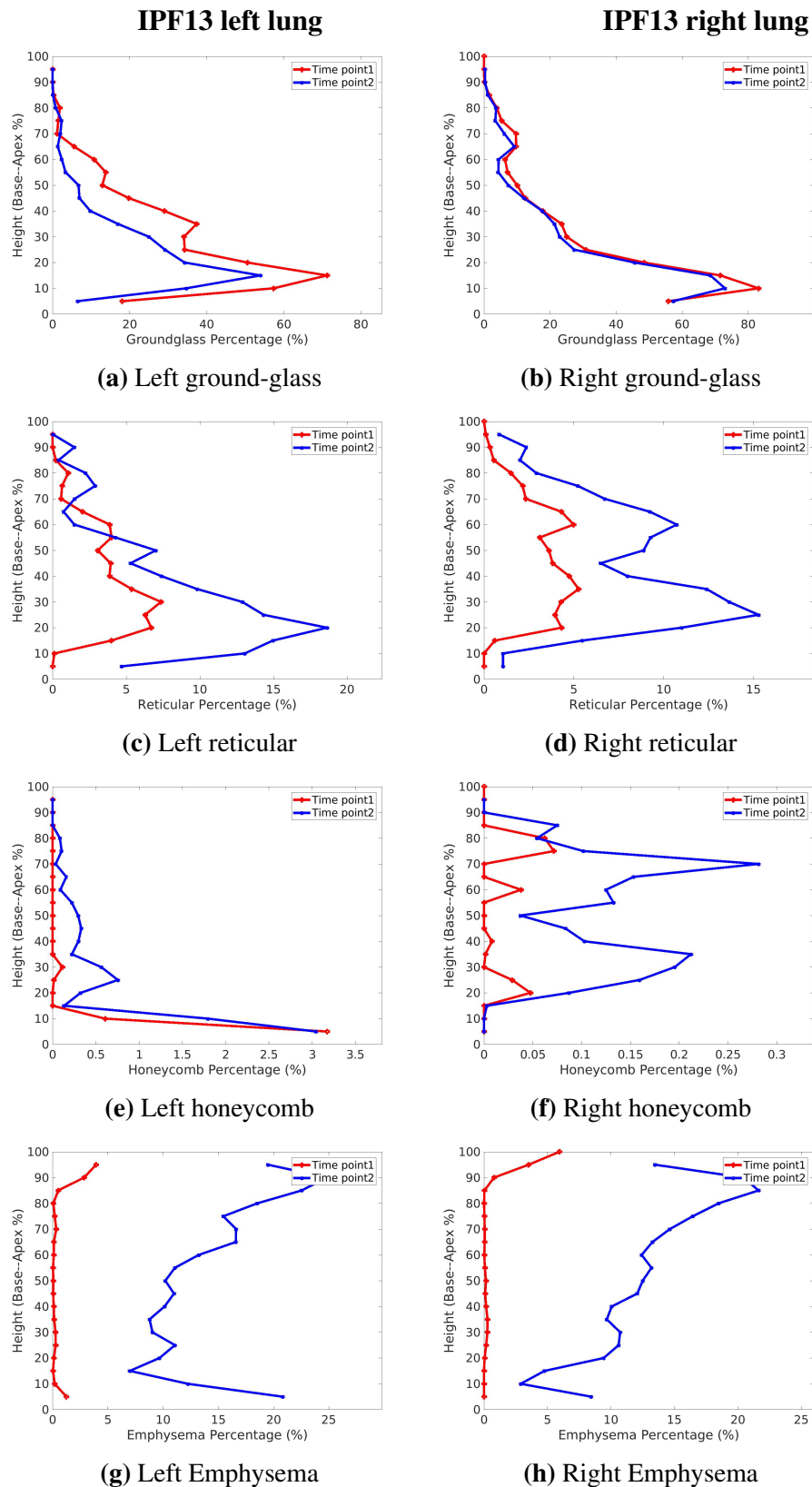


Figure B.7: Volume percentage of each tissue classification plotted against lung height (cranio-caudal axis) of case IPF13 in left and right lungs over time. The average percentage was calculated within 5% sections of the lung height from the base to apex. (a) (b) is ground-glass distribution. (c) (d) is reticular distribution. (e) (f) is honeycomb distribution. (g) (h) is emphysema distribution.

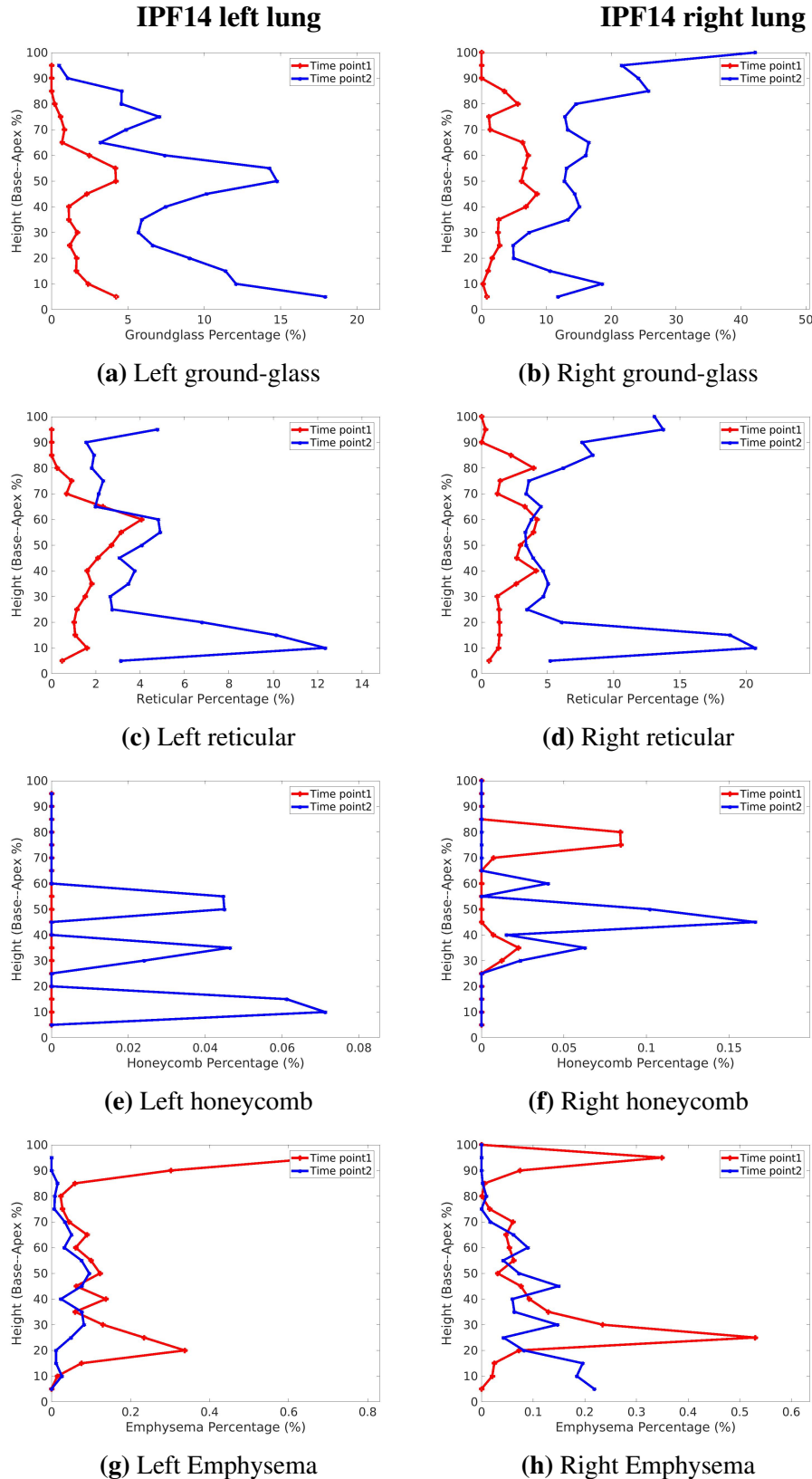


Figure B.8: Volume percentage of each tissue classification plotted against lung height (crano-caudal axis) of case IPF14 in left and right lungs over time. The average percentage was calculated within 5% sections of the lung height from the base to apex. (a) (b) is ground-glass distribution. (c) (d) is reticular distribution. (e) (f) is honeycomb distribution. (g) (h) is emphysema distribution.

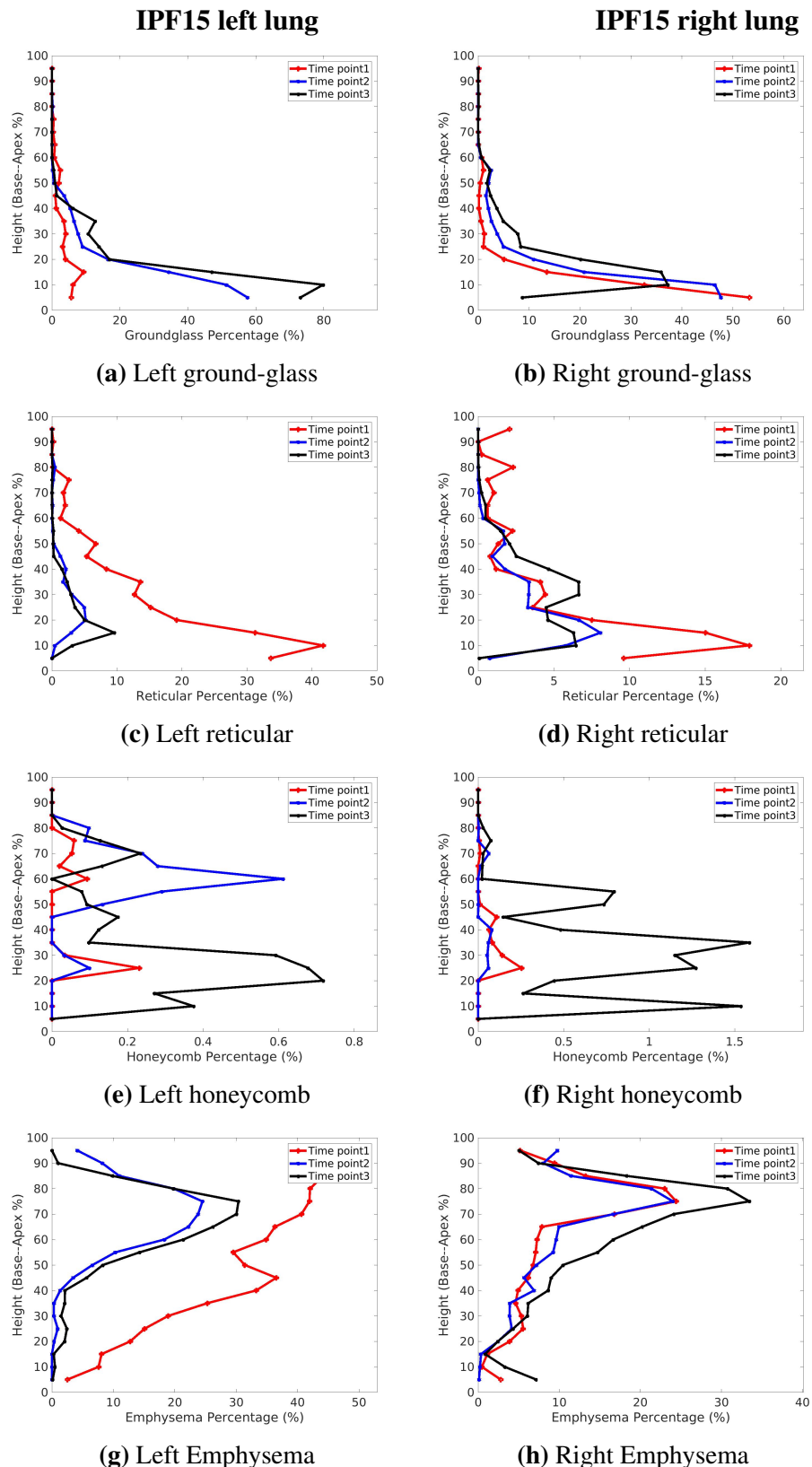


Figure B.9: Volume percentage of each tissue classification plotted against lung height (cranio-caudal axis) of case IPF15 in left and right lungs over time. The average percentage was calculated within 5% sections of the lung height from the base to apex. (a) (b) is ground-glass distribution. (c) (d) is reticular distribution. (e) (f) is honeycomb distribution. (g) (h) is emphysema distribution.

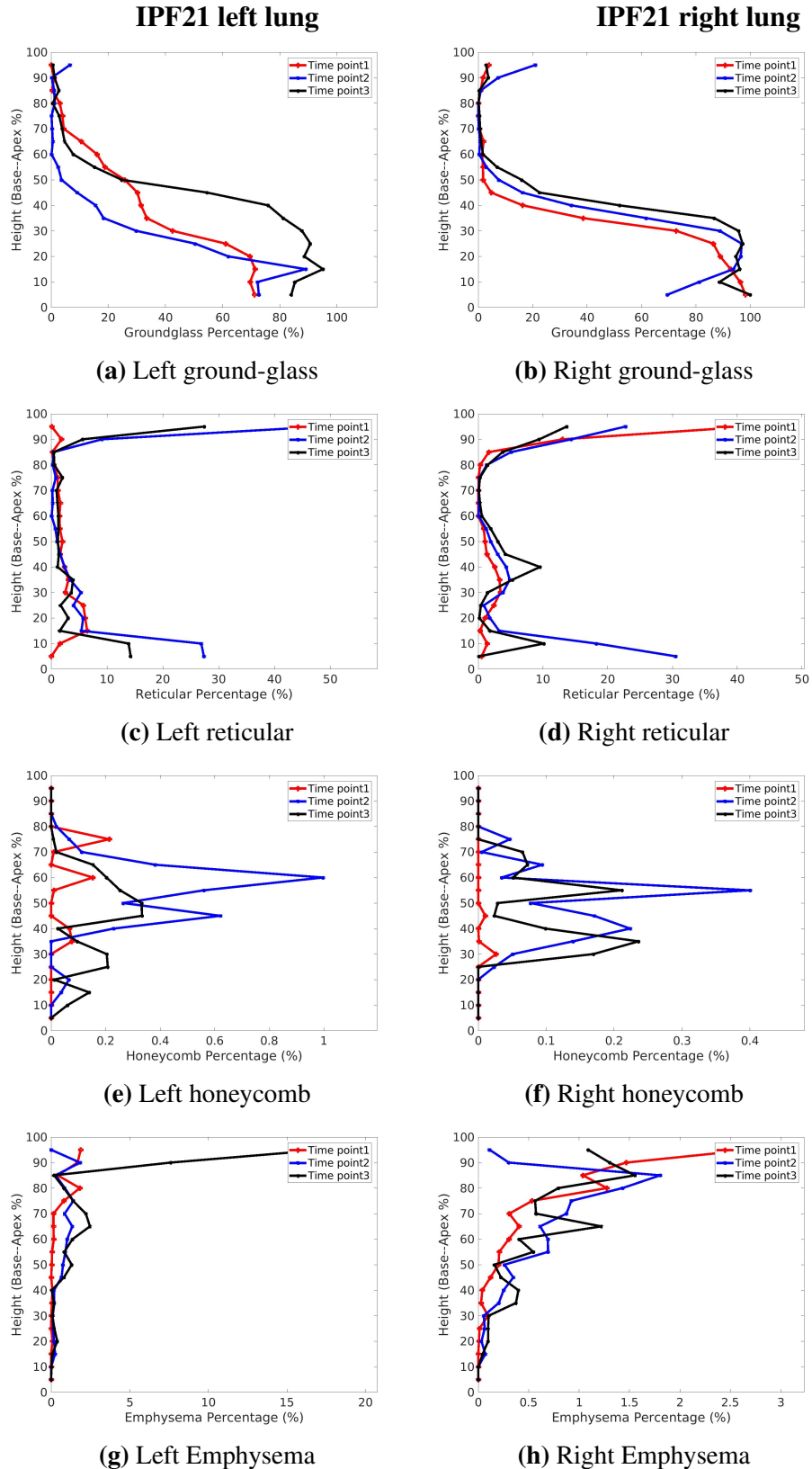


Figure B.10: Volume percentage of each tissue classification plotted against lung height (cranio-caudal axis) of case IPF21 in left and right lungs over time. The average percentage was calculated within 5% sections of the lung height from the base to apex. (a) (b) is ground-glass distribution. (c) (d) is reticular distribution. (e) (f) is honeycomb distribution. (g) (h) is emphysema distribution.

B.2 Dorso-to-ventral distribution over time for each patient

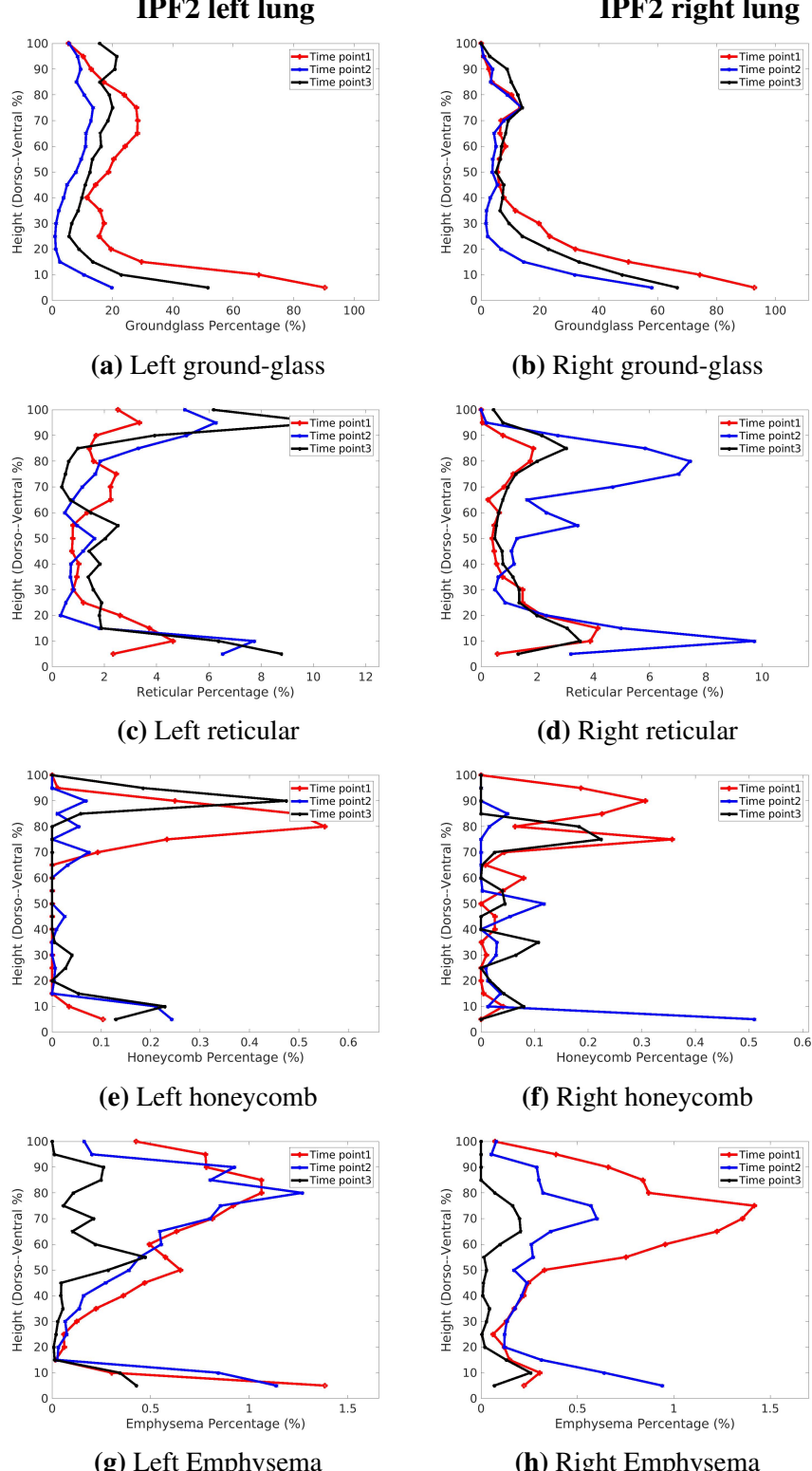


Figure B.11: Volume percentage of each tissue classification plotted in the direction of dorso-ventral axis of case IPF2 in left and right lungs over time. The average percentage was calculated within 5% sections along the axis from posterior to anterior. (a) (b) is ground-glass distribution. (c) (d) is reticular distribution. (e) (f) is honeycomb distribution. (g) (h) is emphysema distribution.

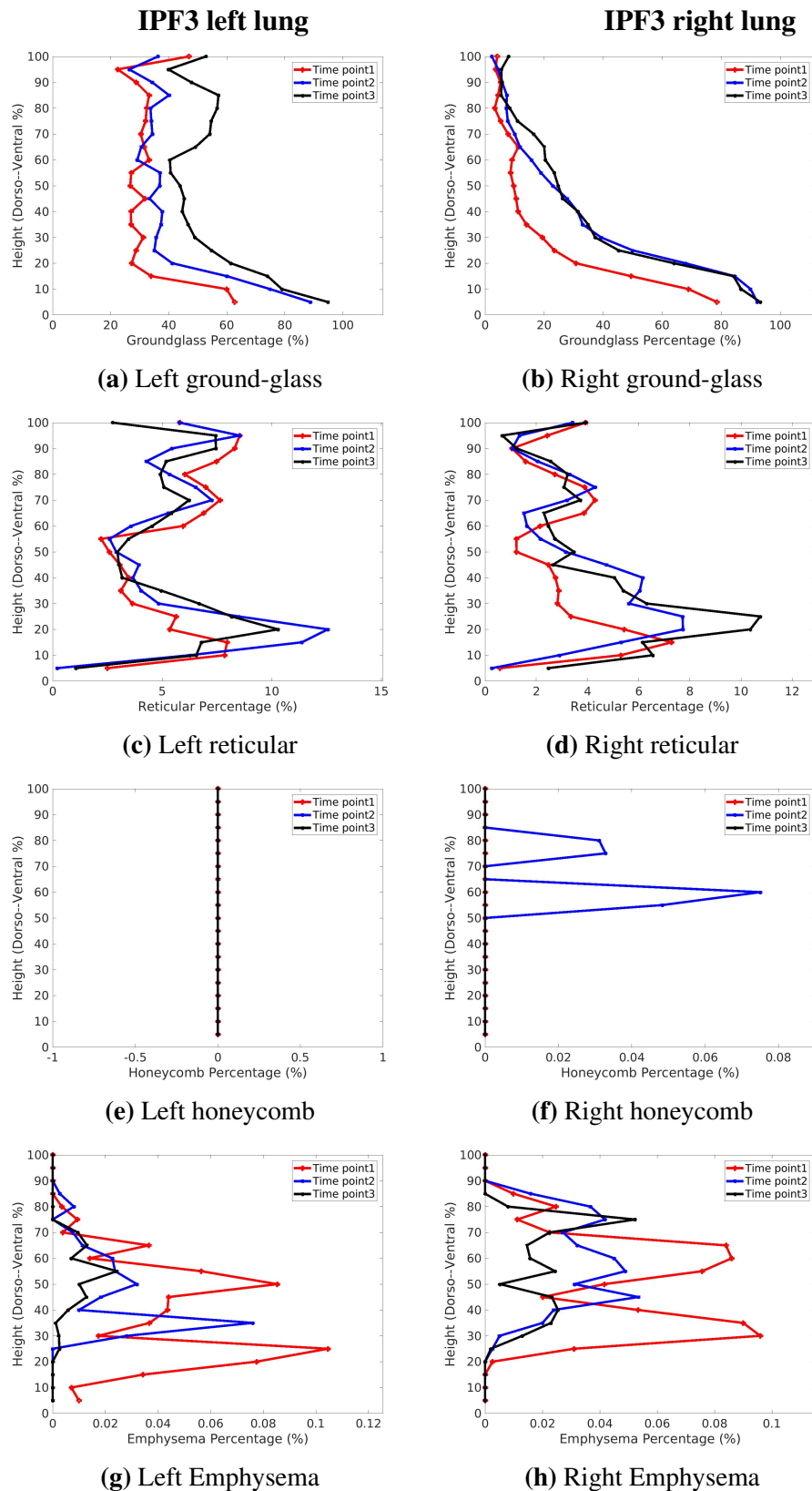


Figure B.12: Volume percentage of each tissue classification plotted in the direction of dorso-ventral axis of case IPF3 in left and right lungs over time. The average percentage was calculated within 5% sections along the axis from posterior to anterior. (a) (b) is ground-glass distribution. (c) (d) is reticular distribution. (e) (f) is honeycomb distribution. (g) (h) is emphysema distribution.

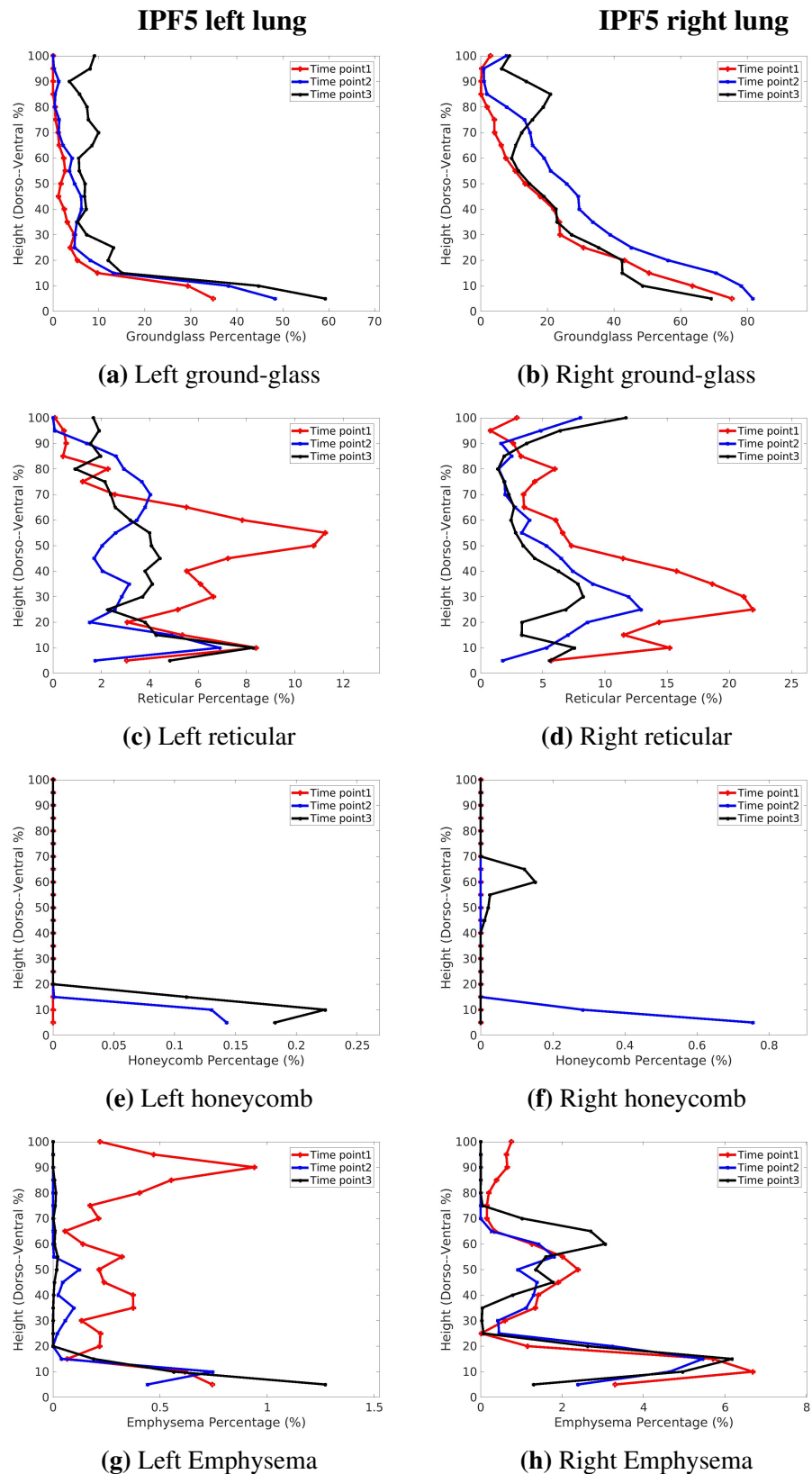


Figure B.13: Volume percentage of each tissue classification plotted in the direction of dorso-ventral axis of case IPF5 in left and right lungs over time. The average percentage was calculated within 5% sections along the axis from posterior to anterior. (a) (b) is ground-glass distribution. (c) (d) is reticular distribution. (e) (f) is honeycomb distribution. (g) (h) is emphysema distribution.

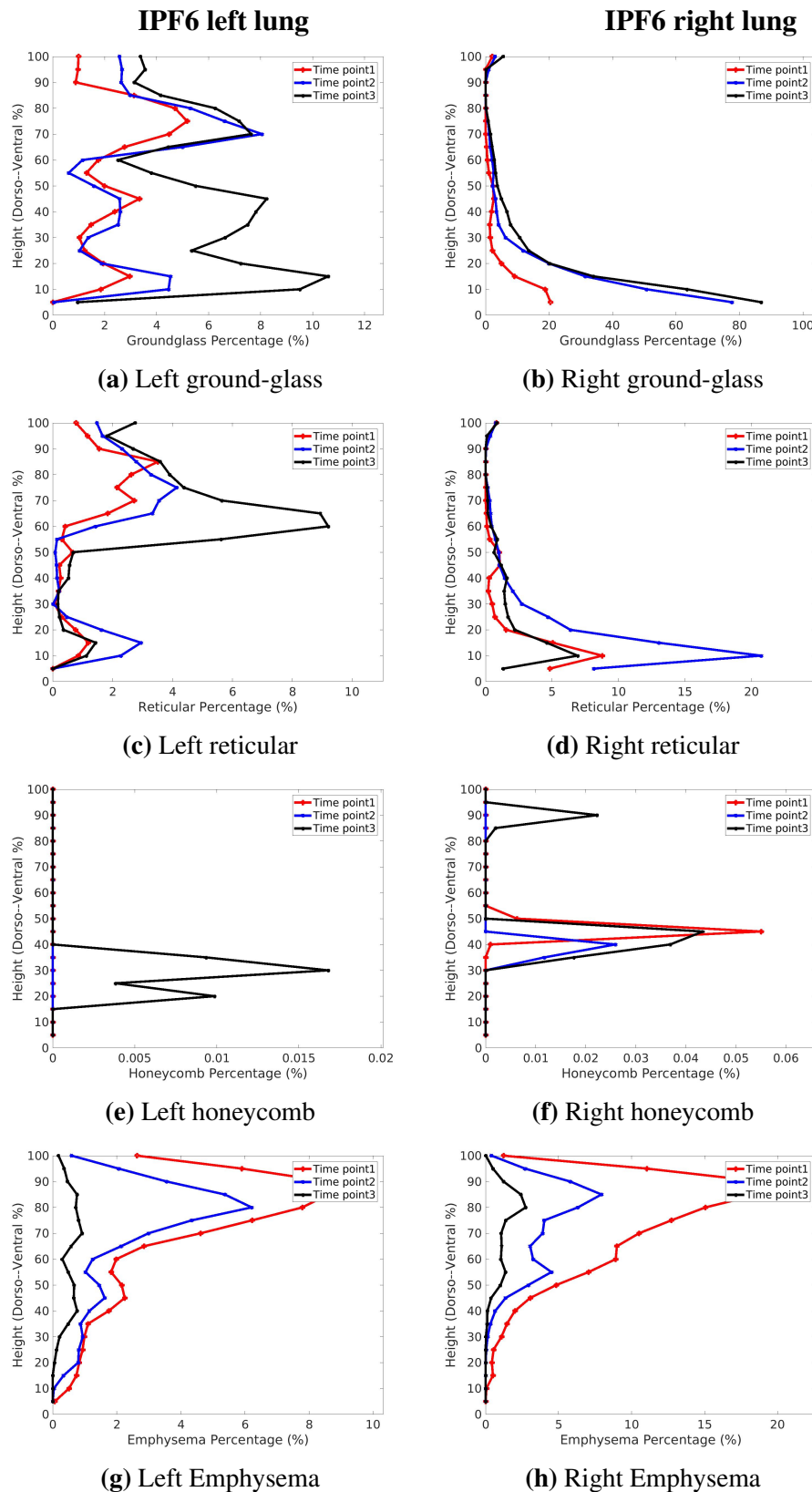


Figure B.14: Volume percentage of each tissue classification plotted in the direction of dorso-ventral axis of case IPF6 in left and right lungs over time. The average percentage was calculated within 5% sections along the axis from posterior to anterior. (a) (b) is ground-glass distribution. (c) (d) is reticular distribution. (e) (f) is honeycomb distribution. (g) (h) is emphysema distribution.

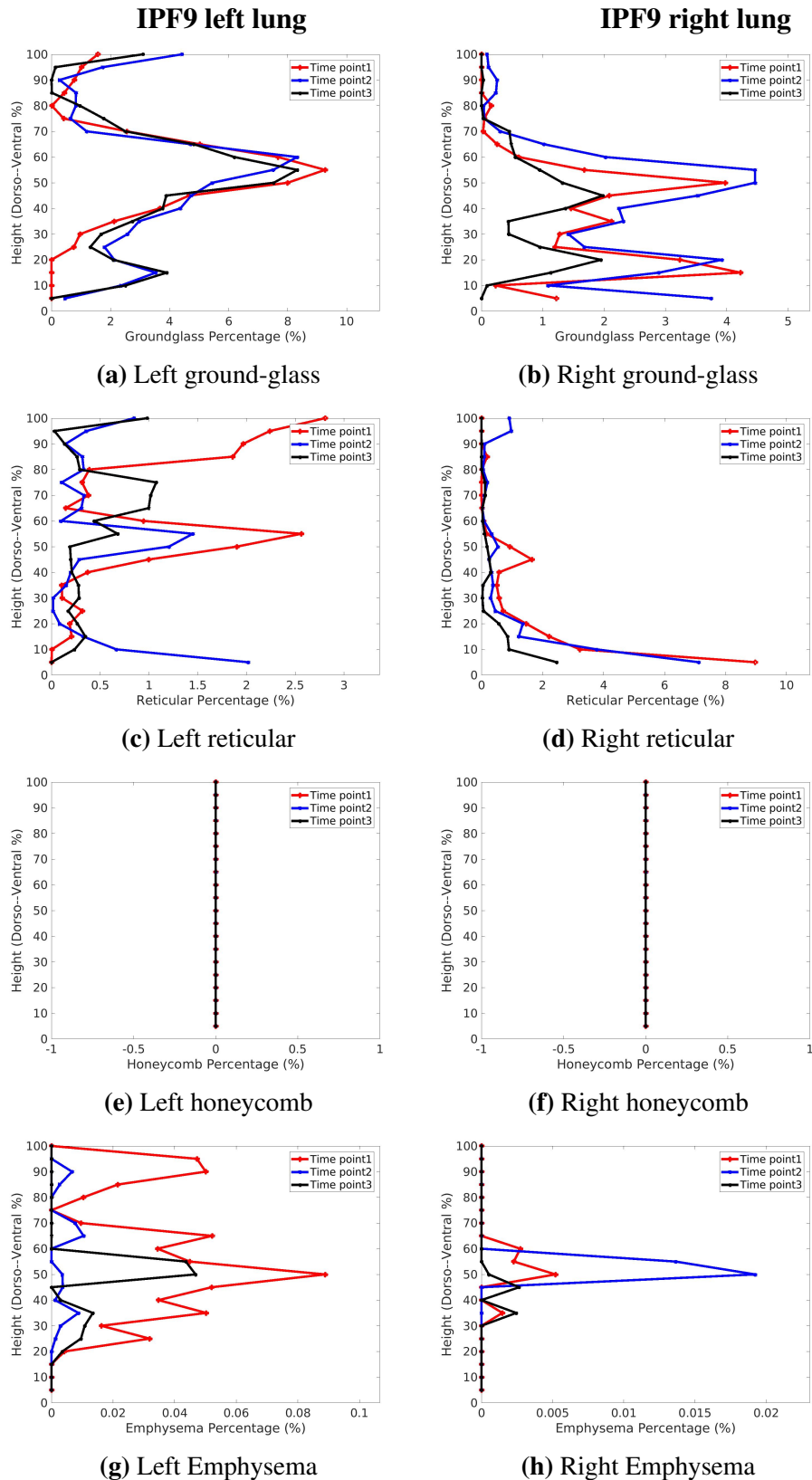


Figure B.15: Volume percentage of each tissue classification plotted in the direction of dorso-ventral axis of case IPF9 in left and right lungs over time. The average percentage was calculated within 5% sections along the axis from posterior to anterior. (a) (b) is ground-glass distribution. (c) (d) is reticular distribution. (e) (f) is honeycomb distribution. (g) (h) is emphysema distribution.

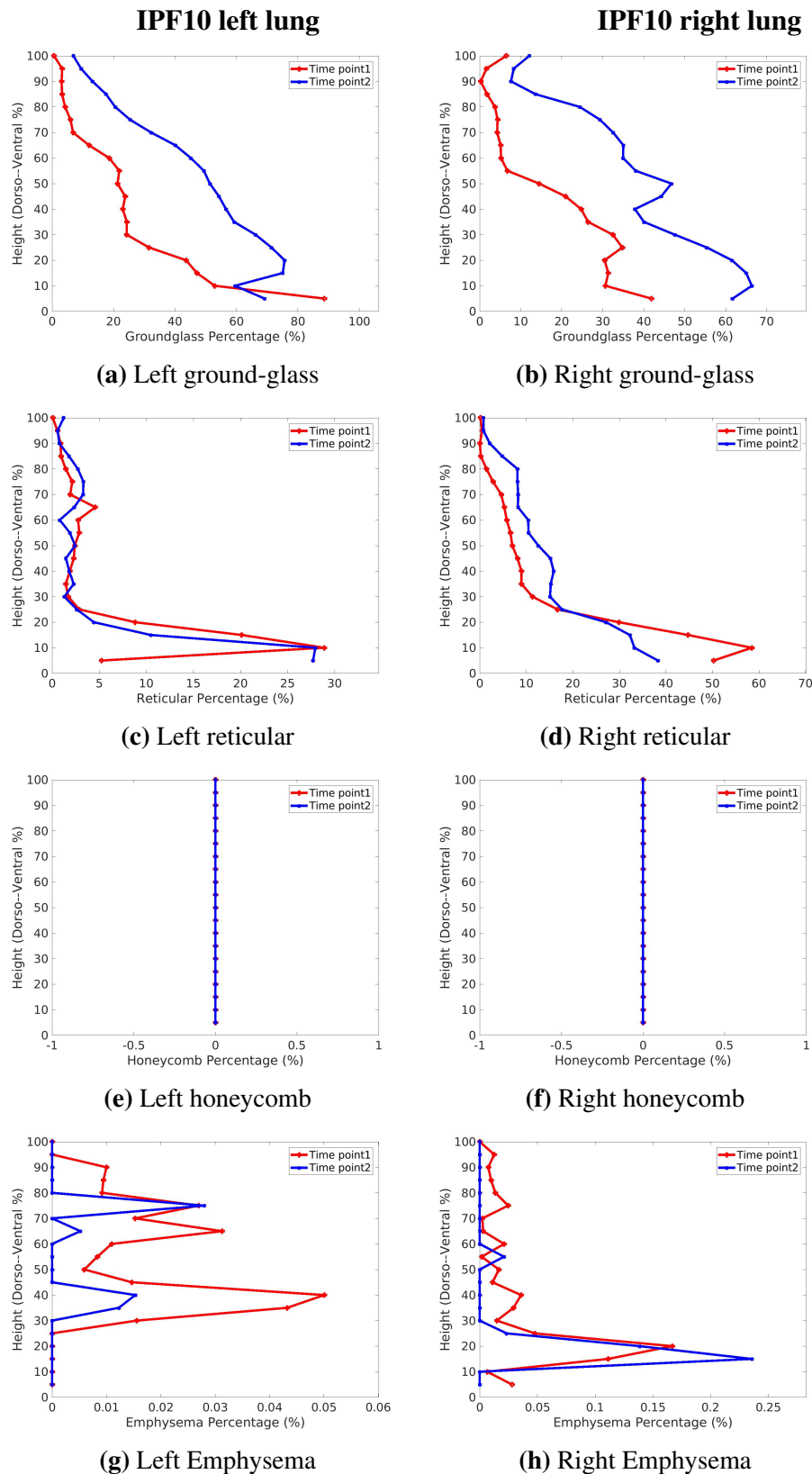


Figure B.16: Volume percentage of each tissue classification plotted in the direction of dorso-ventral axis of case IPF10 in left and right lungs over time. The average percentage was calculated within 5% sections along the axis from posterior to anterior. (a) (b) is ground-glass distribution. (c) (d) is reticular distribution. (e) (f) is honeycomb distribution. (g) (h) is emphysema distribution.

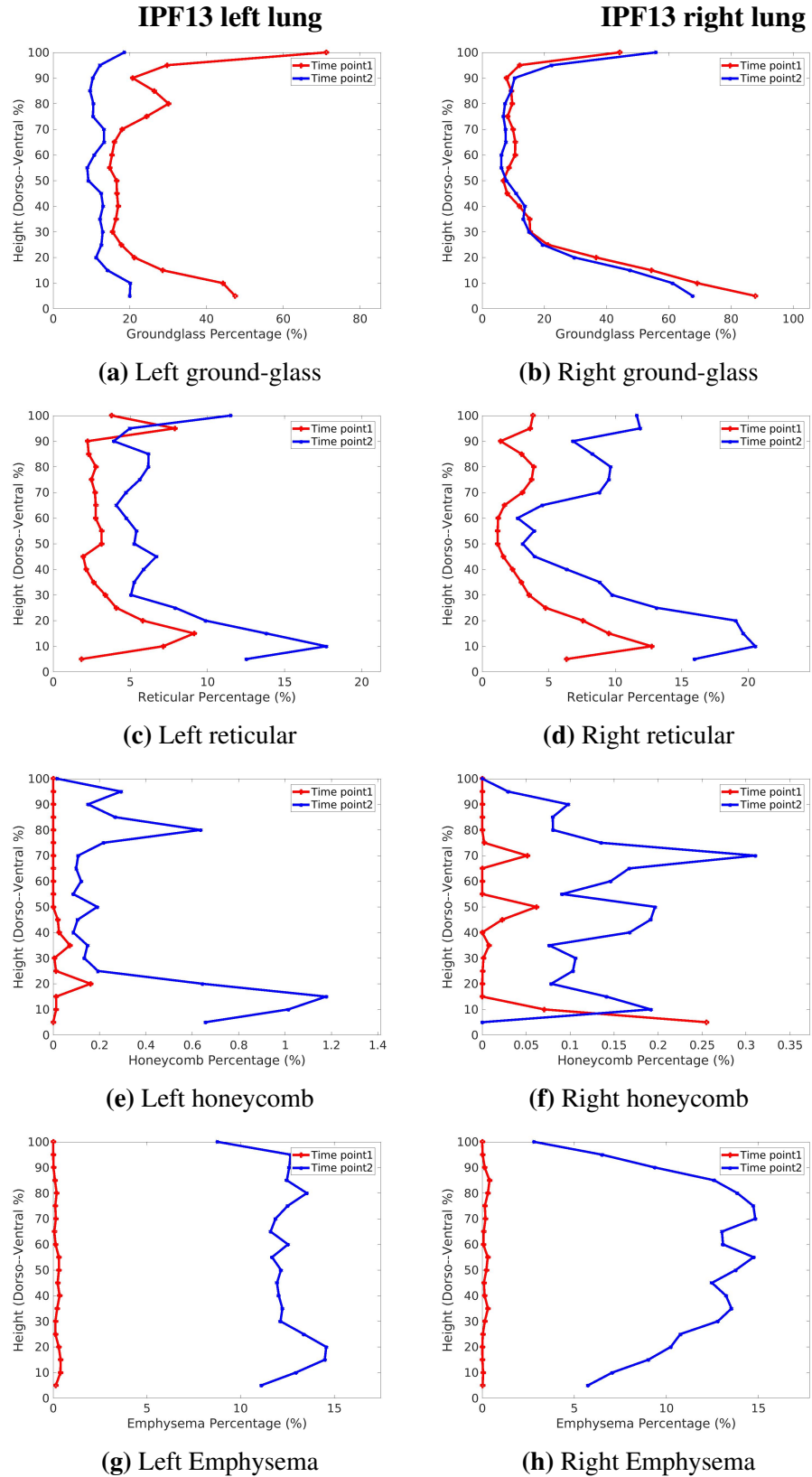


Figure B.17: Volume percentage of each tissue classification plotted in the direction of dorso-ventral axis of case IPF13 in left and right lungs over time. The average percentage was calculated within 5% sections along the axis from posterior to anterior. (a) (b) is ground-glass distribution. (c) (d) is reticular distribution. (e) (f) is honeycomb distribution. (g) (h) is emphysema distribution.

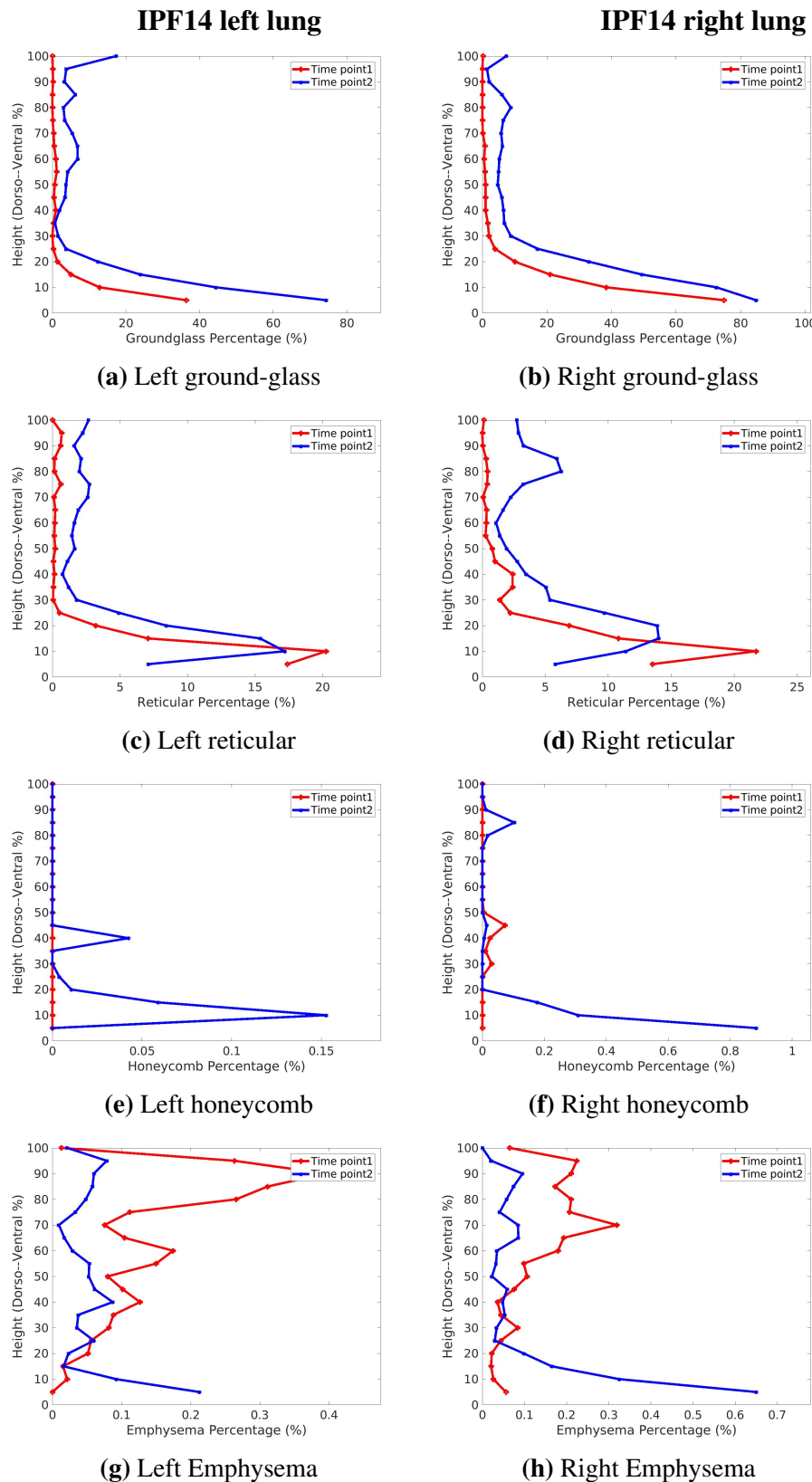


Figure B.18: Volume percentage of each tissue classification plotted in the direction of dorso-ventral axis of case IPF14 in left and right lungs over time. The average percentage was calculated within 5% sections along the axis from posterior to anterior. (a) (b) is ground-glass distribution. (c) (d) is reticular distribution. (e) (f) is honeycomb distribution. (g) (h) is emphysema distribution.

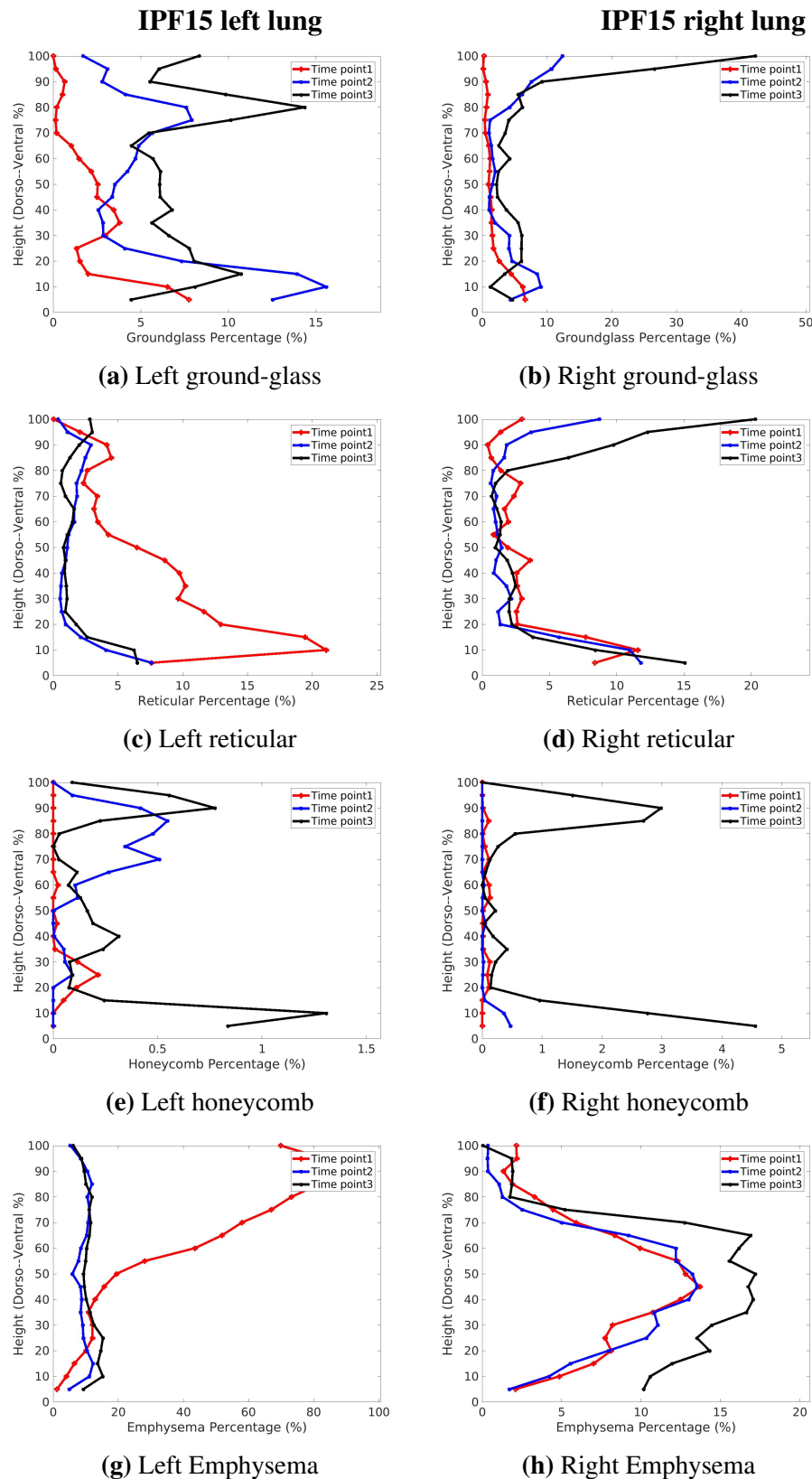


Figure B.19: Volume percentage of each tissue classification plotted in the direction of dorso-ventral axis of case IPF15 in left and right lungs over time. The average percentage was calculated within 5% sections along the axis from posterior to anterior. (a) (b) is ground-glass distribution. (c) (d) is reticular distribution. (e) (f) is honeycomb distribution. (g) (h) is emphysema distribution.

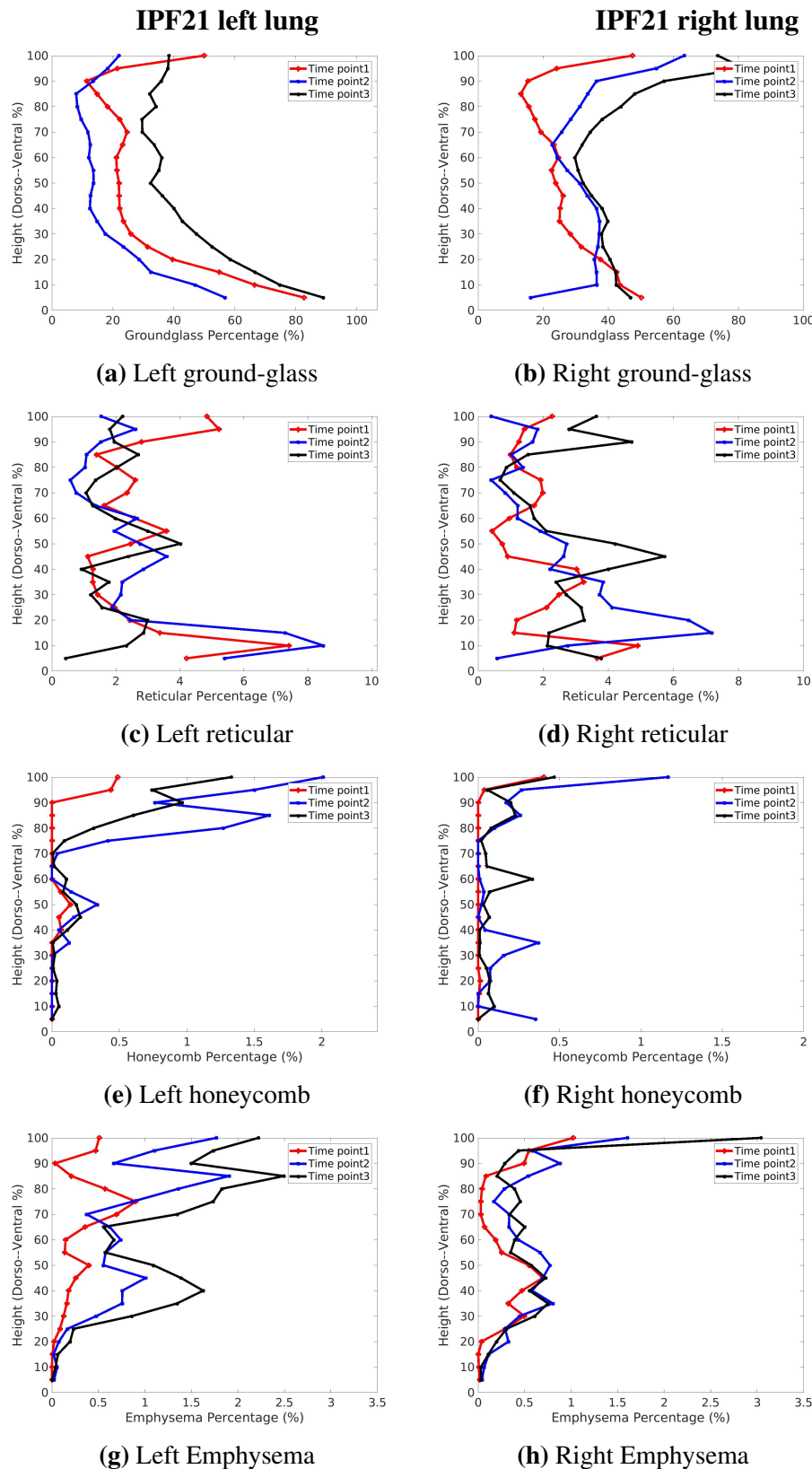


Figure B.20: Volume percentage of each tissue classification plotted in the direction of dorso-ventral axis of case IPF21 in left and right lungs over time. The average percentage was calculated within 5% sections along the axis from posterior to anterior. (a) (b) is ground-glass distribution. (c) (d) is reticular distribution. (e) (f) is honeycomb distribution. (g) (h) is emphysema distribution.

B.3 Lobar distribution over time for each patient

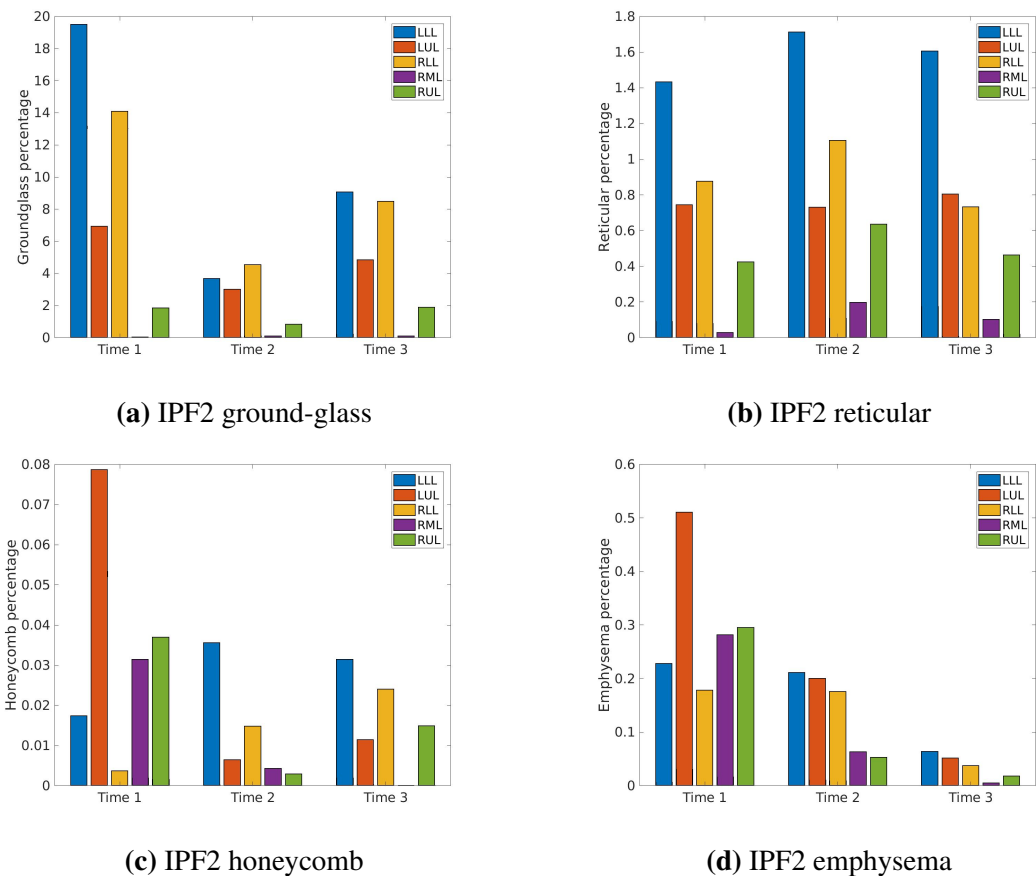


Figure B.21: Lobar distribution of disease CT patterns of case IPF2 diagnosed with IPF over time. The tissue percentage in different lobe is shown in different color, and each bar represents the volume percentage of the CT pattern for one lobe. (a) Ground-glass lobar distribution. (b) Reticular lobar distribution. (c) Honeycomb lobar distribution. (d) Emphysema lobar distribution.

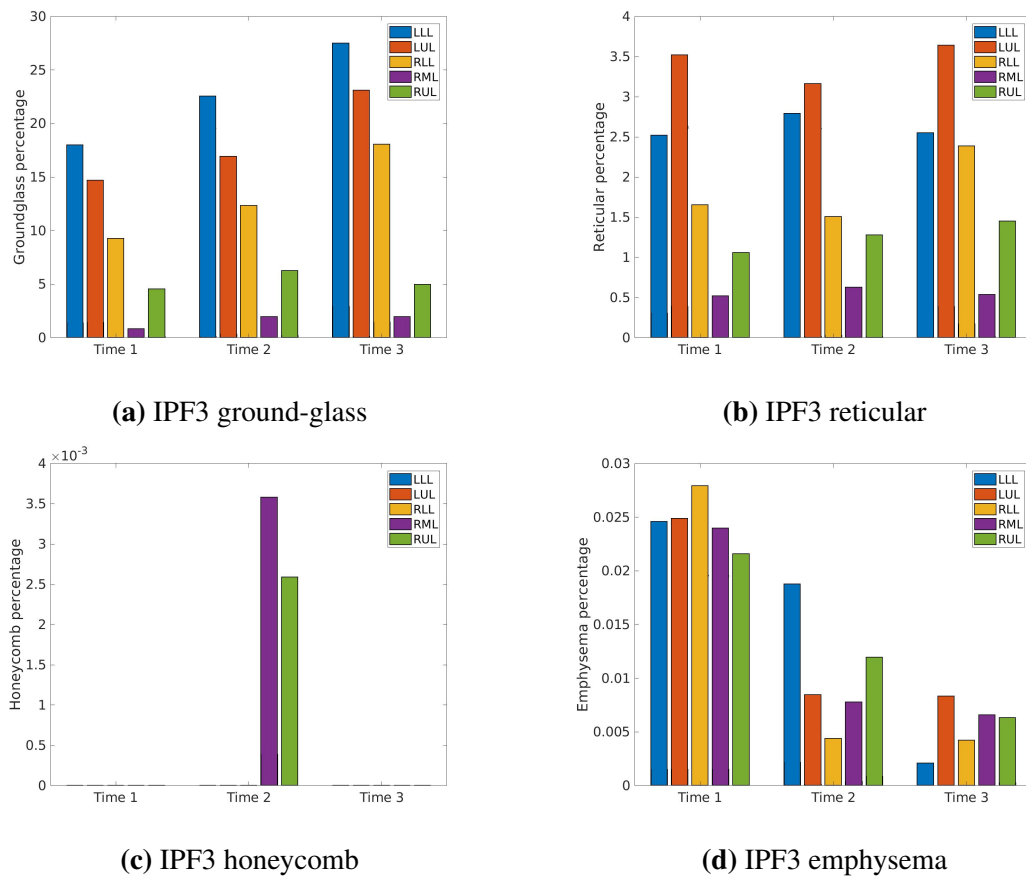


Figure B.22: Lobar distribution of disease CT patterns of case IPF3 diagnosed with IPF over time. The tissue percentage in different lobe is shown in different color, and each bar represents the volume percentage of the CT pattern for one lobe. (a) Ground-glass lobar distribution. (b) Reticular lobar distribution. (c) Honeycomb lobar distribution. (d) Emphysema lobar distribution.

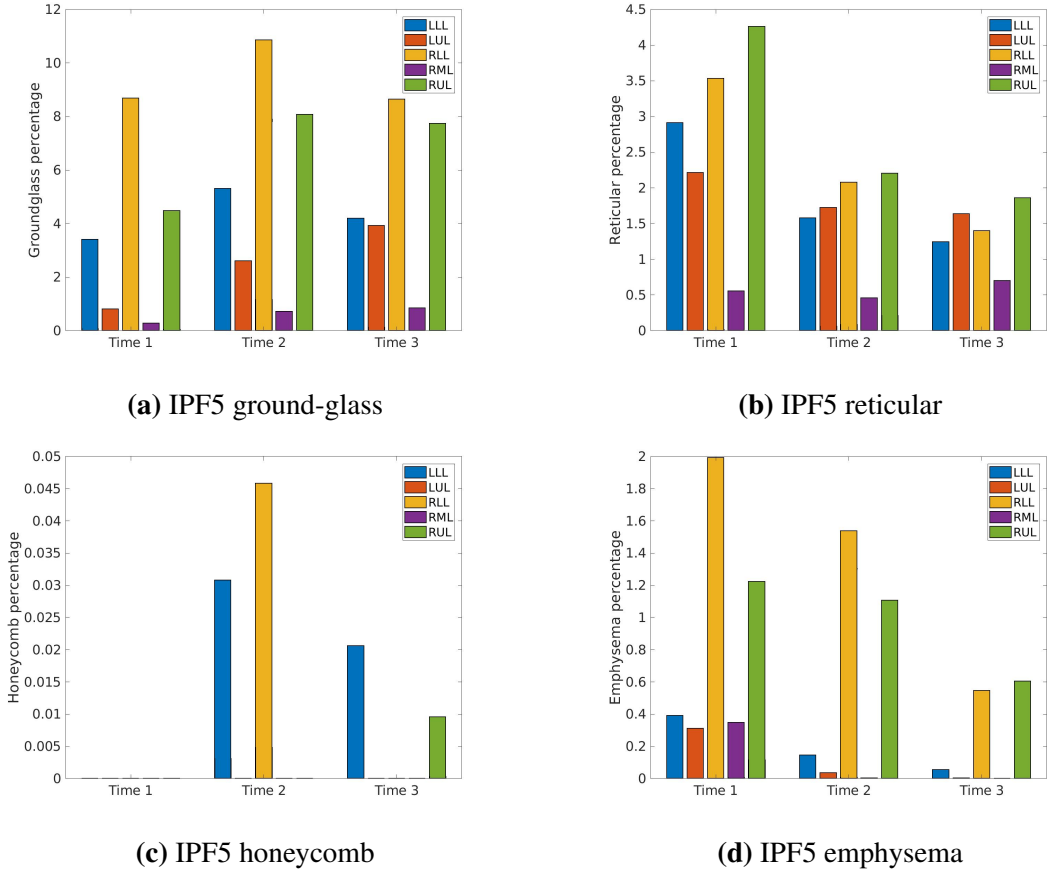


Figure B.23: Lobar distribution of disease CT patterns of case IPF5 diagnosed with IPF over time. The tissue percentage in different lobe is shown in different color, and each bar represents the volume percentage of the CT pattern for one lobe. (a) Ground-glass lobar distribution. (b) Reticular lobar distribution. (c) Honeycomb lobar distribution. (d) Emphysema lobar distribution.

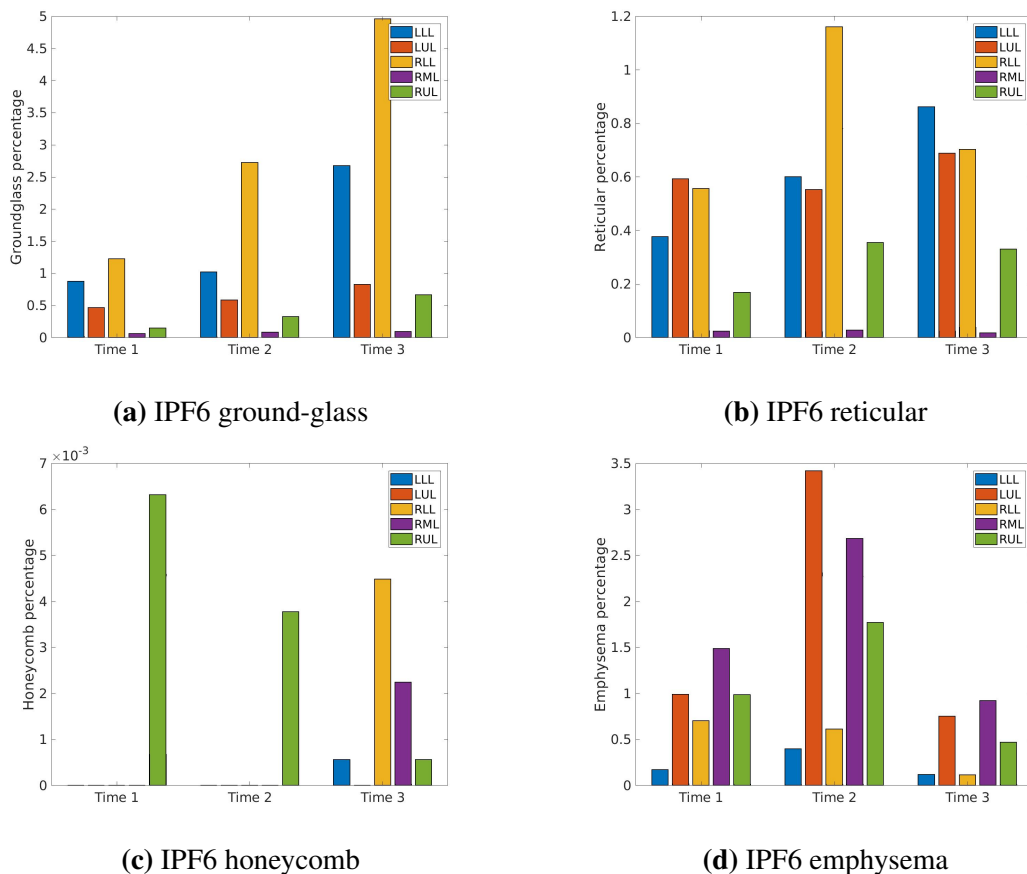


Figure B.24: Lobar distribution of disease CT patterns of case IPF6 diagnosed with IPF over time. The tissue percentage in different lobe is shown in different color, and each bar represents the volume percentage of the CT pattern for one lobe. (a) Ground-glass lobar distribution. (b) Reticular lobar distribution. (c) Honeycomb lobar distribution. (d) Emphysema lobar distribution.

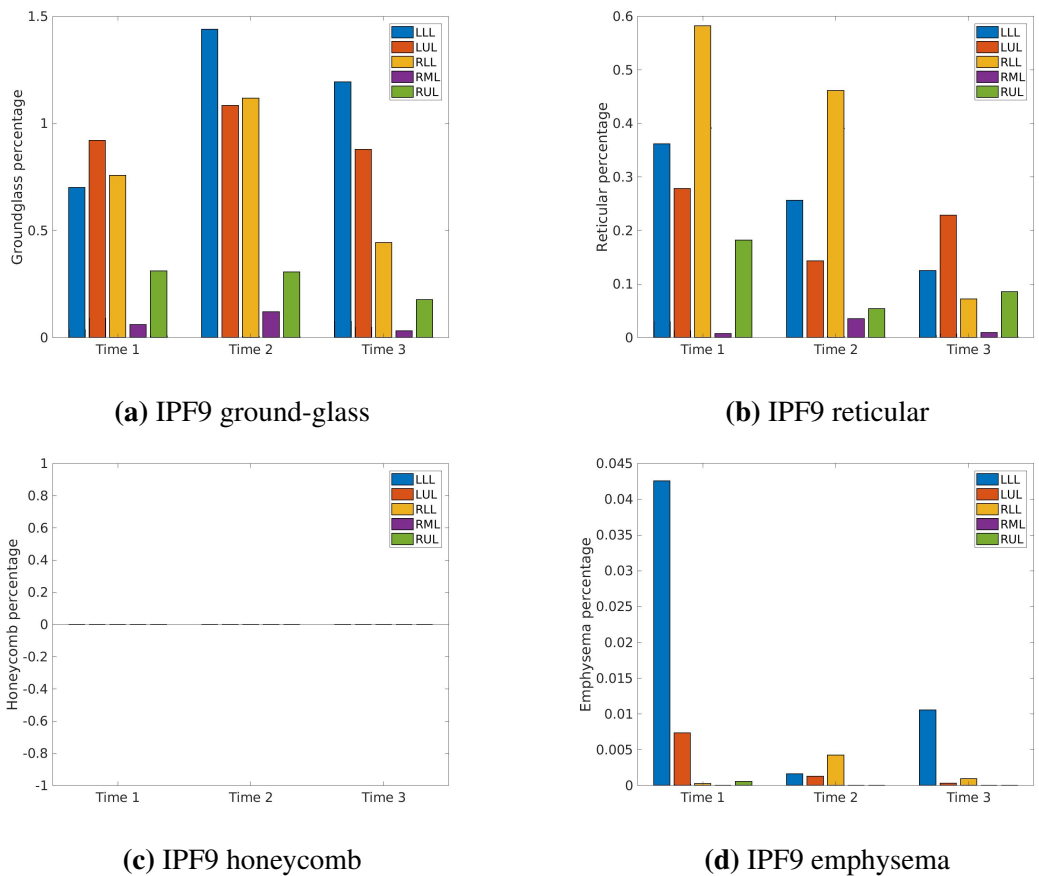


Figure B.25: Lobar distribution of disease CT patterns of case IPF9 diagnosed with IPF over time. The tissue percentage in different lobe is shown in different color, and each bar represents the volume percentage of the CT pattern for one lobe. (a) Ground-glass lobar distribution. (b) Reticular lobar distribution. (c) Honeycomb lobar distribution. (d) Emphysema lobar distribution.

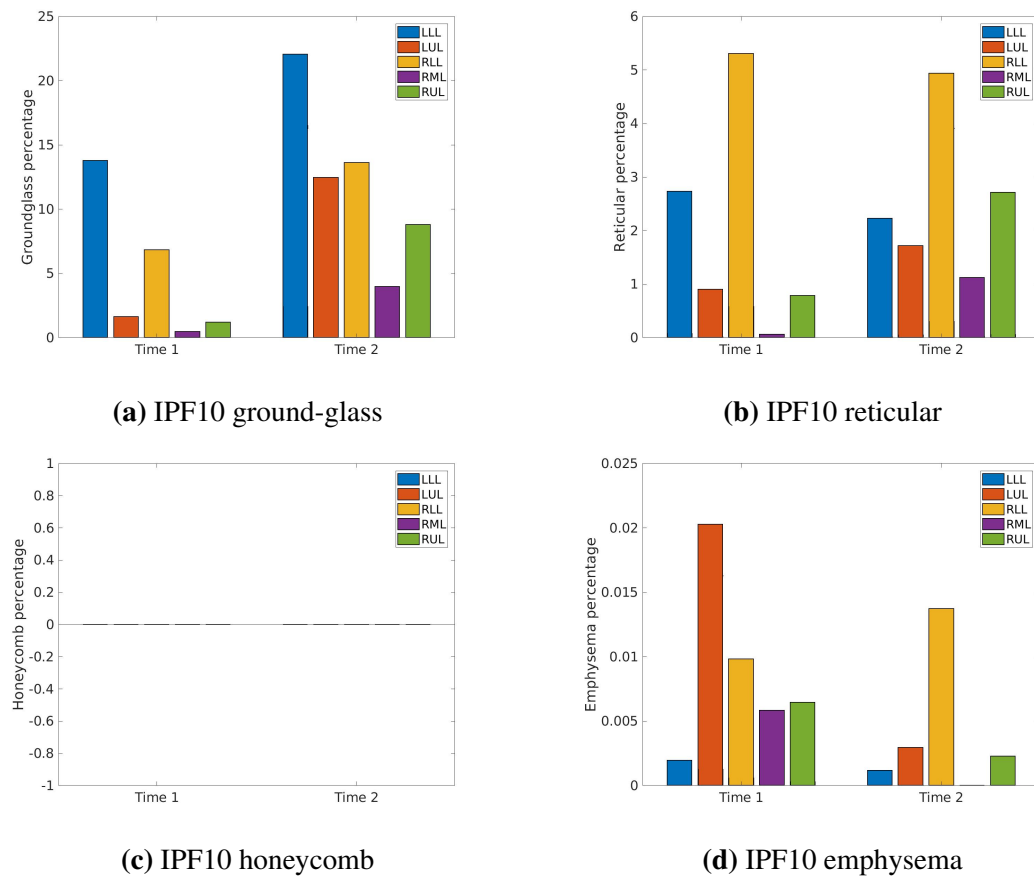


Figure B.26: Lobar distribution of disease CT patterns of case IPF10 diagnosed with IPF over time. The tissue percentage in different lobe is shown in different color, and each bar represents the volume percentage of the CT pattern for one lobe. (a) Ground-glass lobar distribution. (b) Reticular lobar distribution. (c) Honeycomb lobar distribution. (d) Emphysema lobar distribution.

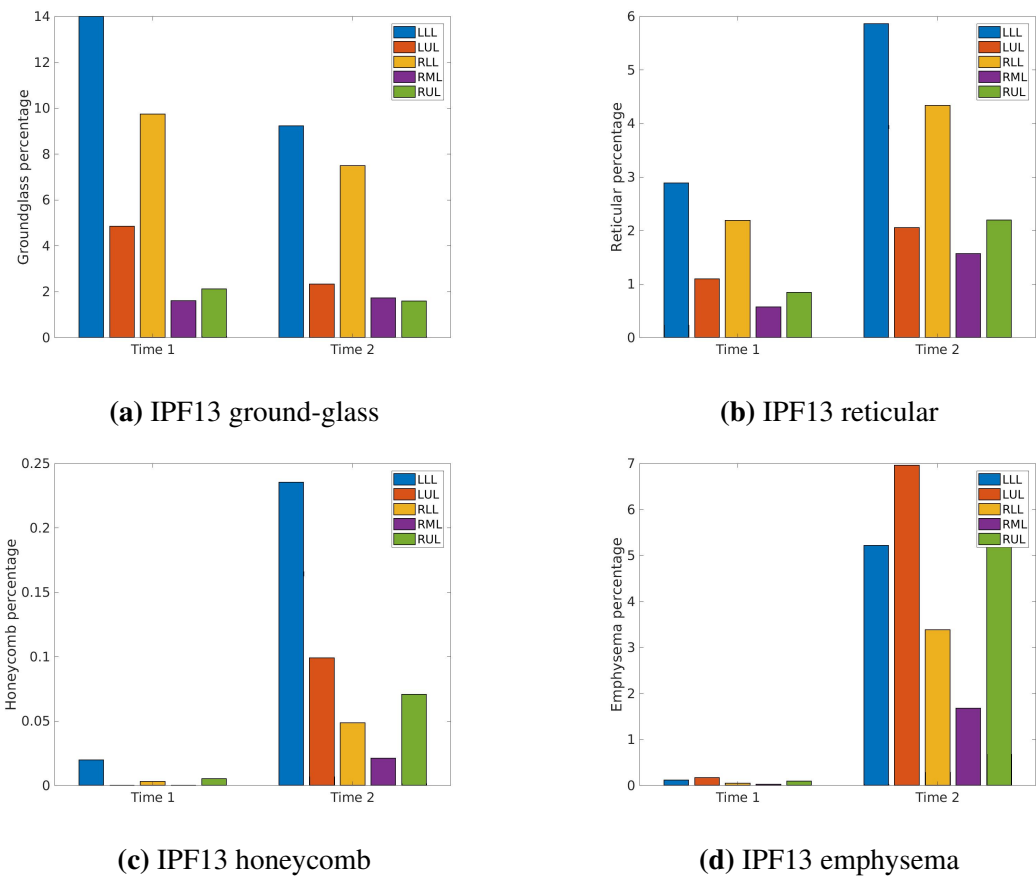


Figure B.27: Lobar distribution of disease CT patterns of case IPF13 diagnosed with IPF over time. The tissue percentage in different lobe is shown in different color, and each bar represents the volume percentage of the CT pattern for one lobe. (a) Ground-glass lobar distribution. (b) Reticular lobar distribution. (c) Honeycomb lobar distribution. (d) Emphysema lobar distribution.

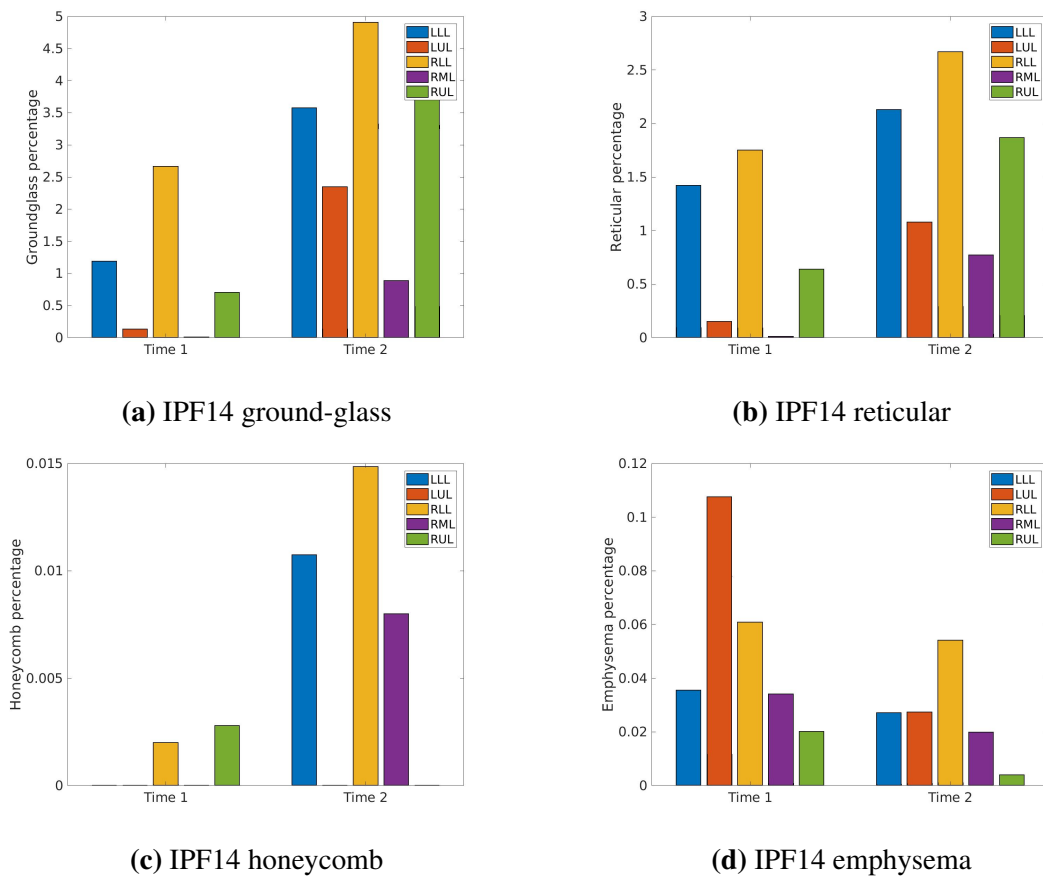


Figure B.28: Lobar distribution of disease CT patterns of case IPF14 diagnosed with IPF over time. The tissue percentage in different lobe is shown in different color, and each bar represents the volume percentage of the CT pattern for one lobe. (a) Ground-glass lobar distribution. (b) Reticular lobar distribution. (c) Honeycomb lobar distribution. (d) Emphysema lobar distribution.

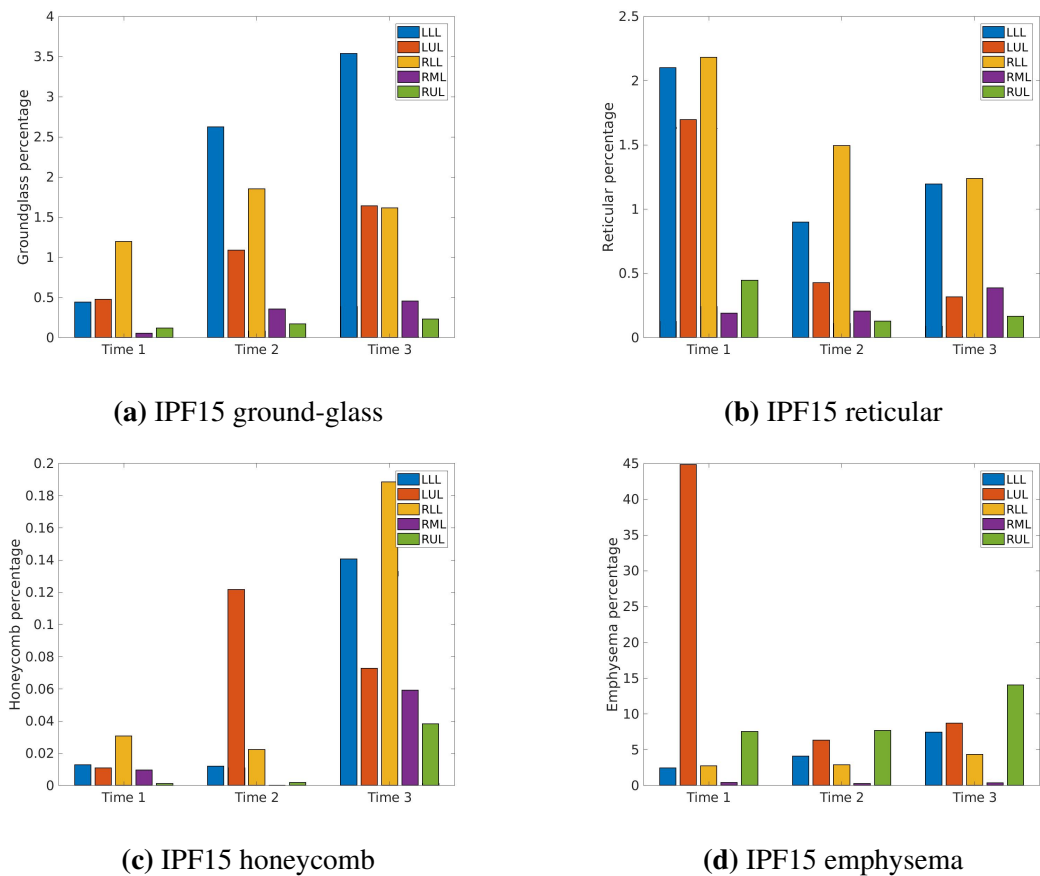


Figure B.29: Lobar distribution of disease CT patterns of case IPF15 diagnosed with IPF over time. The tissue percentage in different lobe is shown in different color, and each bar represents the volume percentage of the CT pattern for one lobe. (a) Ground-glass lobar distribution. (b) Reticular lobar distribution. (c) Honeycomb lobar distribution. (d) Emphysema lobar distribution.

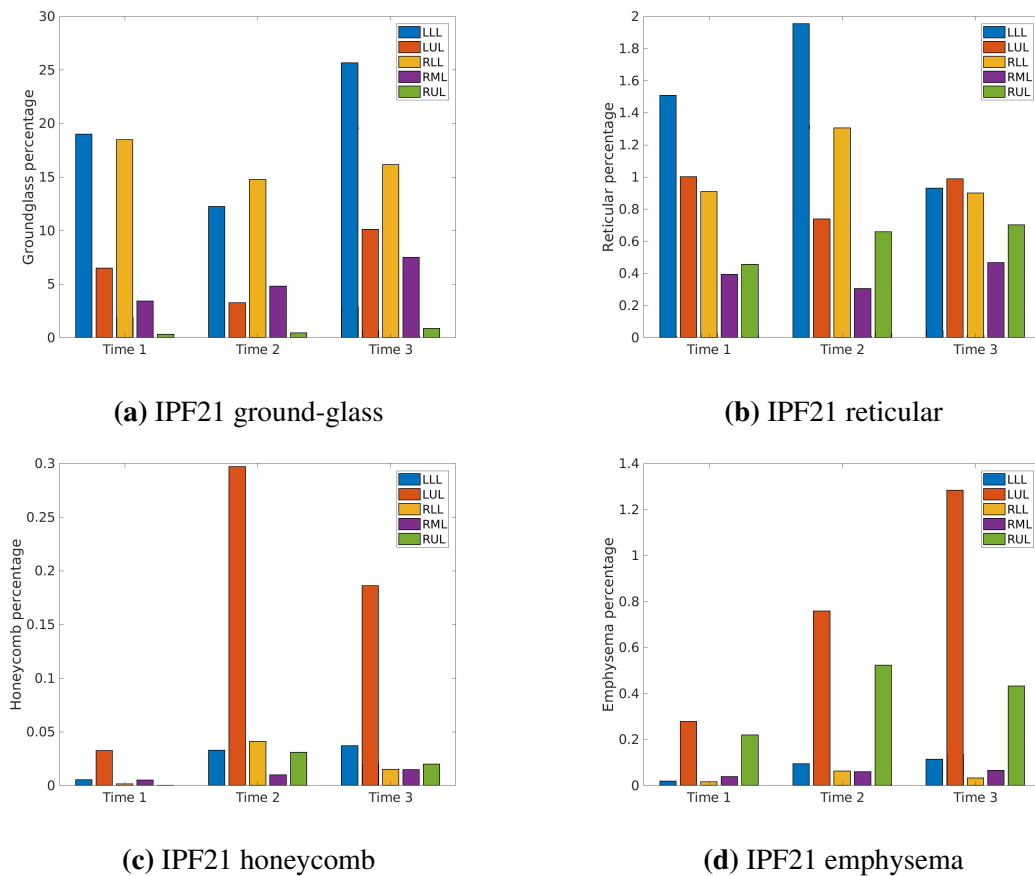


Figure B.30: Lobar distribution of disease CT patterns of case IPF21 diagnosed with IPF over time. The tissue percentage in different lobe is shown in different color, and each bar represents the volume percentage of the CT pattern for one lobe. (a) Ground-glass lobar distribution. (b) Reticular lobar distribution. (c) Honeycomb lobar distribution. (d) Emphysema lobar distribution.

Appendix C

Figures of V/Q ratio and arterial oxygen distribution

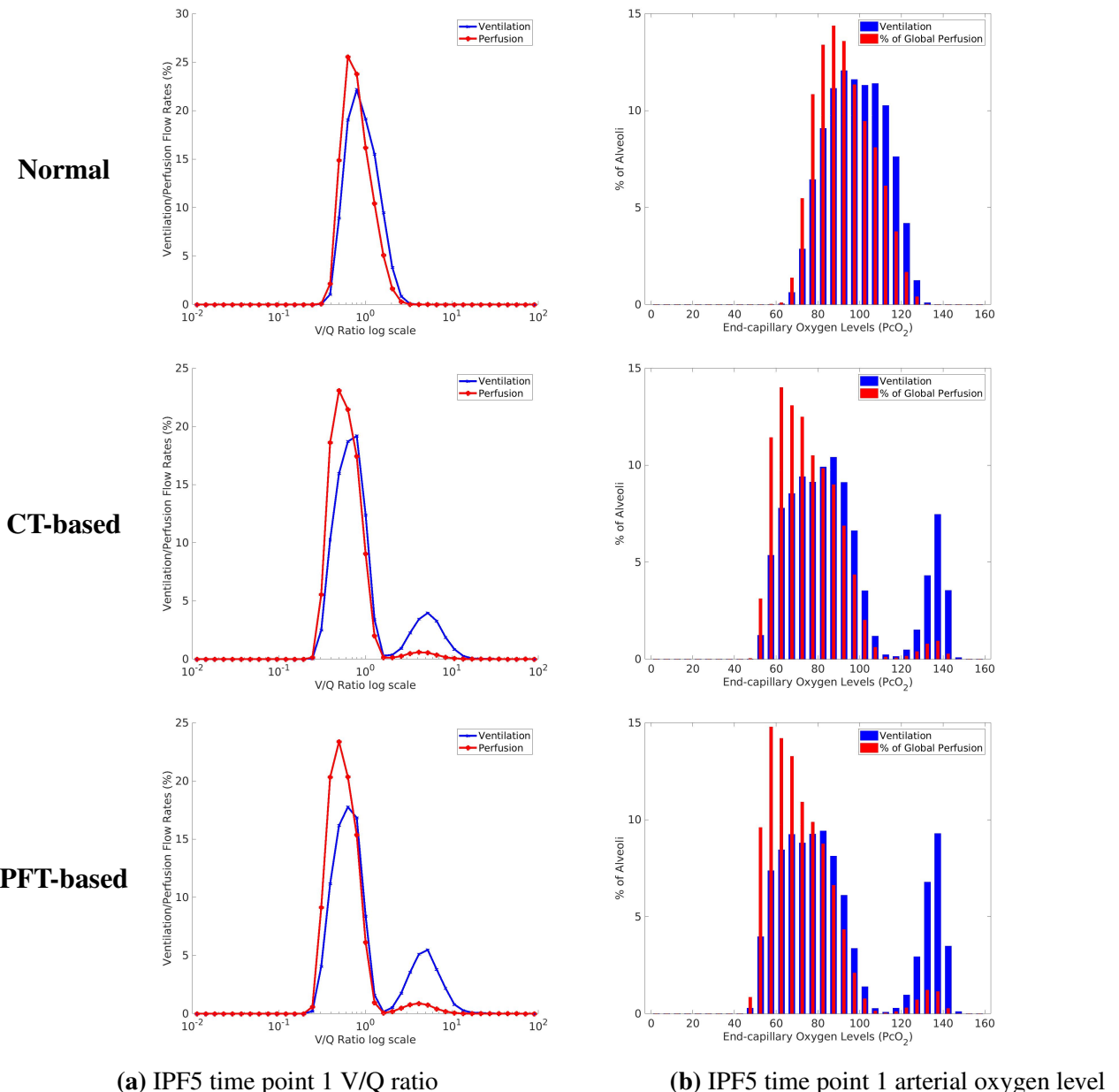
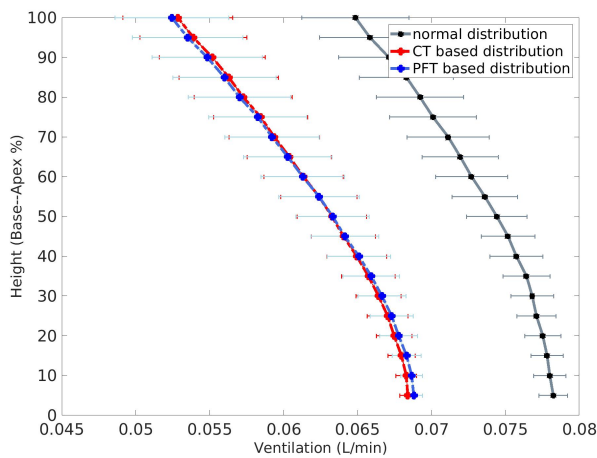
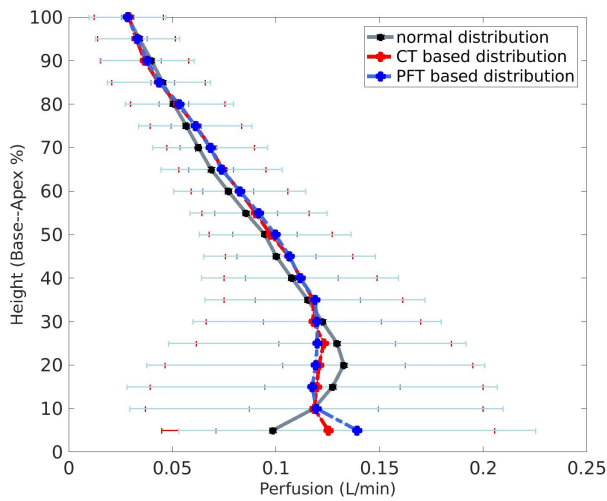


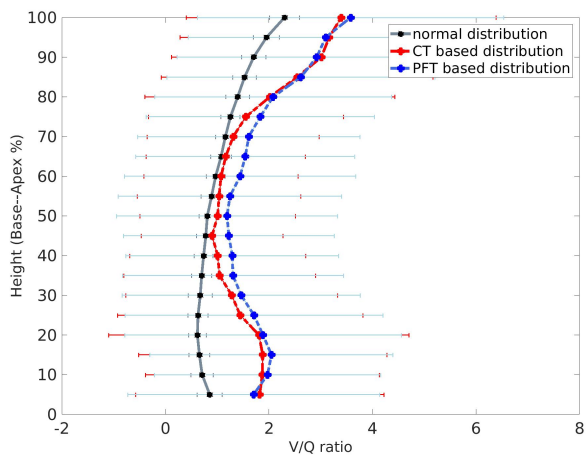
Figure C.1: V/Q ratio distribution and end-capillary oxygen distribution of control, CT-based and PFT-based simulation result at the first time point of case IPF5. (a) V and Q with respect to V/Q ratio. (b) Distribution of end-capillary oxygen levels amongst alveoli.



(a) IPF5 time point 1 ventilation distribution



(b) IPF5 time point 1 perfusion distribution



(c) IPF5 time point 1 V/Q ratio distribution

Figure C.2: Ventilation, perfusion and V/Q ratio distribution against lung height (cranio-caudal axis) of the first time point of case IPF5. (a) Ventilation distribution against lung height. (b) Perfusion distribution against lung height. (c) V/Q ratio distribution against lung height.

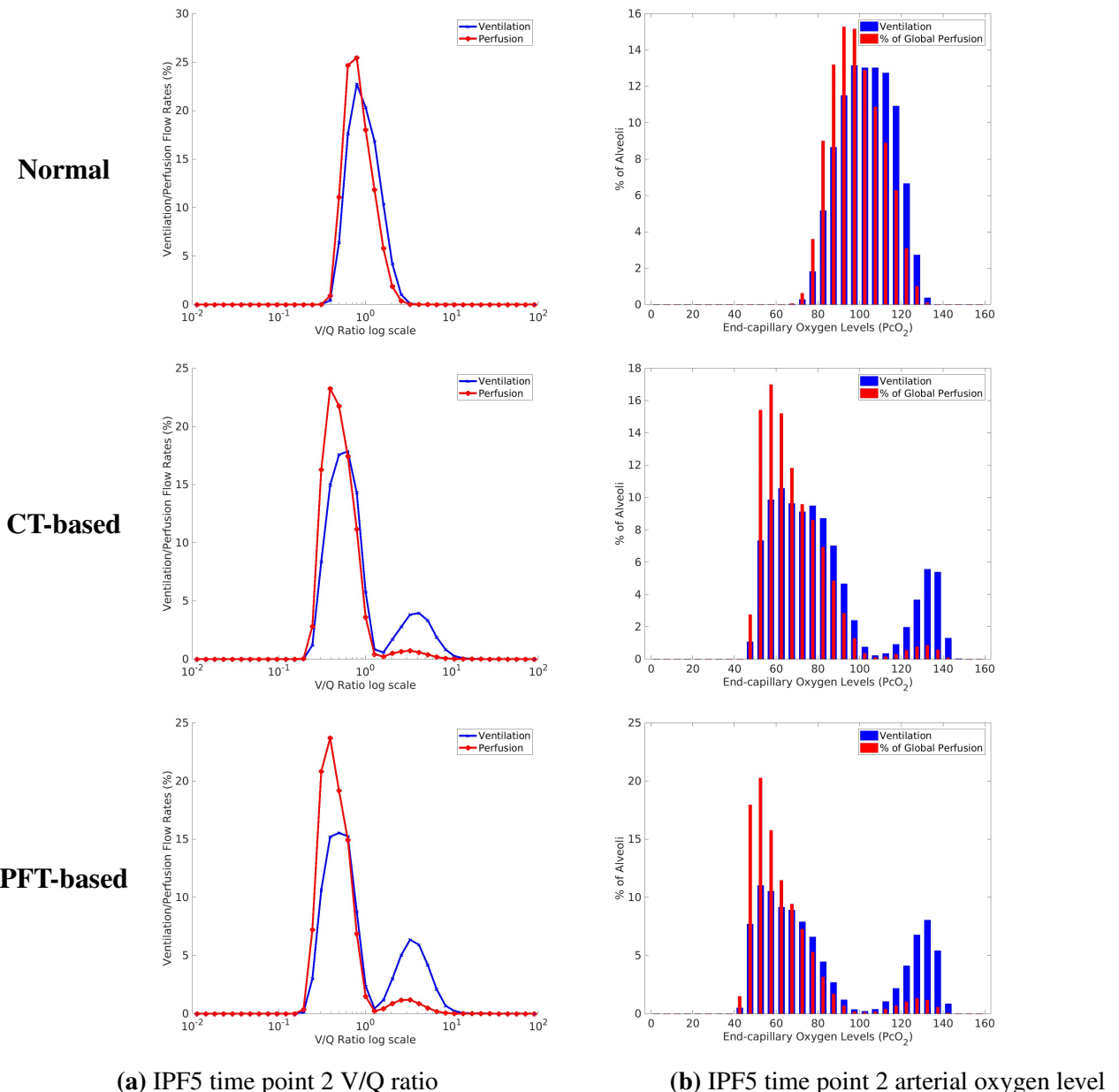
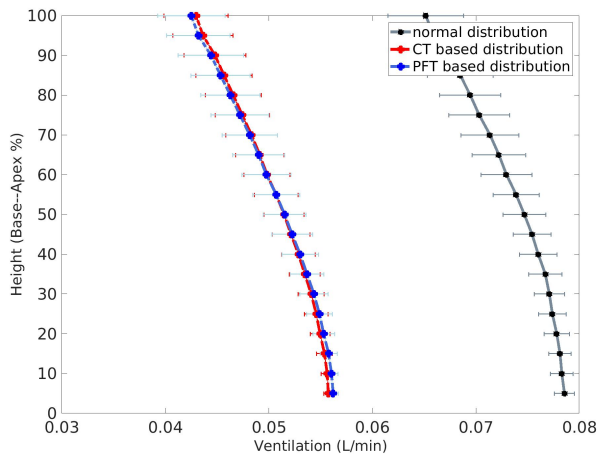
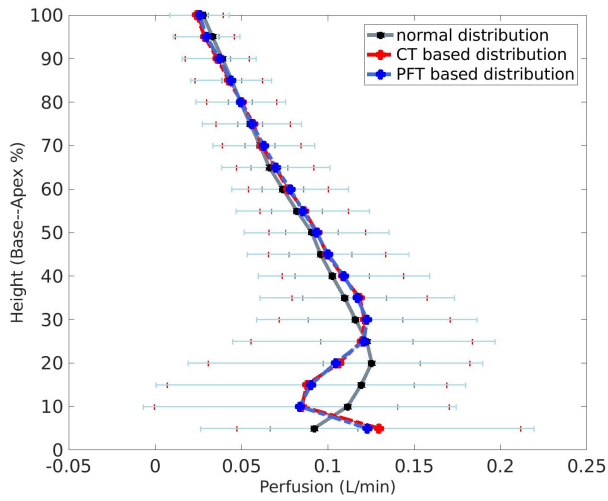


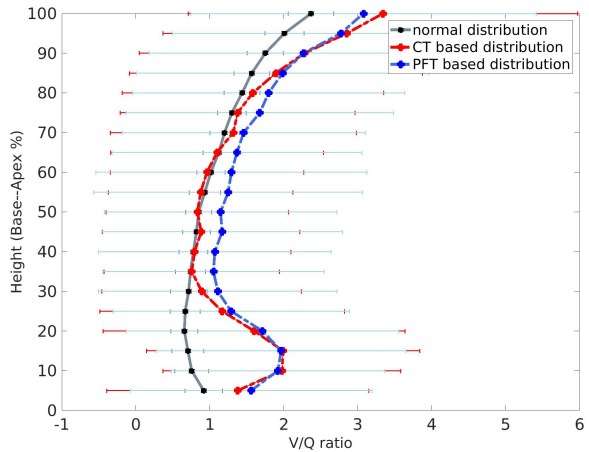
Figure C.3: V/Q ratio distribution and end-capillary oxygen distribution of control, CT-based and PFT-based simulation result at the second time point of case IPF5). (a) V and Q with respect to V/Q ratio. (b) Distribution of end-capillary oxygen levels amongst alveoli.



(a) IPF5 time point 2 ventilation distribution



(b) IPF5 time point 2 perfusion distribution



(c) IPF5 time point 2 V/Q ratio distribution

Figure C.4: Ventilation, perfusion and V/Q ratio distribution against lung height (cranio-caudal axis) of the second time point of case IPF5. (a) Ventilation distribution against lung height. (b) Perfusion distribution against lung height. (c) V/Q ratio distribution against lung height.

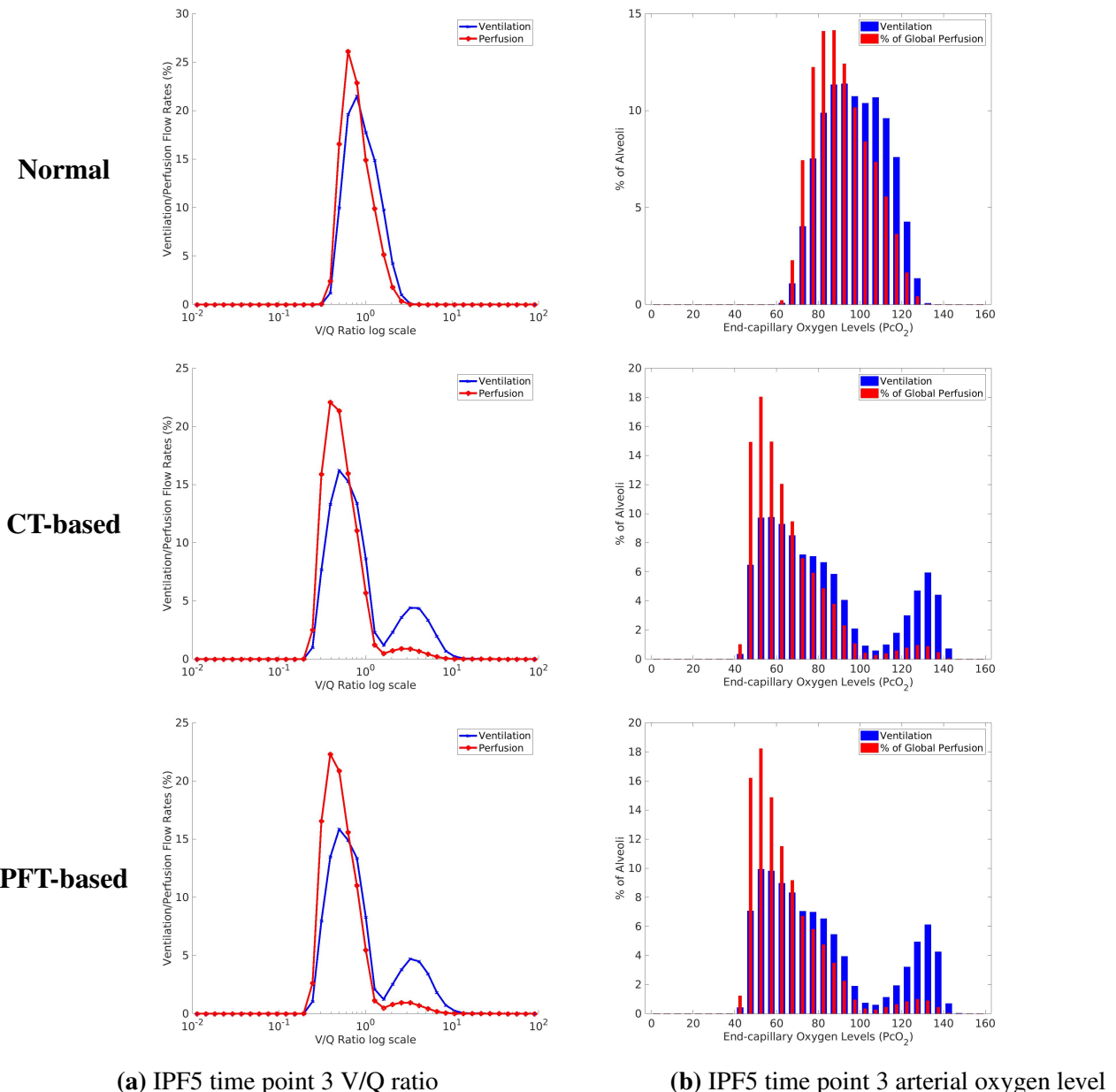
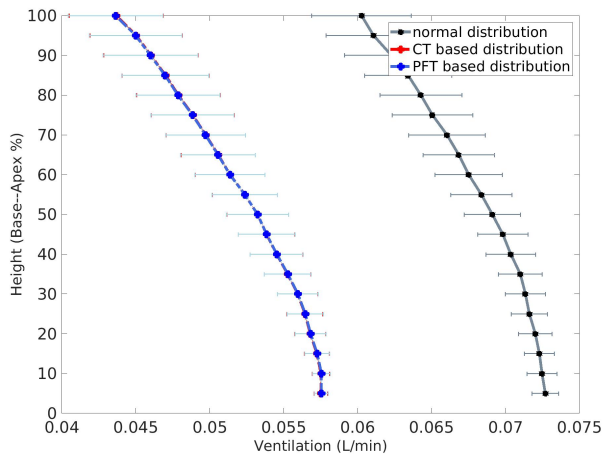
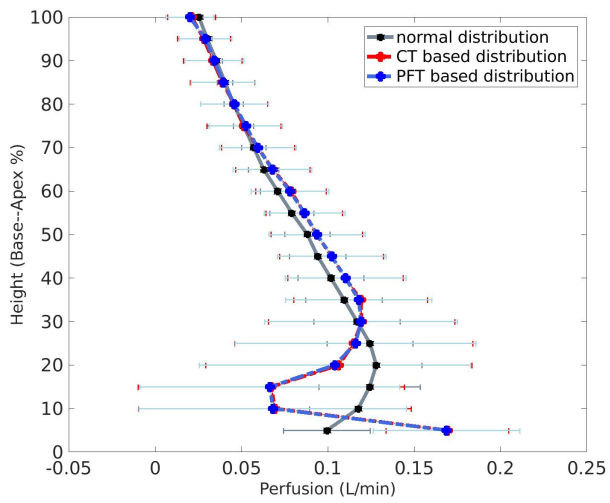


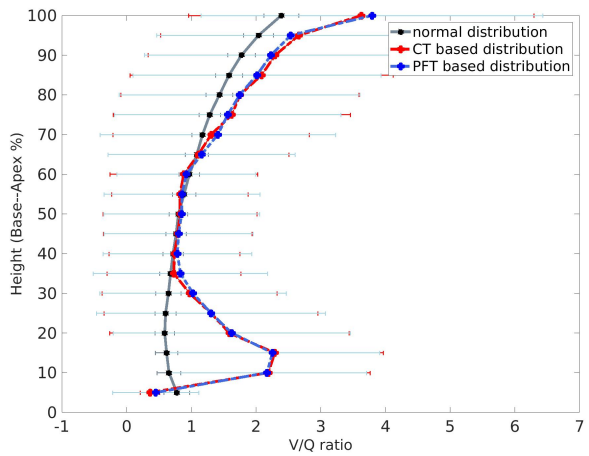
Figure C.5: V/Q ratio distribution and end-capillary oxygen distribution of control, CT-based and PFT-based simulation result at the third time point of case IPF5). (a) V and Q with respect to V/Q ratio. (b) Distribution of end-capillary oxygen levels amongst alveoli.



(a) IPF5 time point 3 ventilation distribution



(b) IPF5 time point 3 perfusion distribution



(c) IPF5 time point 3 V/Q ratio distribution

Figure C.6: Ventilation, perfusion and V/Q ratio distribution against lung height (cranio-caudal axis) of the third time point of case IPF5. (a) Ventilation distribution against lung height. (b) Perfusion distribution against lung height. (c) V/Q ratio distribution against lung height.

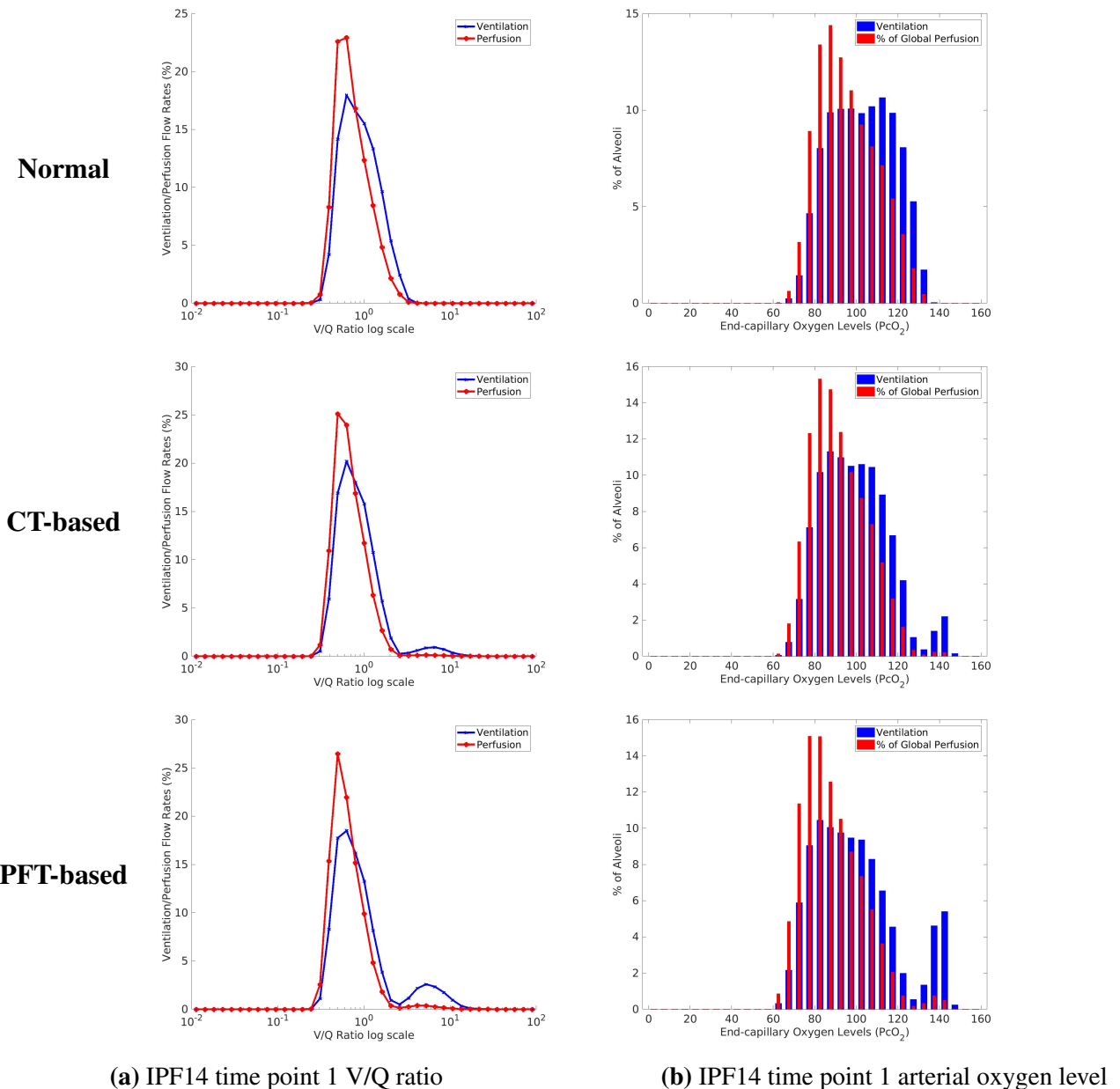
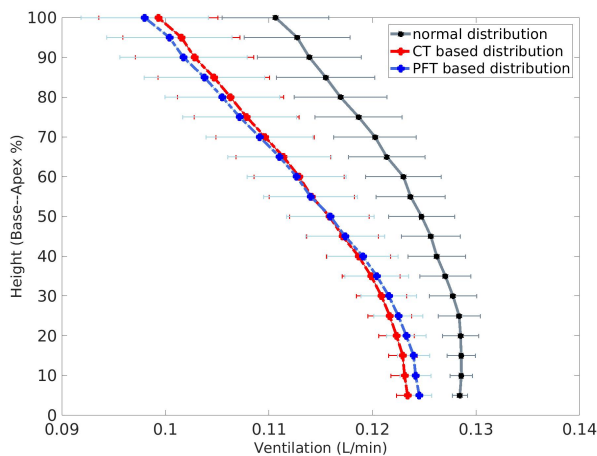
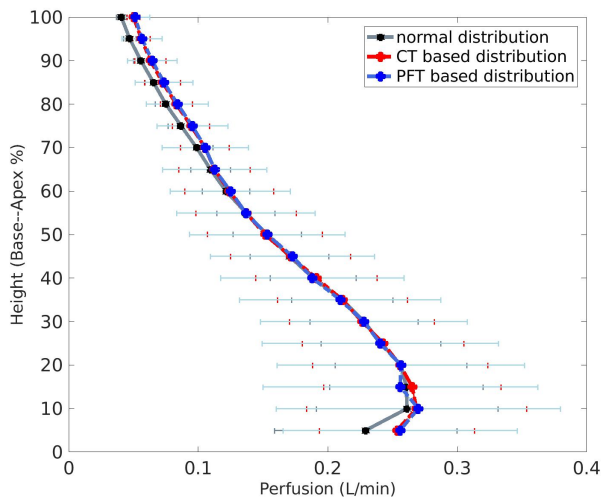


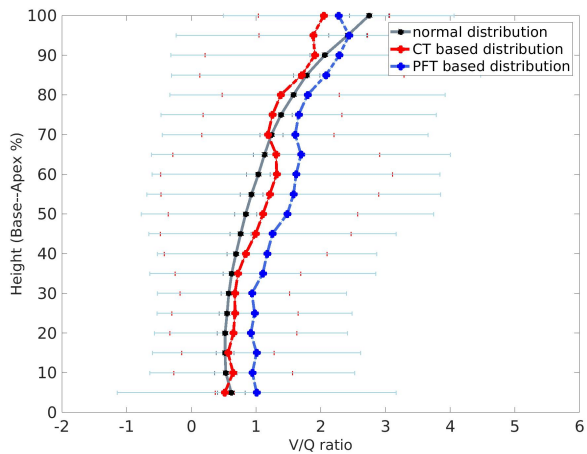
Figure C.7: V/Q ratio distribution and end-capillary oxygen distribution of control, CT-based and PFT-based simulation result at the first time point of case IPF14. (a) V and Q with respect to V/Q ratio. (b) Distribution of end-capillary oxygen levels amongst alveoli.



(a) IPF14 time point 1 ventilation distribution



(b) IPF14 time point 1 perfusion distribution



(c) IPF14 time point 1 V/Q ratio distribution

Figure C.8: Ventilation, perfusion and V/Q ratio distribution against lung height (cranio-caudal axis) of the first time point of case IPF14. (a) Ventilation distribution against lung height. (b) Perfusion distribution against lung height. (c) V/Q ratio distribution against lung height.

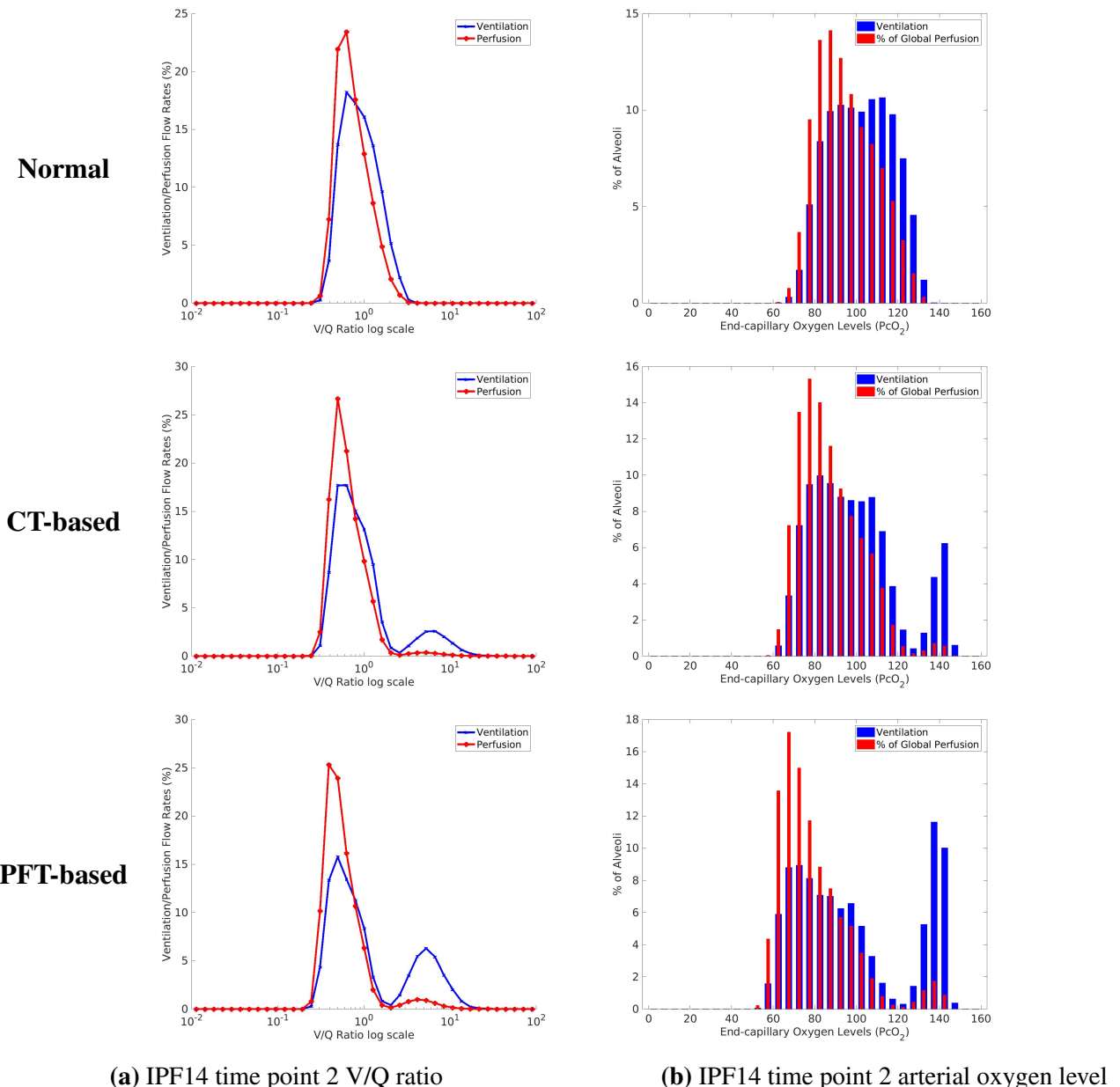
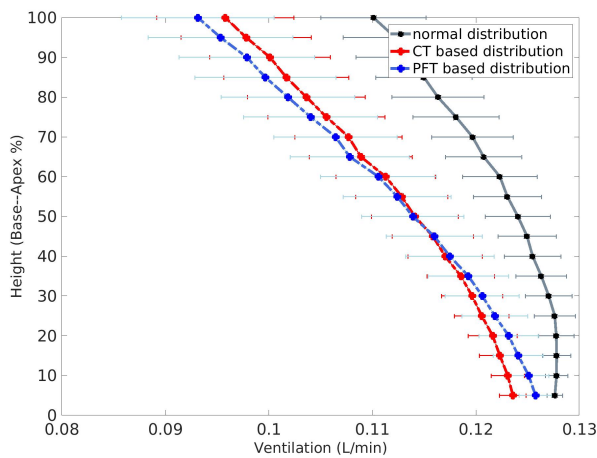
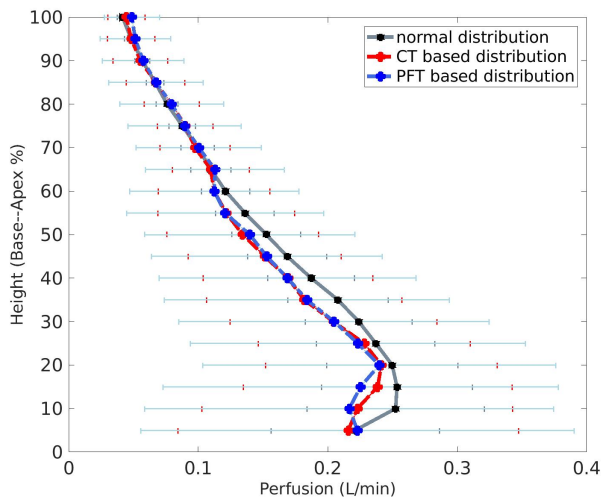


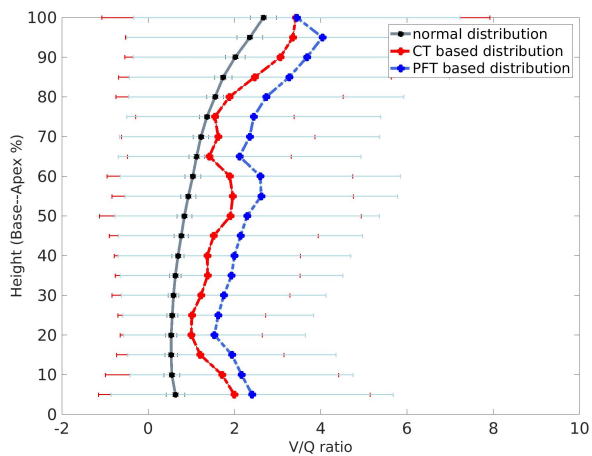
Figure C.9: V/Q ratio distribution and end-capillary oxygen distribution of control, CT-based and PFT-based simulation result at the second time point of case IPF14). (a) V and Q with respect to V/Q ratio. (b) Distribution of end-capillary oxygen levels amongst alveoli.



(a) IPF14 time point 2 ventilation distribution



(b) IPF14 time point 2 perfusion distribution



(c) IPF14 time point 2 V/Q ratio distribution

Figure C.10: Ventilation, perfusion and V/Q ratio distribution against lung height (cranio-caudal axis) of the second time point of case IPF14. (a) Ventilation distribution against lung height. (b) Perfusion distribution against lung height. (c) V/Q ratio distribution against lung height.

List of References

- Agustí, A. G., Roca, J., Gea, J., Wagner, P. D., Xaubet, A., and Rodriguez-Roisin, R. (1991). Mechanisms of gas-exchange impairment in idiopathic pulmonary fibrosis. *American Review of Respiratory Disease*, 143(2):219–225. [Cited on pages 30 and 32.]
- Agusti, C., Xaubet, A., Agusti, A., Roca, J., Ramirez, J., and Rodriguez-Roisin, R. (1994). Clinical and functional assessment of patients with idiopathic pulmonary fibrosis: results of a 3 year follow-up. *European Respiratory Journal*, 7(4):643–650. [Cited on page 30.]
- Ahluwalia, N., Shea, B. S., and Tager, A. M. (2014). New therapeutic targets in idiopathic pulmonary fibrosis. aiming to rein in runaway wound-healing responses. *American Journal of Respiratory and Critical Care Medicine*, 190(8):867–878. [Cited on page 8.]
- Aho, K., Derryberry, D., and Peterson, T. (2014). Model selection for ecologists: the worldviews of aic and bic. *Ecology*, 95(3):631–636. [Cited on page 160.]
- Alder, J. K., Chen, J. J.-L., Lancaster, L., Danoff, S., Su, S.-c., Cogan, J. D., Vulto, I., Xie, M., Qi, X., Tuder, R. M., et al. (2008). Short telomeres are a risk factor for idiopathic pulmonary fibrosis. *Proceedings of the National Academy of Sciences*, 105(35):13051–13056. [Cited on page 12.]

- Allam, J. S. and Limper, A. H. (2006). Idiopathic pulmonary fibrosis: is it a familial disease? *Current Opinion in Pulmonary Medicine*, 12(5):312–317. [Cited on page 12.]
- Ambrosini, V., Cancellieri, A., Chilosi, M., Zompatori, M., Trisolini, R., Saragoni, L., and Poletti, V. (2003). Acute exacerbation of idiopathic pulmonary fibrosis: report of a series. *European Respiratory Journal*, 22(5):821–826. [Cited on page 20.]
- Armato, S. G. and Sensakovic, W. F. (2004). Automated lung segmentation for thoracic ct: Impact on computer-aided diagnosis1. *Academic Radiology*, 11(9):1011–1021. [Cited on page 43.]
- Arora, N. S. and Rochester, D. F. (1982). Respiratory muscle strength and maximal voluntary ventilation in undernourished patients. *American Review of Respiratory Disease*, 126(1):5–8. [Cited on page 153.]
- Arzhaeva, Y., Prokop, M., Tax, D. M., De Jong, P. A., Schaefer-Prokop, C. M., and van Ginneken, B. (2007). Computer-aided detection of interstitial abnormalities in chest radiographs using a reference standard based on computed tomography. *Medical Physics*, 34(12):4798–4809. [Cited on page 99.]
- Azuma, A., Nukiwa, T., Tsuboi, E., Suga, M., Abe, S., Nakata, K., Taguchi, Y., Nagai, S., Itoh, H., Ohi, M., et al. (2005). Double-blind, placebo-controlled trial of pirfenidone in patients with idiopathic pulmonary fibrosis. *American Journal of Respiratory and Critical Care Medicine*, 171(9):1040–1047. [Cited on page 20.]
- Bartholmai, B. J., Raghunath, S., Karwoski, R. A., Moua, T., Rajagopalan, S., Maldonado, F., Decker, P. A., and Robb, R. A. (2013). Quantitative ct imaging of interstitial lung diseases. *Journal of Thoracic Imaging*, 28(5). [Cited on pages 93, 94, 95, 96, 100, 101, 103, and 104.]
- Baumgartner, K. B., Samet, J. M., Stidley, C. A., Colby, T. V., and Waldron, J. A. (1997).

- Cigarette smoking: a risk factor for idiopathic pulmonary fibrosis. *American Journal of Respiratory and Critical Care Medicine*, 155(1):242–248. [Cited on page 11.]
- Behr, J., Mehnert, F., Beinert, T., et al. (1992). Evaluation of interstitial lung disease by quantitative high-resolution computed tomography. *Am Rev Respir Dis*, 145(Suppl.):A191. [Cited on page 97.]
- Best, A. C., Lynch, A. M., Bozic, C. M., Miller, D., Grunwald, G. K., and Lynch, D. A. (2003). Quantitative ct indexes in idiopathic pulmonary fibrosis: relationship with physiologic impairment. *Radiology*, 228(2):407–414. [Cited on page 99.]
- Best, A. C., Meng, J., Lynch, A. M., Bozic, C. M., Miller, D., Grunwald, G. K., and Lynch, D. A. (2008). Idiopathic pulmonary fibrosis: physiologic tests, quantitative ct indexes, and ct visual scores as predictors of mortality. *Radiology*, 246(3):935–940. [Cited on pages 96 and 99.]
- Bjoraker, J. A., Ryu, J. H., Edwin, M. K., Myers, J. L., Tazelaar, H. D., Schroeder, D. R., and Offord, K. P. (1998). Prognostic significance of histopathologic subsets in idiopathic pulmonary fibrosis. *American Journal of Respiratory and Critical Care Medicine*, 157(1):199–203. [Cited on pages 19 and 95.]
- Bradley, C., Pullan, A., and Hunter, P. (1997). Geometric modeling of the human torso using cubic hermite elements. *Annals of Biomedical Engineering*, 25(1):96–111. [Cited on page 59.]
- Brandfonbrener, M., Landowne, M., and Shock, N. W. (1955). Changes in cardiac output with age. *Circulation*, 12(4):557–566. [Cited on page 180.]
- Brandstetter, R. D. and Kazemi, H. (1983). Aging and the respiratory system. *Medical Clinics of North America*, 67(2):419–431. [Cited on page 154.]
- Breatnach, E., Abbott, G. C., and Fraser, R. G. (1984). Dimensions of the normal human trachea. *American Journal of Roentgenology*, 142(5):903–906. [Cited on page 165.]

- Butler, C. and Kleinerman, J. (1970). Capillary density: alveolar diameter, a morphometric approach to ventilation and perfusion. *American Review of Respiratory Disease*, 102(6):886–894. [Cited on page 155.]
- Carrington, C. B., Gaensler, E. A., Coutu, R. E., FitzGerald, M. X., and Gupta, R. G. (1978). Natural history and treated course of usual and desquamative interstitial pneumonia. *New England Journal of Medicine*, 298(15):801–809. [Cited on page 19.]
- Castaldi, P. J., San José Estépar, R., Mendoza, C. S., Hersh, C. P., Laird, N., Crapo, J. D., Lynch, D. A., Silverman, E. K., and Washko, G. R. (2013). Distinct quantitative computed tomography emphysema patterns are associated with physiology and function in smokers. *American Journal of Respiratory and Critical Care Medicine*, 188(9):1083–1090. [Cited on page 97.]
- Chabat, F., Yang, G.-Z., and Hansell, D. M. (2003). Obstructive lung diseases: texture classification for differentiation at ct. *Radiology*, 228(3):871–877. [Cited on page 99.]
- Chakraborty, S., Balakotaiah, V., and Bidani, A. (2004). Diffusing capacity reexamined: relative roles of diffusion and chemical reaction in red cell uptake of o₂, co, co₂, and no. *Journal of Applied Physiology*, 97(6):2284–2302. [Cited on pages 175 and 176.]
- Cherniack, R. M., Colby, T. V., Flint, A., Thurlbeck, W. M., Waldron Jr, J. A., Ackerson, L., Schwarz, M. I., and King Jr, T. E. (1995). Correlation of structure and function in idiopathic pulmonary fibrosis. *American Journal of Respiratory and Critical Care Medicine*, 151(4):1180–1188. [Cited on page 27.]
- Chilosi, M., Poletti, V., Murer, B., Lestani, M., Cancellieri, A., Montagna, L., Piccoli, P., Cangi, G., Semenzato, G., and Doglioni, C. (2002). Abnormal re-epithelialization and lung remodeling in idiopathic pulmonary fibrosis: the role of δn-p63. *Laboratory Investigation*, 82(10):1335. [Cited on page 27.]

- Clark, A., Milne, D., Wilsher, M., Burrowes, K., Bajaj, M., and Tawhai, M. (2014). Lack of functional information explains the poor performance of ‘clot load scores’ at predicting outcome in acute pulmonary embolism. *Respiratory Physiology & Neurobiology*, 190:1–13. [Cited on pages 167 and 173.]
- Clark, A. R., Burrowes, K. S., and Tawhai, M. H. (2010). Contribution of serial and parallel microperfusion to spatial variability in pulmonary inter-and intra-acinar blood flow. *Journal of Applied Physiology*, 108(5):1116–1126. [Cited on pages 165, 167, and 176.]
- Clark, A. R., Tawhai, M. H., Hoffman, E. A., and Burrowes, K. S. (2011). The interdependent contributions of gravitational and structural features to perfusion distribution in a multiscale model of the pulmonary circulation. *Journal of Applied Physiology*, 110(4):943–955. [Cited on pages 165, 167, 170, 175, and 196.]
- Coelho-Ravagnani, C. d. F., Melo, F. C. L., Ravagnani, F. C., Burini, F. H. P., and Burini, R. C. (2013). Estimation of metabolic equivalent (met) of an exercise protocol based on indirect calorimetry. *Revista Brasileira de Medicina do Esporte*, 19(2):134–138. [Cited on page 181.]
- Cootes, T. F., Taylor, C. J., Cooper, D. H., and Graham, J. (1995). Active shape models—their training and application. *Computer Vision and Image Understanding*, 61(1):38–59. [Cited on page 56.]
- Corte, T. J., Collard, H., and Wells, A. U. (2015). Idiopathic interstitial pneumonias in 2015: A new era. *Respirology*, 20(5):697–698. [Cited on page 9.]
- Cortes-Telles, A., Forkert, L., O’Donnell, D. E., and Morán-Mendoza, O. (2014). Idiopathic pulmonary fibrosis: New insights to functional characteristics at diagnosis. *Canadian Respiratory Journal*, 21(3):e55–e60. [Cited on pages 24, 30, and 207.]

- Cosgrove, G. P., Brown, K. K., Schiemann, W. P., Serls, A. E., Parr, J. E., Geraci, M. W., Schwarz, M. I., Cool, C. D., and Worthen, G. S. (2004). Pigment epithelium-derived factor in idiopathic pulmonary fibrosis: a role in aberrant angiogenesis. *American Journal of Respiratory and Critical Care Medicine*, 170(3):242–251. [Cited on pages 28 and 199.]
- Costabel, U., Du Bois, R. M., and Egan, J. J. (2007). Diffuse parenchymal lung disease, volume 36. Karger Medical and Scientific Publishers. [Cited on page 96.]
- Cottin, V., Le Pavec, J., Prévot, G., Mal, H., Humbert, M., Simonneau, G., Cordier, J.-F., et al. (2010). Pulmonary hypertension in patients with combined pulmonary fibrosis and emphysema syndrome. *European Respiratory Journal*, 35(1):105–111. [Cited on page 22.]
- Cottin, V., Nunes, H., Brillet, P., Delaval, P., Devouassoux, G., Tillie-Leblond, I., Israel-Biet, D., Valeyre, D., Cordier, J., et al. (2005). Combined pulmonary fibrosis and emphysema: a distinct underrecognised entity. *European Respiratory Journal*, 26(4):586–593. [Cited on pages 22 and 200.]
- Coxson, H. (2007). Computed tomography and monitoring of emphysema. [Cited on page 38.]
- Crapo, R. (1993). The aging lung. *Lung Biology in Health and Disease*, 63:1–25. [Cited on pages 55, 151, and 154.]
- Crystal, R. G., Fulmer, J. D., Roberts, W. C., Moss, M. L., Line, B. R., and Reynolds, H. Y. (1976). Idiopathic pulmonary fibrosis: clinical, histologic, radiographic, physiologic, scintigraphic, cytologic, and biochemical aspects. *Annals of Internal Medicine*, 85(6):769–788. [Cited on pages 24, 28, 29, 30, 31, 32, 164, and 180.]
- da Silva Felix, J. H., Cortez, P. C., Rebouças Filho, P. P., de Alexandria, A. R., Costa, R. C. S., and Holanda, M. A. (2008). Identification and quantification of pulmonary

- emphysema through pseudocolors. In Mexican International Conference on Artificial Intelligence, pages 957–964. Springer. [Cited on page 97.]
- De Troyer, A. and Yernault, J.-C. (1980). Inspiratory muscle force in normal subjects and patients with interstitial lung disease. *Thorax*, 35(2):92–100. [Cited on pages 179 and 197.]
- Delorme, S., Keller-Reichenbecher, M.-A., Zuna, I., Schlegel, W., and Van Kaick, G. (1997). Usual interstitial pneumonia: quantitative assessment of high-resolution computed tomography findings by computer-assisted texture-based image analysis. *Investigative Radiology*, 32(9):566–574. [Cited on page 97.]
- Depeursinge, A., Iavindrasana, J., Hidki, A., Cohen, G., Geissbuhler, A., Platon, A., Poletti, P.-A., and Müller, H. (2010). Comparative performance analysis of state-of-the-art classification algorithms applied to lung tissue categorization. *Journal of Digital Imaging*, 23(1):18–30. [Cited on page 97.]
- Devaraj, A. (2014). Imaging: how to recognise idiopathic pulmonary fibrosis. *European Respiratory Review*, 23(132):215–219. [Cited on pages 94, 95, and 146.]
- Diaz, A. A., Valim, C., Yamashiro, T., EstŠpar, R. S. J., Ross, J. C., Matsuoka, S., Bartholmai, B., Hatabu, H., Silverman, E. K., and Washko, G. R. (2010). Airway count and emphysema assessed by chest ct imaging predicts clinical outcome in smokers. *CHEST Journal*, 138(4):880–887. [Cited on page 38.]
- Diette, G. B., Scatarige, J. C., Haponik, E. F., Merriman, B., and Fishman, E. K. (2005). Do high-resolution ct findings of usual interstitial pneumonitis obviate lung biopsy? *Respiration*, 72(2):134–141. [Cited on page 96.]
- Doel, T., Gavaghan, D. J., and Grau, V. (2015). Review of automatic pulmonary lobe segmentation methods from ct. *Computerized Medical Imaging and Graphics*, 40:13–29. [Cited on pages xv, 36, 37, and 40.]

- Doel, T., Matin, T. N., Gleeson, F. V., Gavaghan, D. J., and Grau, V. (2012). Pulmonary lobe segmentation from ct images using fissureness, airways, vessels and multilevel b-splines. In *Biomedical Imaging (ISBI), 2012 9th IEEE International Symposium on*, pages 1491–1494. IEEE. [Cited on pages 48, 49, 50, 51, 52, and 89.]
- Doherty, M., Pearson, M., O’grady, E., Pellegrini, V., and Calverley, P. (1997). Cryptogenic fibrosing alveolitis with preserved lung volumes. *Thorax*, 52(11):998–1002. [Cited on page 27.]
- Douglas, W. W., Ryu, J. H., and Schroeder, D. R. (2000). Idiopathic pulmonary fibrosis: impact of oxygen and colchicine, prednisone, or no therapy on survival. *American Journal of Respiratory and Critical Care Medicine*, 161(4):1172–1178. [Cited on pages 13 and 14.]
- Dryden, I. L. and Mardia, K. V. (1998). *Statistical shape analysis*, volume 4. Wiley Chichester. [Cited on pages 56 and 61.]
- Du Bois, R. M., Weycker, D., Albera, C., Bradford, W. Z., Costabel, U., Kartashov, A., Lancaster, L., Noble, P. W., Raghu, G., Sahn, S. A., et al. (2011). Ascertainment of individual risk of mortality for patients with idiopathic pulmonary fibrosis. *American Journal of Respiratory and Critical Care Medicine*, 184(4):459–466. [Cited on page 27.]
- Ebina, M., Shimizukawa, M., Shibata, N., Kimura, Y., Suzuki, T., Endo, M., Sasano, H., Kondo, T., and Nukiwa, T. (2004). Heterogeneous increase in cd34-positive alveolar capillaries in idiopathic pulmonary fibrosis. *American Journal of Respiratory and Critical Care Medicine*, 169(11):1203–1208. [Cited on pages 28 and 199.]
- Ecabert, O., Peters, J., Schramm, H., Lorenz, C., von Berg, J., Walker, M. J., Vembar, M., Olszewski, M. E., Subramanyan, K., Lavi, G., et al. (2008). Automatic model-

- based segmentation of the heart in ct images. *IEEE Transactions on Medical Imaging*, 27(9):1189–1201. [Cited on page 56.]
- El-Baz, A., Beache, G. M., Gimel’farb, G., Suzuki, K., Okada, K., Elnakib, A., Soliman, A., and Abdollahi, B. (2013). Computer-aided diagnosis systems for lung cancer: challenges and methodologies. *International Journal of Biomedical Imaging*, 2013. [Cited on page 38.]
- Fernandez, J. W. (2004). An anatomically based finite element model of patella articulation: towards a diagnostic tool. PhD thesis, University of Auckland. [Cited on page 59.]
- Finley, T., Swenson, E., and Comroe, J. (1962). The cause of arterial hypoxemia at rest in patients with “alveolar-capillary block syndrome”. *The Journal of Clinical Investigation*, 41(3):618–622. [Cited on page 32.]
- Flaherty, K., Thwaite, E., Kazerooni, E., Gross, B., Toews, G., Colby, T. V., Travis, W., Mumford, J., Murray, S., Flint, A., et al. (2003). Radiological versus histological diagnosis in uip and nsip: survival implications. *Thorax*, 58(2):143–148. [Cited on page 17.]
- Flaherty, K., Toews, G., Travis, W., Colby, T., Kazerooni, E., Gross, B., Jain, A., Strawderman, R., Paine, R., Flint, A., et al. (2002). Clinical significance of histological classification of idiopathic interstitial pneumonia. *European Respiratory Journal*, 19(2):275–283. [Cited on page 19.]
- Flaherty, K. R., Andrei, A.-C., King Jr, T. E., Raghu, G., Colby, T. V., Wells, A., Bassily, N., Brown, K., Du Bois, R., Flint, A., et al. (2007). Idiopathic interstitial pneumonia: do community and academic physicians agree on diagnosis? *American Journal of Respiratory and Critical Care Medicine*, 175(10):1054–1060. [Cited on page 94.]

- Flaherty, K. R., King Jr, T. E., Raghu, G., Lynch III, J. P., Colby, T. V., Travis, W. D., Gross, B. H., Kazerooni, E. A., Toews, G. B., Long, Q., et al. (2004). Idiopathic interstitial pneumonia: what is the effect of a multidisciplinary approach to diagnosis? *American Journal of Respiratory and Critical Care Medicine*, 170(8):904–910. [Cited on pages 12 and 95.]
- Flaherty, K. R., Travis, W. D., Colby, T. V., Toews, G. B., Kazerooni, E. A., Gross, B. H., Jain, A., Strawderman I, R. L., Flint, A., Lynch III, J. P., et al. (2001). Histopathologic variability in usual and nonspecific interstitial pneumonias. *American Journal of Respiratory and Critical Care Medicine*, 164(9):1722–1727. [Cited on page 95.]
- Florack, L. M., ter Haar Romeny, B. M., Koenderink, J. J., and Viergever, M. A. (1992). Scale and the differential structure of images. *Image and Vision Computing*, 10(6):376–388. [Cited on page 65.]
- Frangi, A. F., Niessen, W. J., Vincken, K. L., and Viergever, M. A. (1998). Multiscale vessel enhancement filtering. In *International Conference on Medical Image Computing and Computer-Assisted Intervention*, pages 130–137. Springer. [Cited on pages 48, 51, 64, 65, 69, and 70.]
- Fulmer, J., Roberts, W., von Gal, E. R., and Crystal, R. (1979). Morphologic-physiologic correlates of the severity of fibrosis and degree of cellularity in idiopathic pulmonary fibrosis. *The Journal of Clinical Investigation*, 63(4):665–676. [Cited on pages 26 and 198.]
- Fulmer, J. D., Crystal, R. G., and Roberts, W. C. (1976). Diffuse fibrotic lung disease: a correlative study. *Chest*, 69(2):263–265. [Cited on page 30.]
- Fung, Y. and Sabin, S. (1969). Theory of sheet flow in lung alveoli. *Journal of Applied Physiology*, 26(4):472–488. [Cited on pages 171 and 176.]

- Fung, Y.-c. (2013). Biomechanics: circulation. Springer Science & Business Media.
[Cited on page 176.]
- Galbán, C. J., Han, M. K., Boes, J. L., Chughtai, K. A., Meyer, C. R., Johnson, T. D., Galbán, S., Rehemtulla, A., Kazerooni, E. A., Martinez, F. J., et al. (2012). Computed tomography-based biomarker provides unique signature for diagnosis of copd phenotypes and disease progression. *Nature Medicine*, 18(11):1711. [Cited on page 97.]
- Gietema, H. A., Müller, N. L., Fauerbach, P. V. N., Sharma, S., Edwards, L. D., Camp, P. G., Coxson, H. O., of COPD Longitudinally to Identify Predictive Surrogate Endpoints (ECLIPSE) investigators, E., et al. (2011). Quantifying the extent of emphysema:: Factors associated with radiologists' estimations and quantitative indices of emphysema severity using the eclipse cohort. *Academic Radiology*, 18(6):661–671.
[Cited on page 97.]
- Gilbert, R., Auchincloss Jr, J., Brodsky, J., and Boden, W. a. (1972). Changes in tidal volume, frequency, and ventilation induced by their measurement. *Journal of Applied Physiology*, 33(2):252–254. [Cited on page 180.]
- Gilman, M. J., Laurens, J. R., Somogyi, J. W., and Honig, E. G. (1983). Ct attenuation values of lung density in sarcoidosis. *Journal of Computer Assisted Tomography*, 7(3):407–410. [Cited on page 97.]
- Glazier, J., Hughes, J., Maloney, J., and West, J. (1969). Measurements of capillary dimensions and blood volume in rapidly frozen lungs. *Journal of Applied Physiology*, 26(1):65–76. [Cited on page 172.]
- Gotway, M. B., Freemer, M. M., and King, T. E. (2007). Challenges in pulmonary fibrosis- 1: Use of high resolution ct scanning of the lung for the evaluation of patients with idiopathic interstitial pneumonias. *Thorax*, 62(6):546–553. [Cited on pages 95 and 96.]

- Gould, G., MacNee, W., McLean, A., Warren, P., Redpath, A., Best, J., Lamb, D., and Flenley, D. (1988). Ct measurements of lung density in life can quantitate distal airspace enlargement—an essential defining feature of human emphysema. *American Review of Respiratory Disease*, 137(2):380–392. [Cited on page 97.]
- Graham, B. L., Brusasco, V., Burgos, F., Cooper, B. G., Jensen, R., Kendrick, A., MacIntyre, N. R., Thompson, B. R., and Wanger, J. (2017). 2017 ers/ats standards for single-breath carbon monoxide uptake in the lung. *European Respiratory Journal*, 49(1):1600016. [Cited on pages 30 and 207.]
- Graham, M. W., Gibbs, J. D., Cornish, D. C., and Higgins, W. E. (2010). Robust 3-d airway tree segmentation for image-guided peripheral bronchoscopy. *IEEE Transactions on Medical Imaging*, 29(4):982–997. [Cited on page 38.]
- Gross, P. (1962). The concept of the hamman-rich syndrome: a critique. *American Review of Respiratory Disease*, 85(6):828–832. [Cited on page 20.]
- Gross, T. J. and Hunninghake, G. W. (2001). Idiopathic pulmonary fibrosis. *New England Journal of Medicine*, 345(7):517–525. [Cited on page 19.]
- Guenard, H. and Marthan, R. (1996). Pulmonary gas exchange in elderly subjects. *European Respiratory Journal*, 9(12):2573–2577. [Cited on page 155.]
- Gülsün, M., Ariyürek, O. M., Cömert, R. B., and Karabulut, N. (2006). Variability of the pulmonary oblique fissures presented by high-resolution computed tomography. *Surgical and Radiologic Anatomy*, 28(3):293–299. [Cited on page 40.]
- Gunther, A., Schmidt, R., Nix, F., Yabut-Perez, M., Guth, C., Rousseau, S., Siebert, C., Grimmerger, F., Morr, H., Velcovsky, H., et al. (1999). Surfactant abnormalities in idiopathic pulmonary fibrosis, hypersensitivity pneumonitis and sarcoidosis. *European Respiratory Journal*, 14(3):565–573. [Cited on pages 24 and 26.]

- Guo, J., Fuld, M., Alford, S., Reinhardt, J., and Hoffman, E. (2008). Pulmonary analysis software suite 9.0: Integrating quantitative measures of function with structural analyses. In First International Workshop on Pulmonary Image Analysis, pages 283–292. [Cited on page 83.]
- Haefeli-Bleuer, B. and Weibel, E. R. (1988). Morphometry of the human pulmonary acinus. *The Anatomical Record*, 220(4):401–414. [Cited on page 163.]
- Hamada, K., Nagai, S., Tanaka, S., Handa, T., Shigematsu, M., Nagao, T., Mishima, M., Kitaichi, M., and Izumi, T. (2007). Significance of pulmonary arterial pressure and diffusion capacity of the lung as prognosticator in patients with idiopathic pulmonary fibrosis. *Chest*, 131(3):650–656. [Cited on page 30.]
- Hansell, D. M., Bankier, A. A., MacMahon, H., McLoud, T. C., Muller, N. L., and Remy, J. (2008). Fleischner society: glossary of terms for thoracic imaging. *Radiology*, 246(3):697–722. [Cited on page 14.]
- Harari, S., Madotto, F., Caminati, A., Conti, S., and Cesana, G. (2016). Epidemiology of idiopathic pulmonary fibrosis in northern italy. *PLoS One*, 11(2):e0147072. [Cited on page 21.]
- Hayes Jr, D., Black, S. M., Tobias, J. D., Kirkby, S., Mansour, H. M., and Whitson, B. A. (2016). Influence of pulmonary hypertension on patients with idiopathic pulmonary fibrosis awaiting lung transplantation. *The Annals of Thoracic Surgery*, 101(1):246–252. [Cited on page 23.]
- Hedlund, L., Anderson, R. F., Goulding, P., Beck, J., Effmann, E., and Putman, C. (1982). Two methods for isolating the lung area of a ct scan for density information. *Radiology*, 144(2):353–357. [Cited on pages 42 and 43.]
- Heimann, T. and Meinzer, H.-P. (2009). Statistical shape models for 3d medical image segmentation: a review. *Medical Image Analysis*, 13(4):543–563. [Cited on page 56.]

- Hempleman, S. C. and Hughes, J. (1991). Estimating exercise dlo_2 and diffusion limitation in patients with interstitial fibrosis. *Respiration Physiology*, 83(2):167–178. [Cited on page 32.]
- Hoesein, F. A. M. and De Jong, P. A. (2017). Air trapping on computed tomography: regional versus diffuse. [Cited on page 200.]
- Hoffman, E. A. (1985). Effect of body orientation on regional lung expansion: a computed tomographic approach. *Journal of Applied Physiology*, 59(2):468–480. [Cited on page 43.]
- Hoffman, E. A. and McLennan, G. (1997). Assessment of the pulmonary structure-function relationship and clinical outcomes measures: quantitative volumetric ct of the lung. *Academic Radiology*, 4(11):758–776. [Cited on page 37.]
- Hoffman, E. A. and Ritman, E. L. (1985). Effect of body orientation on regional lung expansion in dog and sloth. *Journal of Applied Physiology*, 59(2):481–491. [Cited on pages 42 and 43.]
- Hoffman, E. A., Simon, B. A., and McLennan, G. (2006). State of the art. a structural and functional assessment of the lung via multidetector-row computed tomography: phenotyping chronic obstructive pulmonary disease. *Proceedings of the American Thoracic Society*, 3(6):519–532. [Cited on page 38.]
- Hoffman, E. A., Sinak, L., Robb, R. A., and Ritman, E. L. (1983). Noninvasive quantitative imaging of shape and volume of lungs. *Journal of Applied Physiology*, 54(5):1414–1421. [Cited on pages 42 and 43.]
- Holland, J., Milic-Emili, J., Macklem, P., and Bates, D. (1968). Regional distribution of pulmonary ventilation and perfusion in elderly subjects. *The Journal of Clinical Investigation*, 47(1):81–92. [Cited on page 155.]

- Horsfield, K. (1978). Morphometry of the small pulmonary arteries in man. *Circulation Research*, 42(5):593–597. [Cited on page 166.]
- Horsfield, K., Dart, G., Olson, D. E., Filley, G. F., and Cumming, G. (1971). Models of the human bronchial tree. *Journal of Applied Physiology*, 31(2):207–217. [Cited on page 166.]
- Horsfield, K. and Gordon, W. (1981). Morphometry of pulmonary veins in man. *Lung*, 159(1):211–218. [Cited on page 166.]
- Horsfield, K., Relea, F. G., and Gumming, G. (1976). Diameter, length and branching ratios in the bronchial tree. *Respiration Physiology*, 26(3):351–356. [Cited on page 164.]
- Hsia, C. C., Hyde, D. M., and Weibel, E. R. (2016). Lung structure and the intrinsic challenges of gas exchange. *Comprehensive Physiology*, 6(2):827. [Cited on page 165.]
- Hu, S., Hoffman, E. A., and Reinhardt, J. M. (2001). Automatic lung segmentation for accurate quantitation of volumetric x-ray ct images. *IEEE Transactions on Medical Imaging*, 20(6):490–498. [Cited on pages 38, 40, 42, 43, and 101.]
- Huang, W., Yen, R., McLaurine, M., and Bledsoe, G. (1996). Morphometry of the human pulmonary vasculature. *Journal of Applied Physiology*, 81(5):2123–2133. [Cited on page 166.]
- Hughes, J., Lockwood, D., Jones, H., and Clark, R. (1991). DLCO/q and diffusion limitation at rest and on exercise in patients with interstitial fibrosis. *Respiration Physiology*, 83(2):155–166. [Cited on page 32.]
- Hunninghake, G. W., Zimmerman, M. B., Schwartz, D. A., KING JR, T. E., Lynch, J., Hegele, R., Waldron, J., Colby, T., Muller, N., Lynch, D., et al. (2001). Utility of a lung biopsy for the diagnosis of idiopathic pulmonary fibrosis. *American Journal of Respiratory and Critical Care Medicine*, 164(2):193–196. [Cited on page 17.]

- Hwang, J.-H., Misumi, S., Sahin, H., Brown, K. K., Newell, J. D., and Lynch, D. A. (2009). Computed tomographic features of idiopathic fibrosing interstitial pneumonia: comparison with pulmonary fibrosis related to collagen vascular disease. *Journal of Computer Assisted Tomography*, 33(3):410–415. [Cited on page 14.]
- Hyldgaard, C., Hilberg, O., Muller, A., and Bendstrup, E. (2014). A cohort study of interstitial lung diseases in central denmark. *Respiratory Medicine*, 108(5):793–799. [Cited on page 10.]
- Jacob, J., Bartholmai, B. J., Rajagopalan, S., Brun, A. L., Egashira, R., Karwoski, R., Kokosi, M., Wells, A. U., and Hansell, D. M. (2016a). Evaluation of computer-based computer tomography stratification against outcome models in connective tissue disease-related interstitial lung disease: a patient outcome study. *Bmc Medicine*, 14(1):190. [Cited on pages 28, 189, and 199.]
- Jacob, J., Bartholmai, B. J., Rajagopalan, S., Kokosi, M., Nair, A., Karwoski, R., Walsh, S. L., Wells, A. U., and Hansell, D. M. (2016b). Mortality prediction in ipf: evaluation of automated computer tomographic analysis with conventional severity measures. *European Respiratory Journal*, 49(1):ERJ–01011–2016. [Cited on pages 29, 189, and 199.]
- Janssens, J.-P., Pache, J.-C., and Nicod, L. (1999). Physiological changes in respiratory function associated with ageing. *European Respiratory Journal*, 13(1):197–205. [Cited on pages 150, 151, 153, 154, and 155.]
- Jeffery, P. K. (1998). Structural and inflammatory changes in copd: a comparison with asthma. *Thorax*, 53(2):129. [Cited on page 38.]
- Johkoh, T., Muller, N. L., Cartier, Y., Kavanagh, P. V., Hartman, T. E., Akira, M., Ichikado, K., Ando, M., and Nakamura, H. (1999). Idiopathic interstitial pneumonias:

- diagnostic accuracy of thin-section ct in 129 patients. *Radiology*, 211(2):555–560. [Cited on page 14.]
- Jones, N., McHardy, G., Naimark, A., and Campbell, E. (1966). Physiological dead space and alveolar-arterial gas pressure differences during exercise. *Clinical Science*, 31(1):19–29. [Cited on page 31.]
- Kalender, W. A., Fichte, H., Bautz, W., and Skalej, M. (1991). Semiautomatic evaluation procedures for quantitative ct of the lung. *Journal of Computer Assisted Tomography*, 15(2):248–255. [Cited on pages 42 and 43.]
- Kapitan, K. S. and Happleman, S. C. (1986). Computer simulation of mammalian gas-exchange. *Computers in Biology and Medicine*, 16(2):91–101. [Cited on pages 173, 175, and 181.]
- Katzenstein, A.-L. A. and Myers, J. L. (1998). Idiopathic pulmonary fibrosis: clinical relevance of pathologic classification. *American Journal of Respiratory and Critical Care Medicine*, 157(4):1301–1315. [Cited on page 9.]
- Kazerooni, E. A. (2001). High-resolution ct of the lungs. *American Journal of Roentgenology*, 177(3):501–519. [Cited on page 96.]
- Kazerooni, E. A., Martinez, F. J., Flint, A., Jamadar, D. A., Gross, B. H., Spizarny, D. L., Cascade, P. N., Whyte, R. I., Lynch 3rd, J., and Toews, G. (1997). Thin-section ct obtained at 10-mm increments versus limited three-level thin-section ct for idiopathic pulmonary fibrosis: correlation with pathologic scoring. *AJR. American Journal of Roentgenology*, 169(4):977–983. [Cited on page 96.]
- Kelemen, A., Székely, G., and Gerig, G. (1999). Elastic model-based segmentation of 3-d neuroradiological data sets. *IEEE Transactions on Medical Imaging*, 18(10):828–839. [Cited on page 56.]

- Keller, J. M., Edwards, F. M., and Rundle, R. (1981). Automatic outlining of regions on ct scans. *Journal of Computer Assisted Tomography*, 5(2):240–245. [Cited on pages 42 and 43.]
- Kemerink, G. J., Lamers, R. J., Pellis, B. J., Kruize, H. H., and Van Engelshoven, J. (1998). On segmentation of lung parenchyma in quantitative computed tomography of the lung. *Medical Physics*, 25(12):2432–2439. [Cited on pages 42 and 43.]
- Kim, D., Park, J., Park, B., Lee, J., Nicholson, A., and Colby, T. (2006a). Acute exacerbation of idiopathic pulmonary fibrosis: frequency and clinical features. *European Respiratory Journal*, 27(1):143–150. [Cited on page 20.]
- Kim, D. S., Collard, H. R., and King Jr, T. E. (2006b). Classification and natural history of the idiopathic interstitial pneumonias. *Proceedings of the American Thoracic Society*, 3(4):285–292. [Cited on pages 19 and 20.]
- Kim, E. Y., Lee, K., Chung, M., Kwon, O. J., Kim, T., and Hwang, J. (1999). Non-specific interstitial pneumonia with fibrosis: serial high-resolution ct findings with functional correlation. *AJR. American Journal of Roentgenology*, 173(4):949–953. [Cited on page 96.]
- Kim, H., Tashkin, D., Clements, P., Li, G., Brown, M., Elashoff, R., Gjertson, D., Abtin, F., Lynch, D., Strollo, D., et al. (2010). A computer-aided diagnosis system for quantitative scoring of extent of lung fibrosis in scleroderma patients. *Clinical and Experimental Rheumatology*, 28(5 Suppl 62):S26. [Cited on pages 99 and 100.]
- Kim, H. J., Brown, M. S., Chong, D., Gjertson, D. W., Lu, P., Kim, H. J., Coy, H., and Goldin, J. G. (2015a). Comparison of the quantitative ct imaging biomarkers of idiopathic pulmonary fibrosis at baseline and early change with an interval of 7 months. *Academic Radiology*, 22(1):70–80. [Cited on pages 99 and 100.]

- Kim, H. J., Brown, M. S., Elashoff, R., Li, G., Gjertson, D. W., Lynch, D. A., Strollo, D. C., Kleerup, E., Chong, D., Shah, S. K., et al. (2011). Quantitative texture-based assessment of one-year changes in fibrotic reticular patterns on hrct in scleroderma lung disease treated with oral cyclophosphamide. *European Radiology*, 21(12):2455–2465. [Cited on pages 99 and 100.]
- Kim, H. J., Perlman, D., and Tomic, R. (2015b). Natural history of idiopathic pulmonary fibrosis. *Respiratory Medicine*, 109(6):661–670. [Cited on pages 8 and 21.]
- Kim, K. G., Goo, J. M., Kim, J. H., Lee, H. J., Min, B. G., Bae, K. T., and Im, J.-G. (2005). Computer-aided diagnosis of localized ground-glass opacity in the lung at ct: initial experience. *Radiology*, 237(2):657–661. [Cited on page 99.]
- King, C. S. and Nathan, S. D. (2017). Idiopathic pulmonary fibrosis: effects and optimal management of comorbidities. *The Lancet Respiratory Medicine*, 5(1):72–84. [Cited on pages 21 and 23.]
- King Jr, T. E., Pardo, A., and Selman, M. (2011). Idiopathic pulmonary fibrosis. *The Lancet*, 378(9807):1949–1961. [Cited on pages xv, 1, 7, 8, 12, 13, 14, 16, 19, 20, 21, 22, 23, 24, 94, 144, 145, and 200.]
- King Jr, T. E., Schwarz, M. I., Brown, K., Tooze, J. A., Colby, T. V., Waldron JR, J. A., Flint, A., Thurlbeck, W., and Cherniack, R. M. (2001a). Idiopathic pulmonary fibrosis: relationship between histopathologic features and mortality. *American Journal of Respiratory and Critical Care Medicine*, 164(6):1025–1032. [Cited on page 19.]
- King Jr, T. E., Tooze, J. A., Schwarz, M. I., Brown, K. R., and Cherniack, R. M. (2001b). Predicting survival in idiopathic pulmonary fibrosis: scoring system and survival model. *American Journal of Respiratory and Critical Care Medicine*, 164(7):1171–1181. [Cited on page 13.]

- Kinsella, M., Müller, N. L., Abboud, R. T., Morrison, N. J., and DyBuncio, A. (1990). Quantitation of emphysema by computed tomography using a “density mask” program and correlation with pulmonary function tests. *Chest*, 97(2):315–321. [Cited on page 97.]
- Kitasaka, T., Mori, K., Hasegawa, J.-i., and Toriwaki, J.-i. (2003). Lung area extraction from 3d chest x-ray ct images using a shape model generated by a variable bézier surface. *Systems and Computers in Japan*, 34(4):60–71. [Cited on pages 42 and 45.]
- Kitasaka, T., Nakada, Y., Mori, K., Suenaga, Y., Mori, M., Takabatake, H., and Natori, H. (2006). Recognition of lung lobes and its application to the bronchial structure analysis. In *Pattern Recognition, 2006. ICPR 2006. 18th International Conference on*, volume 3, pages 288–291. IEEE. [Cited on page 51.]
- Knudson, R. J., Slatin, R. C., Lebowitz, M. D., and Burrows, B. (1976). The maximal expiratory flow-volume curve: normal standards, variability, and effects of age. *American Review of Respiratory Disease*, 113(5):587–600. [Cited on page 154.]
- Knudson, R. J., Standen, J. R., Kaltenborn, W. T., Knudson, D. E., Rehm, K., Habib, M. P., and Newell, J. D. (1991). Expiratory computed tomography for assessment of suspected pulmonary emphysema. *Chest*, 99(6):1357–1366. [Cited on page 97.]
- Koenderink, J. J. (1984). The structure of images. *Biological Cybernetics*, 50(5):363–370. [Cited on page 65.]
- Kondoh, Y., Taniguchi, H., Kataoka, K., Keisuke, K., Suzuki, R., Ogura, T., Johkoh, T., Yokoi, T., Wells, A. U., and Kitaichi, M. (2010). Prognostic factors in rapidly progressive interstitial pneumonia. *Respirology*, 15(2):257–264. [Cited on page 20.]
- Kondoh, Y., Taniguchi, H., Kawabata, Y., Yokoi, T., Suzuki, K., and Takagi, K. (1993). Acute exacerbation in idiopathic pulmonary fibrosis: analysis of clinical and pathologic findings in three cases. *Chest*, 103(6):1808–1812. [Cited on page 20.]

- Korfiatis, P., Kalogeropoulou, C., Karahaliou, A., Kazantzi, A., Skiadopoulos, S., and Costaridou, L. (2008). Texture classification-based segmentation of lung affected by interstitial pneumonia in high-resolution ct. *Medical Physics*, 35(12):5290–5302. [Cited on page 45.]
- Kornbluth, R. and Turino, G. (1980). Respiratory control in diffuse interstitial lung disease and diseases of the pulmonary vasculature. *Clinics in Chest Medicine*, 1(1):91–102. [Cited on page 28.]
- Krenz, G. S. and Dawson, C. A. (2003). Flow and pressure distributions in vascular networks consisting of distensible vessels. *American Journal of Physiology-Heart and Circulatory Physiology*, 284(6):H2192–H2203. [Cited on page 176.]
- Kreuter, M., Ehlers-Tenenbaum, S., Palmowski, K., Bruhwyl, J., Oltmanns, U., Muley, T., Heussel, C. P., Warth, A., Kolb, M., and Herth, F. J. (2016). Impact of comorbidities on mortality in patients with idiopathic pulmonary fibrosis. *PLoS One*, 11(3):e0151425. [Cited on page 21.]
- Krumpe, P. E., Knudson, R. J., Parsons, G., and Reiser, K. (1985). The aging respiratory system. *Clinics in Geriatric Medicine*, 1(1):143–175. [Cited on page 55.]
- Kuhnigk, J., Dicken, V., Zidowitz, S., Bornemann, L., Kuemmerlen, B., Krass, S., Peitgen, H., Yuval, S., Jend, H., Rau, W., et al. (2005). Informatics in radiology (inforad): New tools for computer assistance in thoracic ct. part 1. functional analysis of lungs. Lung Lobes, and Bronchopulmonary Segments. *RadioGraphics* 2005; 25: 525, 536. [Cited on pages 48, 49, and 50.]
- Kuhnigk, J.-M., Hahn, H., Hindennach, M., Dicken, V., Krass, S., and Peitgen, H.-O. (2003). Lung lobe segmentation by anatomy-guided 3 d watershed transform. In Proceedings of SPIE, volume 5032, pages 1482–1490. [Cited on pages 48, 49, and 50.]

- Kundel, H. L. (2006). History of research in medical image perception. *Journal of the American College of Radiology*, 3(6):402–408. [Cited on page 94.]
- Kwan, M., Woo, J., and Kwok, T. (2004). The standard oxygen consumption value equivalent to one metabolic equivalent (3.5 ml/min/kg) is not appropriate for elderly people. *International Journal of Food Sciences and Nutrition*, 55(3):179–182. [Cited on page 181.]
- Lalley, P. M. (2013). The aging respiratory system—pulmonary structure, function and neural control. *Respiratory Physiology & Neurobiology*, 187(3):199–210. [Cited on pages xxxviii, 151, 152, 153, 154, and 155.]
- Larsson, L. (1983). Histochemical characteristics of human skeletal muscle during aging. *Acta Physiologica Scandinavica*, 117(3):469–471. [Cited on page 153.]
- Lassen, B., Kuhnigk, J.-M., Friman, O., Krass, S., and Peitgen, H.-O. (2010). Automatic segmentation of lung lobes in ct images based on fissures, vessels, and bronchi. In *Biomedical Imaging: From Nano to Macro, 2010 IEEE International Symposium on*, pages 560–563. IEEE. [Cited on pages 36, 48, 49, and 50.]
- Lassen, B., Kuhnigk, J.-M., Van Rikxoort, E. M., and Peitgen, H.-O. (2011). Interactive lung lobe segmentation and correction in tomographic images. In *Medical Imaging 2011: Computer-Aided Diagnosis*, volume 7963, page 79631S. International Society for Optics and Photonics. [Cited on pages 35, 48, 51, 52, 82, and 91.]
- Lassen, B., van Rikxoort, E. M., Schmidt, M., Kerkstra, S., van Ginneken, B., and Kuhnigk, J.-M. (2013). Automatic segmentation of the pulmonary lobes from chest ct scans based on fissures, vessels, and bronchi. *IEEE Transactions on Medical Imaging*, 32(2):210–222. [Cited on pages 48, 51, 52, 82, and 91.]
- Leader, J. K., Zheng, B., Rogers, R. M., Sciurba, F. C., Perez, A., Chapman, B. E., Patel, S., Fuhrman, C. R., and Gur, D. (2003). Automated lung segmentation in x-ray

- computed tomography: development and evaluation of a heuristic threshold-based scheme1. *Academic Radiology*, 10(11):1224–1236. [Cited on pages 42 and 43.]
- Lee, H.-L., Ryu, J. H., Wittmer, M. H., Hartman, T. E., Lymp, J. F., Tazelaar, H. D., and Limper, A. H. (2005). Familial idiopathic pulmonary fibrosis: clinical features and outcome. *Chest*, 127(6):2034–2041. [Cited on page 12.]
- Lee, S., Wolberg, G., and Shin, S. Y. (1997). Scattered data interpolation with multilevel b-splines. *IEEE Transactions on Visualization and Computer Graphics*, 3(3):228–244. [Cited on pages 72 and 89.]
- Lettieri, C. J., Nathan, S. D., Barnett, S. D., Ahmad, S., and Shorr, A. F. (2006). Prevalence and outcomes of pulmonary arterial hypertension in advanced idiopathic pulmonary fibrosis. *Chest*, 129(3):746–752. [Cited on pages 19, 20, and 23.]
- Leung, A. N. (1999). Pulmonary tuberculosis: the essentials. *Radiology*, 210(2):307–322. [Cited on page 38.]
- Levitzky, M. G. (1984). Effects of aging on the respiratory system. *Physiologist*, 27(2):102–107. [Cited on page 155.]
- Ley, B., Collard, H. R., and King Jr, T. E. (2011). Clinical course and prediction of survival in idiopathic pulmonary fibrosis. *American Journal of Respiratory and Critical Care Medicine*, 183(4):431–440. [Cited on pages xiv, 19, 20, and 21.]
- Ley-Zaporozhan, J., Ley, S., Weinheimer, O., Iliyushenko, S., Erdugan, S., Eberhardt, R., Fuxa, A., Mews, J., and Kauczor, H.-U. (2008). Quantitative analysis of emphysema in 3d using mdct: influence of different reconstruction algorithms. *European Journal of Radiology*, 65(2):228–234. [Cited on page 38.]
- Li, Q., Sone, S., et al. (2003). Selective enhancement filters for nodules, vessels, and airway walls in two-and three-dimensional ct scans. *Medical Physics*, 30(8):2040–2051. [Cited on page 66.]

- Lin, H. and Jiang, S. (2015). Combined pulmonary fibrosis and emphysema (cpfe): an entity different from emphysema or pulmonary fibrosis alone. *Journal of Thoracic Disease*, 7(4):767. [Cited on pages 22, 39, and 200.]
- Lorenz, C., Carlsen, I.-C., Buzug, T. M., Fassnacht, C., and Weese, J. (1997). Multi-scale line segmentation with automatic estimation of width, contrast and tangential direction in 2d and 3d medical images. In *CVRMed-MRCAS'97*, pages 233–242. Springer. [Cited on pages 64, 65, and 66.]
- Lynch, D. A. (2007). Quantitative ct of fibrotic interstitial lung disease. *Chest*, 131(3):643–644. [Cited on page 97.]
- Lynch, D. A., Godwin, J. D., Safrin, S., Starko, K. M., Hormel, P., Brown, K. K., Raghu, G., King Jr, T. E., Bradford, W. Z., Schwartz, D. A., et al. (2005). High-resolution computed tomography in idiopathic pulmonary fibrosis: diagnosis and prognosis. *American Journal of Respiratory and Critical Care Medicine*, 172(4):488–493. [Cited on pages 95 and 96.]
- Lynch, J. P., Saggar, R., Weigt, S. S., Zisman, D. A., and White, E. S. (2006). Usual interstitial pneumonia. In *Seminars in respiratory and critical care medicine*, volume 27, pages 634–651. Copyright© 2006 by Thieme Medical Publishers, Inc., 333 Seventh Avenue, New York, NY 10001, USA. [Cited on page 18.]
- Maldonado, F., Moua, T., Rajagopalan, S., Karwoski, R. A., Raghunath, S., Decker, P. A., Hartman, T. E., Bartholmai, B. J., Robb, R. A., and Ryu, J. H. (2013). Automated quantification of radiologic patterns predicts survival in idiopathic pulmonary fibrosis. *European Respiratory Journal*, pages erj00718–2012. [Cited on pages xix, 101, 102, 103, and 104.]
- Martinez, F. J., Collard, H. R., Pardo, A., Raghu, G., Richeldi, L., Selman, M., Swigris,

- J. J., Taniguchi, H., and Wells, A. U. (2017). Idiopathic pulmonary fibrosis. *Nature Reviews Disease Primers*, 3:17074. [Cited on pages xiii, 8, 15, 21, and 22.]
- Martinez, F. J. and Flaherty, K. (2006). Pulmonary function testing in idiopathic interstitial pneumonias. *Proceedings of the American Thoracic Society*, 3(4):315–321. [Cited on page 27.]
- McClaran, S., Babcock, M., Pegelow, D., Reddan, W., and Dempsey, J. (1995). Longitudinal effects of aging on lung function at rest and exercise in healthy active fit elderly adults. *Journal of Applied Physiology*, 78(5):1957–1968. [Cited on page 150.]
- Mejía, M., Carrillo, G., Rojas-Serrano, J., Estrada, A., Suárez, T., Alonso, D., Barrientos, E., Gaxiola, M., Navarro, C., and Selman, M. (2009). Idiopathic pulmonary fibrosis and emphysema: decreased survival associated with severe pulmonary arterial hypertension. *Chest*, 136(1):10–15. [Cited on pages 19, 22, and 23.]
- Meltzer, E. B. and Noble, P. W. (2008). Idiopathic pulmonary fibrosis. *Orphanet Journal of Rare Diseases*, 3(1):8. [Cited on pages 1, 7, 8, 9, 10, 11, 19, 20, and 22.]
- Miki, K., Maekura, R., Hiraga, T., Hashimoto, H., Kitada, S., Miki, M., Yoshimura, K., Tateishi, Y., Fushitani, K., and Motone, M. (2009). Acidosis and raised norepinephrine levels are associated with exercise dyspnoea in idiopathic pulmonary fibrosis. *Respirology*, 14(7):1020–1026. [Cited on page 30.]
- Misumi, S. and Lynch, D. A. (2006). Idiopathic pulmonary fibrosis/usual interstitial pneumonia: imaging diagnosis, spectrum of abnormalities, and temporal progression. *Proceedings of the American Thoracic Society*, 3(4):307–314. [Cited on page 96.]
- Mittman, C., Edelman, N. H., Norris, A. H., and Shock, N. W. (1965). Relationship between chest wall and pulmonary compliance and age. *Journal of Applied Physiology*, 20(6):1211–1216. [Cited on pages 150 and 153.]

- Miyamura, M. and Honda, Y. (1973). Maximum cardiac output related to sex and age. *The Japanese Journal of Physiology*, 23(6):645–656. [Cited on page 180.]
- Monaghan, H., Wells, A. U., Colby, T. V., Du Bois, R. M., Hansell, D. M., and Nicholson, A. G. (2004). Prognostic implications of histologic patterns in multiple surgical lung biopsies from patients with idiopathic interstitial pneumonias. *Chest*, 125(2):522–526. [Cited on page 95.]
- Monod, J., Wyman, J., and Changeux, J.-P. (1965). On the nature of allosteric transitions: a plausible model. *Biol*, 12:228–113. [Cited on pages 173, 174, and 176.]
- Mueller-Mang, C., Grosse, C., Schmid, K., Stiebellehner, L., and Bankier, A. A. (2007). What every radiologist should know about idiopathic interstitial pneumonias. *Radiographics*, 27(3):595–615. [Cited on page 95.]
- Müller, N. L., Staples, C. A., Miller, R. R., and Abboud, R. T. (1988). “density mask”: an objective method to quantitate emphysema using computed tomography. *Chest*, 94(4):782–787. [Cited on page 97.]
- Mura, M., Zompatori, M., Pacilli, A. M. G., Fasano, L., Schiavina, M., and Fabbri, M. (2006). The presence of emphysema further impairs physiologic function in patients with idiopathic pulmonary fibrosis. *Respiratory Care*, 51(3):257–265. [Cited on page 27.]
- Murray, J. F. (1986). The normal lung: the basis for diagnosis and treatment of pulmonary disease. WB Saunders Company. [Cited on pages 151 and 155.]
- Musk, A., Zilko, P., Manners, P., Kay, P., and Kamboh, M. (1986). Genetic studies in familial fibrosing alveolitis: possible linkage with immunoglobulin allotypes (gm). *Chest*, 89(2):206–210. [Cited on page 12.]
- Nadrous, H. F., Pellikka, P. A., Krowka, M. J., Swanson, K. L., et al. (2005). The impact

- of pulmonary hypertension on survival in patients with idiopathic pulmonary fibrosis. *Chest*, 128(6):616S. [Cited on page 23.]
- Naidich, D. P. (2005). Imaging of the airways: functional and radiologic correlations. Lippincott Williams & Wilkins. [Cited on page 38.]
- Nava, S. and Rubini, F. (1999). Lung and chest wall mechanics in ventilated patients with end stage idiopathic pulmonary fibrosis. *Thorax*, 54(5):390–395. [Cited on page 26.]
- Nicholson, A. G., Colby, T. V., Dubois, R. M., Hansell, D. M., and Wells, A. U. (2000). The prognostic significance of the histologic pattern of interstitial pneumonia in patients presenting with the clinical entity of cryptogenic fibrosing alveolitis. *American Journal of Respiratory and Critical Care Medicine*, 162(6):2213–2217. [Cited on page 19.]
- Nishimura, K., Kitaichi, M., Izumi, T., Nagai, S., Kanaoka, M., and Itoh, H. (1992). Usual interstitial pneumonia: histologic correlation with high-resolution ct. *Radiology*, 182(2):337–342. [Cited on page 14.]
- Ochs, R. A., Goldin, J. G., Abtin, F., Kim, H. J., Brown, K., Batra, P., Roback, D., McNitt-Gray, M. F., and Brown, M. S. (2007). Automated classification of lung bronchovascular anatomy in ct using adaboost. *Medical Image Analysis*, 11(3):315–324. [Cited on pages 48, 51, and 52.]
- Okada, T., Shimada, R., Hori, M., Nakamoto, M., Chen, Y.-W., Nakamura, H., and Sato, Y. (2008). Automated segmentation of the liver from 3d ct images using probabilistic atlas and multilevel statistical shape model. *Academic Radiology*, 15(11):1390–1403. [Cited on page 56.]
- Olson, A. L., Swigris, J. J., Lezotte, D. C., Norris, J. M., Wilson, C. G., and Brown, K. K. (2007). Mortality from pulmonary fibrosis increased in the united states

- from 1992 to 2003. *American Journal of Respiratory and Critical Care Medicine*, 176(3):277–284. [Cited on page 94.]
- Orens, J. B., Kazerooni, E. A., Martinez, F. J., Curtis, J. L., Gross, B. H., Flint, A., and Lynch III, J. P. (1995). The sensitivity of high-resolution ct in detecting idiopathic pulmonary fibrosis proved by open lung biopsy: a prospective study. *Chest*, 108(1):109–115. [Cited on page 26.]
- Organ, L., Bacci, B., Koumoundouros, E., Barcham, G., Milne, M., Kimpton, W., Samuel, C., and Snibson, K. (2015). Structural and functional correlations in a large animal model of bleomycin-induced pulmonary fibrosis. *BMC Pulmonary Medicine*, 15(1):81. [Cited on page 26.]
- Osanlouy, M. (2018). Statistical Shape Analysis to Quantify Lung Structure-Function Relationships over the Adult Lifespan. PhD thesis, University of Auckland. [Cited on pages 146, 156, and 159.]
- Paoletti, P., Viegi, G., Pistelli, G., Di Pede, F., Fazzi, P., Polato, R., Saetta, M., Zambon, R., Carli, G., Giuntini, C., et al. (1985). Reference equations for the single-breath diffusing capacity: a cross-sectional analysis and effect of body size and age. *American Review of Respiratory Disease*, 132(4):806–813. [Cited on page 155.]
- Parambil, J. G., Myers, J. L., and Ryu, J. H. (2005). Histopathologic features and outcome of patients with acute exacerbation of idiopathic pulmonary fibrosis undergoing surgical lung biopsy. *Chest*, 128(5):3310–3315. [Cited on page 20.]
- Pastre, J., Plantier, L., Planes, C., Borie, R., Nunes, H., Delclaux, C., and Israël-Biet, D. (2015). Different k_{co} and va combinations exist for the same dl_{co} value in patients with diffuse parenchymal lung diseases. *BMC Pulmonary Medicine*, 15(1):100. [Cited on pages 27 and 30.]

- Pedley, T., Schroter, R., and Sudlow, M. (1970). Energy losses and pressure drop in models of human airways. *Respiration Physiology*, 9(3):371–386. [Cited on pages 168 and 176.]
- Pelosi, P., Croci, M., Ravagnan, I., Tredici, S., Pedoto, A., Lissoni, A., and Gattinoni, L. (1998). The effects of body mass on lung volumes, respiratory mechanics, and gas exchange during general anesthesia. *Anesthesia & Analgesia*, 87(3):654–660. [Cited on page 180.]
- Plantier, L., Cazes, A., Dinh-Xuan, A.-T., Bancal, C., Marchand-Adam, S., and Crestani, B. (2018). Physiology of the lung in idiopathic pulmonary fibrosis. *European Respiratory Review*, 27(147):170062. [Cited on pages xxxvii, 24, 25, 26, 27, 28, 29, 30, 32, 180, 198, and 207.]
- Plantier, L., Debray, M.-P., Estellat, C., Flamant, M., Roy, C., Bancal, C., Borie, R., Israël-Biet, D., Mal, H., Crestani, B., et al. (2016). Increased volume of conducting airways in idiopathic pulmonary fibrosis is independent of disease severity: a volumetric capnography study. *Journal of Breath Research*, 10(1):016005. [Cited on pages 27, 28, 30, and 165.]
- Pollock, M. L., Mengelkoch, L. J., Graves, J. E., Lowenthal, D. T., Limacher, M. C., Foster, C., and Wilmore, J. H. (1997). Twenty-year follow-up of aerobic power and body composition of older track athletes. *Journal of Applied Physiology*, 82(5):1508–1516. [Cited on page 150.]
- Prasad, M. N., Brown, M. S., Ahmad, S., Abtin, F., Allen, J., da Costa, I., Kim, H. J., McNitt-Gray, M. F., and Goldin, J. G. (2008). Automatic segmentation of lung parenchyma in the presence of diseases based on curvature of ribs. *Academic Radiology*, 15(9):1173–1180. [Cited on pages 42, 45, and 46.]

- Pries, A., Secomb, T., and Gaehtgens, P. (1996). Biophysical aspects of blood flow in the microvasculature. *Cardiovascular Research*, 32(4):654–667. [Cited on page 176.]
- Pu, J., Leader, J. K., Zheng, B., Knollmann, F., Fuhrman, C., Sciurba, F. C., and Gur, D. (2009a). A computational geometry approach to automated pulmonary fissure segmentation in ct examinations. *IEEE Transactions on Medical Imaging*, 28(5):710–719. [Cited on pages 39, 41, and 49.]
- Pu, J., Paik, D. S., Meng, X., Roos, J., and Rubin, G. D. (2011). Shape “break-and-repair” strategy and its application to automated medical image segmentation. *IEEE Transactions on Visualization and Computer Graphics*, 17(1):115–124. [Cited on pages 42, 45, and 46.]
- Pu, J., Roos, J., Chin, A. Y., Napel, S., Rubin, G. D., and Paik, D. S. (2008). Adaptive border marching algorithm: automatic lung segmentation on chest ct images. *Computerized Medical Imaging and Graphics*, 32(6):452–462. [Cited on pages 40, 42, and 45.]
- Pu, J., Zheng, B., Leader, J. K., Fuhrman, C., Knollmann, F., Klym, A., and Gur, D. (2009b). Pulmonary lobe segmentation in ct examinations using implicit surface fitting. *IEEE Transactions on Medical Imaging*, 28(12):1986–1996. [Cited on pages 82 and 91.]
- Quadrelli, S., Molinari, L., Ciallella, L., Spina, J. C., Sobrino, E., and Chertcoff, J. (2010). Radiological versus histopathological diagnosis of usual interstitial pneumonia in the clinical practice: does it have any survival difference? *Respiration*, 79(1):32–37. [Cited on page 17.]
- Raghu, G. (1987). Idiopathic pulmonary fibrosis: a rational clinical approach. *Chest*, 92(1):148–154. [Cited on page 19.]

- Raghu, G., Amatto, V. C., Behr, J., and Stowasser, S. (2015). Comorbidities in idiopathic pulmonary fibrosis patients: a systematic literature review. *European Respiratory Journal*, 46(4):1113–1130. [Cited on page 22.]
- Raghu, G., Collard, H. R., Egan, J. J., Martinez, F. J., Behr, J., Brown, K. K., Colby, T. V., Cordier, J.-F., Flaherty, K. R., Lasky, J. A., et al. (2011). An official ats/ers/jrs/alat statement: idiopathic pulmonary fibrosis: evidence-based guidelines for diagnosis and management. *American Journal of Respiratory and Critical Care Medicine*, 183(6):788–824. [Cited on pages xiv, 1, 2, 7, 8, 10, 11, 12, 13, 14, 15, 16, 17, 18, 19, 20, 21, 23, 24, 94, 144, and 146.]
- Raghu, G., Mageto, Y. N., Lockhart, D., Schmidt, R. A., Wood, D. E., and Godwin, J. D. (1999). The accuracy of the clinical diagnosis of new-onset idiopathic pulmonary fibrosis and other interstitial lung disease: a prospective study. *Chest*, 116(5):1168–1174. [Cited on page 17.]
- Raghu, G., Weycker, D., Edelsberg, J., Bradford, W. Z., and Oster, G. (2006). Incidence and prevalence of idiopathic pulmonary fibrosis. *American Journal of Respiratory and Critical Care Medicine*, 174(7):810–816. [Cited on pages 10 and 14.]
- Raghunath, S., Rajagopalan, S., Karwoski, R. A., Maldonado, F., Peikert, T., Moua, T., Ryu, J. H., Bartholmai, B. J., and Robb, R. A. (2014). Quantitative stratification of diffuse parenchymal lung diseases. *PLoS One*, 9(3):e93229. [Cited on pages 94, 96, 101, and 105.]
- Rees, D. and Murray, J. (2007). Silica, silicosis and tuberculosis [state of the art series. occupational lung disease in high-and low-income countries, edited by m. chan-yeung. number 4 in the series]. *The International Journal of Tuberculosis and Lung Disease*, 11(5):474–484. [Cited on page 38.]

- Renzi, G., Milic-Emili, J., and Grassino, A. (1982). The pattern of breathing in diffuse lung fibrosis. *Bulletin European de Physiopathologie Respiratoire*, 18(3):461–472. [Cited on page 28.]
- Richeldi, L., Collard, H. R., and Jones, M. G. (2017). Idiopathic pulmonary fibrosis. *The Lancet*, 389(10082):1941–1952. [Cited on pages 1, 2, 8, 10, 11, 12, 13, 14, 15, 16, 94, and 144.]
- Rohlf, F. J. (1999). Shape statistics: Procrustes superimpositions and tangent spaces. *Journal of Classification*, 16(2):197–223. [Cited on page 61.]
- Rosenberg, E. (1996). The 1995 update of recommendations for a standard technique for measuring the single-breath carbon monoxide diffusing capacity (transfer factor). *American Journal of Respiratory and Critical Care Medicine*, 154(3):827–828. [Cited on page 29.]
- Ross, J. C., Estépar, R. S. J., Kindlmann, G., Díaz, A., Westin, C.-F., Silverman, E. K., and Washko, G. R. (2010). Automatic lung lobe segmentation using particles, thin plate splines, and maximum a posteriori estimation. In *International Conference on Medical Image Computing and Computer-Assisted Intervention*, pages 163–171. Springer. [Cited on pages 48, 51, and 52.]
- Ross, J. C., Kindlmann, G. L., Okajima, Y., Hatabu, H., Díaz, A. A., Silverman, E. K., Washko, G. R., Dy, J., and Estépar, R. S. J. (2013). Pulmonary lobe segmentation based on ridge surface sampling and shape model fitting. *Medical Physics*, 40(12). [Cited on pages 48 and 52.]
- Rudd, R. M., Prescott, R. J., Chalmers, J., and Johnston, I. D. (2007). British thoracic society study on cryptogenic fibrosing alveolitis: response to treatment and survival. *Thorax*, 62(1):62–66. [Cited on page 19.]

- Ryu, J. H., Moua, T., Daniels, C. E., Hartman, T. E., Eunhee, S. Y., Utz, J. P., and Limper, A. H. (2014). Idiopathic pulmonary fibrosis: evolving concepts. In Mayo Clinic proceedings, volume 89, pages 1130–1142. Elsevier. [Cited on pages 19 and 20.]
- Saita, S., Kubo, M., Kawata, Y., Niki, N., Ohmatsu, H., and Moriyama, N. (2006). An algorithm for the extraction of pulmonary fissures from low-dose multislice ct image. Systems and Computers in Japan, 37(9):63–76. [Cited on pages 48, 49, and 51.]
- Sakamoto, K., Taniguchi, H., Kondoh, Y., Ono, K., Hasegawa, Y., and Kitaichi, M. (2009). Acute exacerbation of idiopathic pulmonary fibrosis as the initial presentation of the disease. European Respiratory Review, 18(112):129–132. [Cited on page 20.]
- Saketkoo, L. A., Matteson, E. L., Brown, K. K., Seibold, J. R., and Strand, V. (2011). Developing disease activity and response criteria in connective tissue disease-related interstitial lung disease. The Journal of Rheumatology, 38(7):1514–1518. [Cited on page 96.]
- Sato, Y., Westin, C.-F., Bhalerao, A., Nakajima, S., Shiraga, N., Tamura, S., and Kikinis, R. (2000). Tissue classification based on 3d local intensity structures for volume rendering. IEEE Transactions on Visualization and Computer Graphics, 6(2):160–180. [Cited on page 101.]
- Schmidt, R., Meier, U., Markart, P., Grimminger, F., Velcovsky, H., Morr, H., Seeger, W., and Gunther, A. (2002). Altered fatty acid composition of lung surfactant phospholipids in interstitial lung disease. American Journal of Physiology-Lung Cellular and Molecular Physiology, 283(5):L1079–L1085. [Cited on page 24.]
- Seibold, M. A., Wise, A. L., Speer, M. C., Steele, M. P., Brown, K. K., Loyd, J. E., Fingerlin, T. E., Zhang, W., Gudmundsson, G., Groshong, S. D., et al. (2011). A common muc5b promoter polymorphism and pulmonary fibrosis. New England Journal of Medicine, 364(16):1503–1512. [Cited on page 12.]

- Selman, M., Carrillo, G., Estrada, A., Mejia, M., Becerril, C., Cisneros, J., Gaxiola, M., Pérez-Padilla, R., Navarro, C., Richards, T., et al. (2007). Accelerated variant of idiopathic pulmonary fibrosis: clinical behavior and gene expression pattern. *PloS One*, 2(5):e482. [Cited on page 19.]
- Shikata, H., McLennan, G., Hoffman, E. A., and Sonka, M. (2009). Segmentation of pulmonary vascular trees from thoracic 3d ct images. *Journal of Biomedical Imaging*, 2009:24. [Cited on page 38.]
- Silva, C. I. S., Muller, N. L., Lynch, D. A., Curran-Everett, D., Brown, K. K., Lee, K. S., Chung, M. P., and Churg, A. (2008a). Chronic hypersensitivity pneumonitis: differentiation from idiopathic pulmonary fibrosis and nonspecific interstitial pneumonia by using thin-section ct. *Radiology*, 246(1):288–297. [Cited on page 18.]
- Silva, D. R., Gazzana, M. B., Barreto, S. S. M., and Knorst, M. M. (2008b). Idiopathic pulmonary fibrosis and emphysema in smokers. *Jornal Brasileiro de Pneumologia*, 34(10):779–786. [Cited on page 22.]
- Slebos, D.-J., van Rikxoort, E. M., and van der Bij, W. (2015). Air trapping in emphysema. *American Journal of Respiratory and Critical Care Medicine*, 192(5):e45–e45. [Cited on page 200.]
- Sluimer, I., Prokop, M., and Van Ginneken, B. (2005). Toward automated segmentation of the pathological lung in ct. *IEEE Transactions on Medical Imaging*, 24(8):1025–1038. [Cited on page 45.]
- Smith, T. (1986). Respiratory effects of aging. In *Seminars in Anesthesia*, volume 5, pages 14–22. Wb Saunders Co Independence Square West Curtis Center, STE 300, Philadelphia, PA 19106-3399. [Cited on page 150.]
- Society, A. T. et al. (2000). Idiopathic pulmonary fibrosis: diagnosis and treatment:

- international consensus statement. *Am J Respir Crit Care Med*, 161:646–664. [Cited on pages 16, 24, 26, 28, 29, 31, and 32.]
- Souza, C. A., Muller, N. L., Lee, K. S., Johkoh, T., Mitsuhiro, H., and Chong, S. (2006). Idiopathic interstitial pneumonias: prevalence of mediastinal lymph node enlargement in 206 patients. *American Journal of Roentgenology*, 186(4):995–999. [Cited on page 14.]
- Sprung, J., Gajic, O., and Warner, D. O. (2006). age related alterations in respiratory function—anesthetic considerations. *Canadian Journal of Anesthesia*, 53(12):1244. [Cited on pages xxxviii, 150, 151, 152, 153, 154, 155, and 191.]
- Steele, M. P., Speer, M. C., Loyd, J. E., Brown, K. K., Herron, A., Slifer, S. H., Burch, L. H., Wahidi, M. M., Phillips III, J. A., Sporn, T. A., et al. (2005). Clinical and pathologic features of familial interstitial pneumonia. *American Journal of Respiratory and Critical Care Medicine*, 172(9):1146–1152. [Cited on page 12.]
- Stegmann, M. B. and Gomez, D. D. (2002). A brief introduction to statistical shape analysis. *Informatics and Mathematical Modelling*, Technical University of Denmark, DTU, 15(11). [Cited on page 56.]
- Stelfox, H. T., Ahmed, S. B., Ribeiro, R. A., Gettings, E. M., Pomerantsev, E., and Schmidt, U. (2006). Hemodynamic monitoring in obese patients: the impact of body mass index on cardiac output and stroke volume. *Critical Care Medicine*, 34(4):1243–1246. [Cited on page 180.]
- Strickland, N., Hughes, J., Hart, D., Myers, M., and Lavender, J. (1993). Cause of regional ventilation-perfusion mismatching in patients with idiopathic pulmonary fibrosis: a combined ct and scintigraphic study. *AJR. American Journal of Roentgenology*, 161(4):719–725. [Cited on pages 30, 31, and 180.]

- Styner, M., Gerig, G., Lieberman, J., Jones, D., and Weinberger, D. (2003). Statistical shape analysis of neuroanatomical structures based on medial models. *Medical Image Analysis*, 7(3):207–220. [Cited on page 56.]
- Sumikawa, H., Johkoh, T., Colby, T. V., Ichikado, K., Suga, M., Taniguchi, H., Kondoh, Y., Ogura, T., Arakawa, H., Fujimoto, K., et al. (2008). Computed tomography findings in pathological usual interstitial pneumonia: relationship to survival. *American Journal of Respiratory and Critical Care Medicine*, 177(4):433–439. [Cited on pages 28 and 96.]
- Sun, S., Bauer, C., and Beichel, R. (2012). Automated 3-d segmentation of lungs with lung cancer in ct data using a novel robust active shape model approach. *IEEE Transactions on Medical Imaging*, 31(2):449–460. [Cited on pages 42, 45, and 47.]
- Sun, X., Zhang, H., and Duan, H. (2006). 3d computerized segmentation of lung volume with computed tomography. *Academic Radiology*, 13(6):670–677. [Cited on pages 40, 42, 43, and 44.]
- Sverzellati, N., Devaraj, A., Desai, S. R., Quigley, M., Wells, A. U., and Hansell, D. M. (2011). Method for minimizing observer variation for the quantitation of high-resolution computed tomographic signs of lung disease. *Journal of Computer Assisted Tomography*, 35(5):596–601. [Cited on page 95.]
- Swan, A. (2010). A multi-scale computational model of pulmonary gas exchange. PhD thesis, University of Auckland. [Cited on pages 150, 175, and 198.]
- Swan, A. J., Clark, A. R., and Tawhai, M. H. (2012). A computational model of the topographic distribution of ventilation in healthy human lungs. *Journal of Theoretical Biology*, 300:222–231. [Cited on pages 167, 169, 175, and 196.]
- Swan, A. J. and Tawhai, M. H. (2010). Evidence for minimal oxygen heterogeneity in

- the healthy human pulmonary acinus. *Journal of Applied Physiology*, 110(2):528–537. [Cited on page 175.]
- Swigris, J. J., Han, M., Vij, R., Noth, I., Eisenstein, E. L., Anstrom, K. J., Brown, K. K., and Fairclough, D. (2012). The ucsg shortness of breath questionnaire has longitudinal construct validity in idiopathic pulmonary fibrosis. *Respiratory Medicine*, 106(10):1447–1455. [Cited on page 30.]
- Taskar, V. S. and Coultas, D. B. (2006). Is idiopathic pulmonary fibrosis an environmental disease? *Proceedings of the American Thoracic Society*, 3(4):293–298. [Cited on page 11.]
- Tawhai, M. H. and Burrowes, K. S. (2003). Developing integrative computational models of pulmonary structure. *The Anatomical Record*, 275(1):207–218. [Cited on pages 59 and 107.]
- Tawhai, M. H., Hunter, P., Tschirren, J., Reinhardt, J., McLennan, G., and Hoffman, E. A. (2004). Ct-based geometry analysis and finite element models of the human and ovine bronchial tree. *Journal of Applied Physiology*, 97(6):2310–2321. [Cited on pages 162, 163, and 196.]
- Tawhai, M. H., Nash, M. P., Lin, C.-L., and Hoffman, E. A. (2009). Supine and prone differences in regional lung density and pleural pressure gradients in the human lung with constant shape. *Journal of Applied Physiology*, 107(3):912–920. [Cited on pages 167 and 168.]
- Taylor, C., Cootes, T., Hill, A., and Haslam, J. (1995). Medical image segmentation using active shape models. *Studies in Health Technology and Informatics*, 19:121–144. [Cited on page 56.]
- Thurlbeck, W. M. and Angus, G. E. (1975). Growth and aging of the normal human lung. *Chest*, 67(2 Suppl):3S–6S. [Cited on page 155.]

- Trahan, S., Hanak, V., Ryu, J. H., and Myers, J. L. (2008). Role of surgical lung biopsy in separating chronic hypersensitivity pneumonia from usual interstitial pneumonia/idiopathic pulmonary fibrosis*: Analysis of 31 biopsies from 15 patients. *Chest*, 134(1):126–132. [Cited on page 18.]
- Travis, W. D., Costabel, U., Hansell, D. M., King Jr, T. E., Lynch, D. A., Nicholson, A. G., Ryerson, C. J., Ryu, J. H., Selman, M., Wells, A. U., et al. (2013). An official american thoracic society/european respiratory society statement: update of the international multidisciplinary classification of the idiopathic interstitial pneumonias. *American Journal of Respiratory and Critical Care Medicine*, 188(6):733–748. [Cited on pages 10 and 94.]
- Travis, W. D., King, T. E., Bateman, E. D., Lynch, D. A., Capron, F., Center, D., Colby, T. V., Cordier, J. F., DuBois, R. M., Galvin, J., et al. (2002). American thoracic society/european respiratory society international multidisciplinary consensus classification of the idiopathic interstitial pneumonias. *American Journal of Respiratory and Critical Care Medicine*, 165(2):277–304. [Cited on page 16.]
- Troy, L. and Corte, T. J. (2012). Management of the idiopathic interstitial pneumonias. *Australian Prescriber*, 35(6):202–6. [Cited on pages xiii and 9.]
- Tsai, A., Yezzi, A., Wells, W., Tempany, C., Tucker, D., Fan, A., Grimson, W. E., and Willsky, A. (2003). A shape-based approach to the segmentation of medical imagery using level sets. *IEEE Transactions on Medical Imaging*, 22(2):137–154. [Cited on page 56.]
- Tukiainen, P., Taskinen, E., Holsti, P., Korhola, O., and Valle, M. (1983). Prognosis of cryptogenic fibrosing alveolitis. *Thorax*, 38(5):349–355. [Cited on page 19.]
- Turner, J. M., Mead, J., and Wohl, M. E. (1968). Elasticity of human lungs in relation to age. *Journal of Applied Physiology*, 25(6):664–671. [Cited on page 153.]

- Uchiyama, Y., Katsuragawa, S., Abe, H., Shiraishi, J., Li, F., Li, Q., Zhang, C.-T., Suzuki, K., et al. (2003). Quantitative computerized analysis of diffuse lung disease in high-resolution computed tomography. *Medical Physics*, 30(9):2440–2454. [Cited on page 99.]
- Ukil, S. and Reinhardt, J. M. (2005). Smoothing lung segmentation surfaces in three-dimensional x-ray ct images using anatomic guidance1. *Academic Radiology*, 12(12):1502–1511. [Cited on pages 40, 42, 43, and 55.]
- Ukil, S. and Reinhardt, J. M. (2009). Anatomy-guided lung lobe segmentation in x-ray ct images. *IEEE Transactions on Medical Imaging*, 28(2):202–214. [Cited on pages xv, xvi, 35, 36, 39, 40, 41, 48, 49, 50, and 82.]
- Uppaluri, R., Hoffman, E. A., Sonka, M., Hartley, P. G., Hunninghake, G. W., and McLennan, G. (1999a). Computer recognition of regional lung disease patterns. *American Journal of Respiratory and Critical Care Medicine*, 160(2):648–654. [Cited on pages 97 and 98.]
- Uppaluri, R., Hoffman, E. A., Sonka, M., Hunninghake, G. W., and McLennan, G. (1999b). Interstitial lung disease: a quantitative study using the adaptive multiple feature method. *American Journal of Respiratory and Critical Care Medicine*, 159(2):519–525. [Cited on pages 97 and 98.]
- Van Ginneken, B., Katsuragawa, S., ter Haar Romeny, B. M., Doi, K., and Viergever, M. A. (2002). Automatic detection of abnormalities in chest radiographs using local texture analysis. *IEEE Transactions on Medical Imaging*, 21(2):139–149. [Cited on page 99.]
- van Rikxoort, E. M., de Hoop, B., Viergever, M. A., Prokop, M., and van Ginneken, B. (2009). Automatic lung segmentation from thoracic computed tomography scans

- using a hybrid approach with error detection. *Medical Physics*, 36(7):2934–2947. [Cited on page 45.]
- Van Rikxoort, E. M. and Van Ginneken, B. (2013). Automated segmentation of pulmonary structures in thoracic computed tomography scans: a review. *Physics in Medicine and Biology*, 58(17):R187. [Cited on pages xvi, 39, 40, 41, and 45.]
- van Rikxoort, E. M., van Ginneken, B., Klik, M., and Prokop, M. (2008). Supervised enhancement filters: Application to fissure detection in chest ct scans. *IEEE Transactions on Medical Imaging*, 27(1):1–10. [Cited on pages 48, 51, and 52.]
- Verbeken, E. K., Cauberghs, M., Mertens, I., Clement, J., Lauweryns, J. M., and Van de Woestijne, K. P. (1992). The senile lung: comparison with normal and emphysematous lungs 1. structural aspects. *Chest*, 101(3):793–799. [Cited on page 155.]
- Vuorinen, K., Ohlmeier, S., Leppäranta, O., Salmenkivi, K., Myllärniemi, M., and Kinnuma, V. L. (2008). Peroxiredoxin ii expression and its association with oxidative stress and cell proliferation in human idiopathic pulmonary fibrosis. *Journal of Histochemistry & Cytochemistry*, 56(10):951–959. [Cited on page 27.]
- Wagner, P., Dantzker, D., Dueck, R., De Polo, J., Wasserman, K., and West, J. (1976). Distribution of ventilation-perfusion ratios in patients with interstitial lung disease. *Chest*, 69(2):256–257. [Cited on pages 31 and 32.]
- Wahba, W. (1983). Influence of aging on lung function-clinical significance of changes from age twenty. *Anesthesia & Analgesia*, 62(8):764–776. [Cited on pages 155 and 191.]
- Wallaert, B., Wemeau-Stervinou, L., Salleron, J., Tillie-Leblond, I., and Perez, T. (2012). Do we need exercise tests to detect gas exchange impairment in fibrotic idiopathic interstitial pneumonias? *Pulmonary Medicine*, 2012. [Cited on page 30.]

- Walsh, S. L., Wells, A. U., Sverzellati, N., Devaraj, A., von der Thüsen, J., Yousem, S. A., Colby, T. V., Nicholson, A. G., and Hansell, D. M. (2015). Relationship between fibroblastic foci profusion and high resolution ct morphology in fibrotic lung disease. *BMC Medicine*, 13(1):241. [Cited on page 28.]
- Wang, J., Betke, M., and Ko, J. P. (2004). Shape-based curve growing model and adaptive regularization for pulmonary fissure segmentation in ct. In *International Conference on Medical Image Computing and Computer-Assisted Intervention*, pages 541–548. Springer. [Cited on pages 48 and 51.]
- Wang, J., Betke, M., and Ko, J. P. (2006). Pulmonary fissure segmentation on ct. *Medical Image Analysis*, 10(4):530–547. [Cited on pages 48 and 51.]
- Wang, J., Li, F., and Li, Q. (2009). Automated segmentation of lungs with severe interstitial lung disease in ct. *Medical Physics*, 36(10):4592–4599. [Cited on pages 40, 42, 45, and 46.]
- Wang, J.-S., Cherng, J.-M., Perng, D.-S., Lee, H.-S., and Wang, S. (2013). High-resolution computed tomography in assessment of patients with emphysema. *Respiratory Care*, 58(4):614–622. [Cited on page 97.]
- Wasserman, K. and Whipp, B. J. (1975). Exercise physiology in health and disease. *American Review of Respiratory Disease*, 112(2):219–249. [Cited on page 31.]
- Watadani, T., Sakai, F., Johkoh, T., Noma, S., Akira, M., Fujimoto, K., Bankier, A. A., Lee, K. S., Müller, N. L., Song, J.-W., et al. (2013). Interobserver variability in the ct assessment of honeycombing in the lungs. *Radiology*, 266(3):936–944. [Cited on page 94.]
- Wei, Q., Hu, Y., Gelfand, G., and Macgregor, J. H. (2009). Segmentation of lung lobes in high-resolution isotropic ct images. *IEEE Transactions on Biomedical Engineering*, 56(5):1383–1393. [Cited on page 82.]

- Weibel, E. R. (1984). The pathway for oxygen: structure and function in the mammalian respiratory system. Harvard University Press. [Cited on page 165.]
- Wells, A. U., Desai, S. R., Rubens, M. B., Goh, N. S., Cramer, D., Nicholson, A. G., Colby, T. V., Du Bois, R. M., and Hansell, D. M. (2003). Idiopathic pulmonary fibrosis: a composite physiologic index derived from disease extent observed by computed tomography. *American Journal of Respiratory and Critical Care Medicine*, 167(7):962–969. [Cited on pages 19, 22, and 96.]
- Wells, A. U., King, A. D., Rubens, M. B., Cramer, D., Du Bois, R., and Hansell, D. M. (1997). Lone cryptogenic fibrosing alveolitis: a functional-morphologic correlation based on extent of disease on thin-section computed tomography. *American Journal of Respiratory and Critical Care Medicine*, 155(4):1367–1375. [Cited on pages 22 and 30.]
- Wiemker, R., Bülow, T., and Blaffert, T. (2005). Unsupervised extraction of the pulmonary interlobar fissures from high resolution thoracic ct data. In *International Congress Series*, volume 1281, pages 1121–1126. Elsevier. [Cited on pages 48, 51, and 52.]
- Wijesinghe, M. and Dow, L. (2005). The effect of aging on the respiratory skeletal muscles. *Principles and Practice of Geriatric Medicine*, 2:671–683. [Cited on page 153.]
- Wootton, S. C., Kim, D. S., Kondoh, Y., Chen, E., Lee, J. S., Song, J. W., Huh, J. W., Taniguchi, H., Chiu, C., Boushey, H., et al. (2011). Viral infection in acute exacerbation of idiopathic pulmonary fibrosis. *American Journal of Respiratory and Critical Care Medicine*, 183(12):1698–1702. [Cited on page 20.]
- Xaubet, A., Ancochea, J., and Molina-Molina, M. (2017). Idiopathic pulmonary fibrosis. *Medicina Clínica (English Edition)*, 148(4):170–175. [Cited on pages 2, 8, 10, 11, 12, 19, 21, 22, and 23.]

- Xu, Y., Sonka, M., McLennan, G., Guo, J., and Hoffman, E. A. (2006a). Mdct-based 3-d texture classification of emphysema and early smoking related lung pathologies. *IEEE Transactions on Medical Imaging*, 25(4):464–475. [Cited on page 98.]
- Xu, Y., van Beek, E. J., Hwanjo, Y., Guo, J., McLennan, G., and Hoffman, E. A. (2006b). Computer-aided classification of interstitial lung diseases via mdct: 3d adaptive multiple feature method (3d amfm). *Academic Radiology*, 13(8):969–978. [Cited on page 98.]
- Yamamoto, T., Kabus, S., Klinder, T., Lorenz, C., Von Berg, J., Blaffert, T., Loo Jr, B. W., and Keall, P. J. (2011). Investigation of four-dimensional computed tomography-based pulmonary ventilation imaging in patients with emphysematous lung regions. *Physics in Medicine and Biology*, 56(7):2279. [Cited on page 38.]
- Zaugg, M. and Lucchinetti, E. (2000). Respiratory function in the elderly. *Anesthesiology Clinics of North America*, 18(1):47–58. [Cited on pages 150, 153, and 154.]
- Zavaletta, V. A., Bartholmai, B. J., and Robb, R. A. (2007). High resolution multidetector ct-aided tissue analysis and quantification of lung fibrosis. *Academic Radiology*, 14(7):772–787. [Cited on pages 99 and 103.]
- Zavaletta, V. A., Karwoski, R. A., Bartholmai, B., and Robb, R. A. (2006). High resolution multidetector ct aided tissue analysis and quantification of lung fibrosis. In *Medical Imaging 2006: Physiology, Function, and Structure from Medical Images*, volume 6143, page 61432Z. International Society for Optics and Photonics. [Cited on page 99.]
- Zhang, J. (2013). Development of an automated system for building a large population-based statistical model of femur morphology. PhD thesis, ResearchSpace@ Auckland. [Cited on page 56.]

- Zhang, L., Hoffman, E. A., and Reinhardt, J. M. (2006). Atlas-driven lung lobe segmentation in volumetric x-ray ct images. *IEEE Transactions on Medical Imaging*, 25(1):1–16. [Cited on page 49.]
- Zhang, X., Smith, N., and Webb, A. (2011). Medical imaging. In Feng, D. D., editor, *Biomedical Information Technology*. Elsevier Science, Oxford. [Cited on page 37.]
- Zhou, X., Hayashi, T., Hara, T., Fujita, H., Yokoyama, R., Kiryu, T., and Hoshi, H. (2004). Automatic recognition of lung lobes and fissures from multislice ct images. In *Proceedings of SPIE*, volume 5370, pages 1629–1633. [Cited on pages 48, 49, and 51.]
- Zhu, C., Qi, S., van Triest, H., Wang, S., Kang, Y., and Yue, Y. (2010). Automatic 3d segmentation of human airway tree in ct image. In *Biomedical Engineering and Informatics (BMEI)*, 2010 3rd International Conference on, volume 1, pages 132–136. IEEE. [Cited on page 38.]
- Zielonka, T., Demkow, U., Radzikowska, E., Bialas, B., Filewska, M., Zycinska, K., Obrowski, M., Kowalski, J., Wardyn, K., and Skopinska-Rozewska, E. (2010). Angiogenic activity of sera from interstitial lung disease patients in relation to pulmonary function. *European Journal of Medical Research*, 15(2):229. [Cited on page 26.]